Design and Synthesis of Cyanine Dyes for Selective Targeting and Imaging of Cellular Mitochondria

THESIS SUBMITTED FOR

THE DEGREE OF DOCTOR OF PHILOSOPHY (SCIENCE)

OF

JADAVPUR UNIVERSITY

JULY, 2022

By

PRANAB CHANDRA SAHA, M.Sc.

DEPARTMENT of CHEMISTRY

INDEX NO*: *76/18/Chem./25

***REGISTRATION NO*: SCHEM1107618**

***DATE OF REGISTRATION*: 21st FEBRUARY, 2018**

JADAVPUR UNIVERSITY, KOLKATA-700032

WEST BENGAL, INDIA

I would like to dedicate this thesis to my beloved parents and all of my teachers.

Jadavpur University
Department of Chemistry
Organic Chemistry Section
Kolkata-700032, India

Dr. Samit Guha
Assistant Professor
Mobile: +91 9163750994
E-mail: samitfsu@gmail.com;
samit.guha@jadavpuruniversity.in

22nd July, 2022

CERTIFICATE FROM THE SUPERVISOR

This is to certify that the thesis entitled "***Design and Synthesis of Cyanine Dyes for Selective Targeting and Imaging of Cellular Mitochondria***" submitted by **Sri Pranab Chandra Saha**, who got his name registered on **21st February, 2018** for the award of **Ph. D. (Science) degree of Jadavpur University**, is absolutely based upon his own work under the supervision of **Dr. SAMIT GUHA** and that neither this thesis nor any part of it has been submitted for either any degree / diploma or any other academic award anywhere before.

Samit Guha 22/07/2022

.....

(Signature of the Supervisor)

Dr. Samit Guha
Assistant Professor
Department of Chemistry
Jadavpur University
Kolkata-700032, India

Design and Synthesis of Cyanine Dyes for Selective Targeting and Imaging of Cellular Mitochondria

INDEX NO.: 76/18/Chem./25

Abstract: The development of selective organelle targeting agents with various imaging modalities is a promising approach for early detection and diagnosis of cellular organelle related deadly diseases. However, rational control for selective targeting of cellular organelles using small molecule fluorescent probes has remained a challenge due to the highly complicated cellular environment. Among all other cellular organelles, mitochondria are unique and indispensable, which not only harness energy through ATP production but also play a pivotal role in regulating cellular protein homeostasis, oxidative metabolism and maintaining intracellular redox balance. In contrary to other cellular organelles, mitochondria are arduous to target because of their distinctive double layer membrane and exceptionally negative inner mitochondrial membrane (IMM) potential [$(\Delta\Psi_m)_{normal} \approx -150$ to -180 mV] that act as barriers for the ingestion of molecules. Moreover, in cancer cells IMM potential [$(\Delta\Psi_m)_{cancer} \approx -220$ mV] is much more hyperpolarized compared to normal cells. In my research work, I have utilised the aforementioned extraordinary biophysical membrane property and hydrophobic nature of mitochondria for the development and synthesis of symmetrical as well as unsymmetrical cyanine fluorophores and their peptide conjugates for selective targeting and imaging of cellular mitochondria. A water soluble lipophilic cationic dual targeting NIR unsymmetrical cyanine-5 probe conjugated with maleimide and mitochondria targeting triphenylphosphonium (TPP^+) functionalities has also been developed for selective targeting and labeling of cysteine (Cys) exposed proteins inside the live cell mitochondria. These cyanine dyes exhibit high photostability, NIR absorption/emission, high molar extinction coefficient, narrow absorption/emission band, high fluorescence lifetime, and high fluorescence quantum yield. Mitochondrial target specificity of all the fluorophores is demonstrated by colocalization experiments carried out with the commercially accessible mitochondrion-tracking probes. Moreover, the mitochondria targeted NIR cyanine/peptide conjugates reaches the critical aggregation concentration inside the mitochondria of cancer cells due to the strong negative inner mitochondrial membrane potential [$(\Delta\Psi_m)_{cancer}$ -220 mV] and self-assembles to form amyloid fibrils or other nanostructures at the target site, which is responsible for the mitochondrial dysfunction and cytotoxicity. The narrow excitation and emission bands also make these probes a perfect choice for multicolor cellular imaging.

Samit Guha 22/07/2022

Signature with Seal of the Supervisor

Dr. Samit Guha
Assistant Professor
Department of Chemistry
Jadavpur University
Kolkata-700032, India

Pranab Chandra Saha
22/07/2022

Full Signature of the Candidate

Acknowledgements

I would like to express my sincere gratitude and deep appreciation to my supervisor Dr. Samit Guha, Department of Chemistry, Jadavpur University, for stimulating discussions, constructive ideas, expert criticism and valuable guidance throughout the progress of this research work. Without his guidance and enthusiasm completion of the thesis would not be possible. The scientific discussions those I had with him motivated me a lot. Besides being an excellent supervisor, Dr. Guha also a great human being. He also helped me in the improvement of my writing skill. I am also grateful to her wife Dr. Pumpa Guha for her valuable advice regarding the joining of Ph.D.

I am grateful to our collaborators Prof. Maitree Bhattacharyya (Department of Biochemistry, University of Calcutta) and Dr. Arunima Sengupta (Department of Life Sciences and Biotechnology, Jadavpur University) for their spontaneous help in biological studies related to my research work.

I would also like to thank my friends Dr. Tanima Chatterjee (Department of Biochemistry, University of Calcutta), Dr. Rudradip Pattanayak (Department of Biochemistry, University of Calcutta), Dr. Jayeeta Samanta (Department of Life Sciences and Biotechnology, Jadavpur University), and Shreya Das (Department of Life Sciences and Biotechnology, Jadavpur University) for their extensive help and valuable suggestions regarding biological work.

I am obliged to the Authorities of Jadavpur University and Department chemistry for providing laboratory, library and proper atmosphere for carrying out my research work. I also thankful to all the teachers of Organic chemistry section, Jadavpur University and all the supporting staff-members of the department.

I am grateful to Dr. Jayati Banerjee (Former Product Manager CEM Bioscience, India) for giving me handful training in microwave peptide synthesizer (CEM, Discover Bio).

It is my pleasure to thank Dr. Nayim Sepay for helping me in Docking study and providing valuable suggestions throughout my research work.

I am also thankful to Indian Institute of Chemical Biology (CSIR-IICB, Kolkata) and Bose Institute, Kolkata for allowing me to use confocal microscopy instrument for my research work.

I take pride in thanking my group members, Ayan Mukherjee, Rabi Sankar Das, and Tapas Bera for their kind support and encouragement. I am thankful to Project students Mr. Shuvasish Sarkar, Mr. Samiran kar for their support in my research work.

I am also thankful to DST-SERB, Govt. of India for financial assistance during the course of my research work.

It is my pleasure to thank Prof. Sujoy baitalik (Jadavpur University, Department of Chemistry), Prof. Tapan Kumar Mondal (Jadavpur University, Department of Chemistry), Prof. Asok Kumar Mallik (Jadavpur University, Department of Chemistry), Prof. Umesh Chnandra Halder (Jadavpur University, Department of Chemistry),Mr. Sounak Bhattacharya (Technical Assistance, confocal microscopy section, CSIR-IICB, Kolkata), Mr. Gopal Krishna Manna (Drawing Section, IACS, Kolkata), Mr. Prantik Saha (confocal microscopy section, Bose Institute) and all the fellow friends of Department of chemistry, Jadavpur University for their overwhelming help and support throughout my research work.

I think this is the best opportunity to convey my heartiest regards to all of my teachers, especially Mr. Tapesh Ganguli for his support in my early school days.

My thanks to all of my friends (especially Mr. Kausik Gayan, Mr. Soumyajit hazra, and Mr. Biplab Mondal, Mr. Soumitra Kumar Mandal), for their spontaneous help throughout my research work.

Last but not least, I embrace the pleasure of expressing my deep regards and love for my parents (Baba and Ma), my uncle, Mr. Biswajit Saha (Mama) for their valuable guidance, encouragement and earnest devotion. Their blessings and well-wishes always guide me to select the right pathway in life.

Pranab Chandra Saha

Pranab Chandra Saha 22/07/2022

22nd *July, 2022*
Department Of Chemistry
Jadavpur University,
188, Raja S. C. Mallick Road,
Jadavpur, Kolkata, West Bengal-700032

PREFACE

The research embodied in the present thesis entitled "***Design and Synthesis of Cyanine Dyes for Selective Targeting and Imaging of Cellular Mitochondria"*** deals with the synthesis and characterization of visible to near-infrared (NIR) symmetrical as well as unsymmetrical cyanine dyes and their conjugates along with their application in selective targeting and imaging of cellular mitochondria of fixed and live cells using confocal laser scanning microscopy. Moreover, these fluorophores are found to be useful in measuring mitochondrial membrane potential as well as detecting dysfunction of mitochondria.

The present investigation described in this thesis have been carried out by the author in the Department of Chemistry, Jadavpur university, Kolkata, during the period December, 2017 to July, 2022 under the supervision of Dr. Samit Guha, Department of Chemistry, Organic section, Jadavpur University, Kolkata-700032, India.

The thesis has been presented in seven chapters:

Chapter 1 consists of a brief discussion on mitochondria and the recent advancement of mitochondria targeting organic molecules, sensors, imaging agents, particularly near-infrared (NIR) fluorophores, aggregation induced emission luminogens, natural and synthetic peptides, enzyme instructed self-assembly, supramolecular self-assembly, their selective translocation into the mitochondrial matrix, mechanism of action, and therapeutic applications.

Chapter 2 describes the reagents used and experimental procedures, carried out to preform the entire work embodied in this thesis.

Chapter 3 deals with design and synthesis of water-soluble mitochondria-selective multicolour imaging agents that consist of a target-specific moiety conjugated with a near-infrared (NIR) imaging agents through variable spacer length. Mitochondrial target specificity was demonstrated by colocalization experiments using the mitochondrion-tracking probe, MitoTracker Red and lysosome-tracking probe, LysoTracker Green in the fixed A549 cells. Moreover, our synthetic NIR cyanine dyes are also useful for determination of mitochondrial membrane potential via monitoring the mitochondrial membrane depolarization process.

Chapter 4 describes the microwave-assisted efficient synthesis of supramolecular β-sheet forming peptide conjugated unsymmetrical near-infrared (NIR) cyanine-5 (Cy-5) chromophore for selective targeting, imaging, and monitoring of mitochondrial dysfunction.

Annexin V-FITC/PI apoptosis detection assay was used to determine the signal pathway of mitochondria targeted cellular dysfunction.

Chapter 5 demonstrates the design and construction of FF dipeptide anchored unsymmetrical visible Cy−3 and NIR Cy−5 chromophores comprising a mitochondria specific triphenylphosphonium (TPP^+) group by using a microwave (MW) aided Fmoc solid phase peptide synthesis (SPPS) procedure on Wang resin. These lipophilic cationic fluorescent peptide molecules spontaneously and selectively accumulate inside the mitochondria of human carcinoma cells because of the extremely negative inner mitochondrial membrane potential [$(\Delta\Psi_m)_{cancer} \approx -220$ mV] and reach the critical aggregation concentration inside the mitochondria to form supramolecular nanotubes which are accountable for malignant mitochondria targeted early apoptosis.

Chapter 6 introduces a water soluble lipophilic cationic dual targeting NIR unsymmetrical cyanine-5 probe conjugated with maleimide and triphenylphosphonium (TPP^+) functionalities for selective targeting and labeling of cysteine (Cys) exposed proteins inside the live cell mitochondria. The lipophilic cationic TPP^+ subunit expected to facilitate the rapid initialization of Cy-5-Mal/TPP^+ through the lipid bilayer and accumulates inside the inner mitochondrial matrix with an elevated concentration where maleimide functionality will selectively label the exposed cysteine residue of mitochondrial proteins by undergoing chemoselective Michael addition reaction with reactive thiols (SH). On the basis of this dual localization effect, Cy-5-Mal/TPP^+ would remain in the mitochondria for longer time period even after membrane depolarization and facilitate the tracking and visualization of mitochondrial movement in live cells using confocal laser scanning microscopy (CLSM). Meanwhile, the fluorescently modified proteins obtained by such spatially limited chemoselective reactions are identified by in-gel fluorescent assay and further characterised by MALDI-TOF-MS carried out with Cy-5-Mal/TPP^+ treated A549 cell lysate to confirm their localization in live cells.

Chapter 7 presents the summary of all the investigations described in this thesis. The significance of the results obtained from those investigations has also been discussed in this chapter.

Chapter 3−6 begins with a brief introduction followed by Experimental Methods, Results & Discussion, and Conclusions.

The list of Publications has been incorporated at the end of this thesis.

Abbreviations

Abbreviations used for amino acids, peptides, amino acid derivatives, substituents, reagents are largely in accordance with the recommendations of IUPAC–IUB commission on Biochemical Nomenclature, **1974**, *Pure and Applied Chemistry*, *40*, 315–331. Other symbols and nomenclature, etc. are based on the list in *J. Biol. Chem.* **1989**, 669–671. Standard three letter coding is used for all the amino acids. Additional abbreviations used in this thesis are listed below–

Aβ	Amyloid-β
ACN	Acetonitrile
AFM	Atomic Force Microscopy
AIE	Aggregation-induced emission
ATP	Adenosine triphosphate
CAC	Critical aggregation concentration
CD	Circular dichroism
Cy	Cyanine
CLSM	Confocal laser scanning microscopy
2-CTC	2-chloro tritylchloride
d	doublet
DBU	1,8-diazabicyclo[5.4.0]undec-7-en
DCM	Dichloromethane
DIPEA	*N*,*N*-Diisopropylethylamine
DLS	Dynamic Light Scattering
DMEM	Dulbecco's modified eagle medium
DMSO	Dimethyl sulfoxide
DMF	*N*, *N* – dimethylformamide
DQF COSY	Double Quantum Filtered Correlation Spectroscopy
EISA	Enzyme instructed self-assembly
FBS	Fetal Bovine Serum
FITC	Fluorescein isothiocyanate
Fmoc	9-Fluorenylmethoxycarbonyl

FACS	Fluorescence-activated cell sorting
GSH	Glutathione
HATU	1-Bis(dimethylamino)methylene]-1H-1,2,3-triazolo[4,5-b]pyridinium 3-oxide hexafluorophosphate
HBTU	*N*, *N*, *N′*, *N′*-Tetramethyl-*O*-(1H-benzotriazol-1-yl)uronium hexafluorophosphate
HRMS	High-resolution mass spectrometry
HRMS-ESI	High-resolution electrospray ionisation mass spectrometry
HOBT	1- hydroxybenzotriazole
IMM	Inner mitochondrial membrane
IMS	Intermembrane space
J	Coupling constant
m	Multiplate
MTDR	Mitotracker Deep Red FM
MTG	MitoTracker Green FM
MTT	3-(4,5-dimethyl-2-thiazolyl)-2,5-diphenyltetrazolium bromide
MW	Microwave
NIR	Near-infrared
NMR	Nuclear Magnetic Resonance
PDT	Photodynamic therapy
PTT	Photothermal therapy
ROS	Reactive oxygen species
s	singlet
SEM	Scanning Electron Microscopy
SPPS	Solid phase peptide synthesis
t	triplet
TCSPC	Time-correlated single photon counting
TLC	Thin layer chromatography
TEM	Transmission Electron Microscopy
TIM	Translocase of the inner membrane
TOM	Translocase of the outer membrane
TPP^+	Triphenylphosphonium cation

Contents

Chapter 1

General Introduction

Origin and Importance of Mitochondria:

Mitochondria were first discovered in 1857 by Albert von Kölliker from the voluntary insect muscles. In 1890 Richard Altman named these structures “bioblasts”.[1] Carl Benda renamed the organelle in 1898 and coined the term "mitochondria" from the Greek *mitos* means “thread”, and *chondros* means "granule".[2] Mitochondria are the “powerhouse of cells” coined by Philip Siekevitz in 1957 as they harvest most of the cell's supply of chemical energy adenosine triphosphate (ATP).[3] Mitochondria play crucial roles in several metabolic processes like the Krebs cycle, biosynthesis of amino acids, lipids, heme, and Fe/S clusters; regulate cellular signalling pathways via reactive oxygen species (ROS) generation, regulate Ca^{2+} homeostasis, differentiation, and programmed cell death such as apoptosis. Mitochondrion has various compartments such as a porous outer mitochondrial membrane (OMM), a hydrophobic heavily packed inner mitochondrial membrane (IMM), the intermembrane space (IMS), cristae, and matrix.[4,5] Although DNA is primarily present inside the cell nucleus, however, the mitochondrion contains its own independent genome known as mitochondrial DNA (mtDNA) discovered by Margit Nass and Sylvan Nass in 1963.[6] mtDNA is inherited exclusively from the mother to children, while nuclear DNA is inherited from both parents. In exceptional cases, human babies sometimes inherit mtDNA from both mother and father resulting in mtDNA heteroplasmy. Human mtDNA is a double-stranded circular molecule comprising of 16569 base pairs and 37 genes which encodes 22 transfer RNAs (tRNAs), 2 ribosomal RNAs (rRNAs), and 13 polypeptides. Mitochondria are spherical, granular, linear, curved or rod shaped and found in most eukaryotic cells. The size of the mitochondria is typically 0.5–1 μm in diameter, 1–10 μm in length, while the distance between the cristae in mitochondrion is around 100 nm. Mitochondria

are frequently altering their shape, size, and position due to mitochondrial dynamics by undergoing fission, fusion, and motility. Monocercomonoides is the first eukaryotes found without mitochondria. Moreover, mature mammalian red blood cells lack a mitochondria, whereas, each liver cell comprises 1000-2000 mitochondria. Malaria cell contains only one mitochondrion. Mammalian mitochondria encompass more than 1500 proteins among that only 13 are encoded by mtDNA for oxidative phosphorylation and rest are by the nuclear DNA which is then post-translationally imported in mitochondria with the help of translocase of the outer membrane (TOM), translocase of the inner membrane (TIM), mitochondrial chaperones, and a sorting and assembly machinery (SAM).[4,5,7] Due to the lack of introns and self-repairing capacity, mtDNA are vulnerable to mutation (10−20 times more susceptible to mutations than nuclear DNA).[8] Mutations in mtDNA cause numerous inherited diseases like Leber's hereditary optic neuropathy (LHON), Kearns-Sayre syndrome, MELAS (myopathy, encephalopathy, lactic acidosis and stroke-like episodes) syndrome, and Leigh syndrome.[8-11] Moreover, mitochondrial dysfunction is responsible for cardiovascular diseases (e.g., ischemia/reperfusion injury, atherosclerosis, heart failure, and stroke), neurodegenerative diseases (Alzheimer's, Huntington's, and Parkinson disease), obesity, diabetes, aging, and different types of malignancies.[5,11-13] Defects in nuclear genes can also causes dysfunction of imported mitochondrial proteins which results various diseases including hereditary spastic paraplegia, Friedreich's ataxia, and Wilson's disease. However, so far most of the mitochondrial diseases don't have a specific and sensitive biomarker. There are still huge cavities in understanding of mitochondrial functions, dynamics, and the molecular root of mitochondria associated diseases. Development of selective mitochondria targeting agents with various imaging modalities are the

key steps for early detection and diagnosis of mitochondria related debilitating diseases and it has gained major attention over last few decades.[5,13-17] New drugs are explicitly required for the treatment of mitochondria related serious and life threatening diseases. In contrary to other cellular organelles, mitochondria are arduous to target because of their distinctive double layer membrane and exceptionally negative inner mitochondrial membrane (IMM) potential [$(\Delta\Psi_m)_{normal} \approx -150$ to -180 mV] that act as barriers for the ingestion of molecules. Moreover, in cancer cells IMM potential [$(\Delta\Psi_m)_{cancer} \approx -220$ mV] is much more hyperpolarized compared to normal cells.[18] The IMM is rich in the negatively charged lipid cardiolipin (contains four fatty acids rather than two) that assists to construct the cristae structure as well as to increase the surface area of the IMM. The huge surface area is vital for the entrapment of the electron transport chain (ETC) proteins which are inserted in the IMM. The ETC is encompassed of four protein complexes I−IV which execute the chain of biochemical reactions, communally known as oxidative phosphorylation (OXPHOS). Nicotinamide adenine dinucleotide (NADH) donates its electrons through complex I to the coenzyme Q (CoQ) pool that also gets electrons from other sources.[4,5] From the CoQ pool, the electrons transports through complex III to cytochrome c (cyt *c*) then these electrons reduce O_2 to form H_2O at complex IV. These redox reactions create a substantial extent of energy, which is exploited by the ETC to transfer the H^+ into the IMS of mitochondria. A proton-motive force resulting from the gradient then empowers the F_1F_0-ATP synthase (also known as complex-V) to synthesize ATP from ADP though transferring the H^+ back into the mitochondrial matrix. ETC and negatively charged lipid cardiolipin is accountable for the high negative IMM potential.[5] Moreover, the distinctive function of mitochondria also related to the mitochondrial pH and in normal conditions; mitochondria preserve an alkaline

pH (pH 8) due to H^+ ejection across the IMM via the ETC. Amendments in mitochondrial pH level may trigger mitochondrial dysfunction and cause apoptosis. Mitochondrial acidification is observed through the mitophagic elimination (mitophagy) of malfunctioning mitochondria by lysosomal (pH 4-5) fusion.[19,20] Moreover, mitochondrial microenvironments such as viscosity, polarity, and membrane tension also plays important role for the unique functions of mitochondria. The temperature of mitochondria is ~50°C which is ~10°C higher than the body ambient temperature.[21] The mitochondrial temperature can be a crucial indicator of cell metabolism.

Recent Developments in Mitochondria Related Research:

Numerous events in mitochondria are affected by amendment in mitochondrial microenvironments. Various turn-on and ratiometric fluorescent probes have recently been developed for the determination of mitochondrial pH, viscosity, polarity, membrane tension, and temperature.[22-32] Mitochondrion-targeting drugs have been recognized to be potentially more effective than their nontargeting compounds. Active targeting to mitochondria may prevent potential off-target toxic side effects of drugs. However, delivery of cargoes inside the mitochondria selectively is one of the foremost problems that remain to be resolved. Amongst the numerous approaches to target mitochondria as well as proteins and lipids residing therein, one of the primarily used methods is to utilize the unusual biophysical membrane property of mitochondria. It helps faster uptake and accumulation of lipophilic cationic moiety conjugated with antioxidants or anticancer drug molecules or sensors or imaging agents inside the mitochondrial matrix. Delocalized lipophilic cations such as triphenylphosphonium (TPP^+, positive charge on P delocalized over the three phenyl groups), quaternary ammonium, pyridinium, dequalinium, isoquinolium, and guanidinium based molecules; visible to near infrared (NIR)

cyanine (Cy) and rhodamine (Rho) dyes; fluorinated boron-dipyrromethene (BODIPY) probes, natural and synthetic mitochondria-targeting peptides, and peptidomimetics have been effectively utilized for mitochondria specific cargos delivery.[33-43] Recently, smart multifunctional nanocarriers based innovative approaches have been used for the development of mitochondria targeted nanotherapeutics.[44-47] Stimuli-responsive targeted nanocarriers have been developed that can allow controlled release of therapeutics at the mitochondrial site.[48] Intensive research efforts have focused on developing targeted therapeutics with imaging diagnostics for mitochondria. Several therapeutic have already been tested *in vitro* and *in vivo*, some of them completed their clinical trials and some are entered into clinical trials. Mitochondria are related with many hallmarks of malignant tumors such as $(\Delta\Psi_m)_{cancer} > (\Delta\Psi_m)_{normal}$, elevated amounts of ROS in cancer, mitochondria in cancer cells express a high level of GSH with respect to normal tissue, swapping glycolysis from OXPHOS to the anaerobic metabolism which is connected with lacking mitochondria functions, certain enzymes are overexpressed in malignant mitochondria etc. Targeted malignant mitochondrial dysfunction can inhibit tumor cell growth. Malignant mitochondrial metabolism is evolving as an innovative drug target for antineoplastic exploration. Till date, no clinical antitumor investigations of targeted mitochondrial drug delivery systems have been performed. So, targeting malignant mitochondria to develop anticancer drugs is an emerging field of current research. How the local concentration of the self-assembling peptides inside the mitochondria can be amplified by transporting them with mitochondria selective targeting groups have been discussed in this chapter.[49-51] Advancement of enzyme instructed self-assembly (EISA) and supramolecular self-assembly of amphiphilic peptide at the target site to induce mitochondrial dysfunction driven programmed cancer

cell deaths have also been reported.[52–54] Mitochondria-mediated apoptosis is governed by the Bcl-2 (B-Cell lymphoma 2) family proteins that exist in the OMM and this family of proteins have either pro- or anti-apoptotic actions. They control the apoptosis by regulating the permeabilization of the OMM, trigger the irreversible leakage of cyt *c* into the cytosol, consequent activation of caspase family proteins which ultimately leads to programmed cell death.[55-58] ROS produced in mitochondria play crucial functions in the inflection of signal transduction cascades and transcription factors. However, extreme formation of ROS and reactive nitrogen species (RNS) potentially induce damage to all cellular components. ROS and RNS seepage consequences in the triggering of cytosolic stress pathways, lipid destruction, mtDNA damage, protein damage, and the upregulation of JNK, p38, and p53.[59,60] Mitochondrial thiol (–SH) containing proteins and mitochondrial GSH (mGSH) play important roles in mitochondrial functions. Research work focusing on the developments of turn-on fluorescence and ratiometric fluorescence sensors for determining mitochondrial –SH containing proteins, mGSH, HCN, ROS, RNS, and ATP levels in living cells have also been reported.[61-69] Enzyme triggered activatable fluorescent probes for mitochondria targeted imaging have also been deliberated.[24,70-72] Mitochondria are very sensitive to ROS and hyperthermia and these features have been explored in NIR light induced photodynamic therapy (PDT), photothermal therapy (PTT) as well as combination therapy for ablation of cancer cells.[73-80] In this chapter the recent development of mitochondria targeting organic molecules, imaging agents, aggregation-induced emission (AIE) biomarkers, photosensitizers including various NIR-I (650-1000 nm) and NIR-II (1000-1700 nm) probes along with fluorophore tagged mitochondria targeting self-assembling amphiphilic peptides, EISA, and their selective translocation into mitochondrial matrix,

mechanism of action, and therapeutic applications in ablation of cancer cells have been discussed and summarized.[81-87] Here, I have also discussed the important features of structural prerequisites and designed principles for mitochondria targeted multifunctional delivery vehicles. To get better understanding of mitochondrial function and metabolic states along with their structure and morphology contemporary mitochondrial investigation profoundly depends on the advancement of live-cell imaging methods. Latest advancement of some mitochondria tracking NIR fluorophores with excellent photophysical properties has opened up a new avenue to monitor mitochondrial dynamics including ultrastructures, mitophagy, and cross talk with other organelles during several pathological conditions by super-resolved fluorescence microscopy.[88-92] In addition, the most important emphasis has recently been focused on the organelle localizable live cell protein labelling approach to explore mitochondrial proteomics.[93,94]

Design of Mitochondria Targeting Organic Molecules:

For the design of effective mitochondriotropics (mitochondria targeting agents) two important biophysical parameters such as lipophilicity and charge of the molecule need to be considered. Furthermore, for successful mitochondrial localization, molecules also need to cross the barrier of both plasma membrane as well as mitochondrial membranes. Typically IMM possesses more negative membrane potential ($\Delta\Psi_m$ −150 to −180 mV) compare to plasma membrane ($\Delta\Psi_p$ −30 to −60 mV) which allows higher accumulation of lipophilic cation inside the mitochondrial matrix. In comparison to normal healthy cells malignant cells mitochondria maintain hyperpolarised IMM potential [$(\Delta\Psi_m)_{cancer}$ ~ −220 mV], which offers designing scope to selectively target cancerous cell mitochondria over non-cancerous mitochondria. Another

approach is to target mitochondrial membrane components, such as negatively charged phospholipid CL (primarily located in the IMM) and proteins residing therein. However, it is challenging to target mitochondria due to the complex biological environment.

Design of Lipophilic Cationic Organic Molecules:

Over the last few decades, covalently modified lipophilic cationic compounds have been widely used as mitochondria-targeting vehicles, due to their convenient synthetic protocol and the high specificity. Higher the lipophilicity and the positive charge density, easier it is to cross the hydrophobic phospholipid bilayers to accumulate inside the mitochondrial matrix. The delocalised lipophilic cationic mitochondriotropics can able to dissipate the positive charge over the large surface area either via shielding the charge or delocalising it while passing through the IMM space and this results dropping of the activation energy for transportation through the phospholipid bilayer. The Nernst equation shows that for every ~61.5 mV increase in $\Delta\Psi_m$, the concentration of the lipophilic molecules rises ten times; thus, in response to the $\Delta\Psi_p$ of −30 to −60 mV these compounds first concentrate in the cytosol 5–10 times more than that in the extracellular matrix, and after that they further accumulate within the mitochondrial matrix 100–1000-fold higher than cytosolic accumulation in response to the hypernegative IMM potential. Inspired by the TPP^+, ammonium, pyridinium, isoquinolinium and other mitochondriotropics having comparable characteristics has also been developed (**Figure 1**).[81,95-101] Among these delocalized cationic guanidinium containing arginine, oligomers comprising of chiral bicyclic guanidinium moieties, nonpeptidic oligoguanidinium, sorbitol conjugated with guanidinium residues, octa-arginine oligomers for mitochondria targeting have been developed

(**Figure 1**).[39,102,103] Delocalized cationic rhodamine, cyanine, dequalinium, and berberinium have also been used (**Figure 1**).[38,40,42,104,105]

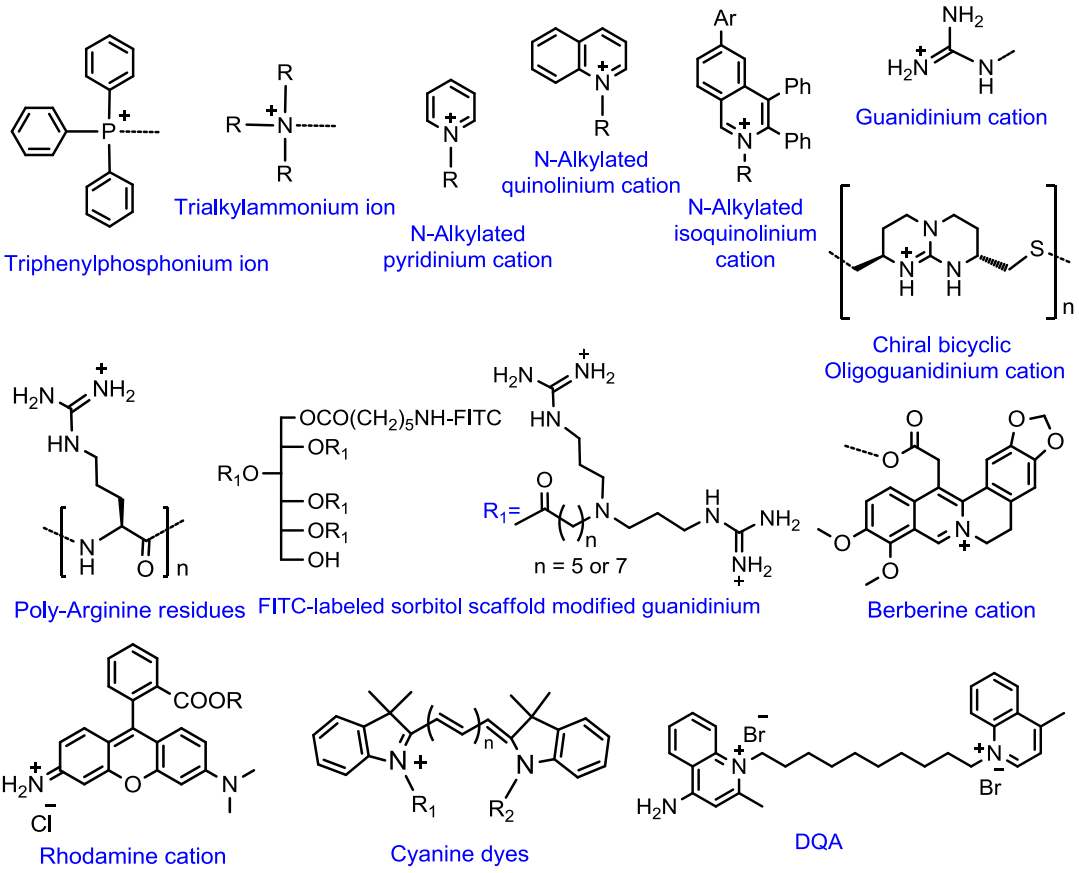

Figure 1. Mitochondria targeting structural scaffolds.

Triphenylphosphonium Ion Conjugated Bioactive Mitochondria Targeting Molecules:

Murphy and co-workers was first applied TPP^+-tethered bioactive molecules for proficient mitochondrial delivery.[106–108] Among the various mitochondria targeting functionalities TPP^+ bioconjugated mitochondria targeting molecules are the most effective and extensively used due to its

delocalized cationic character, high lipophilicity, stability in physiological conditions, relatively simple synthetic and purification method, and the minimal reactivity toward cellular components.[109–111] TPP^+ moiety has been bioconjugated with a variety of small organic molecules such as antioxidants ubiquinone (MitoQ), ebselen (Mito-Ebselen), vitamin E (MitoVitE), curcumin (Mito-Curcumin) and these compounds preferentially accumulate within mitochondria due to the negative IMM potential and detoxify mitochondria via preventing lipid peroxidation and protecting from oxidative damage.[112–114] Other biologically important TPP^+-conjugated mitochondria targeting small molecule superoxide scavenger such as Mito-TEMPOL and MitoHE and superoxide spin trapping agent like Mito-DIPPMPO were also reported.[115–117]

Mitochondria Targeting Fluorophores:

Mitochondria are dynamic organelles that are constantly undergoing fusion and fission to cope up with abnormality in the ETC, excess oxidative stress, and increase in ROS level. Hence, to monitor these important subcellular events, and to measure important physical properties as well as to monitor the morphological change and other critical events in mitochondria, probes are required which can selectively stain and image mitochondria. Currently, there are numerous probes including MitoTracker, MitoSox, CellLight series, BODIPY based, and rhodamine based fluorophores are commercially available that can stain mitochondria or sense ROS generating events.[118] However, many of these dyes have some limitations like low photostability, smaller Stokes shifts; less cell penetrating ability, phototoxicity, and respiration-inhibitory activity. Hence, some structural modifications as well as new probes are required for effective mitochondrial staining and imaging. Due to hydrophobic nature of mitochondrial membrane with high negative IMM

potential most of the commercially available as well as synthesized mitochondria targeting probes are lipophilic and delocalized cationic which enhances membrane permeability and higher accumulation of these probes inside the mitochondrial matrix. In last few years several fluorophores were developed which exhibit improved photophysical properties and these synthetic probes found to be effective when used in *in vivo* and *in vitro* fluorescence imaging purpose. Meanwhile, there are some NIR-I and NIR-II dyes have been used successfully in confocal laser scanning microscopy (CLSM) as well as in super resolution fluorescence microscopy.

Commercially Available Mitochondria Targeting Probes:

Most of the commercially available Mitotracker probes that used for live cell imaging contain lipophilic cationic cyanine and rhodamine scaffold linked with mitochondrial –SH reactive benzyl chloride functionality (**Figure 2**).[119,120] These lipophilic cationic dyes selectively accumulate inside the mitochondria in potential driven manner. A cyanine dye JC-1 (5,5′,6,6′-tetrachloro-1,1′,3,3′-tetraethylbenzimidazolocarbocyanine iodide) is utilized to monitor mitochondrial membrane potential alteration. It accumulates in mitochondria under potential driven force and forms J-aggregates to change the

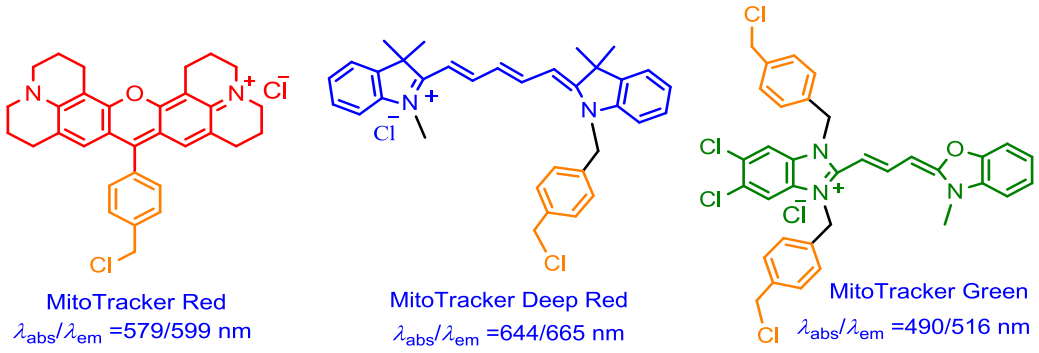

Figure 2. Mitochondrial thiol reactive benzyl chloride group containing commercially available MitoTrackers.

emission from green (λ_{em} 529 nm) to red (λ_{em} 590 nm). Under mitochondrial depolarisation this probes leak out to cytosol to give green fluorescence. The ratio of red/green fluorescence intensity gives a ratiometic measure of mitochondrial membrane potential depolarisation and it is not altered by mitochondrial shape, size or density. Similar to JC-1 other cyanine dyes such as JC-9, $DiOC_6$, Rhodamine-123, tetramethylrhodamine methyl (TMRM) ester, and tetramethylrhodamine ethyl (TMRE) ester were also often used to monitor mitochondrial membrane potential depolarisation (**Figure 3**).[118,121,122] Among these dyes JC-1 is the most consistent and extensively used dye in flow

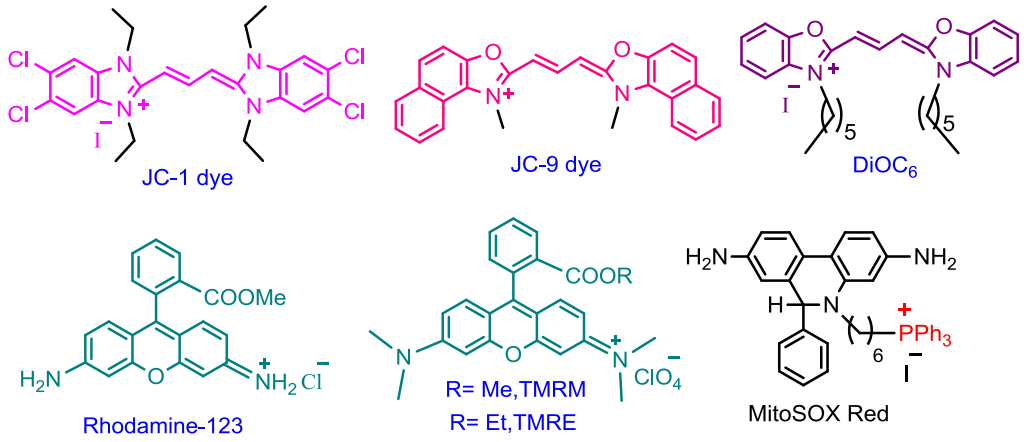

Figure 3. Mitochondrial membrane potential change monitoring cyanine and rhodamine probes. MitoSOX Red for mitochondrial $O_2^{-\bullet}$ sensing in live cells. cytometry to quantify mitochondrial depolarisation.

Mitochondrial superoxide ($O_2^{-\bullet}$), which is the predominant ROS in mitochondria is formed as a byproduct of oxidative phosphorylation (leaky electrons can interact with O_2 to form $O_2^{-\bullet}$). MitoSOX Red ($\lambda_{ex}/\lambda_{em}$ 510/580 nm) is a TPP^+ conjugated fluorogenic probe that used to trace mitochondrial $O_2^{-\bullet}$ in live cells (**Figure 3**). Due to the presence of TPP^+ moiety it readily

accumulates to mitochondria and get oxidised by $O_2^{-\bullet}$ to give red fluorescence. Moreover, the MitoSOX Red is highly selective for $O_2^{-\bullet}$ but inert towards other ROS and RNS.

Mitochondria Targeting Rhodamine, Rosamine, and Rhodocyanine Fluorophores:

Due to more negative IMM potential of cancerous cell compared to that of non-cancerous cell [$(\Delta\Psi_m)_{cancer} \approx -220$ mV vs $(\Delta\Psi_m)_{normal} \approx -150$ to -180 mV] delocalized lipophilic cations such as rhodamines, rosamines, and rhodocyanines selectively accumulate in cancer cell mitochondria and shown anticancer activity when used alone or bioconjugated with other anticancer or drug molecules. During myogenesis mitochondria undergo differentiation to cope up with higher rate of energy consumption that required for muscle contraction and to monitor this process two rosamine based probes A25 and B25 were used (**Figure 4a**).[123] Along with some conventional rhodamine probes those used to monitor mitochondrial membrane potential change a few modified rhodamine based compounds such as SiR-Mito-8, Rhodamine voltage reporter (RhoVR), were also reported (**Figure 4b,c**).[124,125] SPIRIT RhoVR 1 was a voltage sensitive fluorophore developed by Miller et al. that sense the mitochondrial membrane voltage (V_{mem}) via photoinduced electron transfer

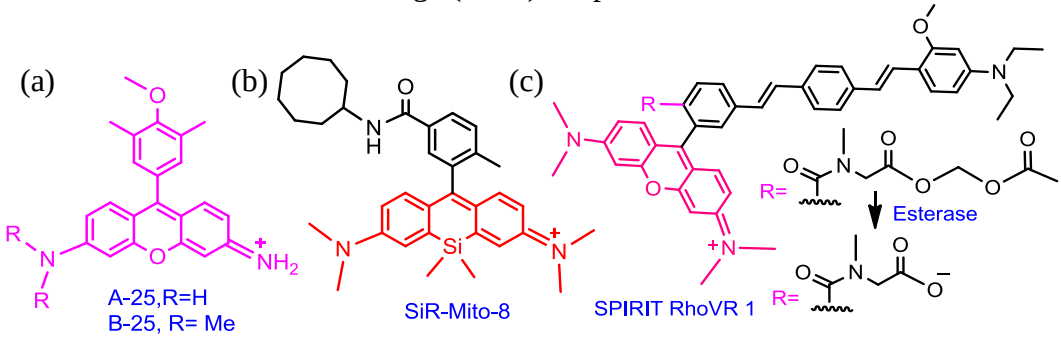

Figure 4. Rhodamine derivatives for (a) monitoring muscle contraction, and (b,c) mitochondrial membrane voltage sensing.

(PET) mechanism. In SPIRIT RhoVR 1 carboxylate group was masked with acetoxymethyl group to form an ester. When SPIRIT RhoVR 1 accumulates within mitochondria, esterases hydrolysed the ester bond to remove acetoxymethyl group and trap the SPIRIT RhoVR 1 inside the IMM to responds reversibly to changes in $\Delta\Psi_m$. Moreover, SPIRIT RhoVR 1 was also compatible with multicolor imaging.

Mitochondria Targeting Cyanine Chromophores and Its Conjugates:

Cy chromophores are delocalized lipophilic cationic molecules that extensively used in fluorescence imaging of mitochondria. Due to the lipophilic cationic character Cy can sneak through energy barrier to enter into mitochondria. Cy dyes can be finely tuned from visible (Cy-3, λ_{em}= 550 nm) to NIR range (Cy-5 and Cy-7, λ_{em} = 650 nm and λ_{em} = 750 nm, respectively) by varying length of the polymethine linker.[126,127] NIR Cy is more advantageous due to negligible autofluorescence and deeper tissue penetrating ability of NIR light. Indocyanine green (ICG) is the only US FDA-approved NIR imaging agent whereas Cy-7 dye IR-DBI is the first NIR molecule that used to target and image mitochondria (**Figure 5a**).[127] Subsequently several modification has been made to improve photostability, organelle selectivity, enhance fluorescence quantum yield as well as water solubility. Cy-7 based IR-26 specifically accumulated inside the mitochondria of acute myeloid leukemia cell line, contingent on the hyperactive glycolysis of cancerous cells, and concurrently damages OXPHOS to exhibit targeted therapeutic effects (**Figure 5b**).[128] A mitochondria targeting cyclooctatetraene conjugated Cy-3 and Cy-5 dyes (PK Mito) were reported for fluorescence cytometry (**Figure 5c**).[129]

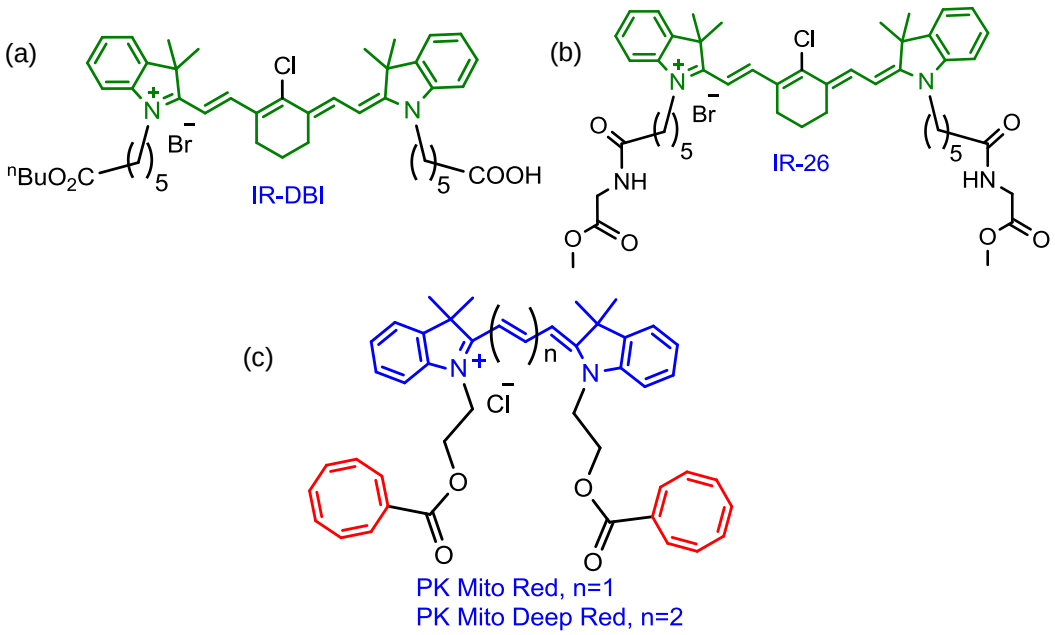

Figure 5. (a-c) Cyanine dyes for selective targeting and imaging of mitochondria.

Cy dye such as Cy-3–Cy-5-R8 reported by Tsai et al. acted as a vector to deliver small molecular cargoes to mitochondria of cancer cells (Figure 6a).[40] Cy-3 and Cy-5 residues when very close in Cy-3–Cy-5-R8 [Cy-3/Cy-5 Förster resonance energy transfer (FRET) pair] excitation of Cy-3 at 554 nm showed fluorescence emission enhancement of Cy-5 at 666 nm. Cy-3–Cy-5-R8 preferentially accumulated inside the mitochondria confirmed by confocal microscopy. The ability of lipophilic cationic Cy dyes to change the subcellular localization of R8 residue was promising. Moreover, several drug molecules (Ciprofloxacin: antibiotic, moreover, can also cause damage to mtDNA; carboplatin: anti-cancer drug which can also diminishes mitochondrial activity and cause apoptosis) were conjugated by coupling with the free –COOH of the Cy-3 or Cy-5 residues (**Figure 6b**).[40] Compared to the parent cargo, toxicity increases after conjugation with Cy dyes due to the targeted delivery of the

cargo molecules at mitochondria. Here, Cy dyes acted as mitochondria trackers, delivery vectors, and as diagnostic tools to visualize cargo localization. Cy-based 3-methoxy pyrrole derivatives was developed that can tightly bind with the BH_3 domain of antiapoptotic Bcl-2 proteins to inhibit its activity and activate pro-apoptotic Bax proteins (Bcl-2 associated X protein) and generate ROS (**Figure 6c**).[130] As a result cell cycle was arrested in the G0/G1 phase to induce late apoptosis via caspase-3/9 dependent pathway.

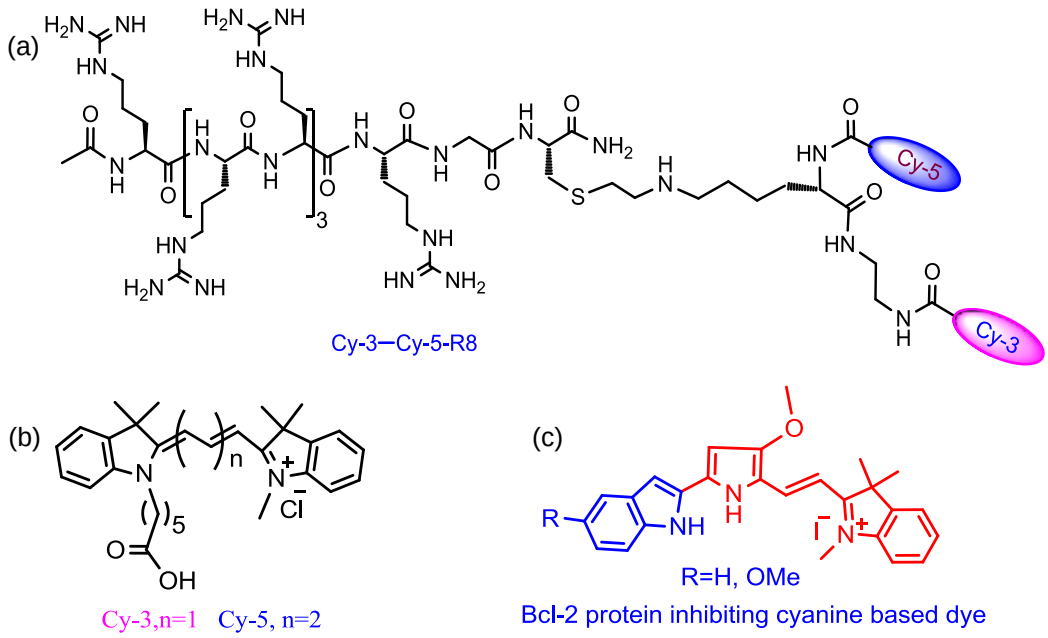

Figure 6. (a-c) Chemical structures of Cy based mitochondria targeting agents.

A NIR probe DATC consisted of a Cy-5 fluorescence unit, a mitochondria targeting TPP^+ moiety and a sulfenic acid-reactive 1,3-cyclohexanedione functionality was designed and synthesised for mitochondrial immobilization by covalent bond formation with sulfenic acid residue of oxidized proteins

under oxidative stress in mitochondria (**Figure 7**).[131] This covalently binding strategy proves to be useful in long-term image-guided therapy.

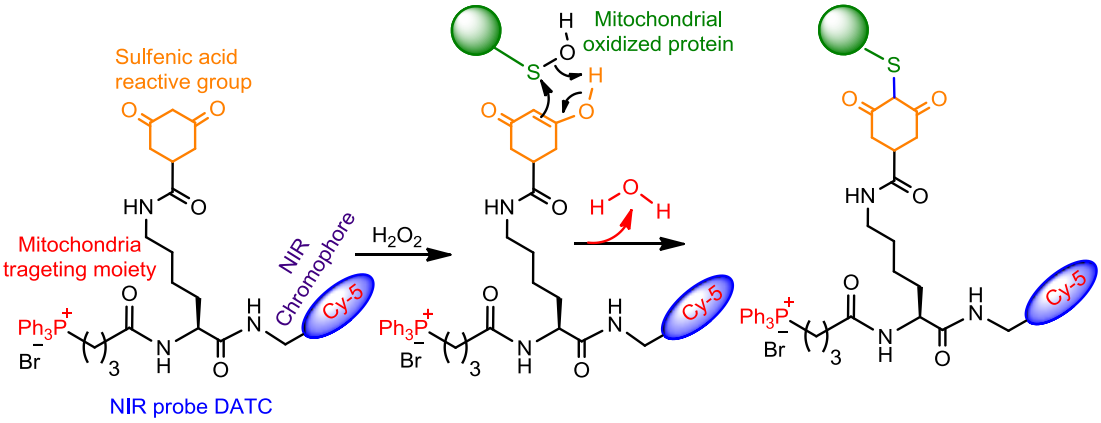

Figure 7. Chemical reactions of sulfenic acid-induced mitochondrial immobilization of targeted Cy-5 conjugated molecule for prolonged tumor imaging.

Mitochondria Targeting Aggregation Induced Emission Luminogens:

Aggregation induced emission (AIE) refers to the photophysical phenomenon where fluorophores are practically nonfluorescent in the solution due to dissipation of excitation energy, however, become highly fluorescent upon aggregation originating from restricted intramolecular vibrational and torsional motions. The AIE concept was first introduced by Tang and co-workers in 2001. To date several multifunctional tetraphenylethylene (TPE) cores containing AIE luminogens (AIEgens) have been developed which were successfully used for mitochondrial targeting, diagnosis, and imaging. Tang et al. first designed and synthesised mitochondria targeting AIEgen, where AIE-active TPE core was conjugated with two TPP^+ functionality (TPE-TPP) and this molecule has been used as imaging agent for mitochondrial tracking and

morphological change monitoring (**Figure 8a**).[132] Another TPE based chromophore was constructed by tethering a pyridinium cation via vinyl functionality (TPE-Py).[133] TPE-Py showed weak fluorescence in solution phase, but became highly emissive upon formation of aggregated nanoparticle suspension. TPE-Py showed excellent colocalization with well-known mitochondria targeting probe MitoTracker Red in live HeLa cells. Liu and co-workers discovered two other AIE fluorophores, AIE-Mitogreen-1 and AIE-Mito-TPP, for selective tracking and imaging of mitochondria (**Figure 8b**).[134–135] Both of these salicyladazine fluorophores exhibited high cell permeability with selective mitochondrial accumulation, minimum cytotoxicity, negligible background fluorescence signal in aqueous medium with a large stoke shift and undergo AIE via restricted intramolecular rotation along the N–N bond and excited-state intramolecular proton transfer (ESIPT) through intramolecular hydrogen bondings to light up mitochondria. Moreover, after selective accumulation of AIE-Mito-TPP inside the cancer cells mitochondria over the normal cells, it aggregates to decrease Ψ_m, enhances intracellular ROS generation upon irradiation with NIR light and impedes ATP production causing cell death. A water-soluble AIE-gen (*E*)-TPEDEPy-DBz was constructed by tethering two pyridinium groups to the TPE core (**Figure 8c**).[136] These cationic quaternary pyridinium salts acted as electron-acceptor, and play a key role for water-solubility and enhanced λ_{em} of this AIE-gen. This cationic AIE-probe showed good membrane permeability and cell viability with potential mitochondria targeting ability. In an effort to design innovative fluorophores, Tang and Jiang independently constructed cationic indolium conjugated red emissive AIE luminogens (TPE-Ph-In), which not only target mitochondria but also have been used to monitor Ψ_m changes (**Figure 8d**).[137]

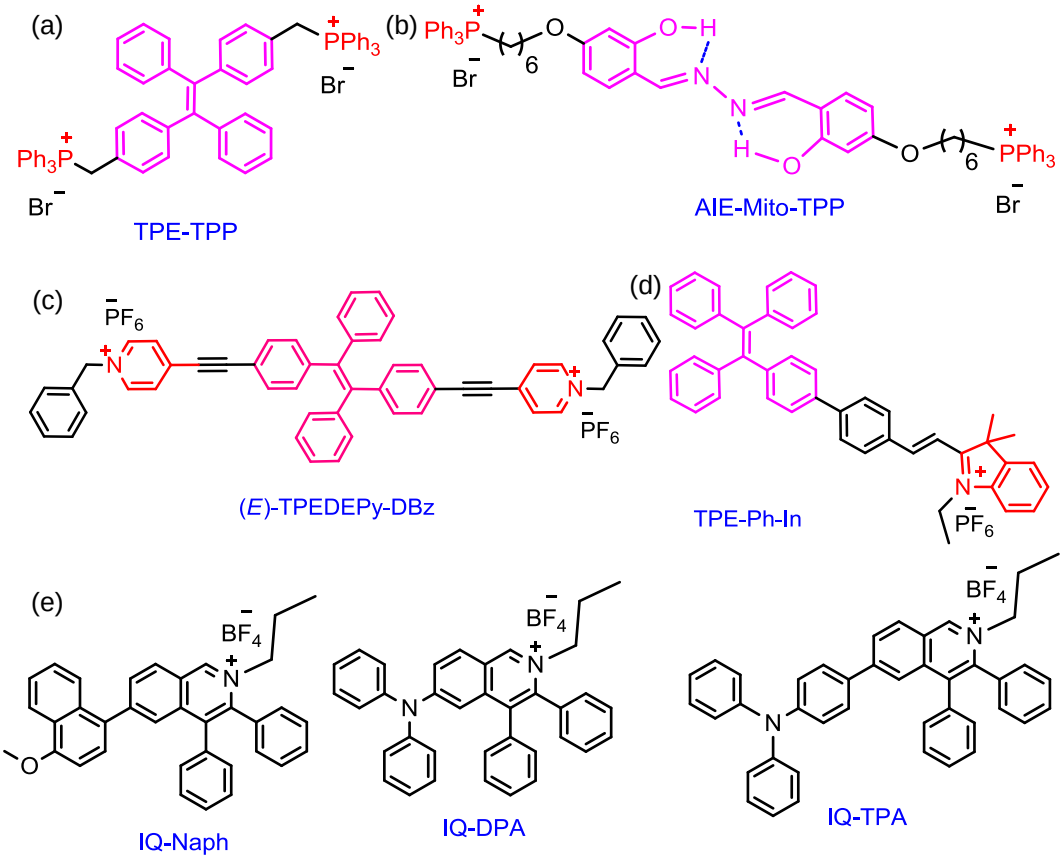

Figure 8. (a-e) Mitochondria targeting AIE probes.

Moreover, three new diphenyl isoquinolinium based AIEgens (IQ-Naph, IQ-DPA, and IQ-TPA) were also introduced by Tang research group that have been used for mitochondrial imaging, and assessment of mitochondrial membrane potential (**Figure 8e**).[81]

Qu et al. developed an AIE-active marker, named as AIE-SRS-Mito, for dual mode tracking of mitochondria in living cells by combination of two-photon excited fluorescence (TPEF) microscopy with stimulated Raman scattering (SRS) microscopy (**Figure 9**).[138] Due to the AIE characteristic of

the prove shows enhanced alkyne Raman peak at 2223 cm^{-1}. Both linear concentration dependency of SRS and dormancy of the alkyne Raman signal to environmental fluctuations, enable to calculate the intracellular scattering of the AIE-SRS-Mito molecule, which exhibited a local concentration of > 2.0 mM in the mitochondrial matrix that was 100-fold greater with respect to incubation concentration. Using this technique the local concentration of AIE-SRS-Mito probe inside cells was measured non-invasively and directly.

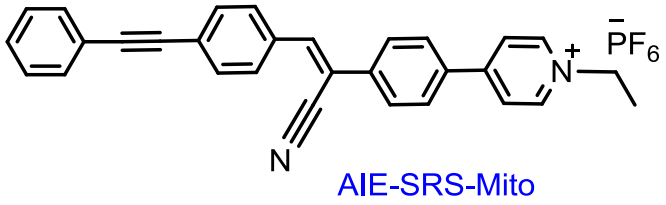

Figure 9. Chemical structure of AIE-SRS-Mito.

Kim and co-workers designed and synthesised an NAD(P)H:quinone oxidoreductase-1 (NQO1) enzyme activatable AIE-fluorophore (TPP-TPE-NQO1) for mitochondria targeted theranostics application (**Figure 10**).[139] NQO1 is an enzyme that found to be overexpressed in several cancerous cells. After preferential accumulation inside the cancer cells AIE-probe with NQO1 cleavable linker was activated *in situ* by NQO1 enzyme to induce apoptosis via caspase pathway resulting mitochondrial dysfunction.

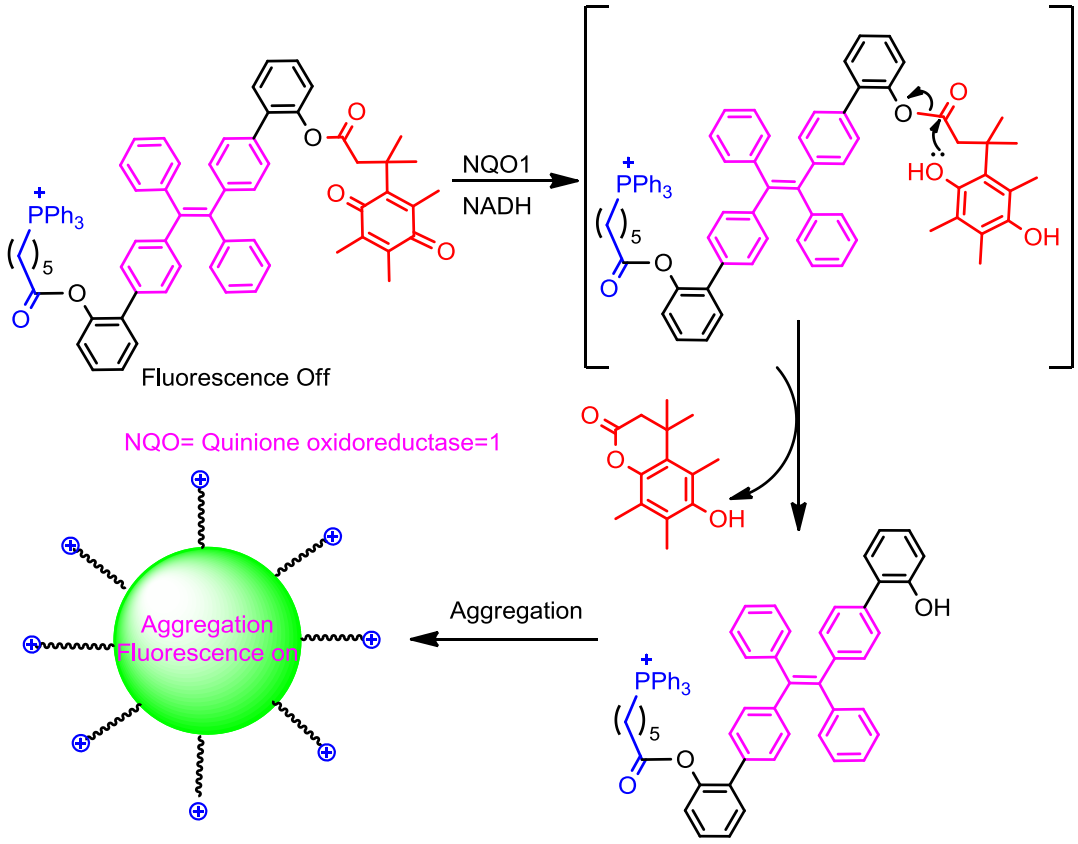

Figure 10. Mechanism of NQO1 enzyme activatable AIE probe.

Probes to Monitor and Image Mitochondrial pH Fluctuation:

Mitochondria maintain an alkaline pH of ~8.0 for regular physiological functioning while anomalies in mitochondrial pH cause its dysfunction which ultimately affects its morphology as well as ETC, ATP synthesis, ROS production, and influence the mitophagy process. Hence, it's essential to precisely monitor minor pH fluctuation in mitochondria to acquire well understanding of its function in various physiological and pathological

conditions. Several approaches have been made to accomplish the mentioned purpose.

Mitochondria Targeting pH Sensing Probes:

Tang and co-workers have described a lipophilic cationic NIR fluorescent dye Spring-Red with large Stokes shift to monitor the mitochondrial pH change in live cells (**Figure 11a**).[140] A fluorescent indicator Mito-pH-1 was developed by Yang et. al. to detect the mitochondrial pH variation in live HeLa cells (**Figure 11b**).[141] They have showed that mitochondrial pH fluctuates with both temperature and H_2O_2 stimulations in live cells.

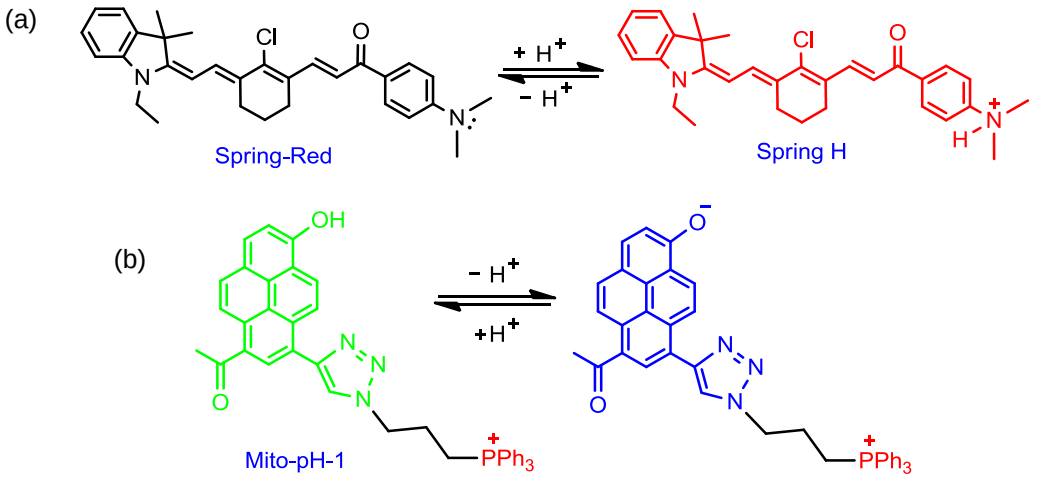

Figure 11. Mechanism of emission switching in response to pH change for (a) Spring-Red and (b) Mito-pH-1.

Dual Localization Probe for Real Time Monitoring of Mitochondrial pH Alteration:

Kim and co-workers have developed mitochondria targeting dual localization probe based on TPP^+ containing piperazine-tethered naphthalimide as a PET driven fluorescence OFF/ON chromophore which is further anchored

with thiol (–SH) reactive benzyl chloride unit to ensure mitochondrial immobilization (**Figure 12**).[22] Co-incubation of the probe with carbonyl cyanide *m*-chlorophenyl hydrazone (CCCP, a $\Delta\Psi_m$ uncoupling agent) confirmed mitochondrial fixation of the probe as the result of nucleophilic substitution of benzyl chloride group with exposed –SH present in various mitochondrial proteins. Furthermore, this biocompatible pH-sensitive probe was utilized for quantitative and the real time monitoring of pH deviations during the mitochondrial acidification and also nutrient deprived cells during mitophagy process.

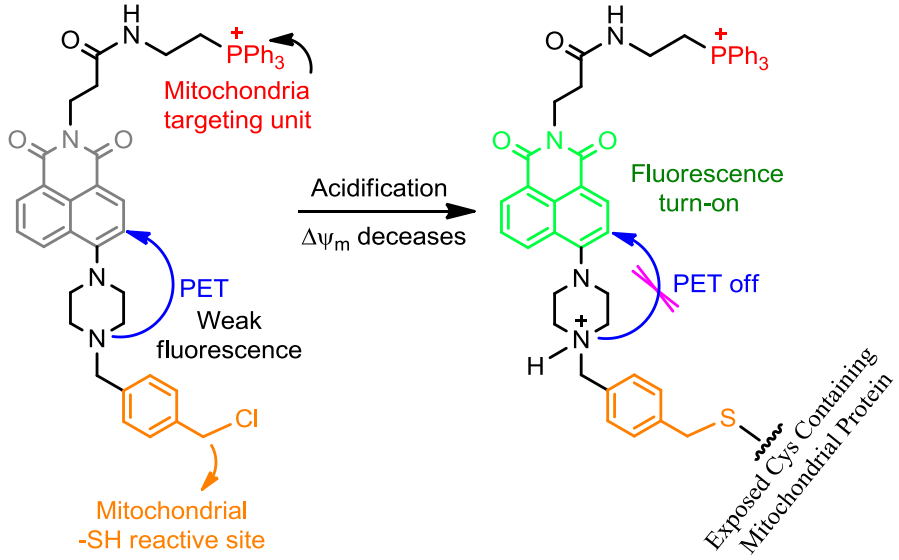

Figure 12. Dual targeting and pH sensitive probe for mitochondria.

Cyanine-Based Probes to Monitor Mitochondrial Morphology and pH Change During Mitophagy Process:

Mithophagy is a biological process by virtue of which damaged mitochondria are eliminated through autophagosome, followed by fusion with nearby lysosome (pH 4-5) where degradation of contents of the autophagosome

will occur. Mitophagy is closely associated to numerous physiological and pathological processes and meticulous study of mitophagy process is necessary. Development of probes to monitor the incidence of mitophagy in living cells can offer deeper understanding into mitochondrial metabolism. During mitophagy process mitochondria undergo morphological and pH change. Xiao and co-workers recently introduced mitochondria specific rhodamine based fluorescent carbon dot MitoCD that can effectively monitor mitochondrial dynamics during mitophagy process.[142] Biocompatibility, high cell permeability, membrane potential independent and –SH reaction free mitochondrial localisation along with excellent optical properties at physiological conditions like high photon counts, low ON/OFF ratio, and burst-like blinking made MitoCD a promising candidate for real-time nanoscopic imaging of mitochondrila dynamics in live cells.

A pH activatable Cy dye HQO was introduced by Shangguan et al. to measure pH changes to obtain greater insight of mitophagy process in live cells via real-time monitoring of mitochondria and autolysosomes (**Figure 13**).[143] HQO ($\lambda_{ex}/\lambda_{em}$ = 530/650 nm) specifically incorporated inside the mitochondria; however, it converted to the red-shifted protonated $HQOH^+$ state ($\lambda_{ex}/\lambda_{em}$ = 710/750 nm) at the diminution of pH when dysfunctional mitochondria fused with lysosome and transform into autolysosomes. This pH switchable HQO molecule was appropriate to inspect mitophagy with the capability to discriminate autolysosomes with other lysosomes.

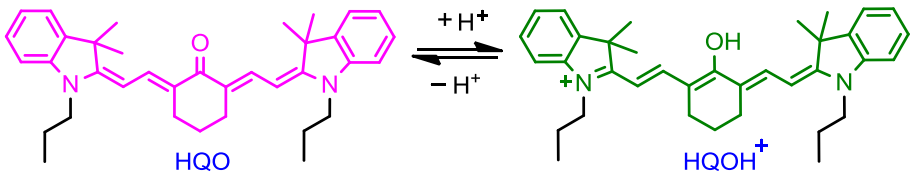

Figure 13. pH sensitive structural transformation of HQO and $HQOH^+$ display greater insight of mitophagy process.

Liu and co-workers have developed a ratiometric NIR fluorophore with large Stokes shift that can monitor mitochondrial pH alterations based upon very effective through-bond energy transfer (TBET) from Cy-3 donor to NIR hemicyanine acceptor connected through a spirolactam ring structure (**Figure 14**).[23] At basic or neutral pH, the probe displayed fluorescence of only the Cy-3 donor (λ_{ex} 520 nm, λ_{ex} 582 nm), however, spirolactam ring opening was observed at acidic pH conditions, leading to extended π-conjugation, resulting in new NIR fluorescence peak at 752 nm (λ_{ex} 520 nm or 686 nm). This outcomes in ratiometric fluorescence signals of the probe to pH alterations designated by diminutions of the donor fluorescence and escalations of the acceptor fluorescence upon donor λ_{ex} at 520 nm owing to a very effectual TBET from the donor to the acceptor. The probe only exhibited Cy-3 donor fluorescence inside the mitochondria (pH 8.0). Nevertheless, the probe displayed reasonable fluorescence diminutions of the Cy-3 donor and substantial fluorescence escalations of the hemicyanine acceptor (ratiometric fluorescence responses to pH changes) during the mitophagy process.

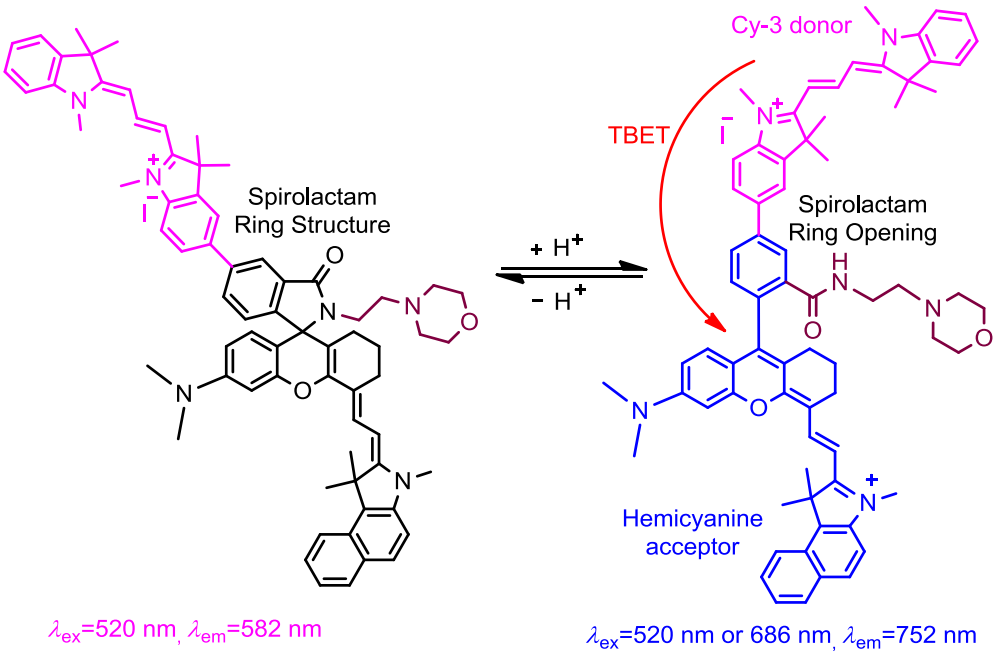

Figure 14. TBET based ratiometric fluorescent probe to monitor pH changes in mitochondria during the mitophagy process.

Design of Peptides to Target Mitochondria as well as Control Cellular Function and Fate:

Over past few decades mitochondria emerged as a novel therapeutic and diagnostic target, especially for cancer therapy. Mitochondria targeting peptide and peptidomimetic based therapeutics and diagnostic agents got immense importance due to ease of their synthesis, functionalization, water solubility, and biocompatibility.[144] Mitochondria targeting peptides were projected as the possible surrogate approach to delocalized lipophilic cations for delivering bioactive molecules or drug molecules to mitochondria. It has several advantages over conventional delocalized cationic lipophilic mitochondria targeting moieties. Secondary structures of peptides can be customized

synthetically to exploit the interactions with mitochondrial membrane and proteins. Peptides can be easily bioconjugated with a diverse range of cargoes to target mitochondria.[145] Two imperative biophysical properties viz. cationic charge and lipophilicity are prerequisite to consider for designing mitochondria-penetrating peptides (MPP). The positive charge of the amino acid side chain residues enables potential driven uptake through the negatively charged plasma membrane as well as outer mitochondrial membrane (OMM). However, the IMM which is much more hydrophobic than plasma membrane, require higher lipophilicity of the peptides to get pass the lipid bilayer. Transactivator of transcription (Tat) peptide, a well know poly-Arg-based cell penetrating peptide (CPP) as well as poly-Lys containing peptides which can effortlessly sneaked through OMM but fails to overcome the energy barrier to transport inner lipid bilayer of mitochondria. So, some modifications in CPP sequences are necessary for the designing of MPPs.

Mitochondria Tracking Peptides and Its Application to Targeted Mitochondrial Delivery of Cargoes:

Several theoretical and experimental studies were carried out by various research groups suggested that for the successful design of MPPs should consist of hydrophobic natural amino acid residues such as Phe, Leu, Ile, Tyr and positively charged residues like Arg and Lys. Furthermore, the modification such as replacement of L-Arg with D-Arg had also been made to overcome the enzymatic cleavage and whereas the introduction of cylohexyalanine in place of Phe enhanced the lipophilicity causing greater mitochondrial uptake.[146] Unnatural L-amino acid and D-amino acid containing peptides are usually preferred over their natural L-analogs for delivering certain anticancer drugs *in vivo* and *in vitro*.

Kelley and co-workers successfully engineered and synthesized a library of MPPs, which can pass through both cellular and mitochondrial membranes. Their designed peptides consist of alternating hydrophobic residues [typically Phe (F) and unnatural amino acid cyclohexylalanine (F_x)] and cationic moieties [predominantly D-Arg (r) and Lys (K)], which provided an electrostatic driving force for higher cellular internalization through negatively charged plasma and mitochondrial membranes, while lipophilic residues provided deeper penetration through lipid bilayer resulting much more mitochondrial localization (**Figure 15**).[147] To get the better understanding of cellular uptake and mitochondrial localization flow cytometry as well as confocal laser scanning microscopy (CLSM) experiments were carried out for all thiazole orange tagged derived peptides as well as transactivating transcriptional activator (TAT) peptides (**Figure 15**). The detailed examination of peptide location within HeLa cells indicated that, cellular uptake of TAT and the lipophilic peptides were similar across the plasma membrane, however, dissimilar at mitochondrial localization. The F_X containing peptide revealed very high localization inside the mitochondria compared to F containing peptide, whereas the Tat peptide exhibited negligible mitochondrial localization. The study revealed that peptides which possessed +3 charge and have log *P* values greater than –1.7 displayed a higher mitochondrial localization (for +5 charge log *P* value should be greater than –2.5 for mitochondrial accumulation). This study clearly indicates the existence of a critical lipophilicity threshold for mitochondrial penetration and hydrophilicity above that level will reduce its affinity to the mitochondrial membrane and precluding access.

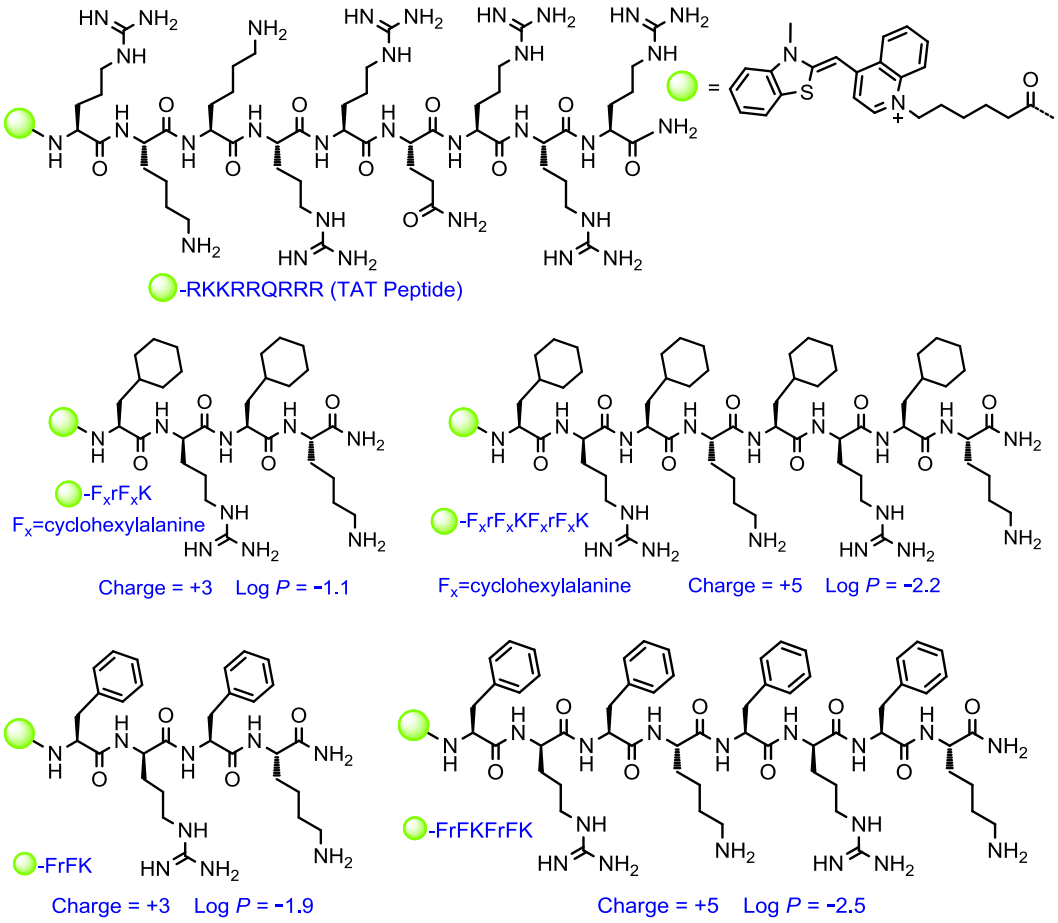

Figure 15. Chemical structures of TAT peptide and mitochondrial penetrating peptides.

Kelly et al. also showed that GSH cleavable disulphide (–S–S–) linker attached to MPPs can act as target specific vectors for transportation of small molecules and cargoes to mitochondrial matrix (**Figure 16**).[43] This unique strategy had proved to be productive for successful delivery of luminespib (an HSP90 inhibitor to mitochondria) to induce mitochondrial dysfunction and cellular apoptosis. Cisplatin and doxorubicin conjugated MPPs have also been used for

the selective delivery of chemotherapeutic agents inside the mitochondria for mitochondria targeted cancer therapy.

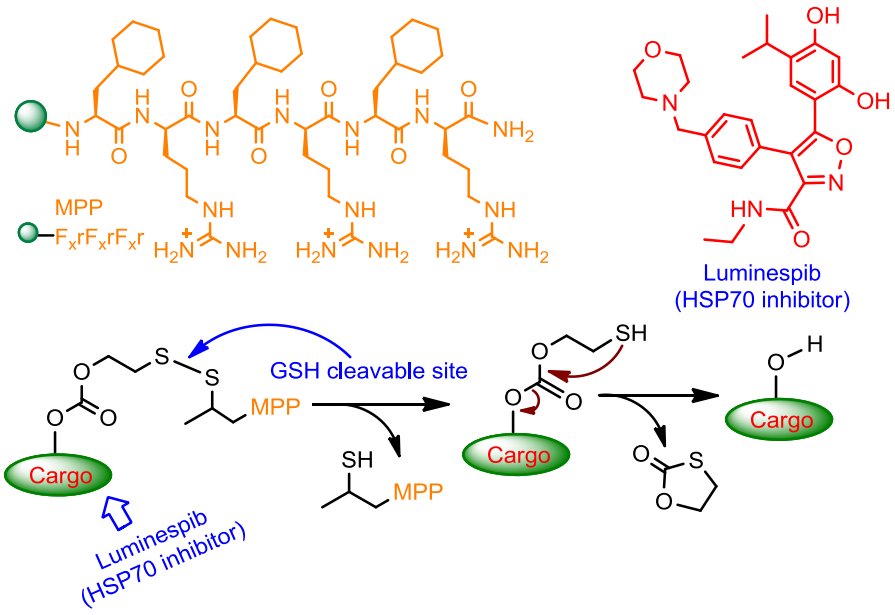

Figure 16. Application of mitochondrial penetrating peptide to deliver cargo to mitochondria.

Numata and coworkers have reported KH peptide (KHKHKHKHKHKHKHKHKH, 18-mer, repeating arrangement of Lys and His) bioconjugated with two different mitochondrial targeting signal (MTS) peptides [MLSLRQSIRFFK (12-mer taken from yeast cyt *c* oxidase unit IV sequence) and MLFNLRILLNNAAFRNGHNFMVRNFRCGQPLQ (32 residues from human hepatic enzyme ornithine transcarbamylase)] to accomplish targeted mitochondrial transport of a plasmid DNA (pDNA) via exploiting electrostatically triggered self-assembly.[148] Cationic Lys residues were able to bind with DNA for intracellular uptake, whereas His moieties were crucial for endosomal escape by the proton sponge effect. The cationic KH

peptide attached to pDNA to form a hydrophilic core, whereas unbound α-helical MTS preserved its conformation. Remarkably, the MTS comprising a fragment from cyt *c* oxidase exhibited superior effectiveness with respect to MTS from ornithine transcarbamylase in mitochondrial transportation. Probably owing to the greater hydrophobicity of the MTS from cytochrome *c* oxidase, this interacts superior with the OMM import receptor TOM20. This peptide/pDNA (encoding the *Renilla luciferase*, RLuc) conjugate was effectively delivered to the mitochondria and mitochondria selective gene expression was perceived. Burke et al. have reported a short MPP conjugated with a Ru(II) complex that can intercalate mtDNA.[149] The Ru(II)−MPP conjugate specifically attached with mtDNA and allowed luminescence lifetime imaging. The Ru(II) molecule also employed photoinduced toxicity upon exposure of 470 nm light, that can serve as a prospective theranostic agent for mitochondria related diseases.

Szeto−Schiller (SS) peptides belong to a class of short mitochondrion-targeting synthetic tetrapeptides, containing alternative aromatic and cationic amino acid residues. Electrostatic and hydrophobic interaction between the cationic SS-31 (D-Arg-Dmt-Lys-Phe-NH_2; Dmt = 2′,6′-dimethyltyrosine) and anionic cardiolipin on the IMM believed to be the reason for selective localization of SS-31 within mitochondria (**Figure 17a**).[150−153] The mitochondrial ROS scavenging and antioxidant activity of the SS peptides is due to the presence of Dmt residue, which inhibits the catalytic peroxidase activity of cyt *c* and prevents mitochondrial oxidative damage. Due to the structural resemblance to vitamin E, Dmt is more effective than Tyr in scavenging ROS. The SS peptides have ability to transport small cargoes, which can exhibit mutualistic activity in amalgamation with their antioxidant activity. Cerrato et al. showed that when the Lys residue in SS-31 replaced with ornithine and further conjugated with

glutathione analogue (UPF-25) it exhibited enhanced cellular and mitochondrial uptake as well as improved ROS scavenging ability (**Figure 17b**).[154] In another approach, Zhou et al. recently developed SS-31 doped biodegradable poly(lactic-co-glycolic acid) (PLGA) nanoparticle based vehicle for successful delivery of cyclosporin A to mitochondria and restore it function.[155] Indeed, Kuang and co-workers utilized similar nanoparticles system for efficient delivery of geranylgeranylacetone [a 70 kDa heat shock protein (HSP70) inducer] to mitochondria.[156] Harashima et al. developed the SS peptide conjugated liposome based nanocarrier known as DF-MITO-Porter for selective delivery of bioactive cargos to mitochondria of the living cells. This MITO porter (**Figure 17c**) showed efficient mitochondrial uptake via stepwise membrane fusion.[157]

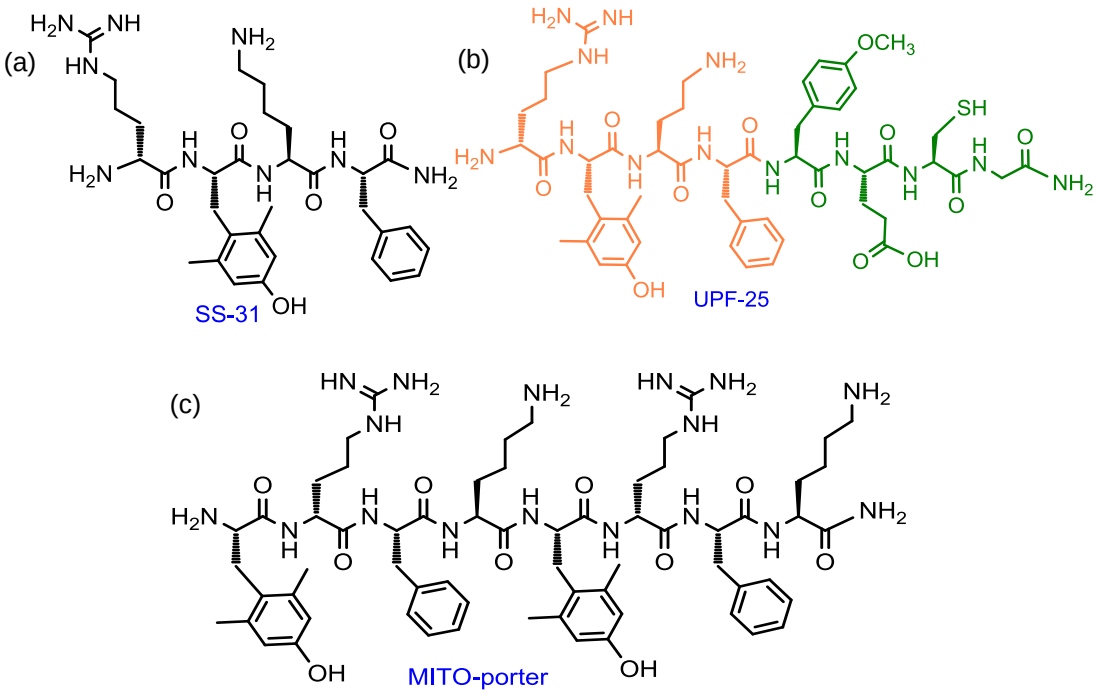

Figure 17. (a-c) SS-peptides as mitochondrial delivery vehicles.

Polymer-Peptide Conjugates for Malignant Mitochondrial Dysfunction:

ROS-sensitive polymer-peptide conjugates (PPCs) and mitochondria locational morphology transformation by KLA peptide (KLAKLAKKLAKLAK) is another class of antimicrobial peptide which builds up the defence against invading pathogens.[158] Structural resemblance of the mitochondrial membrane and the bacterial outer membrane, the KLA peptide was substantially examined as a mitochondrial membrane-disintegrating protein. Replacing L with more hydrophobic amino acids including F_x, F, and hexyl moieties, the mitochondrial disintegrate activity and the potency of the anticancer peptide were boosted.[159] Yamada et al. showed that KALA peptide linked to liposomal nanocarrier also able to selectively deliver therapeutic agents to mitochondria. This liposome based mitochondrial delivery system proved to be a promising approach for mitochondrial gene therapy.[45] Cheng et al. developed a self-assembled poly(vinyl alcohol) based nanoparticles through thiol-ene reaction via alternatively conjugating a self-assembling β-sheet-forming CGGGKLVFF peptide tethered with hydrophilic PEG via ROS-cleavable thioketal linker and a mitochondria targeting cytotoxic KLAK [$CGGG(KLAKLAK)_2$] peptide (**Figure 18**).[160] This pegylated nanoparticles offer high circulation lifetime and tumor targeting by the enhanced permeability and retention (EPR) effect. The PPCs with the help of KLAK residue enter into mitochondria of the cancer cells and high concentration of malignant mitochondrial ROS cleaves the thioketal bond to generate the residue CGGGKLVFF-SH and the hydrophilic PEG moiety was detached from PPCs hence hampered the hydrophilic/hydrophobic balance and induced the transformation into nanofibers from nanoparticles. The nanofibers with exposed KLAK residue display greater multivalent interactions with mitochondria (KLAK can interact with the mitochondrial membrane

through hydrophobic and electrostatic interactions), which causes malignant mitochondrial dysfunctions and selective cytotoxicity against cancer cells. This organelle-located morphology transformation provides a powerful tool for cancer and tumor theranostics.

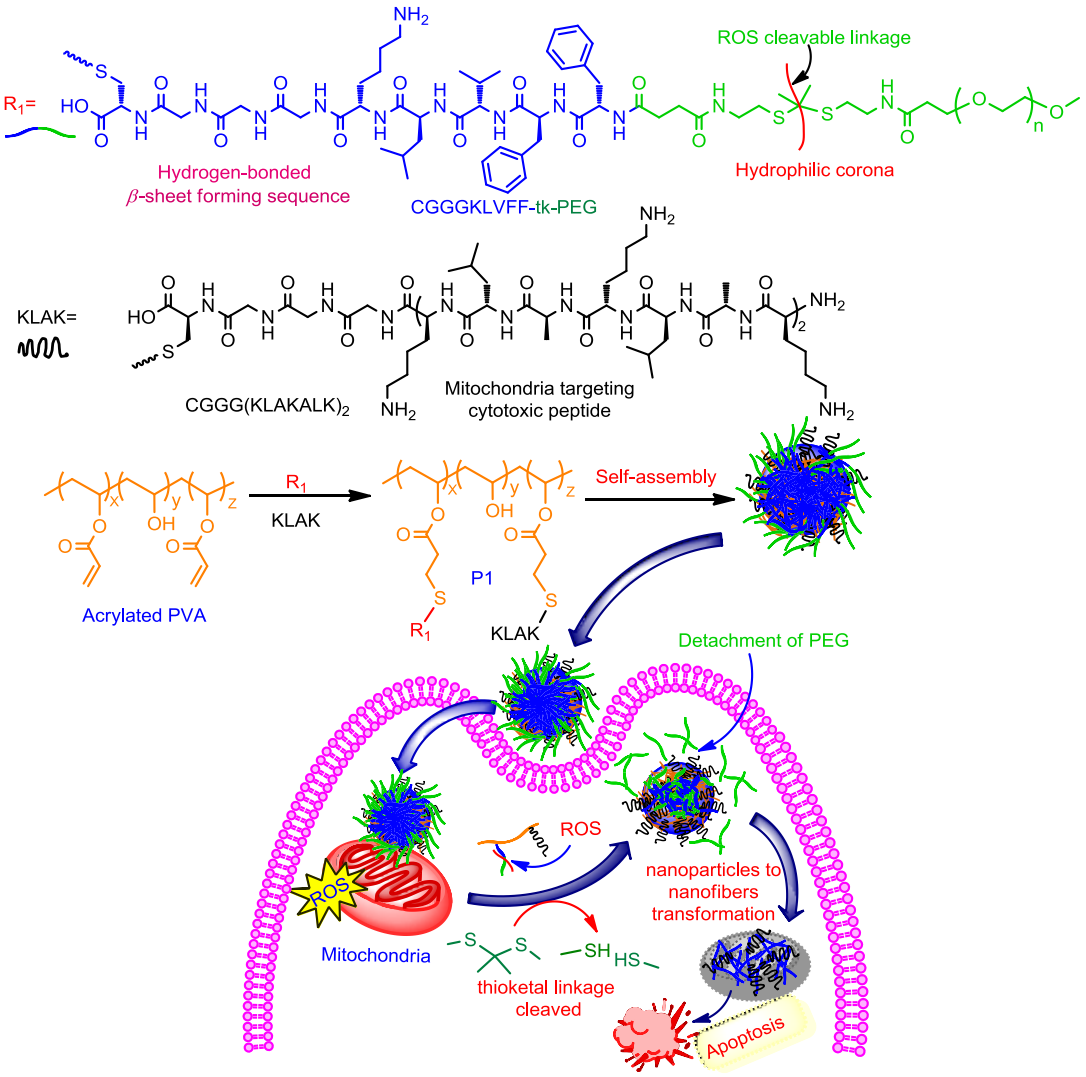

Figure 18. ROS-sensitive morphology transformation of peptide-polymer conjugates upon mitochondrial accumulation.

Enzyme Instructed Self-Assembly for Selective Targeting of Cancer Cell Mitochondria Over Normal Cell:

Majority of the mitochondrial targeting compounds are cationic as well as lipophilic in nature and after accumulating in mitochondrial matrix via potential driven force sometimes it exhibits cytotoxicity. Recently, Xu and co-workers have reported unique bioinspired strategy named as enzyme instructed self-assembly (EISA), to precisely target mitochondria of cancer cells over the normal cells. This EISA technique not only helped to selectively target cancerous cells mitochondria to trigger apoptosis driven cell death but also found useful in translocation of endogenous proteins such as histone protein via influencing inter-organelle communication. It is worthwhile to say that EISA proves to be a promising approach to selectively deliver drug molecules at target sites to interrupt the metabolism of cancer cells.[161,162] This group was first reported an N-terminal nitrobenzoxadiazole (NBD) fluorophore tagged peptide (FFY_pK, Y_p = L-Phosphotyrosine) containing a mitochondria targeting TPP^+ group at the ε-amino group of Lys residue and phosphorylated Tyr (Y_p) unit that undergo dephosphorisation catalysed by ectophosphatases (alkaline phosphatase, overexpressed in cancer cells) to form nanoscale assemblies of NBD-FFYK-TPP^+ in the pericellular space exclusively in the cancer cells (**Figure 19**).[52] These self-assemblies internalized in the cancer cells via endocytosis pathway, and escaped from lysosome to accumulate inside the mitochondria to induce its dysfunction, triggering the leakage of cyt *c*, stimulate caspase cascade and consequence in cellular apoptosis. A high concentration of peptides (several hundred μM to mM) was required for pericellular self-assembly; moreover, the enzymatic expression differs from cell to cell that impedes its efficacy as a therapeutic agent.

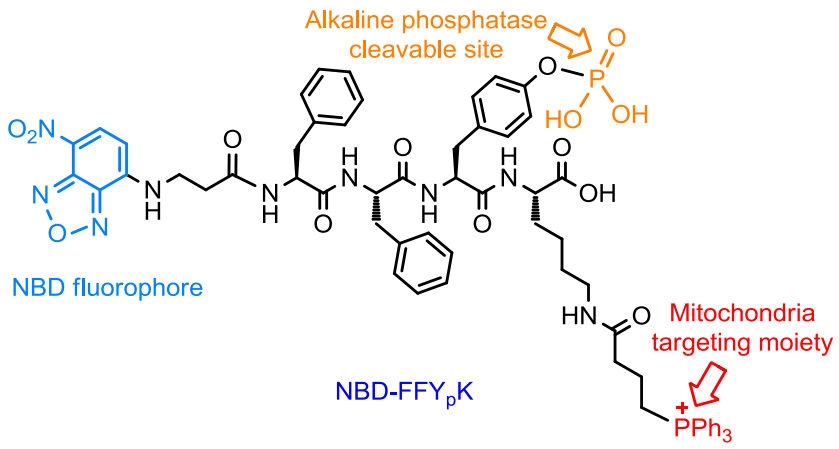

Figure 19. Selective targeting of mitochondria using EISA approach.

Xu et al. have reported an enzymatic cleavage of branched peptides which possess negative charges to target mitochondria. They have designed an enzyme cleavable FLAG motif (DYKDDDDK) conjugated with self-assembling motif to form micelles. Here, the precursor peptide composed of hydrophilic FLAG-tag motif and a short self-assembling D-amino acids containing tripeptide sequence (D-Phe-D-Phe-D-Lys, ffk) linked with 2-acetylnaphthyl moiety (Nap) for micelle formation. NBD-ethylenediamino fluorophore moiety (NBD-EA) was anchored at the *C*-terminal of this Nap-ffk peptide through –COOH of D-Lys while the ε-NH_2 group of D-Lys was conjugated to the FLAG motif through a Gly spacer (**Figure 20**).[163] D-Amino acids containing ffk peptide residue possessed durable stability both *in vivo* and *in vitro* owing to their resistance to enzymatic degradation. NBD also served as an efficient reporter where bright fluorescence was observed for intracellular peptide-based fiber formation. The precursor peptide self-assembled to forms micelles that were loaded with R-phycoerythrin proteins or doxorubicin, and were quickly incorporated through clathrin-dependent macropinocytosis. After internalization, the FLAG motif was detached by intracellular enterokinase

(ENTK, a transmembrane serine protease), and the residual peptides subsequently converted from micelles to nanofibers with a net negative charge that seem to be confined inside the IMS of the mitochondria and were able to deliver cargos (e.g., red phycoerythrin protein or doxorubicin) into mitochondria. It was the first report of enzymatic self-assembly in mitochondria targeted delivery of payloads. The strategy demonstrated in the work could be applied for other enzymes to target mitochondria. Same group of researchers also developed a peptide-lipid conjugate known as Flag-$(C16)_2$ (hydrophilic Flag-tag and hydrophobic lipid) for selective delivery of antibiotic chloramphenicol (CLRP, a clinically utilized antibiotic nonfunctional in presence of glucuronidases in cytosol, however, functional inside the mitochondria) to mitochondria of liver cancer cells over the normal cells.[54] The lipid part helped in the self-assembly to form micelles. In micelles the Flag-tag present in the hydrophilic "head" regions surrounded by H_2O and hence exposed, which was the substrate of ENTK. As mitochondria lack the glucuronidases enzyme for glucuronidation, so Flag-$(C16)_2$ encapsulated CLRP was accumulated inside the mitochondria of cancer cells. When Flag-tag was cleaved by perimitochondrial ENTK, CLRP selectively delivered to cancer cells mitochondria (but not into the normal cells mitochondria) to inhibit malignant mitochondrial protein synthesis triggered the leakage of cyt *c* into the cytosol, caused cancer cell death. Inspiring form Protein Data Bank (PDB) Xu and co-workers also discovered that negatively charged peptide sequences are typical characteristic of histone-binding proteins. Hence, they synthesised a negatively charged peptide sequence NBD-MitoFlag (L-D) containing repeating L-Asp residue and observed that after enzymatic cleavage it facilitates the localization of histone protein (H2B), to the cancerous cells mitochondria. Here, the MitoFlag binds with the nuclear location sequence (NLS) of H2B to

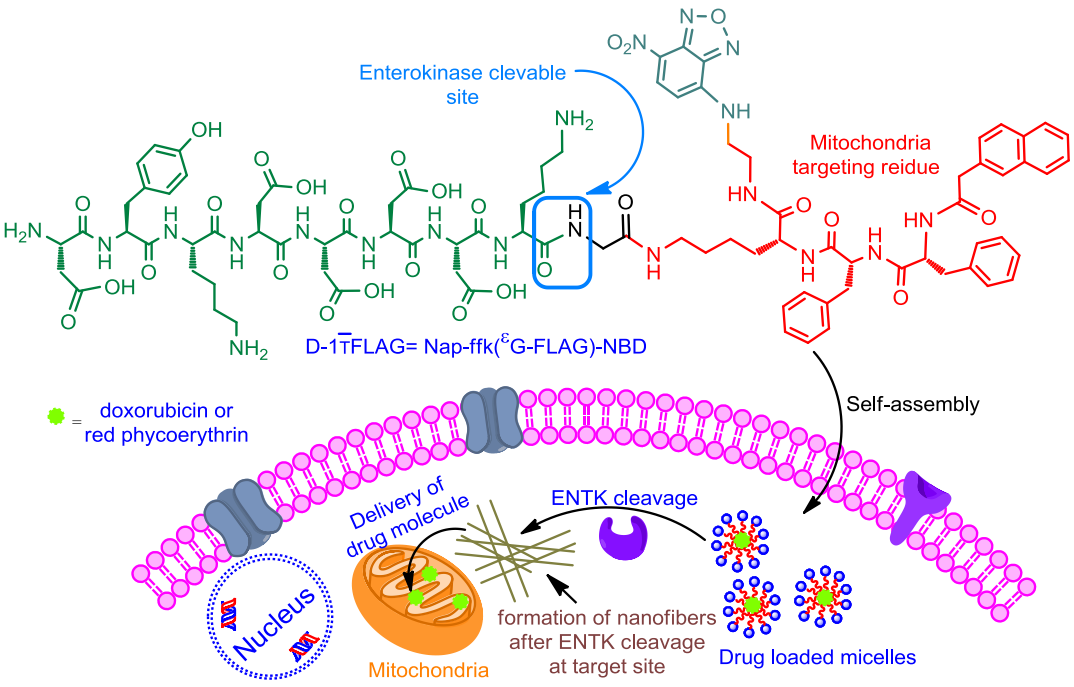

Figure 20. Schematic representation of enterokinase cleavage of FLAG-tag branch peptide to convert precursor's micelles into nanofibers as well as effective delivery of drug molecules at mitochondria.

prevent its bypass to nucleus whereas mitochondrial protease enterokinase (ENTK) cuts the Flag from the MitoFlag and H2B complex to form nanofibrillar structures which preserve H2B on the mitochondria and enable the H2B entrance to mitochondria.[164] When L-Asp residues were replaced with L-Glu or D-Asp residues it wiped out the transportation of H2B into mitochondria of HeLa cells. So, it interpreted that inter-organelle crosstalk played significant role in stress response cellular signalling.

Supramolecular Chemistry at the Target Site for Mitochondrial Imaging and Programmed Cell Death:

Molecular self-assembly is one of the most promising fields for the growth of new functional materials for mitochondria targeted delivery of small-molecules and drugs. Over the last few years nanostructural assemblies of amphiphilic peptides inside the specific cellular organelles have been extensively used for drug-free supramolecular therapeutics and diagnosis of cancer.[49–51,165–167] Noncovalent interactions like hydrogen bonding, electrostatic interaction, π-π interaction, and hydrophobic effect are responsible for the formation of self-assembling nanomaterials such as nanofibers, nanotubes, nanoribbons etc. However, it is very challenging to transport as well as to augment the local concentration of the self-assembling peptides inside the mitochondria. It is also challenging to control the self-assembly process of peptides inside the cellular organelle due to the complexity of biological environment. Unlike EISA approach where enzymatic cleavage of precursor hydrophilic peptide within the cell or pericellular space give rise to hydrophobic self-assembling moiety, organelle targeted supramolecular self-assembly (OTSA) strategy is an enzyme independent molecular self-assembling process. Moreover, OTSA is more generalised and less time-consuming approach; low dosage is required, applicable for various types of cancer cells and independent of biological enzyme as well as external stimuli. They have recently reported mitochondria localized supramolecular self-assembly based approach where TPP containing fluorophore tagged small amiphilic peptide unit selectively localised within cancer cell mitochondria 500-1000 times higher than the extracellular space to reach the critical aggregation concentration (CAC) and ultimately undergo self-assembling process to form nanostructure that trigger mitochondrial dysfunction induced cell death. Ryu and co-workers have designed and

synthesised N-terminal pyrene fluorophore tagged FFK tripeptide (both L and D variants) linked with TPP^+ through ε-amine of Lys residue (Pyr-FFK-TPP^+ and Pyr-ffk-TPP^+) for selective targeting of cancer cells mitochondria (**Figure 21**).[49] Pyrene not only functions as a fluorophore but also assisted in the self-assembly process by enhancing π–π and hydrophobic interactions. Self-assembly process was confirmed from pyrene excimer formation in the aggregated state. Owing to positive surface charge and hydrophobicity of Pyr-FFK-TPP^+ it preferentially accumulated inside the mitochondrial matrix to reach CAC (~60 μm) resulting the formation of nanofibrillar assembly (10 nm diameter) that eventually disrupted the mitochondrial membrane potential. Furthermore, it has also been reported that due to faster accumulation and higher concentration of Pyr-FFK-TPP^+ inside the mitochondria it showed similar activity and therapeutic efficiency as that of its D-analogue Pyr-ffk-TPP^+.[176] Another study carried out by the same group of researchers showed that co-assembly (1:1) of Pyr-FFK-TPP^+/Pyr-ffk-TPP^+ (containing both L and D isomers) racemic peptides followed faster kinetics with higher aggregation propensity and lower CAC (30 μm) compared to individual L or D enantiomer.[50] This racemic mixture self-assembled to form "rippled β-sheet" orientation which was enthalpically more favorable than individual isomeric assembly resulting in enzymatically stable mechanically rigid superfibril assemblies. Orientation of side chain amino acid and pyrene residues played a major role in the supramolecular assembly process. TEM experiment in HeLa cells treated with racemic mixture indicated rapid accumulation and superfibril formation (diameter = 30-100 nm and length = several μm) inside the mitochondria resulting higher cellular cytotoxicity. Furthermore, *in vivo* tumor shrinkage ability of supramolecular racemic peptides was higher in comparison with individual self-assembling enantiomers.

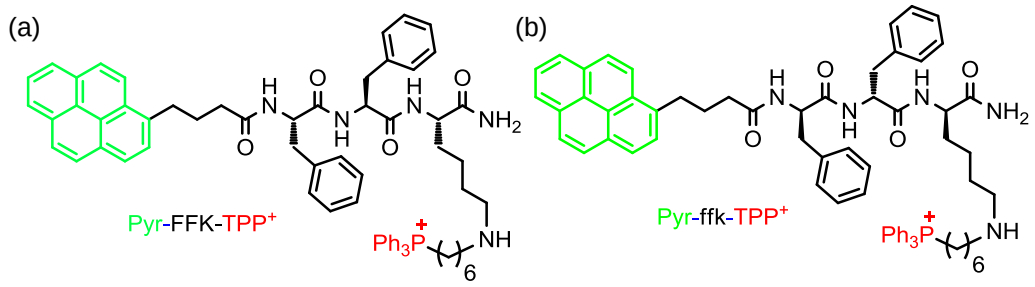

Figure 21. Mitochondria targeting fluorophore conjugated self-assembling peptides (a) Pyr-FFK-TPP^+ and (b) Pyr-ffk-TPP^+.

Recently supramolecular antagonists promoted mitochondria targeted cellular dysfunction has been reported by Yu et al. The supramolecular antagonist (Py^{Me}AmpBC) was developed through co-assembly of a mitochondria targeting pyridinium containing pentapeptide (Py^{Me}Amp) with its two products derivatized with a BH3 domain (Py^{Me}Amp-BH3) or the drug camptothecin (CPT, Py^{Me}Amp-CPT) (**Figure 22**).[168] Here, *N*-methylpyridinium-alanine (Py^{Me}) residue at the *N*-terminal end of pentapeptide was used to target mitochondria and also exhibited strong assembling propensity, whereas the Amp residue was responsible for pH dependent morphological transformation due to isomerisation of Amp amide bond. The BH3 domain within coassemblies adopted α-helical conformation at acidic tumor environment (pH 6.5) associated with anti-apoptotic proteins Bcl-xL and inhibited the heterodimerization of Bcl-xL with pro-apoptotic BAX proteins. On the other hand CPT released from the antagonist through -S–S- bond cleavage by mGSH that reduced the IMM potential as well as supressed topoisomerase I activity in tumor cells and triggered cyt *c* release, caspase activation which was responsible for tumor cells apoptosis. Both *in vitro* and *in vivo* experiments established the combined therapeutic result due to the CPT drug and BH3 domain within the supramolecular antagonist on cellular dysfunction and thus

preventing tumor growth. These combined mechanisms of supramolecular antagonist to trigger mitochondrial dysfunction driven apoptosis can serve as potential contributor for mitochondria targeted tumor therapy.

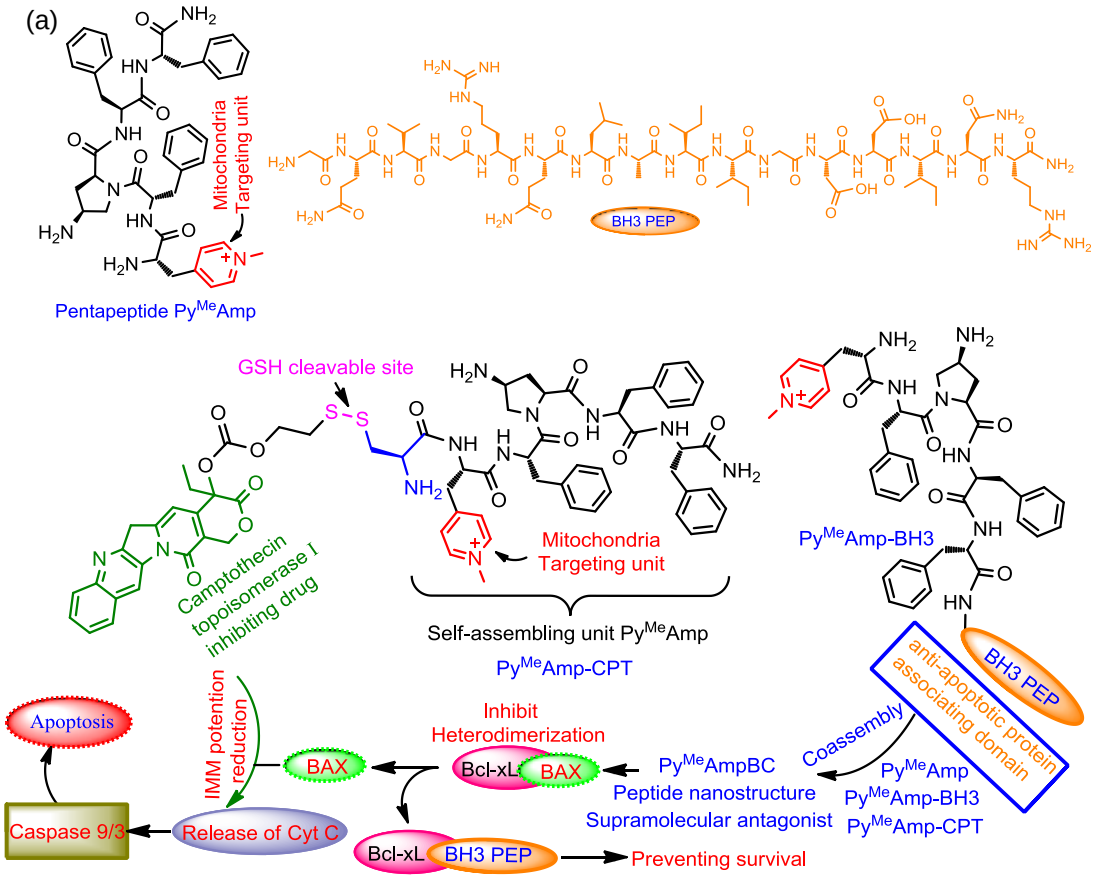

Figure 22. (a) Structures of mitochondria targeting self-assembling pentapeptide Py^{Me}Amp and BH3 domain of pro-apoptotic protein BAK. (b) Schematic representation of mitochondria targeting supramolecular antagonist Py^{Me}AmpBC [coassembly of Py^{Me}Amp(85%), Py^{Me}Amp-CPT(5%), and Py^{Me}Amp-BH3(10%)] to induce cellular apoptosis.

Confocal Laser Scanning Microscopy:

Confocal laser scanning microscopy (CLSM) is a specialised fluorescence imaging technique often used in bioimaging applications. It works on the same principle as a conventional fluorescence microscope to form an image, however instead of a lamp or LED lights; a focused beam of laser light is used for CLSM. Various wavelength laser excitation sources or white light laser are used in CLSM. Laser light illuminates the small part of a specimen, and emitted light is passed through a pinhole (placed right in front of the detector), which eliminates out-of-focus light from the neighbouring planes to reduce the background noise and significantly enhance the quality of the image. Initially, a photomultiplier tube (PMT) was used in CLSM to detect and amplify the fluorescence signal from the specimen, but technological advancements and the introduction of the HyD hybrid detector offer better contrast with improved image quality. In contrast to traditional fluorescence microscopy, CLSM offers a number of distinct advantages, like reduction of out-of-focus blurring effects by using spatial filtering techniques, enhancement of the contrast, sharpness, and optical resolution of the captured images. The major advantage of CLSM is the construction of 3D cellular images using suitable dyes by harvesting several Z-stack slices collected at various depths of the specimen. This gives better structural details of cellular organelles.

Fixed cell and live cell confocal imaging:

Both fixed cell and live cell confocal imaging techniques are frequently used to ensure the cellular uptake of a probe. However, live cell imaging is quite different and more challenging than fixed cell imaging technique. In case of fixed cell imaging cells were first grown on the coverslip and then fixed with 4% paraformaldehyde solution. During this process, cells are mostly preserved

with their intact shape and contents, and further staining as well as imaging processes become much easier as compared to live cells. However, during fixed cell protocol, the integrity of the cell membrane can be broken and fixed cells become more permeabilized to external substances. Moreover, the dynamic behaviour of the cells, which is imperative biological data, is missing from the images obtained after cell fixation. On the other hand, live cell imaging is just like it sounds; cells are alive in the phenol red free growth media and images are captured over time (time-lapse imaging) at 37°C, 5% CO_2 incubation depicting the dynamic nature of cellular organelles. Live cell imaging is more complex compared to fixed cell imaging and requires a special set up (**Figure 23**). Most importantly, for live cell imaging, the fluorophores used must have low toxicity and excellent photophysical properties so that they can withstand a longer period of laser exposure.

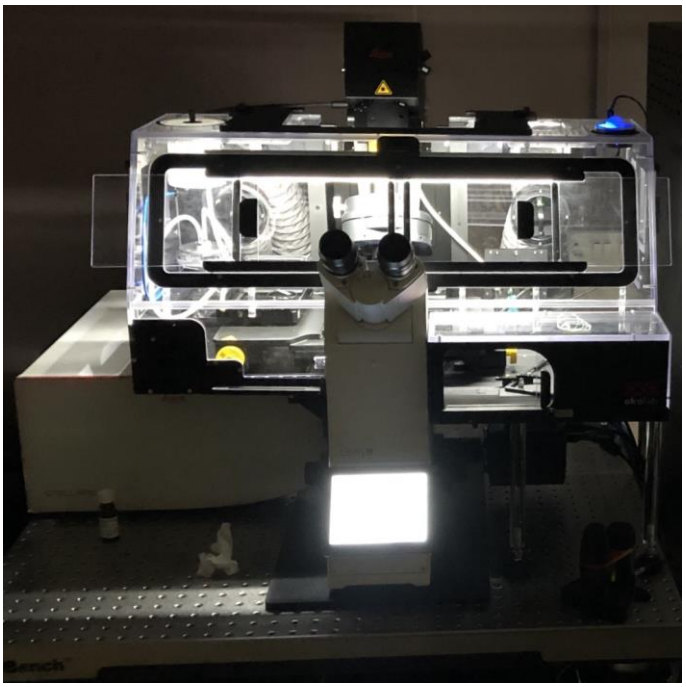

Figure 23. Special instrumental set up for live cell confocal imaging.

Multicolor cellular imaging:

A multicolor live cell confocal imaging technique has become an emerging field to understand and visualize complex and dynamic biological events. However, it is a challenging task to track various cellular organelles of the same cell simultaneously due to lack of suitable dyes. For multicolor cellular imaging, fluorophores conjugated with organelle selective functional groups and having distinct narrow excitation and emission bands are required. Multicolor imaging reveals different cellular events of the same cell in a single image by visualising the morphological and structural changes of different organelles that take place under various pathological events. Recently, Kai Johnsson and Collot groups reported NIR fluorophores having narrow absorption and emission bands for multicolor imaging purposes.[169-171]

Live cell protein labeling:

Living cells can be functionalised in well-organized manner by expressing a wide range of proteins and their diverse functionality has prodigious impact on different physiological processes. A range of internal and external stresses can exert significant pressures on living cells, resulting in fluctuations in various protein levels. Protein bioconjugation inside a crowded living cell environment in a rapid and cost-effective manner without affecting their inherent function have proved to be a valuable tool in current research.[93,94,172-176] In the last few years, organelle specific tracking and quantitative monitoring of protein activities in living cells with small molecular probes have gained significant attention in the fields of cellular biology, biotechnology, and the development of medicine.[93,175,177] The widely used methodology for conventional proteomic investigations is the selective enrichment of certain subcellular organelle proteins from their purified lysate

fraction by ultracentrifugation, followed by 2D or 1D gel electrophoresis and MS-based analysis for their identification.[94] Nevertheless, despite meticulous preparation, the isolated organelle frequently becomes contaminated by other organelles and is likely to have lost some crucial components, leading to false-positive and false-negative results. Recently, Ting and co-workers developed an enzymatic oxidation method to selectively modify mitochondrial proteins by introducing an engineered ascorbate peroxidase (APEX) with a biotin affinity tag.[172] In this method, oxidation of biotin-phenol (an APEX substrate) takes place in the vicinity of APEX protein upon addition of H_2O_2. Although this method is effective and reliable, however, APEX technology always requires an engineered peroxidase expression and also requires the addition of cytotoxic H_2O_2 to start the labelling process, which may potentially perturb natural biological conditions. In contrast, Hamachi et al. introduced a range of organelle localizable small molecular probe bearing reactive moieties, which exhibit variable chemical reactivity and selectivity towards endogenous proteins (**Figure 24**).[93] After preferential accumulation within the target specific organelle of living cells, the local concentration of these small molecules increases and they selectively react with side chains of endogenous proteins, which is further resolved by gel-electrophoresis and identified through mass spectrometry analysis. Thus, the chemo-selective based mild protein labeling approach is rather simple and does not require any organelle fractionation or genetic manipulation. Hamachi and co-workers successfully used this protein labeling technique in profiling of mitochondrial proteomics in living HeLa cells.[93]

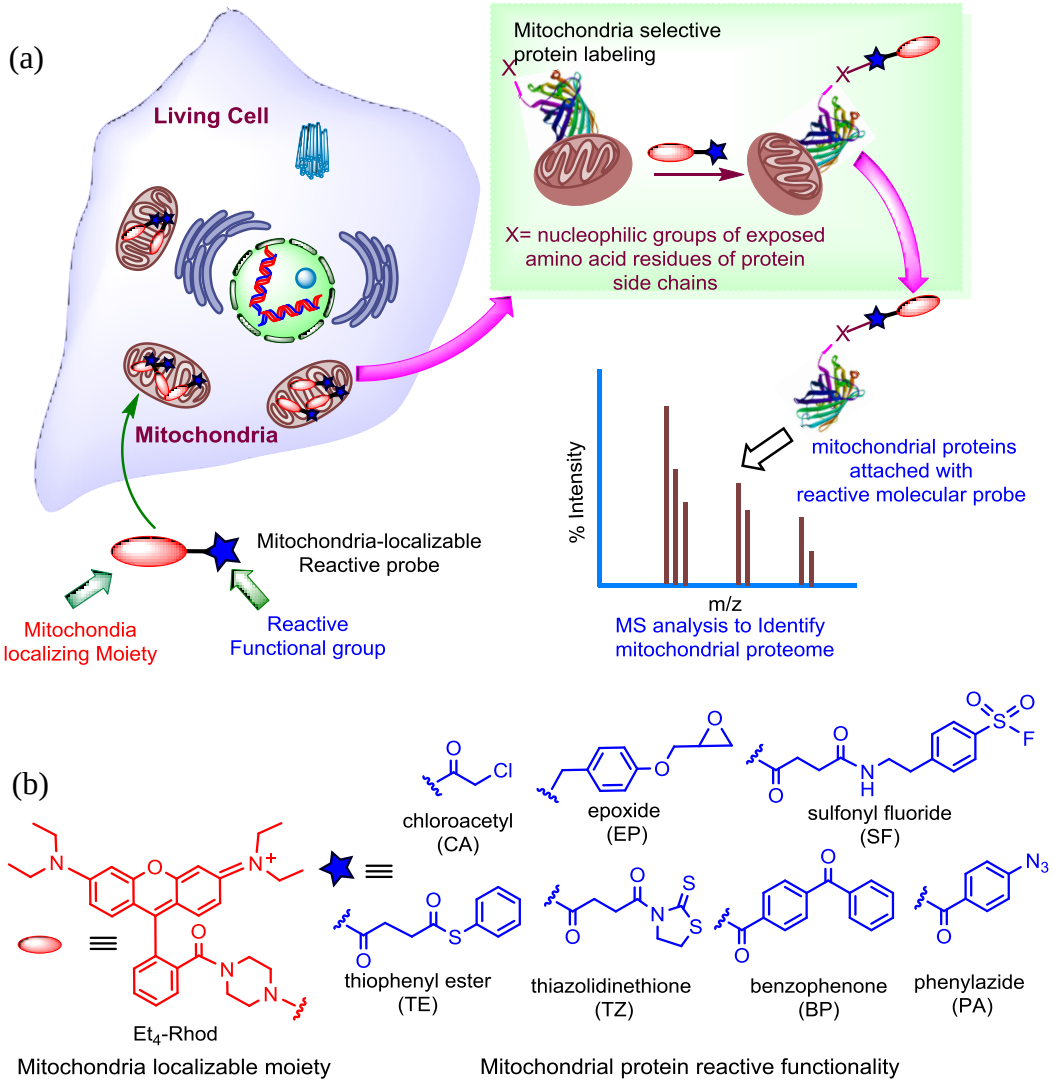

Figure 24. (a) Schematic presentation of mitochondria targeting protein labeling. (b) Structure of mitochondria localizable reactive molecules.

References:

[1] Altmann, R. *Die Elementarorganismen und ihreBeziehungenzu den ZellenVeit (The cellular organelles and their relations to cells)* **1890,** Veit & Co., Leipzig, Germany.

[2] Benda, C. *Arch. Anal. Physiol.* **1898**, *73*, 393–398.

[3] Siekevitz, P. *Sci. Am*. **1957**, *197*, 131-140.

[4] Frazier, A. E.; Thorburn, D. R.; and Compton, A. G. *J. Biol. Chem.* **2019**, *294*, 5386–5395.

[5] Murphy, M.; and Hartley, R. *Nat. Rev. Drug Discovery* **2018**, *17*, 865–886.

[6] Nass, S.; and Nass, M. M. *J. Cell Bio.* **1963**, *19*, 613-629.

[7] Wiedemann, N.; and Nikolaus, P. *Annu. Rev. Biochem*. **2017**, *86*, 685–714.

[8] Kazak, L.; Reyes, A.; and Holt, I. *Nat. Rev. Mol. Cell Biol.* **2012**, *13*, 659–671.

[9] Taylor, R.; and Turnbull, D. *Nat. Rev. Genet.* **2005**, *6*, 389–402.

[10] Nunnari, J.; and Suomalainen, A. *Cell* **2012**, *148*, 1145-1159.

[11] Vyssokikh, M. Y.; Holtze, S.; Averina, O. A.; Lyamzaev, K. G.; Panteleeva, A. A.; Marey, M. V.; Zinovkin, R. A.; Severin, F. F.; Skulachev, M. V.; Fasel, N.; Hildebrandt, T. B.; and Skulachev, V. P. *Proc. Natl. Acad. Sci. U. S. A.* **2020**, *117*, 6491−6501.

[12] Galluzzi, L.; Blomgren, K.; and Kroemer, G. *Nat. Rev. Neurosci.* **2009**, *10*, 481−494.

[13] Ma, C.; Xia, F.; and Kelly, S. O. *Bioconjugate Chem.* **2020**, *31*, 2650–2667.

[14] Lu, P.; Bruno, B. J.; Rabenau, M.; and Lim, C. S. *Journal of Controlled Release* **2016**, *240*, 38-51.

[15] Fulda, S.; Galluzzi, L.; and Kroemer, G. *Nat. Rev. Drug Discovery* **2010**, *9*, 447−464.

[16] Weinberg, S. E.; and Chandel, N. S. *Nat. Chem. Biol.* **2015**, *11*, 9−15.

[17] Chen, H.; He, C.; Chenb, T.; and Xue, X. *Biomater. Sci.* **2020**, *8*, 3994–4002.

[18] L. B. Chen, *Annu.Rev. Cell Biol.* **1988**, *4*, 155−181.

[19] Ashrafi, G.; and Schwarz, T. L. *Cell Death Differ*. **2013**, *20*, 31–42.

[20] Mukherjee, A.; Saha, P. C.; Das, R. S.; Bera, T.; and Guha, S. *ACS Sens.* **2021**, *6*, 2141–2146.

[21] Chrétien, D.; Bénit, P.; Ha, H.-H.; Keipert, S.; El-Khoury, R.; Chang,Y.-T.; Jastroch, M.; Jacobs, H. T.; Rustin, P.; and Rak, M. *PLoS Biol*. **2018**, *16*, e2003992.

[22] Lee, M. H.; Park, N.; Yi, C.; Han, J. H.; Hong, J. H.; Kim, K. P.; Kang, D. H.; Sessler, J. L.; Kang, C.; and Kim, J. S. *J. Am. Chem. Soc.* **2014**, *136*, 14136−14142.

[23] Xia, S.; Wang, J.; Zhang, Y.; Whisman, N.; Bi, J.; Steenwinkel, T. E.; Wan, S.; Medford, J.; Tajiri, M.; Luck, R. L.; Werner, T.; and Liu, H. *J. Mater. Chem. B* **2020**, *8*, 1603-1615.

[24] Jiang, A.; Chen, G.; Xu, J.; Liu, Y.; Zhao, G.; Liu, Z.; Chen, T.; Li, Y.; and James, T. D. *Chem. Commun.* **2019**, *55*, 11358−11361.

[25] Yang, Z.; He, Y.; Lee, J. -H.; Park, N.; Suh, M.; Chae, W. -S.; Cao, J.; Peng, X.; Jung, H.; Kang, C.; and Kim, J. S.; *J. Am. Chem. Soc.* **2013**, *135*, 9181–9185.

[26] Chen, B.; Mao, S.; Sun, Y.; Sun, L.; Ding, N.; Li.; C.; and Zhou, J. *Chem. Commun.* **2021**, *57*, 4376–4379.

[27] Yu, L.; Zhang, J. F.; Li, M.; Jiang, D.; Zhou, Y.; Verwilst, P.; and Kim, J. S. *Chem. Commun*. **2020**, *56*, 6684-6687.

[28] Li, X.; Li, X.; and Ma, H. *Chem. Sci.* **2020**, *11*, 1617–1622.

[29] Xiao, H.; Li, P.; Zhang, W.; and Tang, B. *Chem. Sci.* **2016**, *7*, 1588–1593.

[30] Goujon, A.; Colom, A.;Strakova, K.; Mercier, V.;Mahecic, D.; Manley, S.; Sakai, N.; Roux, A.; and Matile, S. *J. Am. Chem. Soc.* **2019**, *141*, 3380−3384.

[31] Arai, S.; Suzuki, M.; Park, S.-J.; Yoo, J. S.; Wang, Lu.; Kang, N.-Y.; Ha, H.-H.; and Chang, Y.-T. *Chem. Commun*. **2015**, *51*, 8044−8047.

[32] Huang, Z.; Li, N.; Zhang,X.; and Xiao, Y. *Anal. Chem.* **2021**, *93*, 5081−5088.

[33] Zielonka, J.; Joseph, J.; Sikora, A.; Hardy, M.; Ouari, O.; Vasquez-Vivar, J.; Cheng, G.; Lopez, M.; and Kalyanaraman, B. *Chem. Rev.* **2017**, *117*, 10043−10120.

[34] Xiao, Q.; Du.; W.; Dong, X.; Du, S.; Ong, S. Y.; Tang, G.; Zhang, C.; Yang, F., Li, L.; Gao, L.; and Yao, S. Q. *Chem. -Eur. J.* **2021**, *27*, 12207−12214.

[35] Biswas, S., Dodwadkar, N. S., Piroyan, A., and Torchilin, V. P. *Biomaterials* **2012**, *33*, 4773–4782.

[36] Lee, J. H.; Kim, K. Y.; Jin, Hanyong.; Baek, Y. E.; Choi, Y.; Jung, S. H.; Lee, S. S.; Bae, J.; and Jung, J. H. *ACS Appl. Mater. Interfaces* **2018**, *10*, 3380−3391.

[37] Jeena, M.T.; Kim, S.; J.; S.; and Ryu, J.-H. *Cancers* **2020**, *12*, 4.

[38] Shi, M.; Zhang, J.; Li, X.; Pan, S.; Li, J.; Yang, C.; Hu, H.; Qiao, M.; Chen, D.; and Zhao, X. *Int. J. Nanomed.* **2018**, *13*, 4209–4226.

[39] Maiti, K. K.; Lee, W. S.; Takeuchi, T.; Watkins, C.; Fretz, M.; Kim, D. C.; Futaki, S.; Jones, A.; Kim, K. T.; and Chung, S. K. *Angew. Chem., Int. Ed.* **2007**, *46*, 5880−5884.

[40] Nodling A. R.; Mills, E. M.; Li, X.; Cardella, D.; Sayers, E. J.; Wu, S.-H.; Jones, A.T.; Luk, L. Y. P.; and Tsai, Y.-H. *Chem. Commun.* **2020**, *56*, 4672-4675.

[41] Lincoln, R.; Greene, L.E.; Zhang, W.; Louisia, S.; and Cosa, G. *J. Am. Chem. Soc.* **2017**, *139*, 16273–16281.

[42] Paul, A.; Mengji, R.; Bera, M.; Ojha, M.; Jana, A.; and Singh, N. D. P. *Chem. Commun.* **2020**, *56*, 8412-8415.

[43] Lei, E. K.; and Kelley, S. O. *J. Am. Chem. Soc.* **2017**, *139*, 9455−9458.

[44] Weissig, V. DQAsomes as the Prototype of Mitochondria-Targeted Pharmaceutical Nanocarriers: Preparation, Characterization, and Use. In: V. Weissig, M. Edeas (eds.) Mitochondrial Medicine. *Methods in Molecular Biology*, vol 1265. *Humana Press, New York, NY,* **2015**, *doi.org/10.1007/978-1-4939-2288-8_1*.

[45] Katayama, T.; Kinugawa, S.; Takada, S.; Furihata, T.; Fukushima, A.; Yokota, T.; Anzai, T.; Hibino, M.; Harashima, H.; and Yamada, Y. *Mitochondrion* **2019**, *49*, 66−72.

[46] Liew, S. S.; Qin, X.; Zhou, J.; Li, L.; Huang, W.; and Yao, S. Q. *Angew. Chem., Int. Ed.* **2021**, *60*, 2232–2256.

[47] Wang, D.; Huang, H.; Zhou, M.; Lu, H.; Chen, J.; Chang, Y.-T.; Gao, J.; Chai, Z.; and Hu, Y. *Chem. Commun.* **2019**, *55*, 4051−4054.

[48] Yang, G.; Xu, L.; Xu, J.; Zhang, R.; Song, G.; Chao, Y.; Feng, L.; Han, F.; Dong, Z.; Li, B.; and Liu, Z. *Nano Lett.* **2018**, *18*, 2475−2484.

[49] Jeena, M. T.; Palanikumar, L.; Go, E. M.; Kim, I.; Kang, M. G.; Lee, S.; Park, S.; Choi, H.; Kim, C.; Jin, S.-M.; Bae, S. C.; Rhee, H. W.; Lee, E.; Kwak, S. K.; and Ryu, J.-H. *Nat. Commun.* **2017**, *8*, 26.

[50] Jeena, M. T.; Jeong, K.; Go, E. M.; Cho, Y.; Lee, S.; Jin, S.; Hwang, S.-W.; Jang, J. H.; Kang, C. S.; Bang, W.-Y.; Lee, E; Kwak, S. K.; Kim, S.; and Ryu, J.-H. *ACS Nano* **2019**, *13*, 11022−11033.

[51] Saha, P. C.; Das, R. S.; Chatterjee, T.; Bhattacharyya, M.; Guha, S. *Bioconjugate Chem.* **2020**, *31*, 1301−1306.

[52] Wang, H.; Feng, Z.; Wang, Y.; Zhou, R.; Yang, Z.; and Xu, B. *J. Am. Chem. Soc.* **2016**, *138*, 16046−16055.

[53] Zhou, J.; Du, X.; and Xu, B. *Angew. Chem., Int. Ed.* **2016**, *55*, 5770−5775.

[54] He, H.; Lin, X.; Guo, J.; Wang, J.; and Xu, B. *ACS Nano* **2020**, *14*, 6947−6955.

[55] Joza, N.; Susin, S. A.; Daugas, E.; Stanford, W. L.; Cho, S. K.; Li, C. Y. J.; Sasaki, T.; Elia, A. J.; Cheng, H.-Y. M.; Ravagnan, L.; Ferri, K. F.; Zamzami, N.; Wakeham, A.; Hakem, R.; Yoshida, H.; Kong, Y.- Y.; Mak, T. W.; Zuń̃iga-Pflücker, J. C.; Kroemer, G.; and Penninger, J. M. *Nature* **2001**, *410*, 549−554.

[56] Cory, S.; and Adams, J. M. *Nat. Rev. Cancer* **2002**, *2*, 647−656.

[57] Danial, N. N.; and Korsmeyer, S. J. *Cell* **2004**, *116*, 205−219.

[58] Lakhani, S. A.; Masud, A.; Kuida, K.; Porter, G. A.; J, Booth, C. J.; Mehal, W. Z.; Inayat, I.; and Flavell, R. A. *Science* **2006**, *311*, 847−851.

[59] Liu, T.; Roh, S. E.; Woo, J. A.; Ryu, H.; and Kang, D. E. *Cell Death Dis.* **2013**, *4*, e476.

[60] Shi,Y.; Nikulenkov, F.; Zawacka-Pankau, J.; Li, H.; Gabdoulline, R.; Xu, J.; Eriksson, S.; Hedstro¨m, E.; Issaeva, N.; Kel, A.; Arner, E.; and Selivanova, G. *Cell Death Differ.* **2014**, *21*, 612–623.

[61] Chen, J.; Jiang, X.; Zhang, C.; MacKenzie, K. R.; Stossi, F.; Palzkill, T.; Wang, M. C.; and Wang, J. *ACS Sens.* **2017**, *2*, 1257−1261.

[62] Ling, X.; Gong, D.; Shi, W.; Xu, Z.; Han, W.; Lan, G.; Li, Y.; Qin, W.; and Lin, W. *J. Am. Chem. Soc.* **2021**, *143*, 1284-1289.

[63] Long, L.; Huang, M.; Wang, N.; Wu, Y.; Wang, K.; Gong, A.; Zhang, Z.; and Sessler, J. L. *J. Am. Chem. Soc.*, **2018**, *140*, 1870−1875.

[64] Reshetnikov, V.; Daum, S.; Janko, C.; Karawacka, W.; Tietze, R.; Alexiou, C.; Paryzhak, S.; Dumych, T.; Bilyy, R.; Tripal, P.; Schmid, B.; Palmisano, R.; and Mokhir, A. *Angew. Chem., Int. Ed.* **2018**, *57*, 11943–11946.

[65] Liu, Y.; Liu, Y.; Zang, J.; Abdullah, A. A. I.; Li, Y.; and Dong, H. *ACS Biomater. Sci. Eng.* **2020**, *6*, 6510–6527.

[66] Murfin, L. C.; Weber, M.; Park, S. J.; Kim, W. T.; Lopez-Alled, C. M.; McMullin, C. L.; Pradaux-Caggiano, F.; Lyall, C. L.; Kociok-Köhn, G.; Wenk, J.; Bull, S. D.; Yoon, J.; Kim, H. M.; James, T. D.; and Lewis, S. E. *J. Am. Chem. Soc.* **2019**, *141*, 19389–19396.

[67] Shi, D.; Chen, S.; Dong, B.; Zhang, Y.; Sheng, C.; James, T. D., and Guo, Y. *Chem. Sci.* **2019**, *10*, 3715–3722.

[68] Hong, S.; Zhang, X.; Lake, R. J.; Pawel, G. T.; Guo, Z.; Pei, R.; and Lu, Y. *Chem. Sci.* **2020**, *11*, 713–720.

[69] Ren, T.-B.; Wen, S.-Y.; Wang, L.; Lu, P.; Xiong, B.; Yuan, L.; Zhang, and X.-B. *Anal. Chem.* **2020**, *92*, 4681−4688.

[70] Chevalier, A.; Zhang, Y.; Khdour, O. M.; Kaye, J. B.; and Hecht, S. M. *J. Am. Chem. Soc.* **2016**, *138*, 12009−12012.

[71] Thiel, Z.; and Rivera-Fuentes, P. *Angew. Chem., Int. Ed.* **2019**, *58*, 11474–11478.

[72] Zhu, N.; Xu, G.; Wang, R.; Zhu, T.; Tan, J.; Gu, X.; and Zhao. C. *Chem. Commun.* **2020**, *56*, 7761-7764.

[73] G Yuan, G.; Lv, C.; Liang, J.; Zhong, X.; Li, Y.; He, J.; Zhao, A.; Li, L.; Shao, Y.; Zhang, X.; Wang, S.; Cheng, Y.; and He, H. *Adv. Funct. Mater.* **2021**, *31*, 2104026.

[74] Nash, G. T.; Luo, T.; Lan, G.; Ni, K.; Kaufmann, M.; and Lin, W. *J. Am. Chem. Soc.* **2021**, *143*, 2194–2199.

[75] Yang, Z.; Zhang, Z.; Lei, Z.; Wang, D.; Ma, H.; and Tang, B. Z. *ACS Nano* **2021**, *15*, 7328−7339.

[76] Qiu, K.; Wang, J.; Rees, T. W.; Ji, L.; Zhang, Q.; and Chao, H. *Chem. Commun.* **2018**, *54*, 14108−14111.

[77] Ning, P.; Huang, L.; Bao, Y.; Fu, Y.; Xu, C.; Shen, Y.; Zhou, X.; Wen, X.; Cheng, Y.; and Qin, Y. *Bioconjugate Chem*. **2020**, *31*, 2719−2725.

[78] Wang, Z.; Chen, Y.; Zhang, H.; Li, Y.; Ma, Y.; Huang, J.; Liu, X.; Liu, F.; Wang, T.; and Zhang. X. *Bioconjugate Chem.* **2018**, *29*, 2415−2425.

[79] Chen, Y.; Ai, W.; Guo, X.; Li, Y.; Ma, Y.; Chen, L.; Zhang, H.; Wang, T.; Zhang, X.; and Wang, Z. *Small* **2019**, *15*, 1902352.

[80] Jung, H. S.; Lee, J.-H.; Kim, K.; Koo, S.; Verwilst, P.; Sessler, J. L.; Kang, C.; and Kim, J. S. *J. Am. Chem. Soc.* **2017**, *139*, 9972−9978.

[81] Jiang, M.; Gu, Xi.; Kwok, R. T. K.; Li, Y.; Sung, H. H. Y.; Zheng, X.; Zhang, Y.; Lam, J. W. Y.; Williams, I. D.; Huang, X.; Wong, K. S.; and Tang, B.Z. *Adv. Funct. Mater.* **2018**, *28*, 1704589.

[82] Guo, B.; Wu, M.; Shi, Q.; Dai, T.; Xu, S.; Jiang, J.; and Liu, B. *Chem. Mater.* **2020**, *32*, 4681−4691.

[83] Wang, D.; Lee, M. M. S.; Shan, G.; Kwok, R. T. K.; Lam, J.W. Y.; Su, H.; Cai., Y.; and Tang, B. Z. *Adv. Mater.* **2018**, *30*, 1802105.

[84] Jana, B.; Thomas, A. P.; Kim, S.; Lee, I. S.; Choi, H.; Jin, S.; Park, S. A.; Min, S. K.; Kim, C.; and Ryu, J,-H. *Chem. -Eur. J.* **2020**, *26*, 10695–10701.

[85] Thomas, A. P.; Palanikumar, L.; Jeena, M. T.; Kim, K.; and Ryu, J.-H. *Chem. Sci.* **2017**, *8*, 8351−8356.

[86] Zheng, Y.; Li, Q.; Wu, J.; Luo, Z.; Zhou, W.; Li, A.; Chen, Y.; Rouzi, T.; Tian, T.; Zhou, H.; Zeng, X.; Li, Y.; Cheng, X.; Wei, Y.; Deng, Z.; Zhou, F.; and Hong, X. *Chem. Sci.* **2021**, *12*, 1843–1850.

[87] Wang, Q., Xu, J., Geng, R., Cai, J., Li, J., Xie, C., Tang,W., Shen, Q., Huang, W., and Fan. Q. *Biomaterials* **2020**, *231*, 119671.

[88] Xu, Y., Xu, R., Wang, Z., Zhou, Y., Shen, Q., Ji, W., Dang, D., Meng, L., and Tang, B. Z. *Chem. Soc. Rev.* **2021**, *50*, 667-690.

[89] Wang, C.; Taki, M.; Sato, Y.; Tamura, Y.; Yaginuma, H.; Okada, Y.; and Yamaguchi, S. *Proc. Natl. Acad. Sci. U. S. A.* **2019**, *116*, 15817–15822.

[90] Chen, Q.; Fang, H.; Shao, X.; Tian, Z.; Geng, S.; Zhang, Y.; Fan, H.; Xiang, P.; Zhang, J.; Tian, X.; Zhang, K.; He, W.; Guo, Z.; and Diao, J. *Nat. Commun.* **2020**, *11*, 6290.

[91] Han, Y.; Li, M.; Qiu, F.; Zhang. M.; and Zhang., Y.-H. *Nat. Commun.* **2017**, *8*, 1307.

[92] Yang, X.; Yang, Z.; Wu, Z.; He, Y.; Shan, C.; Chai, P.; Ma, C.; Tian, M.; Teng, J.; Jin, D.; Yan, W.; Das, P.; Qu, J.; and Xi, P. *Nat. Commun*. **2020**, *11*, 3699.

[93] Yasueda, Y.; Tamura, T.; Fujisawa, A.; Kuwata, K.; Tsukiji, S.; Kiyonaka, S.; and Hamachi, I. *J. Am. Chem. Soc.* **2016**, *138*, 7592−7602.

[94] Bak, D. W.; Pizzagalli, M. D.; and Weerapana. E. *ACS Chem. Biol.* **2017**, *12*, 947–957.

[95] Chalmers, S.; Caldwell, S. T.; Quin, C.; Prime, T. A.; James, A. M.; Cairns, A. G.; Murphy, M. P.; McCarron, J. G.; and Hartley, R. C. *J. Am. Chem. Soc.* **2012**, *134*, 758−761.

[96] Prag, H. A.; Kula-Alwar, D.; Pala, L.; Caldwell, S. T.; Beach, T. E.; James, A. M.; Saeb-Parsy, K.; Krieg, T.; Hartley, and R. C.; Murphy, M. P. *Mol. Pharmaceutics* **2020**, *17*, 3526−3540.

[97] Chen, H.; Wang, J.; Feng, X.; Zhu, M.; Hoffmann, S.; Hsu, A.; Qian, K.; Huang, D.; Zhao, F.; Liu, W.; Zhang, H.; and Cheng, Z. *Chem. Sci.* **2019**, *10*, 7946–7951.

[98] Zhang, R.; Niu, G.; Li, X.; Guo, L.; Zhang, H.; Yang, R.; Chen, Y.; Yu, X.; and Tang, B. Z. *Chem. Sci.* **2019**, *10*, 1994–2000.

[99] Tian, M.; Ge, E.; Dong, B.; Zuo, Y.; Zhao, Y.; and Lin, W. *Anal. Chem.* **2021**, *93*, 3602−3610.

[100] Chen, W.-H.; Luo, G.-F.; and Zhang. X.-Z. *Adv. Mater.* **2019**, *31*, 1802725.

[101] Wu, S.; Cao, Q.; Wang, X.; Chenga, K.; and Cheng, Z. *Chem. Commun.* **2014**, *50*, 8919–8922.

[102] Ferna´ndez-Carneado, J.; Gool, M. V.;Vera, M.; Castel, S.; Prados, P.; de Mendoza, J.; and Giralt., E. *J. Am. Chem. Soc.* **2005**, *127*, 869–874.

[103] Valero, J.; Van Gool, M.; Perez-Fernandez, R.; Castreno, P.; Sanchez-Quesada, J.; Prados, P.; and de Mendoza, J. *Org. Biomol. Chem.* **2012**, *10*, 5417−5430.

[104] D'Souza, G. G. M.; Rammohan, R.; Cheng, S. M.; Torchilin, V. P.; and Weissig, V. *J. Controlled Release* **2003**, *92*, 189–197.

[105] Cheng, Y.; and Ji, Y. *J. Controlled Release* **2020**, *318*, 38–49.

[106] Burns, R. J.; Smith, R. A.; and Murphy, M. P. *Arch. Biochem. Biophys.* **1995**, *322*, 60−68.

[107] Murphy, M. P. *Trends Biotechnol.* **1997**, *15*, 326−330.

[108] Smith, R. A.; Porteous, C. M.; Coulter, C. V.; and Murphy, M. P. *Eur. J. Biochem.* **1999**, *263*, 709−716.

[109] Huang, Y.; Zhou, Q.; Feng, Y.; Zhang, W.; Fang, G.; Fang, M.; Chen, M.; Xu, C.; and Meng, X. *Chem. Commun.* **2018**, *54*, 10495−10498.

[110] Li, X.; Tian, M.; Zhang, G.; Zhang, R.; Feng, R.; Guo, L.; Yu, X.; Zhao, N.; and He, X. *Anal.Chem.* **2017**, *89*, 3335-3344.

[112] Kelso, G. F.; Porteous, C. M.; Coulter, C. V.; Hughes, G.; Porteous, W. K.; Ledgerwood, E. C.; Smith, R. A.; and Murphy, M. P. *J. Biol. Chem.* **2001**, *276*, 4588−4596.

[113] Filipovska, A.; Kelso, G. F.; Brown, S. E.; Beer, S. M.; Smith, R. A.; and Murphy, M. P. *J. Biol. Chem.* **2005**, *280*, 24113−24126.

[114] Jameson, V. J.; Cocheme, H. M.; Logan, A.; Hanton, L. R.; Smith, R. A.; and Murphy, M. P. *Tetrahedron* **2015**, *71*, 8444−8453.

[115] Trnka, J.; Blaikie, F. H.; Logan, A.; Smith, R. A.; and Murphy, M. P. *Free Radical Res.* **2009**, *43*, 4−12.

[116] Kauffman, M. E.; Kauffman, M. K.; Traore, K.; Zhu, H.; Trush, M. A.; Jia, Z.; and Li, Y. R. *React. Oxygen Species* **2016**, *2*, 361−370.

[117] Hardy, M.; Poulhe, F.; Rizzato, E.; Rockenbauer, A.; Banaszak, K.; Karoui, H.; Lopez, M.; Zielonka, J.; Vasquez-Vivar, J.; Sethumadhavan, S.; Kalyanaraman, B.; Tordo, P.; and Ouari, O. *Chem. Res. Toxicol.* **2014**, *27*, 1155−1165.

[118] Johnson, I. D. Molecular Probes Handbook: A Guide to Fluorescent Probes and Labeling Technologies, *Life Technologies Corporation*, United States, **2010,** *DOI: 10.1007/978-1-61779-968-6*.

[119] Kawazoe, Y.; Shimogawa, H.; Sato, A.; and Uesugi, M. *Angew. Chem., Int. Ed.* **2011**, *50*, 5478−5481.

[120] Kubi, G. A.; Qian, Z.; Amiar, S.; Sahni, A.; Stahelin, R. V.; and Pei, D. *Angew. Chem., Int. Ed.* **2018**, *57*, 17183−17188.

[121] Salvioli, S.; Ardizzoni, A.; Franceschi, C.; and Cossarizza, A. *FEBS Lett.* **1997**, *411*, 77−82.

[122] S Biswas, S.; Dodwadkar, N. S.; Sawant, R. R.; Koshkaryev, A.; and Torchilin, V. P. *J. Drug Target.* **2011**, *19*, 552−561.

[123] Kim, Y. K.; Ha, H.-H.; Lee, J.-S.; Bi, X.; Ahn, Y.-H.; Hajar, S.; Lee, J.-J.; and Chang, Y.-T. *J. Am. Chem. Soc.* **2010**, *132*, 576–579.

[124] Sung, J.; Rho, J. G.; Jeon, G. G.; Chu, Y.; Min, J. S.; Lee, S.; Kim, J. H.; Kim, W.; and Kim, E. *Bioconjugate Chem.* **2019**, *30*, 210−217.

[125] Klier, P.E. Z.; Martin, J. G.; and Miller, E. W. *J. Am. Chem. Soc.* **2021**, *143*, 4095−4099.

[126] Schnermann, M. J. *Nature* **2017**, *551*, 176–177.

[127] Tan, X.; Luo, S.; Long, L.; Wang, Y.; Wang, D.; Fang, S.; Ouyang, Q.; Su, Y.; Cheng, and T.; Shi, C. *Adv. Mater.* **2017**, 29, 1704196.

[128] Zhang, C.; Liu, T.; Luo, P.; Gao, L.; Liao, X.; Ma, L.; Jiang, Z.; Liu, D.; Yang, Z.; Jiang, Q.; Wang, Y.; Tan, X.; Luo, S.; Wang, Y.; and Shi, C. *Sci. Adv.* **2021**, *7*, eabb6104.

[129] Yang, Z.; Li, L.; Ling, J.; Liu, T.; Huang, X.; Ying, Y.; Zhao, Y.; Zhao, Y.; Lei, K.; Chen, L.; and Chen, Z. *Chem. Sci.* **2020**, *11*, 8506–8516.

[130] Patil, S.; Ghosh, D.; Radhakrishna, M.; and Basu, S. *ACS Med. Chem. Lett.* **2020**, *11*, 23–28.

[131] Gao, Y.; Sun, R.; Zhao, M.; Ding, J.; Wang, A.; Ye, S.; Zhang, Y.; Mao, Q.; Xie, W.; Ma, G.; and Shi, H. *Anal.Chem.* **2020**, *92*, 6977−6983.

[132] Leung, C. W. T.; Hong, Y.; Chen, S.; Zhao, E.; Lam, J. W. Y.; and Tang, B. Z. *J. Am. Chem. Soc.* **2013**, *135*, 62−65.

[133] Zhao, N.; Li, M.; Yan, Y.; Lam, J. W. Y.; Zhang, Y. L.; Zhao, Y. S.; Wong, K. S.; and Tang, B. Z. *J. Mater. Chem. C* **2013**, *1*, 4640–4646.

[134] Gao, M.; Sim, C. K.; Leung, C. W. T.; Hu, Q.; Feng, G.; Xu, F.; Tang, B. Z.; and Liu, B. *Chem.Commun.* **2014**, *50*, 8312–8315.

[135] Hu, Q.; Gao, M.; Feng, G.; and Liu, Bin. *Angew. Chem., Int. Ed.* **2014**, *53*, 14225–14229.

[136] Wang, Z.; Gu, Y.; Liu, J.; Cheng, X.; Sun, J. Z.; Qin, A.; and Tang, B. Z. *J. Mater. Chem. B* **2018**, *6*, 1279−1285.

[137] Zhao, N.; Chen, S.; Hong, Y.; and Tang, B. Z. *Chem.Commun.* **2015**, *51*, 13599−13602.

[138] Li, X.; Jiang, M.; Lam, J. W. Y.; Tang, B. Z.; and Qu, J. Y. *J. Am. Chem. Soc.* **2017**, *139*, 17022−17030.

[139] Shin, W. S.; Lee, M.-G.; Verwilst, P.; Lee, J. H.; Chi, S.-G.; and Kim. J. S. *Chem. Sci.* **2016**, *7*, 6050−6059.

[140] Li, P.; Xiao, H.; Cheng, Y.; Zhang, W.; Huang, F.; Zhang, W.; Wang, H.; and Tang, B. *Chem. Commun.* **2014**, *50*, 7184−7187.

[141] Cao, L.; Zhao, Z.; Zhang, T.; Guo, X.; Wang, S.; Li, S.; Li, Y.; Yang. and G. Yang, *Chem. Commun*. **2015**, *51*, 17324−17327.

[142] Ye, Z.; Wei, L.; Geng, X.; Wang, X.; Li, Z.; and Xiao L. *ACS Nano* **2019**, *13*, 11593−11602.

[143] Liu, Y.; Zhou, J.; Wang, L.; Hu, X.; Liu, X.; Liu, M.; Cao, Z.; Shangguan, D.; and Tan W. *J. Am. Chem. Soc.* **2016**, *138*, 12368−12374.

[144] Kim, S.; Nam, H.Y.; Lee, J.; and Seo, J. *Biochemistry* **2020**, *59*, 270−284.

[145] Jean, S. R.; Ahmed, M.; Lei, E. K.; Wisnovsky, S. P.; and Kelley, S. O. *Acc. Chem. Res.* **2016**, *49*, 1893−1902.

[146] Zhao, T.; Liu, X.; Singh, S.; Liu, X.; Zhang, Y.; Sawada, J.; Komatsu, M.; and Belfield, K. D. *Bioconjugate Chem*. **2019**, *30*, 2312−2316.

[147] Horton, K. L.; Stewart, K.M.; Fonseca, S. B.; Guo, Q.; and Kelley, S. O.*Chem. Biol.* **2008**, *15*, 375–382.

[148] Chuah, J. A.; Matsugami, A.; Hayashi, F.; Numata, and K. *Biomacromolecules* **2016**, *17*, 3547−3557.

[149] Burke, C. S.; Byrne, A.; and Keyes, T. E. *Angew. Chem., Int. Ed.* **2018**, *57*, 12420 –12424.

[150] Zhao, K. S.;, Zhao, G. M.; Wu, D. L.; Soong, Y.; Birk, A. V.; Schiller, P. W.; and Szeto, H. H. *J. Biol. Chem.* **2004**, *279*, 34682−34690.

[151] Birk, A. V.; Liu, S. Y.; Soong, Y.; Mills, W.; Singh, P.; Warren, J. D.; Seshan, S. V.; Pardee, J. D.; and Szeto, H. H. *J. Am. Soc. Nephrol.* **2013**, *24*, 1250−1261.

[152] Birk, A. V.; Chao, W. M.; Bracken, C.; Warren, J. D.; and Szeto, H. H. *Br. J. Pharmacol.* **2014**, *171*, 2017−2028.

[153] Cerrato, C. P.; Pirisinu, M.; Vlachos, E. N.; and Langel, U. *FASEB J.* **2015**, *29*, 4589−4599.

[154] Cerrato, C. P.; and Langel, Ü. *Mol. Ther.–Methods Clin. Dev.* **2017**, *5*, 221−231.

[155] Zhang, C. X.; Cheng, Y.; Liu, D. Z.; Liu, M.; Cui, H.; Zhang, B. L.; Mei, Q. B.; Zhou, S. Y. *J. Nanobiotechnol.* **2019**, *17*, 18.

[156] Kuang, X.; Zhou, S.; Guo, W. L.; Wang, Z. J.; Sun, Y. H.; and Liu, H. Z. *Drug Deliv.*, **2017**, *24*, 1750−1761.

[157] Yamada, Y.; and Harashima, H. *Biomaterials* **2012**, *33*, 1589−1595.

[158] Zasloff, M. *Nature* **2002**, *415*, 389−395.

[159] Horton, K. L.; and Kelley, S. O. *J. Med. Chem.* **2009**, *52*, 3293–3299.

[160] Cheng, D.-B.; Zhang, X.-H.; Gao, Y.-J.; Ji, L.; Hou, D.; Wang, Z.; Xu, W.; Qiao, Z.-Y.; Wang, and H. Wang, *J. Am. Chem. Soc.* **2019**, *141*, 7235−7239.

[161] Wanga, H.; Fenga, Z.; and Xu, B. *Chem. Soc Rev.***2017**, *46*, 2421–2436.

[162] Gao, Y.; Shi, J.; Yuan, D.; and Xu, B. *Nat. Commun.* **2012**, *3*, 1−8.

[163] He, H.; Wang, J.; Wang, H.; Zhou, N.; Yang, D.; Green, D. R.; and Xu, B. *J. Am. Chem. Soc.* **2018**, *140*, 1215−1218.

[164] He, H., Guo J., Lin, X., and Xu, B. *Angew. Chem., Int. Ed.* **2020**, *59*, 9330–9334.

[165] Jeena, M. T.; Barui, A. K.; Jin, S.; Cho, Y.; Hwang, S. -W.; Kim, S.; and Ryu, J. -H. *Chem. Commun.* **2020**, *56*, 6265-6268.

[166] Jin, S.; Jeena, M. T.; Jana, B.; Moon, M.; Choi, H.; Lee, E.; and Ryu, J. -H. *Biomacromolecules* **2020**, *21*, 4806−4813.

[167] Hong, T. H.; Jeena, M. T.; Kim, O.‑H.; Kim, K.‑H.; Choi, H. J.; Lee, K. H.; Hong, H.‑E.; Ryu, J.‑H.; and Kim, S.‑J. *Sci. Rep.* **2021**, *11*, 874.

[168] Li, M.; Song, Y.; Song, N.; Wu, G.; Zhou, H.; Long, J.; Zhang, P.; Shi, L.; and Yu, Z. *Nano Lett.* **2021**, *21*, 5730–5737.

[169] Wang, L.; Tran, M.; D'Este, E.; Roberti, J.; Koch, B.; Xue, L.; and Johnsson, K. *Nat. Chem.* **2020**, *12*, 165–172.

[170] Lukinavicius, G.; Reymond, L.; Umezawa, K.; Sallin, O.;ˇ D'Este, E.; Gottfert, F.; Ta, H.; Hell, S. W.; Urano, Y.; and Johnsson, K. *J. Am. Chem. Soc.* **2016**, *138*, 9365−9368.

[171] Collot, M.; Fam, T. K.; Ashokkumar, P.; Faklaris, O.; Galli, T.; Danglot, L.; and Klymchenko, A. S. *J. Am. Chem. Soc.* **2018**, *140*, 5401−5411.

[172] Rhee, H. W.; Zou, P.; Udeshi, N. D.; Martell, J. D.; Mootha, V. K.; Carr, S. A.; and Ting, A. Y. *Science* **2013**, 339, 1328−1331.

[173] Tamura, T.; and Hamachi, I. *J. Am. Chem. Soc.***2019**, *141*, 2782−2799.

[174] Matsuo, K.; Nishikawa, Y.; Masuda, M.; and Hamachi, I. *Angew. Chem., Int. Ed.* **2018**, *57*, 659−662.

[175] Fujisawa, A.; Tamura, T.; Yasueda, Y.; Kuwata, K.; and Hamachi I. *J. Am. Chem. Soc.* **2018**, *140*, 17060−17070.

[176] Adusumalli, S. R.; Rawale, D. G.; Thakur, K.; Purushottam, L.; Reddy, N. C.; Kalra, N.; Shukla, S.; and Rai, V. *Angew. Chem., Int. Ed.* **2020**, 59, 10332-10336.

[177] Kumar, M.; Reddy, N. C.; and Rai, V. *Chem. Commun.* **2021**, *57*, 7083-7095.

Chapter 2

Materials and Methods

Introduction

This chapter deals with detailed information of general materials and a brief description of experimental procedures employed in this thesis for the synthesis of cyanine dyes for selective targeting and imaging of mitochondria. The chapter also provides full information of all the spectroscopic measurements and microscopic procedure, along with several biological studies relevant to this research work. A special emphasis has been also given to confocal laser scanning microscopy (CLSM) for imaging of fixed as well as live cell mitochondria and multicolor imaging. All the respective chapters provided with full description of the synthetic procedures relating to compounds studied in this thesis and also the biological studies which were relevant to this research work.

Experimental Procedures

General Materials:

3-methyl-2-butanone, 1,1,3,3-tetramethoxy propane, 1,5-dibromopentane, 6-bromohexanoic acid, 1-bromohexane, *N*, *N*-Diisopropylethylamine, HATU (1-Bis(dimethylamino)methylene]-1H-1,2,3-triazolo[4,5-b]pyridinium 3-oxide hexafluorophosphate, 2-Mercaptoethanol, Bisbenzimide trihydrochloride (Hoechst 33342) and all the HPLC grade solvents used for the spectroscopic experiments were obtained from Sigma-Aldrich. All NMR deuterated solvents were purchased from Cambridge Isotope Laboratories, Inc. Zinc phthalocyanine and Rhodamine-B were procured from TCI chemicals and carbonyl cyanide m-chlorophenyl hydrazine was purchased form Alfa- aesar. All the Fmoc-amino acid building blocks: Fmoc-Leu-OH, Fmoc-Lys(Boc)-OH, Fmoc-Phe-OH, Fmoc-Val-OH, LL (100-200 mesh), *N*, *N*, *N′*, *N′*-Tetramethyl-

O-(1H-benzotriazol-1-yl)uronium hexafluorophosphate (HBTU), HOBt, and TLC silica gel 60 F254 Merck. 2-Chlorotrityl chloride was obtained from Aapptec. HeLa carcinoma cell, human ductal pancreatic cancer cells (MIA PaCa-2), lung adenocarcinoma cell (A549), noncancerous human embryonic kidney (HEK293) cell, lung fibroblast (WI38) cells and C2C12 a mouse myoblast cell lines were procured from The National Centre for Cell Science, India. 3-(4,5-dimethyl-2-thiazolyl)-2,5-diphenyltetrazolium bromide (MTT), Dulbecco's modified eagle medium (DMEM), Trypsin EDTA mixture, Fetal Bovine Serum (FBS), and Antibiotic Antimycotic Solution were obtained from Himedia. MitoTracker Green FM (M7514) and Mitotracker Red FM (M22425) mitochondria targeting dye, Cell Mask Green (C37608) and FM 1-43FX Plasma membrane staining probe, LysoTracker Green DND-26 lysosome targeting probe, Coomassie Brilliant Blue R-250 and protease inhibitor cocktail were acquired from Thermo Fisher Scientific. DOPC and cholesterol were purchased from Avanti Polar Lipids (USA) and stored in a freezer at −20°C. Acrylamide(30% Acrylamide / Bis Solution 37.5.1(Cat. No: 1610158), lameli buffer (pH6.8) was procured from BIO-RAD. *Millipore* ultra-pure H_2O was used for all the experiments.

Purification of Reagents required for Synthesis of Cyanine Dyes:

For the synthesis of symmetrical as well as unsymmetrical cyanine dyes acetic anhydride is an essential reagent. It was prepared by dropwise addition of acetyl chloride at 0°C to anhydrous sodium acetate taken in a round bottom flask and the mixture was stirred continuously. After complete addition of acetyl chloride the mixture was allowed to come at room temperature and the resultant mixture was distilled to get pure acetic anhydride.

Microwave Synthesizer: Unsymmetrical cyanine dyes as well as their associated precursor molecules were synthesized using manual microwave

synthesizer (*CEM* corporation, USA make) whereas synthesis of cyanine–peptide conjugates were carried out using manual microwave-assisted Fmoc-SPPS protocol on a microwave peptide synthesizer (*CEM*, *Discover Bio*). 2-CTC (2-chloro tritylchloride) resin (LL, 0.85 mmol/g loading density) and Wang resin (LL, 0.60 mmol/g loading density) were used for synthesis of peptides and cyanine–peptide conjugates.

Characterization of Cyanine Dyes and their precursors:

Spectroscopic Measurements:

NMR Spectroscopy: All the cyanine dyes as well as their precursor molecules were characterised by 1D (^{1}H, ^{13}C, ^{31}P) and 2D NMR (^{1}H–^{1}H DQF COSY) spectroscopy. All the NMR experiments were carried on Bruker DPX300 MHz, DPX400 MHz, and Bruker DPX500 MHz spectrometers at ambient temperature in appropriate deuterated solvents.

Mass spectrometry: High-resolution electrospray ionisation mass spectrometry (HRMS-ESI) was performed using a Q-TofmicroTM (Waters Corporation) mass spectrometer.

Absorption Spectroscopy: Absorption spectra were recorded using a Shimadzu UV-1800 spectrometer in a quartz cuvette with a path length of 1 cm.

Fluorescence Spectroscopy: Fluorescence measurement was obtained on a Horiba Jobin Yvon FluoroMax-4 spectrofluorometer.

Time-correlated single photon counting (TCSPC) experiment: Fluorescence lifetime (τ) of the cyanine derivatives were measured by time-correlated single photon counting (TCSPC) technique on Horiba DeltaFlex lifetime instrument (Horiba Jobin Yvon IBH Ltd, Glasgow, Scotland, UK). 510 nm (Model: DD-510L, Horiba Scientific) and 650 nm (Model: DD-650L, Horiba Scientific) Delta diode laser excitation source were used to determine the fluorescence

lifetime of cyanine derivatives in various solvents. Lifetime measurements and data analysis were obtained using Horiba EzTime decay analysis software.

FT-IR Spectroscopy: FT-IR spectrum of peptide conjugated cyanine probes were recorded on a PerkinElmer Spectrum Two FT-IR spectrometer.

CD Spectroscopy: CD spectrum was recorded on a JASCO instrument, Model J-815–150S. Data were collected in a quartz cuvette with a path length of 1 mm at wavelengths between 190 nm to 260 nm with a 0.5 nm step, 1 nm bandwidth, and 2 s collection times per step at 25°C, taking three averages. The CD signal from the solvent as background was subtracted from the CD data of the sample solution.

X-Ray powder Diffraction: The X-ray diffraction from dried film of cyanine–peptide conjugates were collected with a Bruker D8 Advance X-ray diffractometer using Cu K_α radiation (λ = 1.5418 Å) operating at 40 kV and 40 mA.

Microscopic Studies:

Field Emission Scanning Electron Microscopy (FE-SEM): The nanomorphology of the cyanine–peptide conjugates was determined using FE-SEM. For this purpose 10 μL of aqueous stock solution of respective compounds were separately drop casted on a glass cover slip and allowed to dry completely in air at room temperature. Samples were coated with gold and the images were obtained in INSPECT F50 Scanning Electron Microscope instrument with a 10 kV accelerating voltage.

Atomic Force Microscopy: To get the topographical information of the cyanine–peptide conjugates AFM experiment was performed in AUTOPROBE CP base unit, di CP-II instrument (Model no: AP-0100). A small amount of freshly prepared aqueous solution of the corresponding compounds were drop

casted on a mica foil and allowed to dry at room temperature for 2days before the AFM experiment.

Transmission Electron Microscopy (TEM): 10 μL of freshly prepared aqueous stock solution of respective cyanine–peptide conjugates were separately drop casted on a carbon coated copper grid (300 mesh) and waited for 2 m followed by blotting with filter paper to remove the excess fluid. Finally, for negative staining 10 μL of 2 % (w/v) uranyl acetate in H_2O solution was drop casted on the grid and waited for 30 s followed by blotting with filter paper. The grid was allowed to dry completely in air then vacuum drying for 1 day. TEM images of respective compounds were acquired on JEM-2100F Field Emission Electron microscope (JEOL) instrument with acceleration voltage 200 kV.

Dynamic Light Scattering (DLS): DLS experiments were performed using a Malvern instrument (Malvern, UK) to inspect the hydrodynamic diameters of the nanostructure formed by cyanine–peptide conjugates in solution.

Biological Studies:

Cell culture: Both the cancerous and noncancerous cell lines were maintained in growth media containing DMEM (pH 7.4) supplemented with 10% Fetal Bovine Serum (FBS) and antibiotic-(6H, m) antimycotic solution 100× (containing 10,000 units penicillin, 10 mg streptomycin and 25 μg amphotericin B per mL in 0.9% normal saline). All the cell lines were maintained at 37°C in the incubator with routine passage of 5% CO_2.

Cell viability assay: The cytotoxicity of all the synthesized cyanine derivatives on cancerous cell lines as well as noncancerous were determined by MTT assay.

Cellular uptake and mitochondrial localization study: To confirm the cellular uptake and organelle selectivity of cyanine conjugates as well as for

multicolor imaging in fixed and live cells, confocal laser scanning microscopic technique was used.

Chapter 3

Symmetrical Near-Infrared Cyanine Chromophore for Selective Targeting and Imaging of Mitochondria

Introduction

Selective targeting and staining of particular cellular organelles such as mitochondria, Golgi apparatus, endoplasmic reticulum etc. is an emerging field of current research.[1-8] However, it is exigent to work on cellular environment due to the intricacy in biological system. Among the different cellular organelles, mitochondria are widespread targets for all cancer cells.[9-13] Mitochondria play a fundamental role in programmed cell death such as apoptosis.[14-18] Mitochondrial targeting, incorporation, and imaging are the critical steps for new drug design and development processes. Inner mitochondrial membrane (IMM) of normal healthy cells maintains a strong negative membrane potential [$(\Delta\Psi_m)_{normal}$ –150 to –180 mV].[19,20] Amendment in $\Delta\Psi_m$ is an imperative feature of cancer [$(\Delta\Psi_m)_{cancer}$ ~ –220 mV].[20] This high negative $\Delta\Psi_m$ of mitochondria is unique and is not present in any other cellular organelle (plasma membrane potential, $\Delta\Psi_p$ –30 to –60 mV), which offers a design scope for selective targeting and tracking of mitochondria. Fluorescent probes are handy for monitoring a variety of biological processes in cells using confocal microscopy and flow cytometry. However, near-infrared (NIR) fluorescent dyes (650–900 nm) have a significant advantage over the visible fluorescent dyes.[21-28] Cellular or tissue components have negligible absorption and minimal autofluorescence in the NIR region; hence, a highly sensitive, less scattered, and precise detection is possible when exogenous NIR dyes are incorporated. However, it is challenging to construct organelle-selective organic NIR imaging agent because most NIR dyes are restricted within their biological applications due to photobleaching, propensity to aggregate in buffer solution, low quantum yield, fast fluorescence decay, and insufficient stability in biological systems. Moreover, less target selectivity and

broad absorption/emission band of most NIR probes limit its application to multicolor imaging of cells. Multicolor imaging and tracking of distinct cellular organelles inside the same cell is crucial for understanding complex biological processes.[29-34] Our strategy is to exploit the extraordinary biophysical membrane property of mitochondria to target IMM, as cationic molecules should attract and accumulate preferentially within the negatively charged mitochondrial matrix.[19,20] In addition to the cationic character, adequate lipophilicity is also necessary to accomplish a significant uptake in mitochondria.[35,36] Methodical explorations of tunable partition coefficient (log *P*) and lipophilicity of the target-specific cationic moiety anchor to an NIR cyanine-5 (Cy-5) chromophore through relatively flexible linker with variable length have been investigated for selective targeting and staining of mitochondria. In this chapter, we have utilized our synthesized NIR fluorescent molecules (Cy-5a and Cy-5b) that exhibit excellent photophysical properties, exceptional photostability, narrow NIR absorption and emission band, high molar extinction coefficient, long fluorescence lifetime with high fluorescence quantum yield, good water solubility, outstanding biocompatibility, and low cytotoxicity. We envision that– (1) targeting functionality containing NIR molecules (Cy-5a and Cy-5b) should lead to a more selective, greater and faster uptake by mitochondria than non-targeting Cy-5c molecule. However, the triply positive charged Cy-5a and Cy-5b might restrict the transportation of trications through cell membrane and little is known about their interaction with mitochondria. Therefore, there is a need to inspect their mitochondrial uptake; (2) because of narrow NIR absorption and emission band of mitochondria-targeting Cy-5, acquisition of multicolor imaging of cellular organelles in the same cell could be possible using a combination of suitable dyes with distinct excitation and emission characteristics; (3) because of more hyperpolarized

$\Delta\Psi_m$ of cancer cells compared to normal healthy cells, the dye should accumulate more in the cancer cell mitochondria than noncancerous cell mitochondria; (4) cancer cell mitochondrial incorporation of the triply positive charged Cy-5 dye is expected to depolarize mitochondrial membrane potential. Therefore, its effect on malignant mitochondrial targeting, incorporation, staining, membrane potential depolarization, and multicolor imaging application is investigated using human carcinoma cell lines.

Experimental Methods

General Methods and Materials

Synthesis, Purification, and Characterization of Cy-5a, Cy-5b, and Cy-5c dyes:

All the syntheses were performed under N_2 atmosphere using dry solvents. Analytical thin layer chromatography (TLC) was carried out on silica gel coated aluminium sheets (TLC silica gel 60 F_{254}) with appropriate solvents and the results were detected by naked eye or UV lamp and/or developing with I_2. The compounds were purified via column chromatography using silica gel 100-200 mesh. The solvents for column chromatography were distilled prior to their use.

The heterocyclic 2,3,3-trimethylindolenine molecule is synthesized by Fischer indole synthesis and the N of the indolenine residue is covalently conjugated with the mitochondria targeting triphenylphosphonium (TPP^+) moiety using alkylating agents 2 and 3 (Scheme 1).[37-39] All the compounds were characterised by 1D (^1H, ^{13}C and ^{31}P) and 2D (^1H-^1H DQF-COSY) NMR spectroscopy, as well as high resolution ESI-MS. The full ^1H NMR

assignments including $^{1}H–^{1}H$ correlation of Cy-5a, Cy-5b, and Cy-5c dyes were done using $^{1}H–^{1}H$ DQF COSY experiment (**Figures 13, 16, and 18b**).

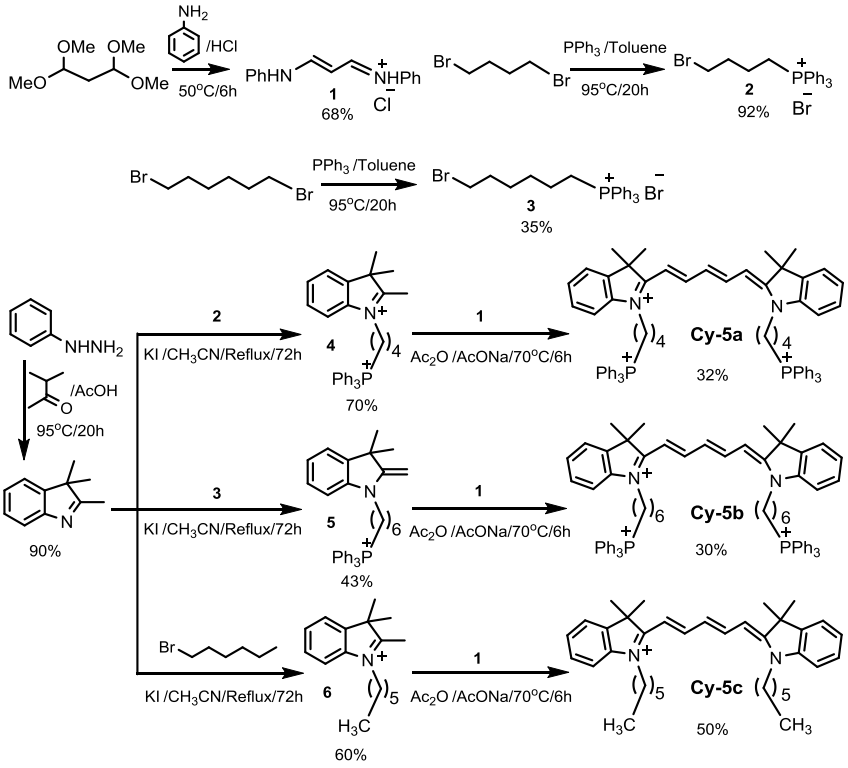

Scheme 1. Synthesis of Cy-5a, Cy-5b, and Cy-5c dyes.

Malonaldehyde bis(phenylimine) monohydrochloride (1):

1,1,3,3-tetramethoxy propane (10.50 mL, 60 mmol) and dilute HCl (8.5 mL concentrated HCl and 171 mL H_2O) were taken in a round bottom flask and heated to 50ºC while being continuously stirred. A solution of aniline (11.10 mL, 120 mmol) in dilute HCl (15 mL concentrated HCl and 200 mL H_2O) was added drop wise to the solution of 1,1,3,3-tetramethoxy propane using an additional funnel over a period of 2 h. The reaction mixture's color gradually changed from colorless to orange during the addition of aniline solution. After

the addition was completed, the reaction mixture was stirred for an additional 4 h at 50ºC. The reaction mixture was then cooled to room temperature to get an orange precipitate. The orange precipitate was filtered and dried under vacuum. The product was used in the next step without any further purification [R_f = 0.50 (DCM:MeOH= 9:1)].

Yield: 10.6 g (68.3%).

^{1}H NMR (500 MHz, DMSO-d_6, 25°C): δ = 12.76 (2H, s), 8.98 (2H, d, J = 11.0 Hz), 7.45–7.42 (8H, m), 7.24–7.21 (2H, m), 6.57 (1H, t, J = 11.5 Hz) ppm. ^{13}C NMR (125 MHz, DMSO-d_6, 25°C): δ = 158.4, 138.6, 129.7, 125.7, 117.3, and 98.6 ppm.

HRMS (ESI +ve) *m*/*z*: Observed for $C_{15}H_{15}N_2^+$ $[M]^+$ = 223.1224, $[M]^+$ calcd = 223.1230.

4-Bromobutyl)triphenylphosphonium bromide (2): 1,4-dibromobutane (2.7 mL, 23 mmol) was added to a stirred solution of PPh_3 (3.01 g, 11.2 mmol) in toluene (25 mL) at 95°C and the mixture was refluxed for 20 h. The reaction mixture was then cooled to room temperature to get a white precipitate. The precipitate was filtered and washed several times with Et_2O. The product was dried under vacuum to yield a white amorphous solid.

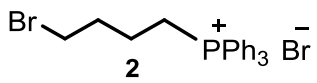

2

Yield: 5.06 g (91.9%).

^{1}H NMR (500 MHz, DMSO-d_6, 25°C): δ = 7.92–7.77 (15H, m), 3.70–3.61 (4H, m), 2.04–1.99 (2H, m), 1.73–1.62 (2H, m) ppm. ^{13}C NMR (125 MHz, DMSO-d_6, 25°C): δ = 134.8, 134.7, 133.4, 130.2, 130.1, 118.8, 118.6, 118.1, 117.9, 33.5, 32.8, 32.4, 20.3, 20.2, and 18.6 ppm.

HRMS (ESI +ve) *m*/*z*: Observed for $C_{22}H_{23}BrP^+$ $[M]^+$ = 397.0710, $[M]^+$ calcd = 397.0716.

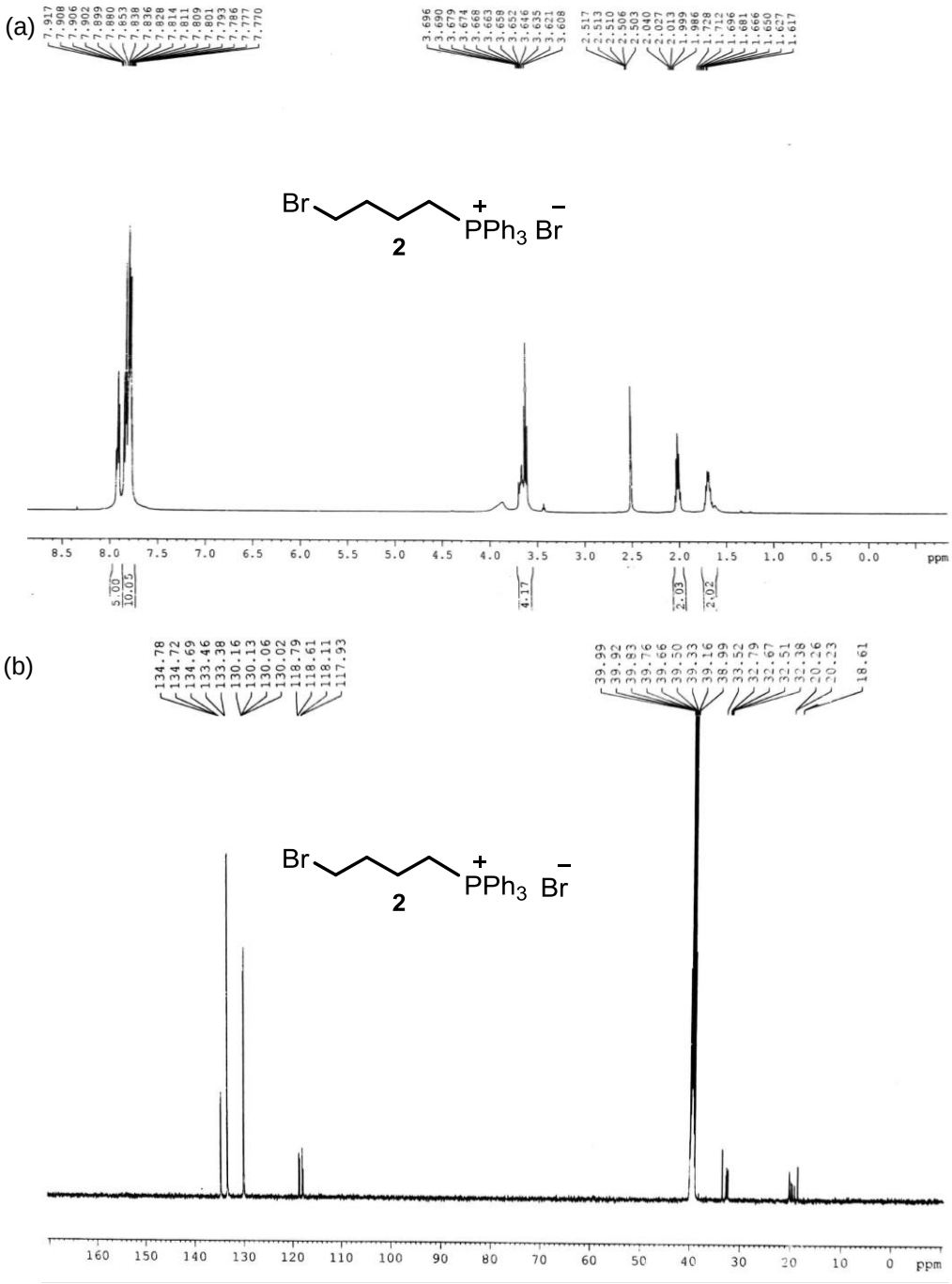

Figure 1. (a) ^{1}H NMR (500 MHz, DMSO-d_6, 25°C) spectrum and (b) ^{13}C NMR (101 MHz, DMSO-d_6, 25°C) spectrum of compound 2.

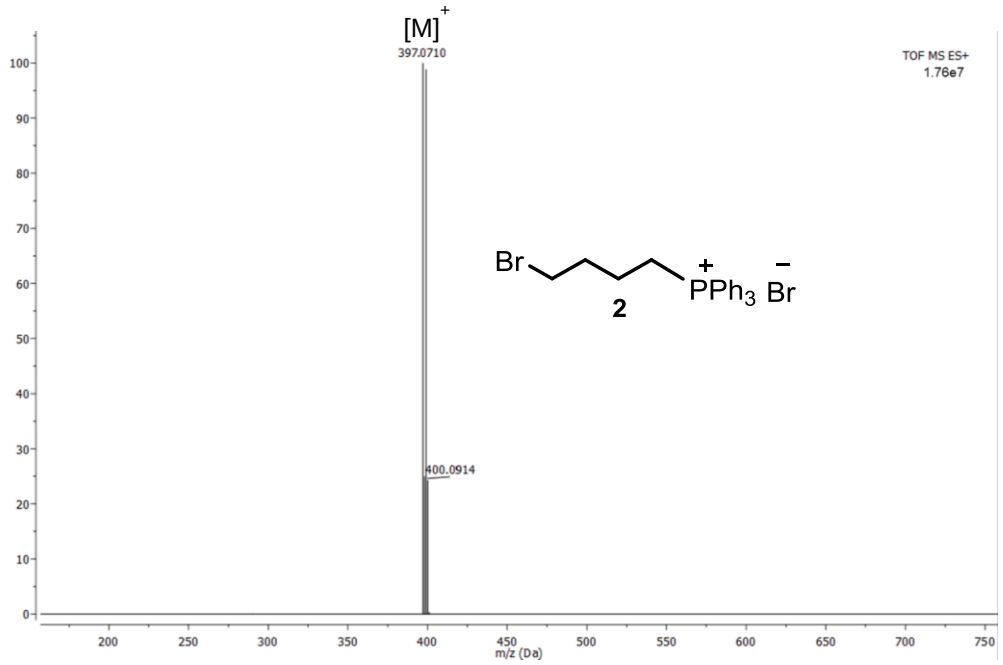

Figure 2. HRMS (ESI +ve) spectrum of compound 3.

6-Bromohexyl)triphenylphosphonium bromide (3): 1,6-dibromobutane (1.50 g, 3 mmol) was added to a stirred solution of PPh_3 (0.52 g, 2.0 mmol) in toluene (35 mL) at 95°C and the mixture was refluxed for 20 h. The reaction mixture was thereafter cooled to room temperature and the solvent was removed under reduced pressure to obtain a gummy solid. The gummy residue was washed with CH_3CN:EtOAc (4:1) several times to get the desired product as an off-white solid.

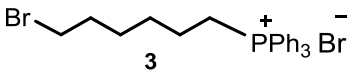

Yield: 0.36 g (35%).

^{1}H NMR (400 MHz, DMSO-d_6, 25°C): δ = 7.90–7.72 (15H, m), 3.78–3.73 (2H, m), 3.61–3.57 (2H, m), 1.52–1.30 (8H, m) ppm. ^{13}C NMR (101 MHz, DMSO-d_6, 25°C): δ = 134.7, 133.4, 133.3, 118.7, 118.0, 28.6, 28.5, 21.4, 21.3, 20.4, and 20.0 ppm.

HRMS (ESI +ve) *m*/*z*: Observed for $C_{24}H_{27}BrP^+$ $[M]^+$ = 425.1016, $[M]^+$ calcd = 425.1028.

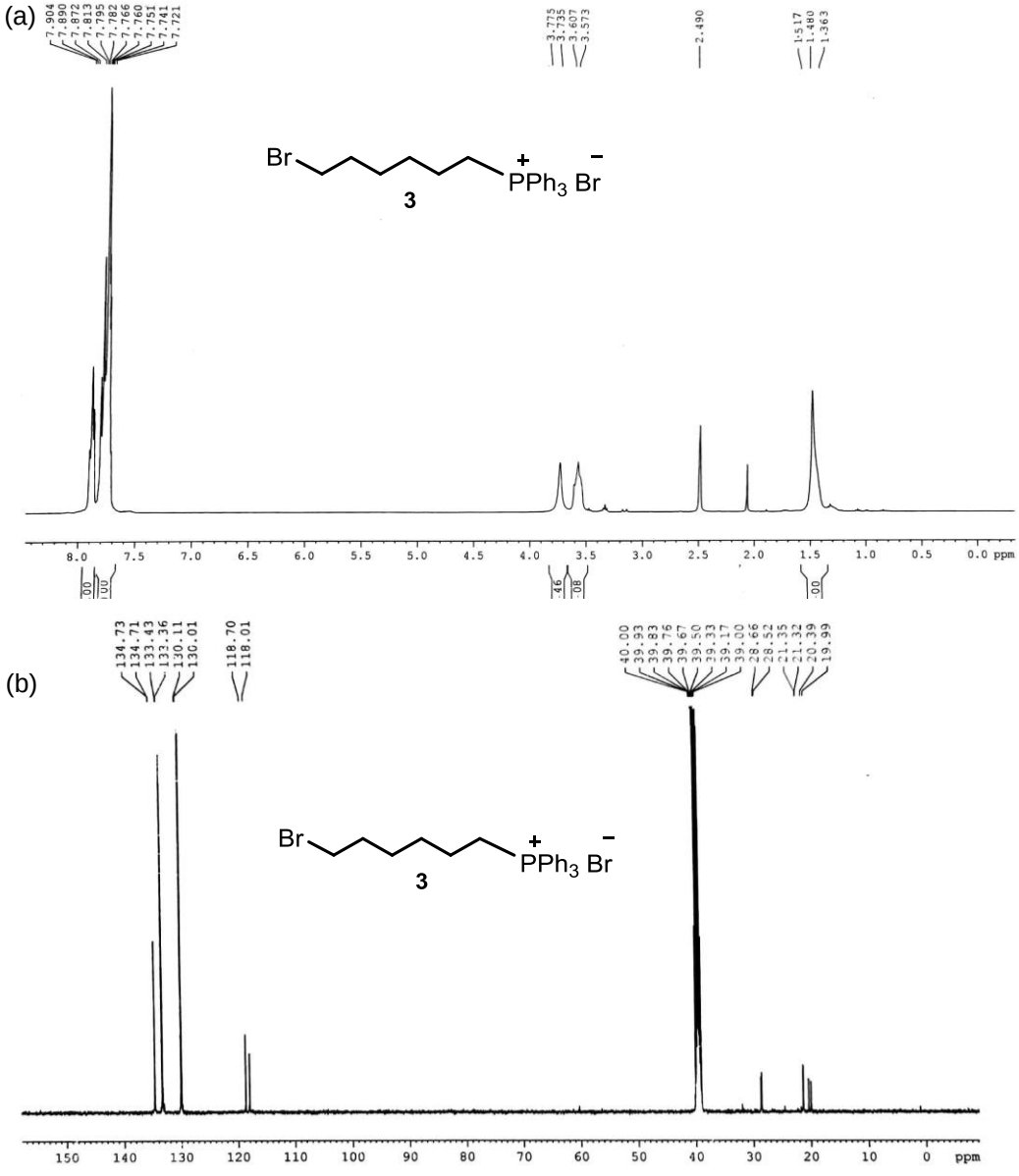

Figure 3. (a) ^{1}H NMR (400 MHz, DMSO-d_6, 25°C) spectrum and (b) ^{13}C NMR (101 MHz, DMSO-d_6, 25°C) spectrum of compound 3.

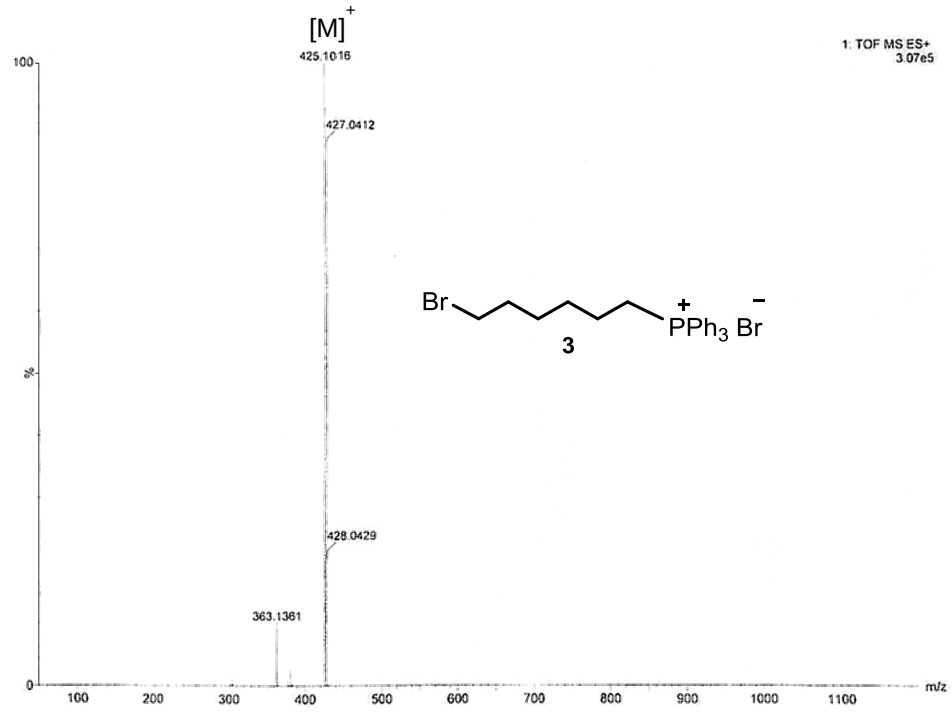

Figure 4. HRMS (ESI +ve) spectrum of compound 3.

4-(3,3-dimethyl-2-methyleneindolin-1-yl)butyl)triphenylphosphonium iodide (4): 2,3,3-Trimethylindolenine (0.99 g, 6.23 mmol), 2 [(4-bromobutyl)triphenylphosphonium bromide] (3.28 g, 6.85 mmol), and KI (1.14 g, 6.85 mmol) were taken in a 50 mL round bottom flask and dissolved in 25 mL CH_3CN at room temperature. The reaction mixture was heated under reflux for 72 h and then cooled to room temperature. The resulting solution was decanted from the solid and the solvent was removed under reduced pressure to get a reddish brown precipitate. The precipitate was poured in water and extracted with EtOAc (3 × 25 mL). The organic layer was separated and dried over anhydrous Na_2SO_4, filtered, and concentrated under reduced pressure. The

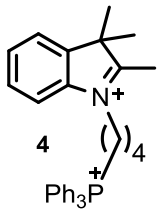

residue was washed with Et_2O and dried under vacuum to get the pure compound 4 as a reddish brown solid.

Yield: 2.63 g (70%).

^{1}H NMR (400 MHz, CD_3OD, 25°C): δ = 8.00–7.93 (2H, m), 7.92–7.74 (16H, m), 7.69–7.63 (2H, m), 4.64–4.59 (2H, m), 3.75–3.65 (2H, m), 3.36 (3H, s), 2.39–2.28 (2H, m), 1.97–1.89 (2H, m), 1.59 (6H, s) ppm. ^{13}C NMR (101 MHz, CD_3OD, 25°C): δ = 196.8, 165.8, 141.8, 141.1, 134.9, 133.7, 133.56, 130.3, 130.1, 129.7, 123.2, 118.7, 117.5, 115.5, 54.5, 28.4, 28.2, 21.5, 20.8, and 19.9 ppm.

HRMS (ESI +ve) *m*/*z*: Observed for $C_{33}H_{35}NP^+$ $[M]^+$ = 476.2805, $[M]^+$ calcd = 476.2507.

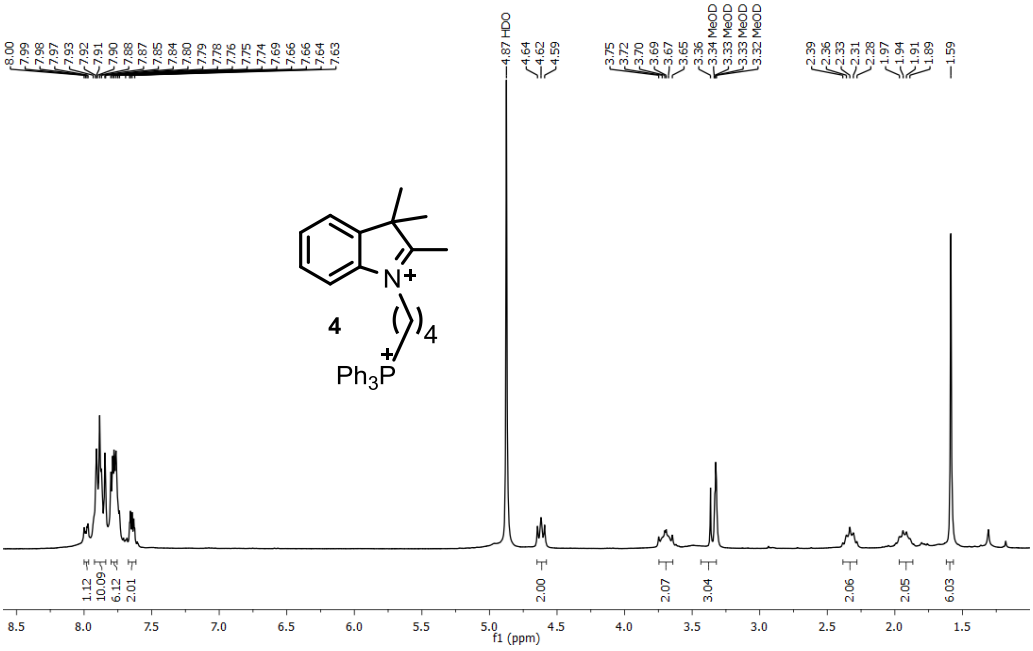

Figure 5. ^{1}H NMR (400 MHz, CD_3OD, 25°C) spectrum of compound 4.

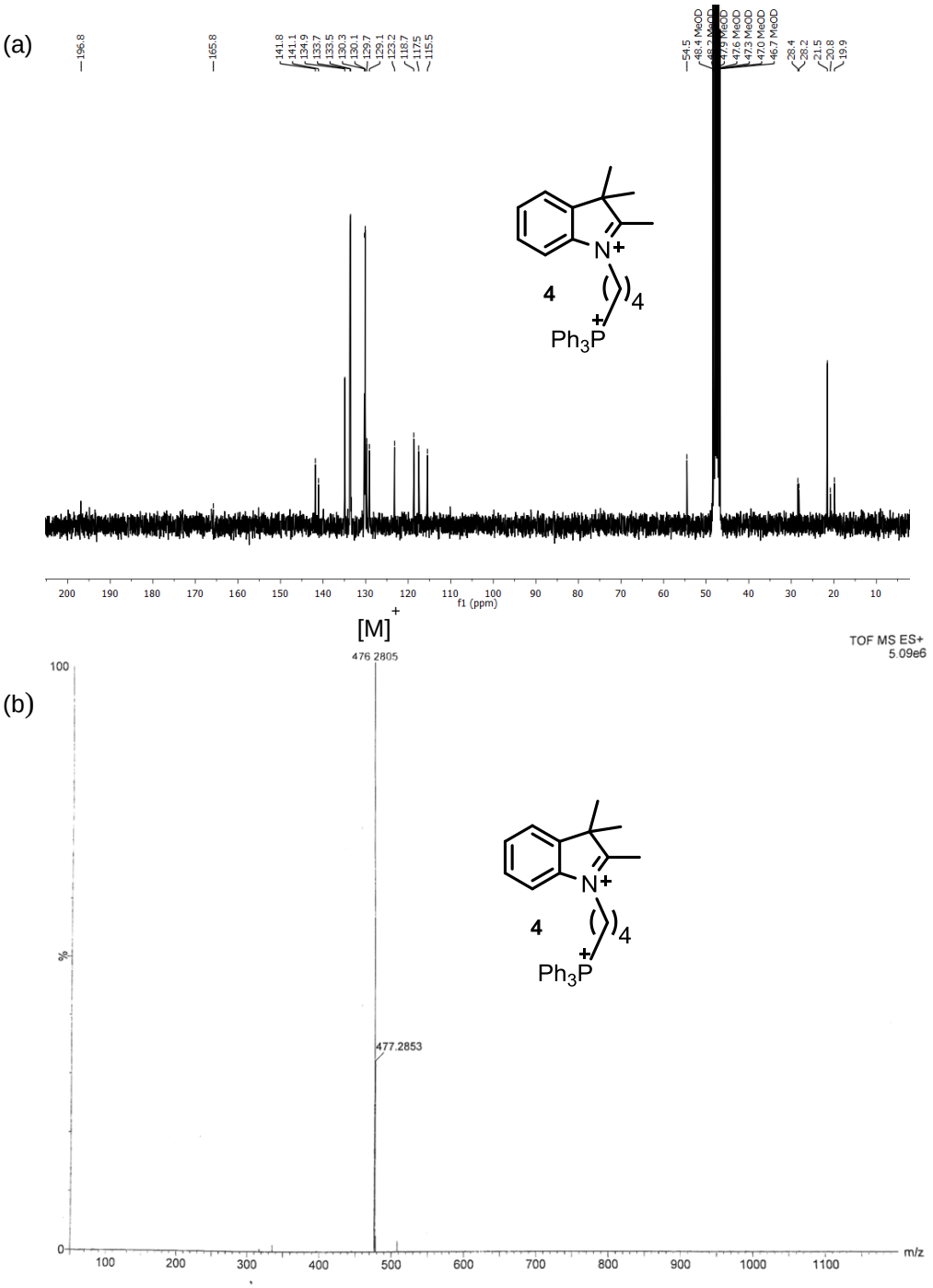

Figure 6. (a) ^{13}C NMR (101 MHz, CD_3OD, 25°C) spectrum and (b) HRMS (ESI +ve) spectrum of compound 4.

6-(3,3-dimethyl-2-methyleneindolin-1-yl)hexyl)triphenylphosphonium iodide (5): 2,3,3-Trimethylindolenine (0.99 g, 6.23 mmol), 3 [(6-bromohexyl)triphenylphosphonium bromide] (3.47 g, 6.85 mmol, 1.1 eqv), and KI (1.14 g, 6.85 mmol, 1.1eqv) were taken in a 50 mL round bottom flask and dissolved in 25 mL CH_3CN at room temperature. The reaction mixture was heated under reflux for 72 h and then cooled to room temperature. The resulting solution was decanted from the solid and the solvent was removed under reduced pressure to get a reddish brown residue. The residue was purified through column chromatography using DCM:MeOH (95:5) (R_f = 0.46) to acquire the desired compound 5 as a reddish brown solid.

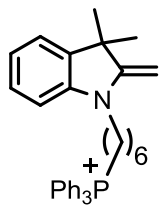

5

Yield: 1.70 g (43%).

^{1}H NMR (400 MHz, $CDCl_3$, 25°C): δ = 7.81–7.67 (15H, m), 7.05 (2H, t, J = 8.4 Hz) , 6.69 (1H, t, J = 7.2 Hz), 6.49 (1H, d, J = 7.2 Hz), 3.77 (2H, br), 3.67–3.60 (2H, m), 3.43 (2H, t, J = 6.8 Hz), 1.78–1.64 (6H, m), 1.26 (6H, s) ppm. ^{13}C NMR (101 MHz, $CDCl_3$, 25°C): δ = 161.6, 146.1, 137.5, 135.1, 133.8, 130.6, 127.6, 121.8, 118.6, 118.2, 117.8, 105.3, 73.2, 44.2, 42.1, 30.1, 29.7, 26.7, 25.9, 23.4, 22.9, and 22.4 ppm.

HRMS (ESI +ve) *m*/*z*: Observed for $C_{35}H_{39}NP^+$ $[M]^+$ = 504.2821, $[M]^+$ calcd = 504.2820.

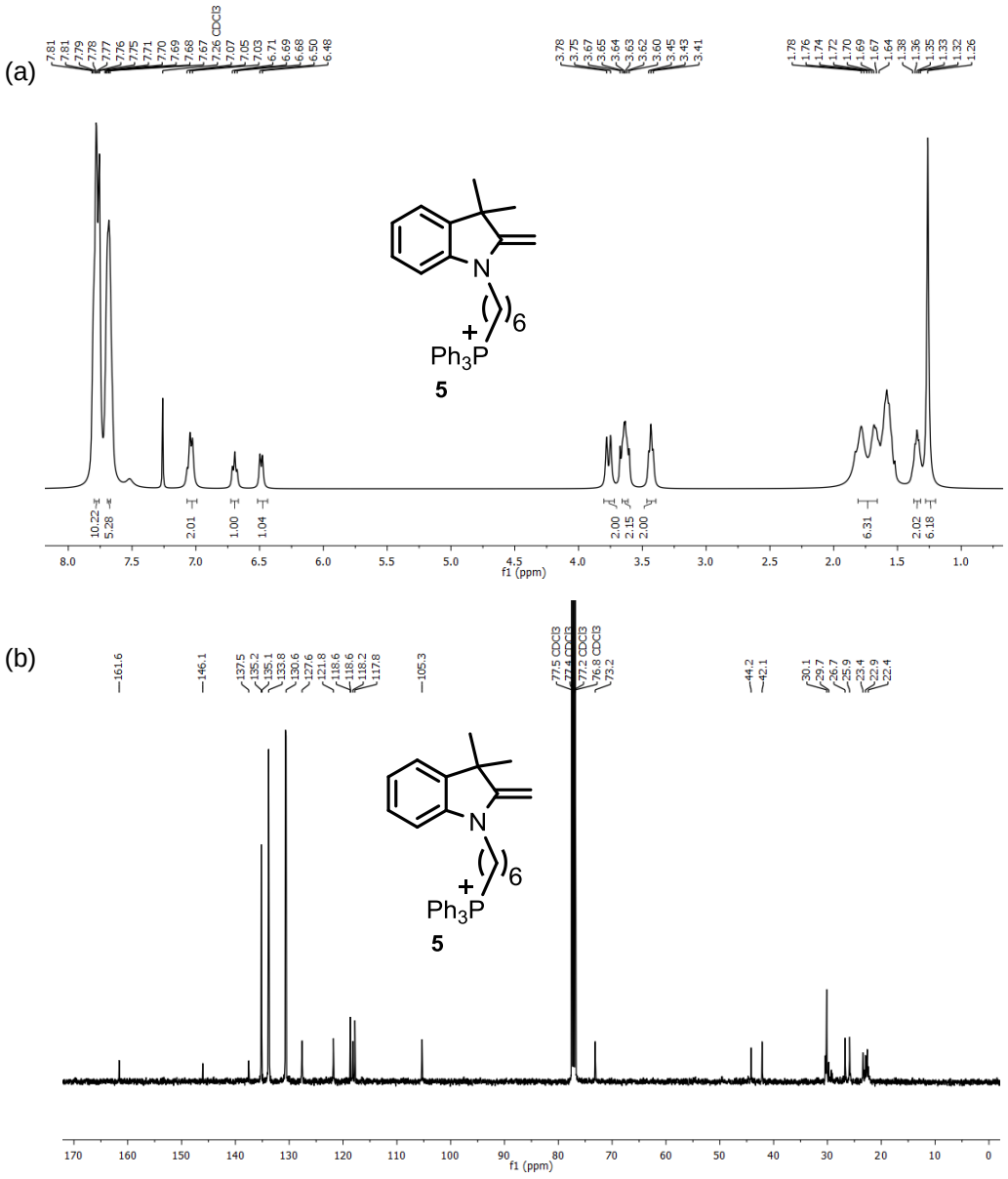

Figure 7. (a) ^{1}H NMR (400 MHz, $CDCl_3$, 25°C) spectrum and (b) ^{13}C NMR (101 MHz, $CDCl_3$, 25°C) spectrum of compound 5.

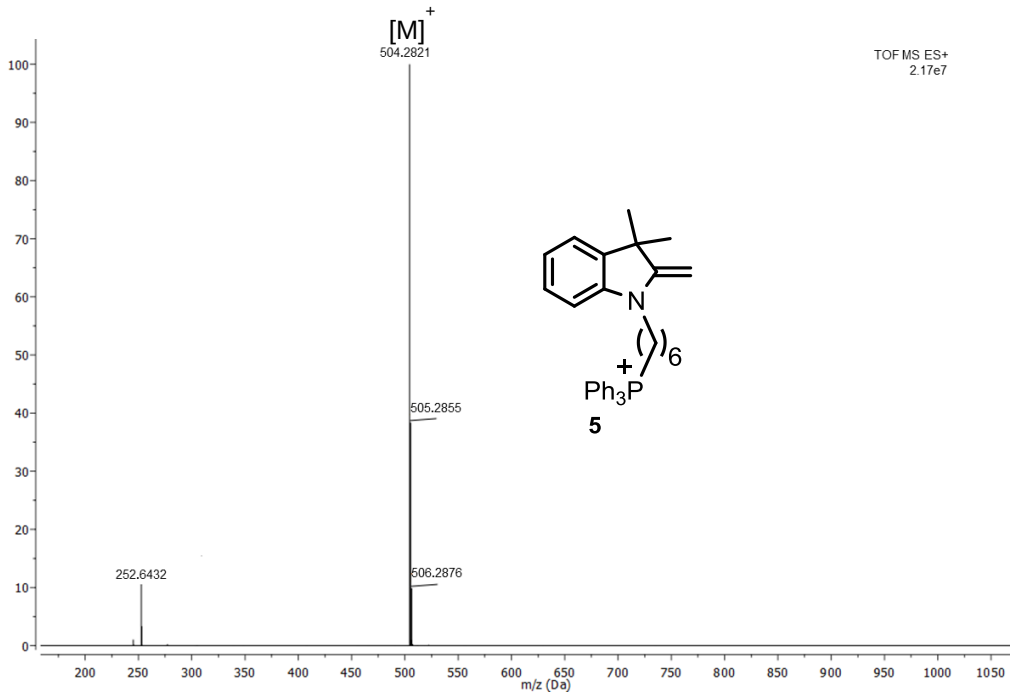

Figure 8. HRMS (ESI +ve) spectrum of compound 5.

1-Hexyl-2,3,3-trimethyl-3*H*-indol-1-ium iodide (6): 2,3,3-Trimethylindolenine (0.50 g, 3.15 mmol), 1-bromo hexane (0.57 g, 3.47 mmol), and KI (0.58 g, 3.47 mmol) were taken in a round bottom flask and dissolved in 25 mL CH_3CN at room temperature. The reaction mixture was heated under reflux for 72 h and cooled to room temperature. The resulting solution was decanted from the solid and the solvent was removed under reduced pressure to get a reddish brown residue. The residue was washed with Hexane:EtOAc mixture (4:1) several times. The crude product was purified by column chromatography using DCM:MeOH (97:3) (R_f = 0.75) to get the desired compound 6 as a brown solid.

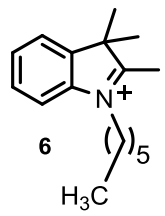

Yield: 0.70 g (60%).

^{1}H NMR (400 MHz, $CDCl_3$, 25°C): δ = 7.64–7.57 (4H, m), 4.67 (2H, t, J = 7.8 Hz), 3.11 (3H, s), 1.94–1.89 (2H, m), 1.65 (6H, s), 1.48–1.42 (2H, m), 1.36–1.27 (4H, m), 0.87 (3H, t, J = 7.0 Hz) ppm. ^{13}C NMR (101 MHz, $CDCl_3$, 25°C): δ = 195.7, 141.8, 141.0, 130.2, 129.6, 123.5, 115.4, 54.8, 50.2, 31.2, 28.0, 26.5, 23.3, 22.4, 17.1, and 13.9 ppm.

HRMS (ESI +ve) *m*/*z*: Observed for $C_{17}H_{26}N^+$ $[M]^+$ = 244.2056, $[M]^+$ calcd = 244.2060.

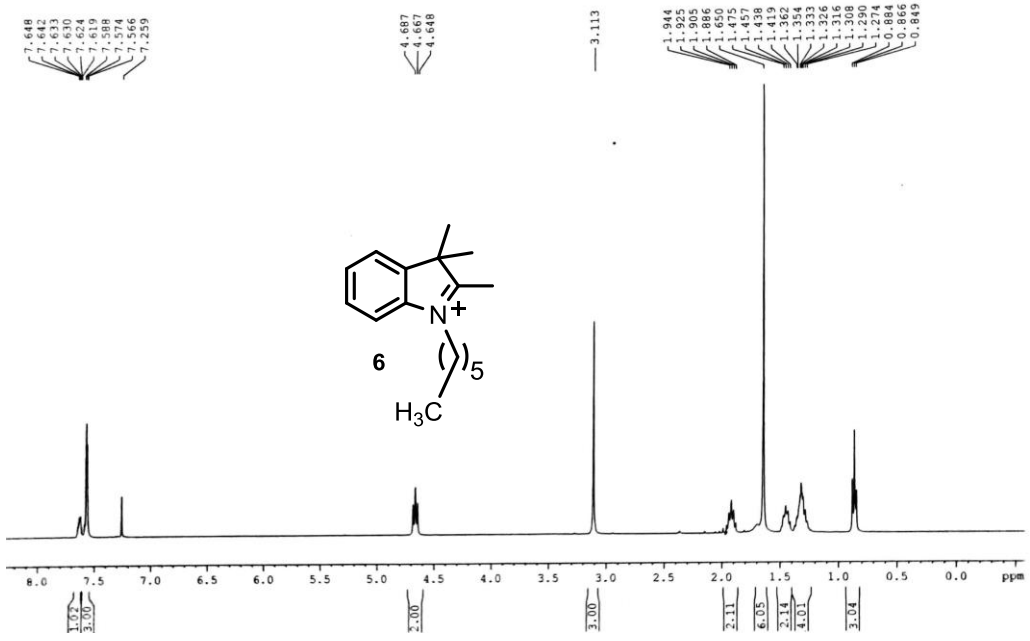

Figure 9. ^{1}H NMR (400 MHz, $CDCl_3$, 25°C) spectrum of compound 6.

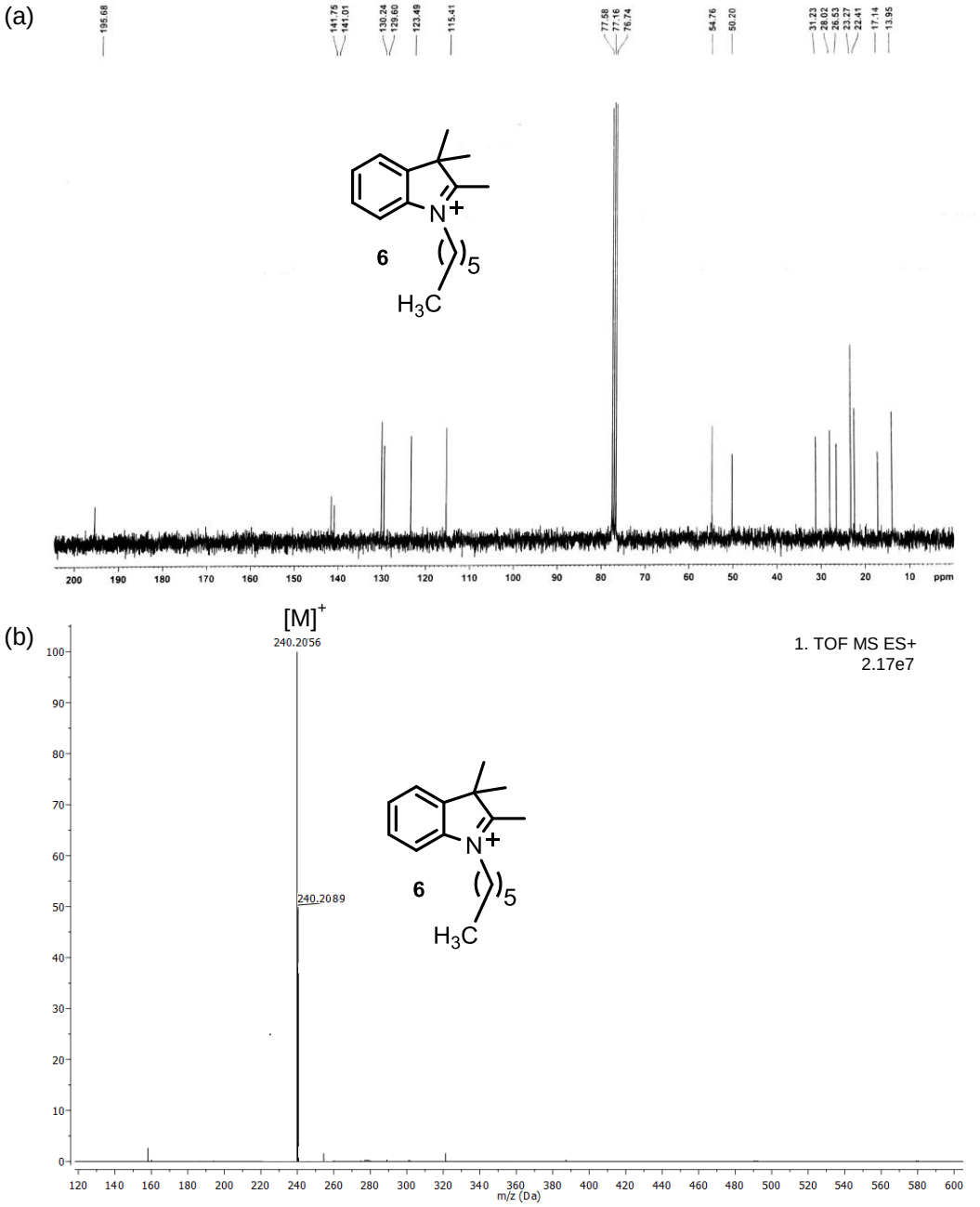

Figure 10. (a) ^{13}C NMR (101 MHz, $CDCl_3$, 25°C) and (b) HRMS (ESI +ve) spectrum of compound 6.

Cy-5a dye: Compound 4 (0.56 g, 0.93 mmol), 1 (0.12 g, 0.465 mmol), and NaOAc (0.12 g, 1.4 mmol) were heated to 70°C for 6 h in Ac_2O (5 mL). The reaction mixture was allowed to cool to room temperature and the solvent was removed under reduced pressure. Et_2O was added to get a blue color residue and this solution was kept overnight in the refrigerator. The blue solid was collected by filtration and washed with ether (3 × 5 mL). The crude product was purified by silica gel column chromatography using DCM:MeOH (95:5) (R_f = 0.34) to obtain the desired compound Cy-5a as a blue solid.

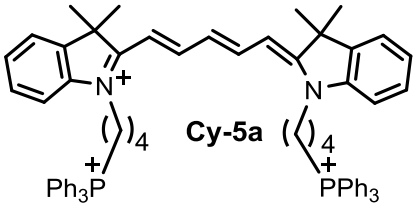

Yield: 0.19 g (32%).

^{1}H NMR (500 MHz, $CDCl_3$, 25°C): δ = 7.87–7.65 (34H, m), 7.58 (2H, d, *J* = 8.0 Hz), 7.38 (2H, t, *J* = 8.0 Hz), 7.27–7.22 (1H, m), 7.19–7.14 (2H, m), 6.48 (2H, d, *J* = 13.2 Hz), 4.23 (4H, t, *J* = 8.0 Hz), 3.82–3.74 (4H, m), 2.24–2.18 (4H, m), 2.04–1.98 (4H, m), 1.62 (12H, s) ppm. ^{13}C NMR (125 MHz, $CDCl_3$, 25°C): δ = 172.4, 152.9, 142.0, 140.7, 135.2, 135.2, 134.2, 134.1, 130.8, 129.3, 127.4, 125.2, 121.8, 118.4, 117.6, 112.5, 104.3, 49.3, 44.2, 29.8, 28.2, 23.4, 22.9, and 20.7 ppm.

^{31}P NMR (202 MHz, $CDCl_3$, 25°C): δ = 24.78 ppm.

HRMS (ESI +ve) *m*/*z*: Observed for $C_{69}H_{71}N_2P_2^{3+}$ $[M]^{3+}$ = 329.8297, $[M]^{3+}$ calcd = 329.8359.

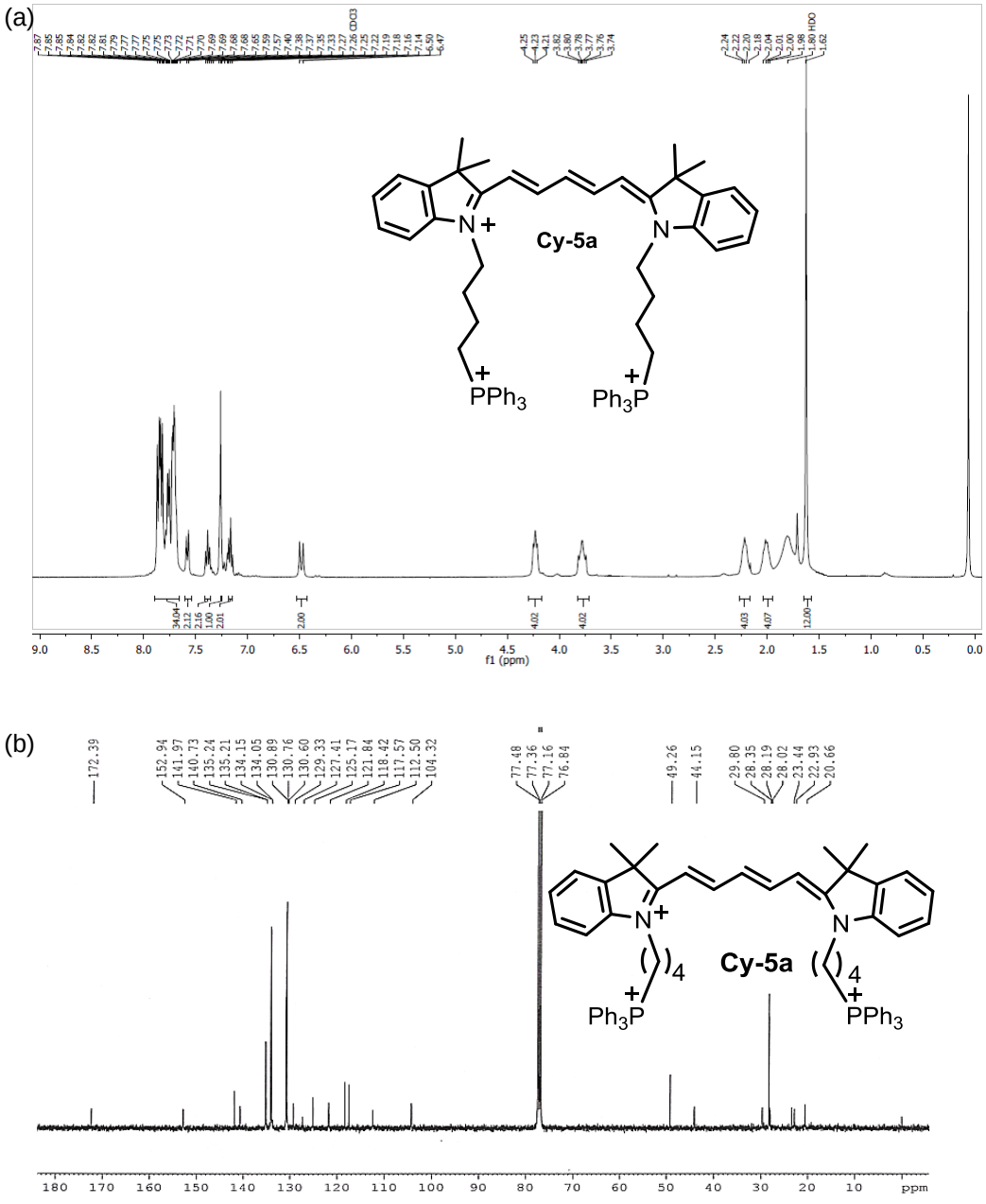

Figure 11. (a) ^{1}H NMR (500 MHz, $CDCl_3$, 25°C) spectrum and (b) ^{13}C NMR (125 MHz, $CDCl_3$, 25°C) spectrum of Cy-5a.

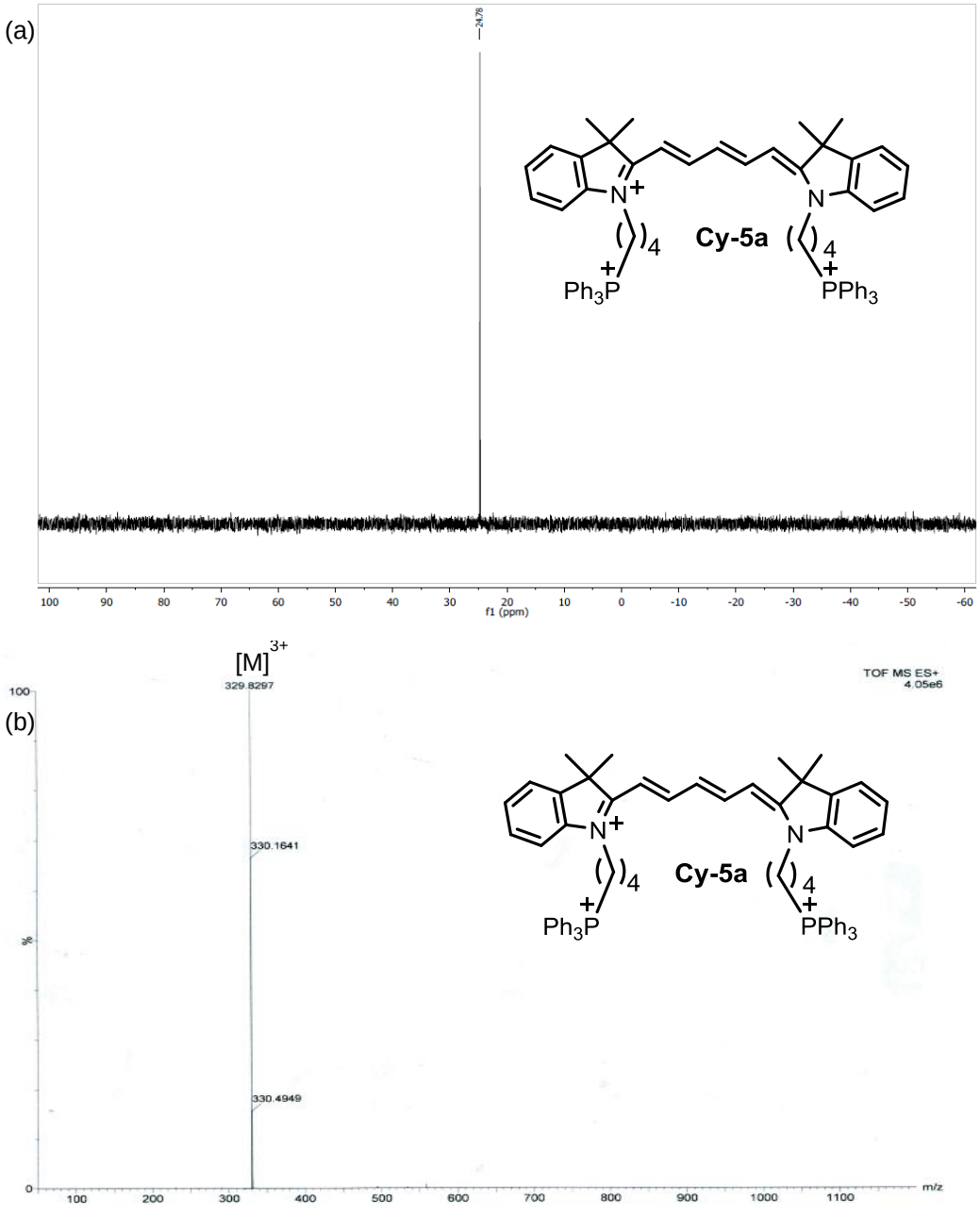

Figure 12. (a) ^{31}P NMR (202 MHz, $CDCl_3$, 25°C) spectrum and (b) HRMS (ESI +ve) spectrum of Cy-5a.

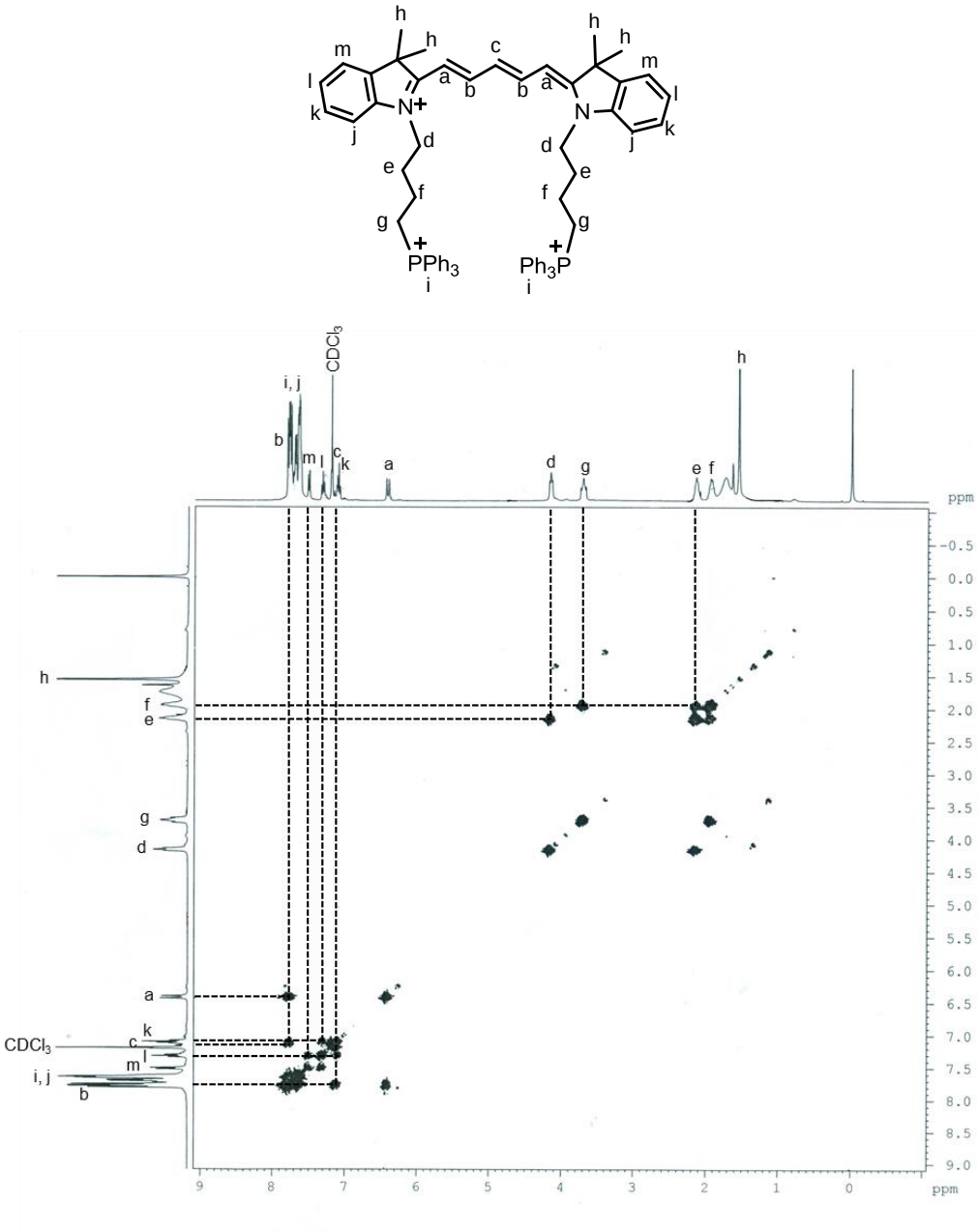

Figure 13. ^{1}H-^{1}H DQF COSY NMR spectrum of Cy-5a (500 MHz, $CDCl_3$, 25°C).

Cy-5b dye: Compound 5 (0.65 g, 1.03 mmol), 1 (0.13 g, 0.52 mmol), and NaOAc (0.13 g, 1.56 mmol) were heated to 70°C for 6 h in Ac_2O (5 mL) under N_2 atmosphere. The reaction mixture was then allowed to cool and the solvent was removed under reduced pressure. Et_2O was added to get a blue color residue and this solution was kept overnight in the refrigerator. The blue solid was collected by filtration and washed with Et_2O (3 × 5 mL). The crude product was purified by silica gel column chromatography using DCM:MeOH (92:8) (R_f = 0.30) to get the desired compound Cy-5b as a blue solid.

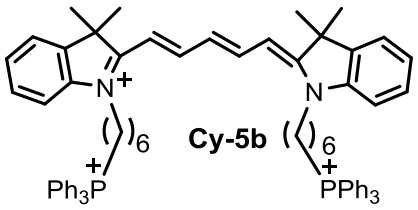

Yield: 0.20 g (30%).

^{1}H NMR (500 MHz, $CDCl_3$, 25°C): δ = 7.91 (2H, t, J = 13.0 Hz), 7.84–7.70 (30H, m), 7.38–7.35 (2H, m), 7.30 (4H, t, J = 7.5 Hz), 7.18 (2H, t, J = 7.5 Hz), 7.04 (1H, t, J = 12.5 Hz), 6.37 (2H, d, J = 14.0), 4.11 (4H, t, J = 7.0 Hz), 3.71–3.65 (4H, m), 1.81–1.74 (12H, m), 1.69 (12H, s), 1.68–1.62 (4H, m) ppm. ^{13}C NMR (125 MHz, $CDCl_3$, 25 °C): δ = 172.7, 153.1, 142.1, 141.2, 135.2, 133.9, 133.8, 130.8, 130.7, 129.0, 125.1, 122.1, 118.7, 118.0, 111.6, 104.0, 49.4, 44.5, 29.8, 28.3, 27.2, 26.1, 23.3, and 22.6 ppm.

^{31}P NMR (202 MHz, $CDCl_3$, 25°C): δ = 24.24 ppm.

HRMS (ESI +ve) *m*/*z*: Observed for $C_{73}H_{79}N_2P_2^{3+}$ $[M]^{3+}$ = 348.5202, $[M]^{3+}$ calcd = 348.5234.

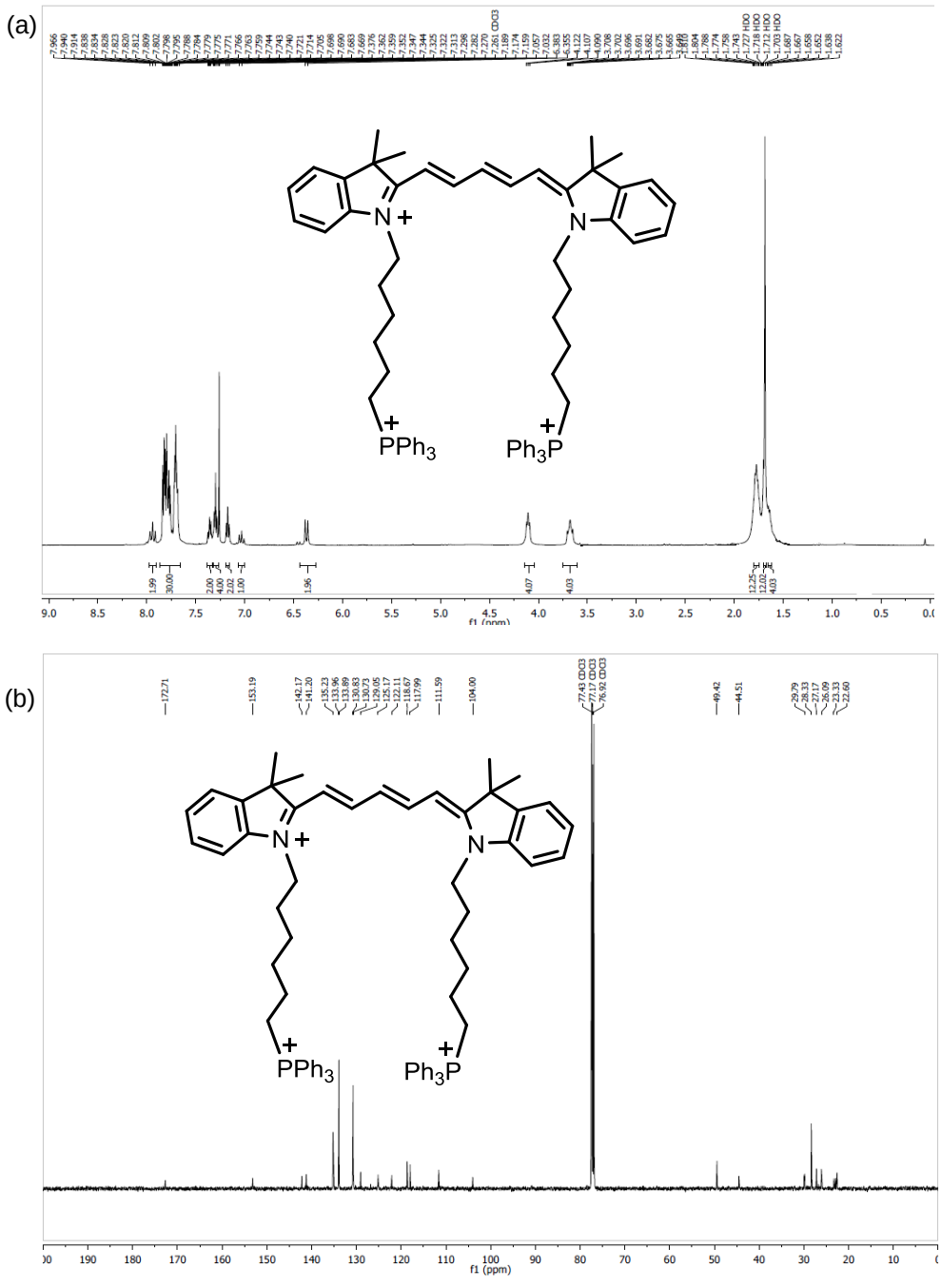

Figure 14. (a) ^{1}H NMR (500 MHz, $CDCl_3$, 25°C) spectrum and (b) ^{13}C NMR (125 MHz, $CDCl_3$, 25°C) spectrum of Cy-5b.

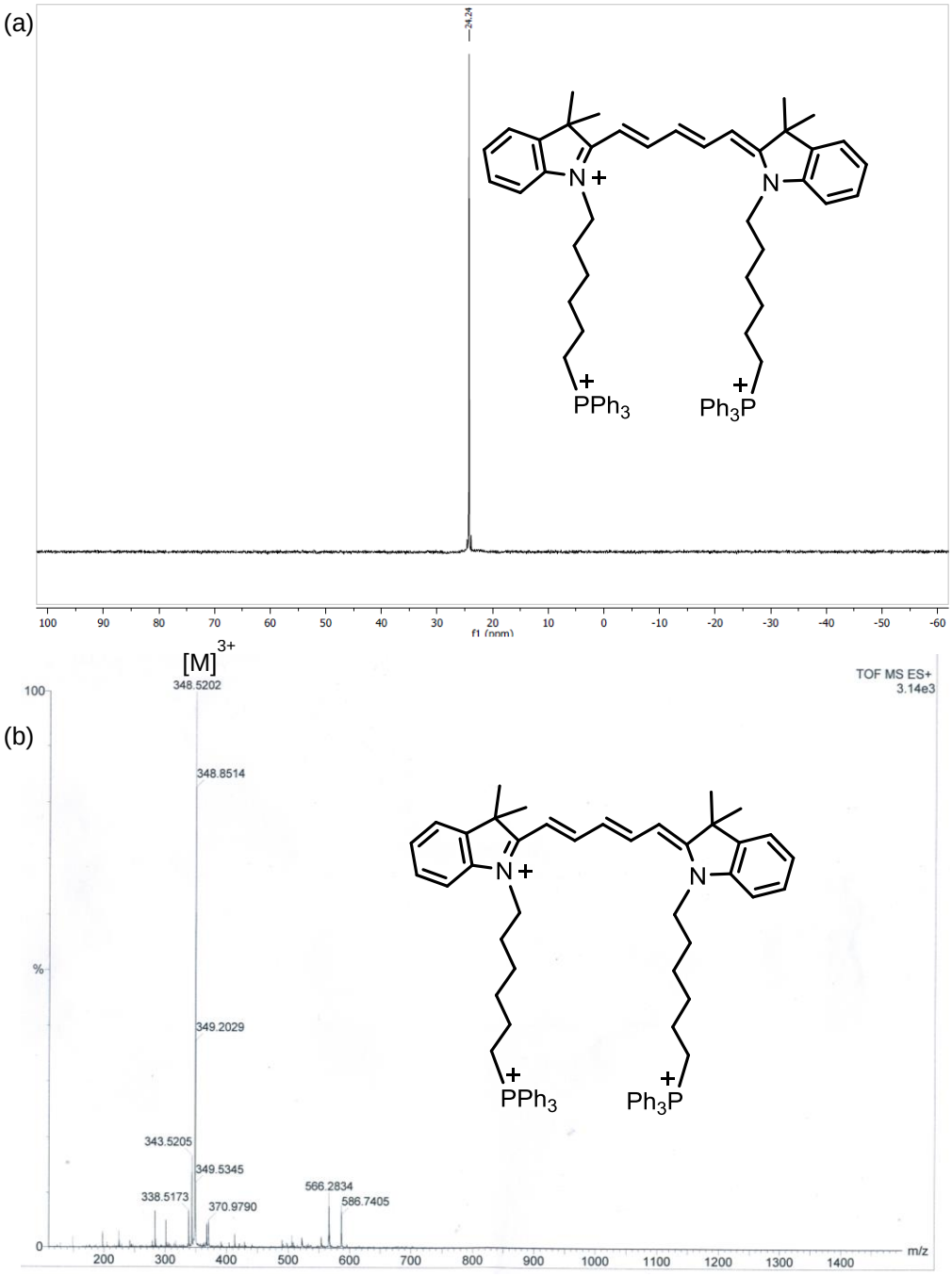

Figure 15. (a) ^{31}P NMR (202 MHz, $CDCl_3$, 25°C) spectrum and (b) HRMS (ESI +ve) spectrum of Cy-5b.

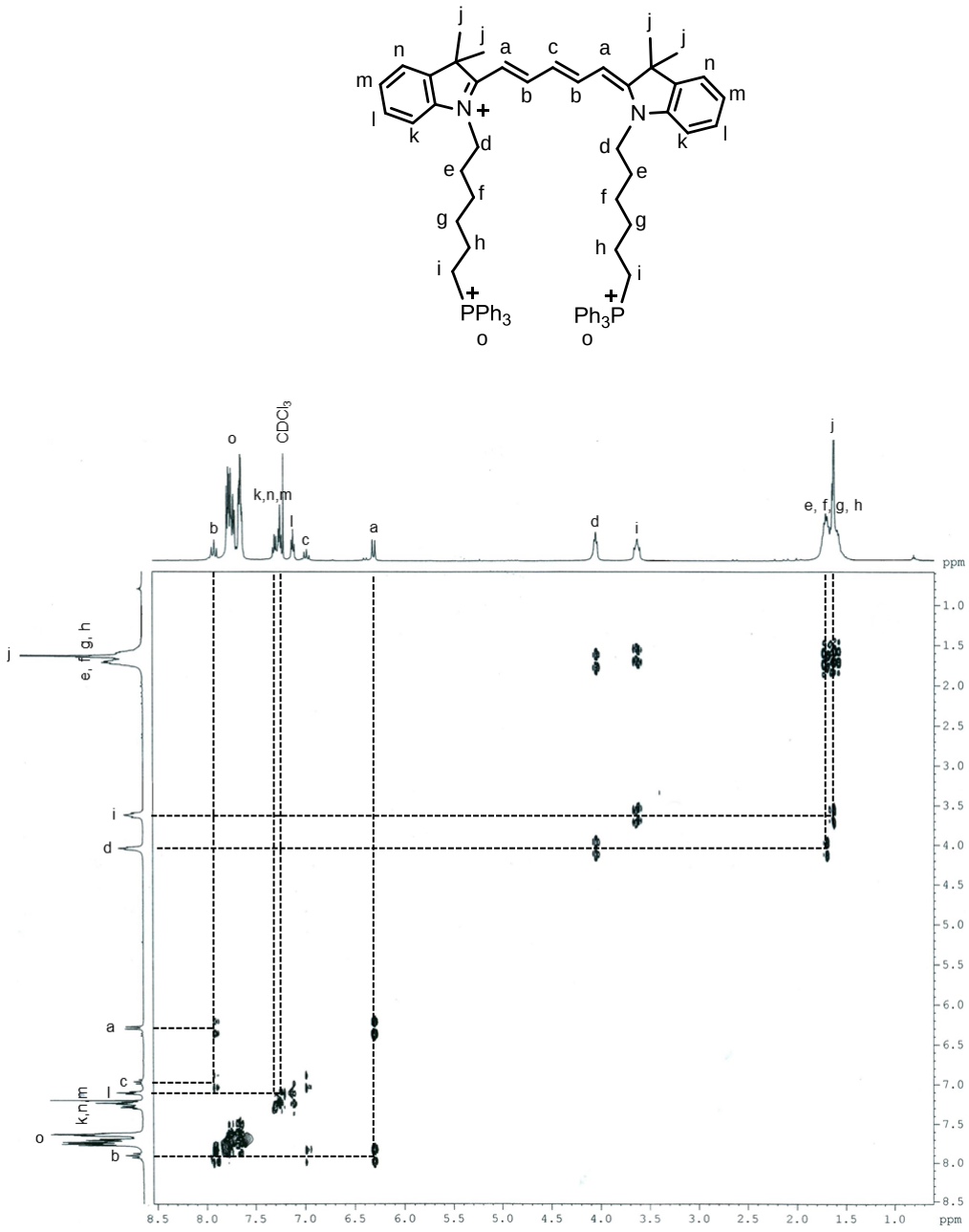

Figure 16. ^{1}H-^{1}H DQF COSY NMR spectrum of Cy-5b ($CDCl_3$, 500 MHz, 25°C).

Cy-5c dye: Compound 6 (0.24 g, 0.66 mmol), 1 (0.09 g, 0.33 mmol), and NaOAc (0.08 g, 0.99 mmol) were heated to 70°C for 6 h in Ac_2O (5 mL) under

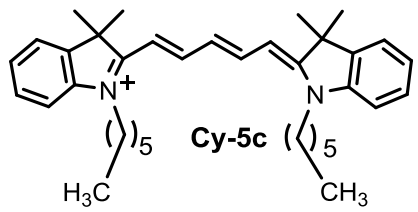

N_2 atmosphere. The reaction mixture was then allowed to cool and the solvent was removed under reduced pressure. Et_2O was added to get a blue color residue and this solution was kept overnight in the refrigerator. The residue was collected by filtration. The crude product was purified by column chromatography using DCM:MeOH (96:4) (R_f = 0.63) to obtain the pure compound Cy-5c as a blue solid.

Yield: 0.11 g (50%).

^{1}H NMR (500 MHz, $CDCl_3$, 25°C): δ = 8.24 (2H, t, *J* = 13.0 Hz), 7.37–7.33 (4H, m), 7.21 (2H, t, *J* = 7.5 Hz), 7.06 (2H, d, *J* = 8.0 Hz), 6.78 (1H, t, *J* = 13.0 Hz), 6.27 (2H, d, *J* = 13.5 Hz), 4.04 (4H, t, *J* = 7.5 Hz), 1.84–1.80 (4H, m), 1.79 (12H, s), 1.47–1.41 (4H, m), 1.37–1.25 (8H, m), 0.88 (6H, t, *J* = 7.0 Hz).

^{13}C NMR (125 MHz, $CDCl_3$, 25°C): δ = 173.3, 154.1, 142.3, 141.7, 128.6, 126.4, 125.2, 122.5, 110.6, 103.8, 49.7, 44.7, 31.6, 28.3, 27.5, 26.7, 22.6, and 14.1 ppm.

HRMS (ESI +ve) *m*/*z*: Observed for $C_{37}H_{51}N_2^+$ $[M]^+$ = 523.4341, $[M]^+$ calcd = 523.4047

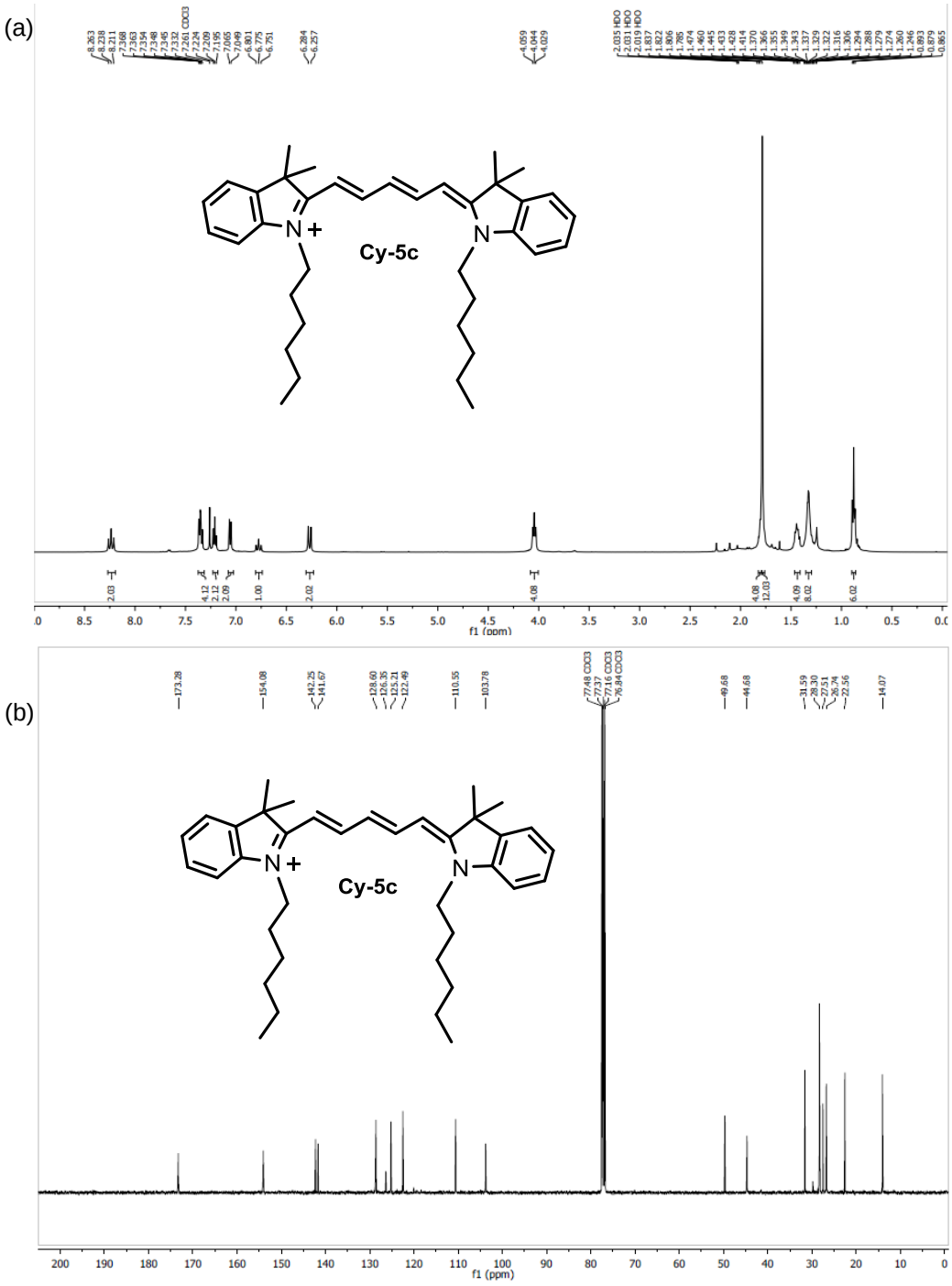

Figure 17. (a) ^{1}H NMR (500 MHz, $CDCl_3$, 25°C) spectrum and (b) ^{13}C NMR (125 MHz, $CDCl_3$, 25°C) spectrum of Cy-5c.

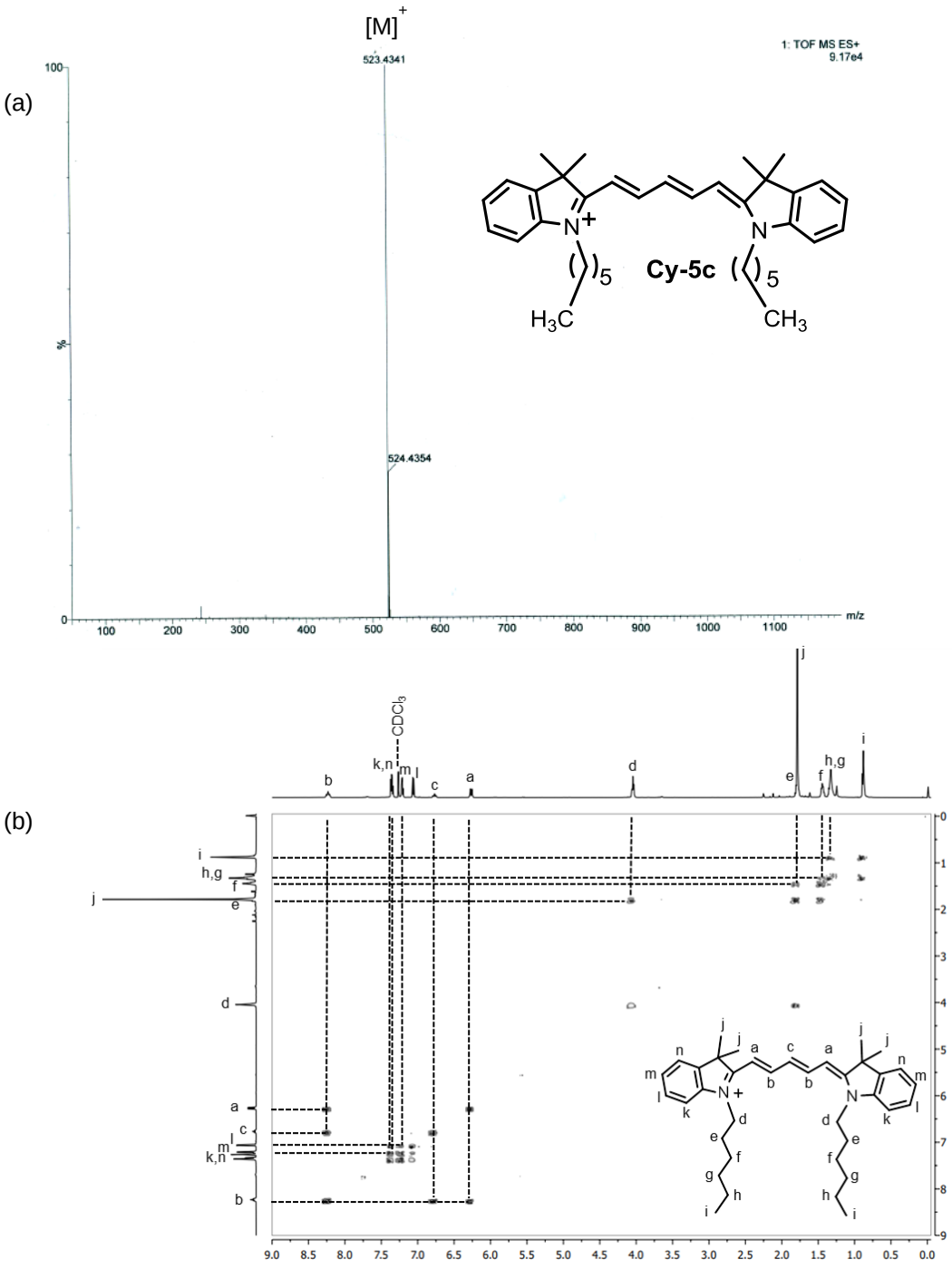

Figure 18. (a) HRMS (ESI +ve) spectrum and (b) ^{1}H-^{1}H DQF COSY NMR spectrum of Cy-5c ($CDCl_3$, 500 MHz, 25°C).

METHODS

NMR Spectroscopy: ^{1}H, ^{13}C, ^{31}P NMR, and ^{1}H-^{1}H DQF COSY spectra were recorded on Bruker DPX400 MHz and Bruker DPX500 MHz spectrometers at 25°C in suitable deuterated solvents.

HRMS (ESI): High-resolution electrospray ionization mass spectrometry (HRMS-ESI) result was obtained using a Q-Tofmicro (Waters Corporation) mass spectrometer.

Absorption Spectroscopy: Absorption spectra were recorded in various solvents on a Shimadzu UV-1800 spectrometer. All measurements were carried out in a quartz cuvette with a path length of 1 cm. Stabilities of the Cy-5a and Cy-5b dyes were measured in PBS at pH 7.4, 37°C, over 24 h using a peltier temperature controlling unit attached with the UV/vis instrument.

Fluorescence Spectroscopy: Fluorescence experiment was performed on a Horiba Jobin Yvon FluoroMax-4 spectrofluorometer in various solvents.

Time-correlated single photon counting (TCSPC) experiment: Fluorescence lifetimes of the probes were measured in various solvents using time-correlated single photon counting (TCSPC) technique on Horiba DeltaFlex lifetime instrument (Horiba Jobin Yvon IBH Ltd, Glasgow, Scotland, UK). 650 nm delta diode laser excitation source (Model: DD-650L, Horiba Scientific) was used to measure fluorescence lifetimes of Cy-5a and Cy-5b. Data analysis and lifetime measurements were carried out using Horiba EzTime decay analysis software.

pH Meter: Mettler Toledo pH meter was used to prepare PBS and HEPES buffer solutions at pH 7.4.

Calculation of relative quantum yield of Cy-5a and Cy-5b dyes: Fluorescence quantum yields (Φ_f) of Cy-5a and Cy-5b dyes were measured by relative method.[40] Here, the integrated fluorescence intensities of the samples

were compared with fluorescence intensities of a reference compound according to the following equation:

$\Phi_f(x) = \Phi_f(st) \times [(A_{st} \times F_x \times \eta_x^2) / (A_x \times F_{st} \times \eta_{st}^2)]$

$\Phi_f(st)$ and $\Phi_f(x)$ are fluorescence quantum yield of the reference and sample compounds respectively; A_{st} and A_x are absorbance of reference and sample at the excitation wavelength, respectively. F_{st} and F_x are the integrated fluorescence areas under the corrected fluorescence spectra for the reference and sample compound, respectively. η_{st} and η_x are the refractive indices of the solvent in which the reference and sample compounds are measured, respectively [here, both the reference and sample compounds were dissolved in DMSO; so $(\eta_x^2 / \eta_{st}^2) = 1$]. "st" stands for the standard and "x" refers to the unknown sample. $\Phi_f(st)$ of Zinc pthalocyanine in DMSO is 0.20, which is used as the reference.

The relative Quantum yields (Φ_f) of Cy-5a and Cy-5b were measured as 0.30 and 0.24 respectively in DMSO.

Water solubility of Cy-5a and Cy-5b dyes: Cy-5a and Cy-5b dyes was separately dissolved in water with maximum known amount and the solubility were determined by the UV/vis spectroscopic method. With known concentration of Cy-5a and Cy-5b an absorbance vs concentration calibration curve was plotted for both the dye. Then the absorbance of the saturated solution of both the dye with proper dilution was measured and using the abs vs conc. calibration curve corresponding concentration of the dye was determined. This give the measure of the solubility of Cy-5a and Cy-5b dyes in water. Cy-5a and Cy-5b are small molecules with excellent solubility in water due to triply positive charge (5.65×10^{-5} mol L^{-1} for Cy-5a and 8.15×10^{-6} mol L^{-1} for Cy-5b).

Determination of Octanol/PBS partition coefficient values of Cy-5a and Cy-5b dyes: Octanol/PBS partition coefficient values of Cy-5a and Cy-5b were measured according to the literature procedure.[37,38] To measure the partition coefficient of Cy-5 dye, 1 mg of each Cy-5a and Cy-5b was separately dissolved in 2 mL octanol. Absorbance of the stock solution in octanol for Cy-5a and Cy-5b was determined separately by UV/vis spectroscopy using proper dilution. 1 mL of PBS (pH 7.4) and equal volume of stock solution in octanol were mixed and vortexed for 1 m, and kept at 37ºC for 1 h to achieve equilibrium. The mixture was centrifuged at 2500 rpm for 10 m to separate the organic and aqueous layer. After centrifugation, absorbance of the organic (A_o) layer was determined by UV/vis spectroscopy with appropriate dilution. The ratio of absorbance in organic layer (after mixing) to that of an aqueous layer (determined from difference in absorbance value of organic layer before and after mixing with PBS) gives the partition coefficient value and it is expressed as A_o/A_w.

Partition coefficient (P) = $(A_o)_f / [(A_o)_i - (A_o)_f]$

Where $(A_o)_i$ and $(A_o)_f$ are initial and final absorbance in octanol layer, respectively.

Partition coefficient (P) values of Cy-5a and Cy-5b were found 2.88 and 7.12; and log P values were 0.46 and 0.85, respectively.

Preparation of Lipid Film: DOPC (10 mg mL^{-1}) and Cholesterol (10 mg mL^{-1}) were dissolved in $CHCl_3$. Appropriate quantities were mixed to get a defined composition of DOPC: Cholesterol = 80:20. The solvent ($CHCl_3$) was removed by N_2 stream for 20 min and the residual solvent was removed under high vacuum for 2 h to form DOPC: Cholesterol lipid film on the test tube walls. The lipid films were rehydrated with an appropriate amount of HEPES buffer solution (20 mM, 150 mM NaCl, pH 7.4).

Multilamellar Vesicles (MLVs): After 1 h of incubation at $T > t_m$, the hydrated lipid films were subjected to five freeze/thaw cycles (immerse the sample in liquid N_2 followed by 40°C at water bath) to detach the lipid film from the wall of the test tube, while also dispersing the vesicles. The dispersed MLVs were incubated at $T > t_m$ for 5 min and vortexed.

Large Unilamellar Vesicles (LUVs): The MLV suspensions were extruded 31 times through a polycarbonate membrane (200 nm pore size, 19 mm diameter) using a *Liposofast* extruder (*Avestin*, Ottawa, Canada) at $T > t_m$ to produce unilamellar vesicle suspension.

Dynamic Light Scattering (DLS): Dynamic light scattering experiments were performed using Malvern instrument (UK) to examine the hydrodynamic diameters of the liposomes in HEPES buffer at pH 7.4. All measurements were conducted at a backscattering angle 173° and a temperature of 25°C. Three runs were conducted per measurement and the average values were taken. A monodisperse population of the liposome with hydrodynamic diameter = 168 nm and PDI = 0.115 was observed in HEPES buffer.

Cell culture: Human pancreatic cancer cell (MIA PaCa-2), lung carcinoma (A549) cell, noncancerous peripheral blood mononuclear cell (PBMC), human embryonic kidney (HEK293) cell, and lung fibroblast (WI38) cell were cultured in DMEM media (pH 7.4) supplemented with 10% FBS and antibiotic-antimycotic solution 100× (containing 10,000 units penicillin, 10 mg streptomycin, and 25 µg amphotericin B per mL in 0.9% normal saline). The cell lines were maintained at 37°C in an air-jacketed 5% CO_2 incubator and were routinely passaged.

MTT assay for cell viability: All the cells were separately plated at a density of ~10^3 cells in a 96-well plate separately using DMEM media with a 24 h incubation to allow appropriate cell growth. The cytotoxic effects of Cy-5a and

Cy-5b on the various cancerous and noncancerous cell lines were determined by MTT assay. After the 24 h incubation, Cy-5 dye was treated at specified concentrations (0.25, 0.5, 0.75 μM) for 24 h at 37°C. The cells were then treated with 10 μL of MTT solution (5 mg mL^{-1} in PBS) for 4 h in darkness at 37°C. Dark blue formazan crystals was formed which were dissolved in DMSO and the absorbance (*A*) was measured at 575 nm using an ELISA plate reader. The results were expressed as the percentages of the viable cells by the following equation:

Viable cells (%) = (*A* of treated cells / *A* of untreated cells) × 100

Flow Cytometric Analyses: Flow cytometric analyses were carried out by BD FACSVerse flow cytometer (BD Biosciences, San Jose, CA) and the data were analyzed by BD Cell Quest software (BD Biosciences).

Cell penetration dose determination: A549 cells (10^4 in numbers) were treated with different dose of Cy-5 dyes for 10 m in darkness. Then, the cells were washed with PBS and re-suspended in 400 μL PBS. The samples were subjected to flow cytometric analysis using BD FACSVerse instrument. The overall fluorescence intensity of dye positive cells was measured and the optimal concentration was calculated from the titration.

Confocal microscopy: Fluorescence confocal microscopic images were acquired with an Olympus instrument (Model IX81) equipped with a 60× and 100× oil plan apochromatic objective with numerical aperture (NA) = 1.49. Colocalization experiments involving Cy-5a and Cy-5b ($\lambda_{ex}/\lambda_{em}$ 650/675) were performed in fixed A549 carcinoma cell line using a mitochondrion-tracking fluorescent probe MitoTracker Red ($\lambda_{ex}/\lambda_{em}$ 579/599).[43] A549 cells were seeded on the cover slip and grown in DMEM media. Cells were fixed for 30 min with 4% paraformaldehyde and subjected to confocal microscopic studies. Fixed cells were incubated with 0.7 μM solution of Cy-5 dye at 37°C for 10 m

in darkness and then washed twice using 1x PBS. Cells were then incubated with 0.2 μM MitoTracker Red in darkness for 15 m, washed twice with 1x PBS, and incubated with DAPI for 15 m. After washing in the same procedure, cells were mounted with antiquench agent *n*-propyl gallate for microscopic slide preparation and detected by confocal fluorescence microscope. High resolution images were analyzed by Olympus FV1000 software.

For DAPI: laser excitation wavelength = 405 nm, emission wavelength = 461 nm, BF range = 50 nm, BF position = 425 nm. For MitoTracker Red: laser excitation wave length = 561 nm, emission wavelength = 598 nm, BF range = 55 nm, BF position = 570 nm. For Cy-5 dye: laser excitation wave length = 635 nm, emission wavelength = 668 nm, BF range = 655-755.

Mitochondrial Selectivity of Cy-5a and Cy-5b Over Lysosome: Colocalization experiments were performed using a green-fluorescent lysosome tracking probe, LysoTracker Green DND-26 (**Figure 29b,c**). Fixed cells were incubated with 0.7 μM solution of Cy-5 dye at 37 °C for 10 m in darkness and then washed twice using 1× PBS. Cells were then incubated with 50 nM LysoTracker Green in darkness for 15 m, washed twice with 1× PBS, and incubated with DAPI for 15 m. After washing with the same method, cells were mounted with n-propyl gallate for microscopic slide preparation and detected by confocal fluorescence microscope. High-resolution images were analyzed by Olympus FV1000 software. For LysoTracker Green DND-26: laser excitation wave length = 488 nm, emission wavelength = 519 nm, BF range = 100 nm, BF position = 495 nm.

Multicolor Confocal Imaging: Multicolor imaging of cellular organelles in the same cell was achieved using a combination of suitable targeting dyes with distinct excitation and emission bands. Lipophilic green emitting FM 1-43FX was used to selectively label the plasma membrane, blue-fluorescent DAPI to

stain the nucleus, and Cy-5 to target and stain the mitochondria of A549 cells. Multicolor confocal imaging of cells was acquired by using appropriate filters for FM 1-43FX (laser ex/em 488/590 nm), DAPI (laser ex/em 405/461 nm), and Cy-5 dye (laser ex/em 635/668 nm). Fixed cells were incubated with 0.7 μM solution of Cy-5 dye at 37°C for 10 m in darkness and then washed twice using 1× PBS. Cells were then incubated with DAPI for 15 m followed by incubation with 8 μM FM 1-43FX in darkness for 1 m. After washing, following the same process, cells were mounted with n-propyl gallate for microscopic slide preparation and detected by confocal fluorescence microscope. High-resolution images were analyzed by Olympus FV1000 software.

Determination of Mitochondrial Membrane Potential Using JC1 Dye: Alteration in mitochondrial membrane potential was determined with JC-1 dye (Mitochondrion membrane potential assay kit) using FACS flow cytometer and the data were analyzed by Cell Quest software (BD Biosciences).[S5] When the potential of mitochondria was high, JC-1 was entered from the cell membrane to the cytosol to the mitochondria and the J-aggregates of JC-1 were formed. However, in case of membrane depolarization the J-aggregates leak out from the mitochondria to the cytosol as monomers. The λ_{ex} for JC-1 was 494 nm and the λ_{em} was observed at 535 nm (green fluorescence for JC-1 monomers) and at 595 nm (orange-red fluorescence for JC-1 aggregates). Then the fluorescence emission ratio of monomers to aggregates (535/595) was evaluated. The higher value of this ratio indicates higher membrane depolarization. A549 cells were stained with JC-1 dye for 15 min with 1 mg mL^{-1} JC-1 in culture medium at 37°C in darkness; then, mitochondrial membrane potential was determined using FACSVerse flow cytometer and the data were analyzed by Cell Quest software (BD Biosciences). After cellular staining with JC-1 dye, the

fluorescent signal is analyzed in the FITC and PE channels using a 494 nm laser.

Results and discussion

Design and synthesis of Cy-5a, Cy-5b,and Cy-5c:

The heterocyclic 2,3,3-trimethylindolenine molecule is synthesized by the Fischer indole synthesis and the N of indolenine moiety is covalently modified with mitochondria targeting triphenylphosphonium (TPP^+) moiety using alkylating agents 2 and 3 (**Scheme 1**).[37,38] The synthesis of Cy-5a [two $-(CH_2)_4-$ spacer] and Cy-5b [two $-(CH_2)_6-$ spacer] involves the condensation of heterocyclic compounds containing an activated methyl group (4 and 5) with malonaldehyde bis(phenylimine) monohydrochloride (**1**), which is prepared from the commercially available 1,1,3,3-tetramethoxypropane (**Scheme 1**). Cy-5a and Cy-5b (dark blue powder) are characterized by 1D (^1H, ^{13}C, and ^{31}P) NMR, 2D (^1H-^1H DQF COSY) NMR, and high-resolution ESI-MS (**Figure 10-16**). Both the symmetric molecules Cy-5a and Cy-5b consist of two P atoms, exhibit one ^{31}P NMR peak at ~24 ppm (**Figure 12a and Figure 15a**). A control dye lacking the mitochondria targeting TPP^+ moiety (Cy-5c) is also synthesized and characterized (**Figures 1,17, and 18**).

Study of photophysical properties of Cy-5a and Cy-5b:

The synthesized Cy-5a and Cy-5b are small molecules with excellent solubility in aqueous solutions (5.66×10^{-5} mol L^{-1} for Cy-5a and 8.16×10^{-6} mol L^{-1} for Cy-5b, **Figure 21**) due to triply positive charge. The absorption and emission features of Cy-5a and Cy-5b are examined in various solvents (H_2O, DMF, DMSO, CH_3OH, CH_3CN, $CHCl_3$) including phosphate-buffered saline (PBS) and 2-[4-(2-hydroxyethyl)- piperazin-1-yl]ethanesulfonic acid (HEPES) buffer solutions (**Figure 19 and Figure 20**). The absorption spectra exhibited

an intense peak (λ_{max}) at 660 nm in $CHCl_3$ due to $\pi \rightarrow \pi^*$ transitions with large molar extinction coefficient of ca. $1.90 \times 10^5\ M^{-1}\ cm^{-1}$ for Cy-5a as well as Cy-5b (**Table 1**). For both the probes, the fluorescence maximum (λ_{em}) is observed at ca. 685 nm in $CHCl_3$ (λ_{ex} = 660 nm) with ca. 25 nm Stokes shift (**Table 1**). Cy-5a and Cy-5b exhibit modest solvatochromism in the absorption and emission with ~20 nm bathochromic shifts being observed by decreasing the solvent polarity from H_2O to $CHCl_3$, which is probably due to combined effects of dielectric constant and refractive indices of the solvents (**Table 1**, **Figure 19 and Figure 20**). The absorption and emission spectra, shapes, and $\lambda_{ex}/\lambda_{em}$ of Cy-5b in PBS and HEPES buffer (pH 7.4, 37°C) are comparable to those observed in H_2O (**Figure 20**). Cy-5a and Cy-5b exhibit narrow absorption and emission band, which is extremely important for multicolor imaging process where a combination of various dyes is frequently applied. Additionally, no evidence of aggregation is observed for Cy-5a and Cy-5b (**Figure 19 and Figure 20**). The lack of aggregation is due to the presence of two cationic TPP^+ residues, which provide electrostatic repulsion between molecules. Fluorescence quantum yield, $\Phi_f = 0.30$ and $\Phi_f = 0.24$ are observed in DMSO for Cy-5a and Cy-5b, respectively, which are higher than that of NIR dyes zinc phthalocyanine (Φ_f = 0.20 in DMSO), oxazine 1 (Φ_f = 0.141 in EtOH), cryptocyanine (Φ_f = 0.012 in EtOH), IR-125 (Φ_f = 0.132 in EtOH), and comparable with other Cy-5 dyes (**Table 2**). Fluorescence lifetime (τ) of Cy-5a and Cy-5b are determined in various solvents by TCSPC technique. Values of $\tau \approx 1.948$ ns for Cy-5a and $\tau \approx 1.769$ ns for Cy-5b in DMSO are found (**Figure 19e, Figure 22a, and Table 3**). Cy-5a and Cy-5b dyes also exhibit modest solvatochromism in their fluorescence lifetime and τ is longer in $CHCl_3$ than in H_2O (**Table 3**).

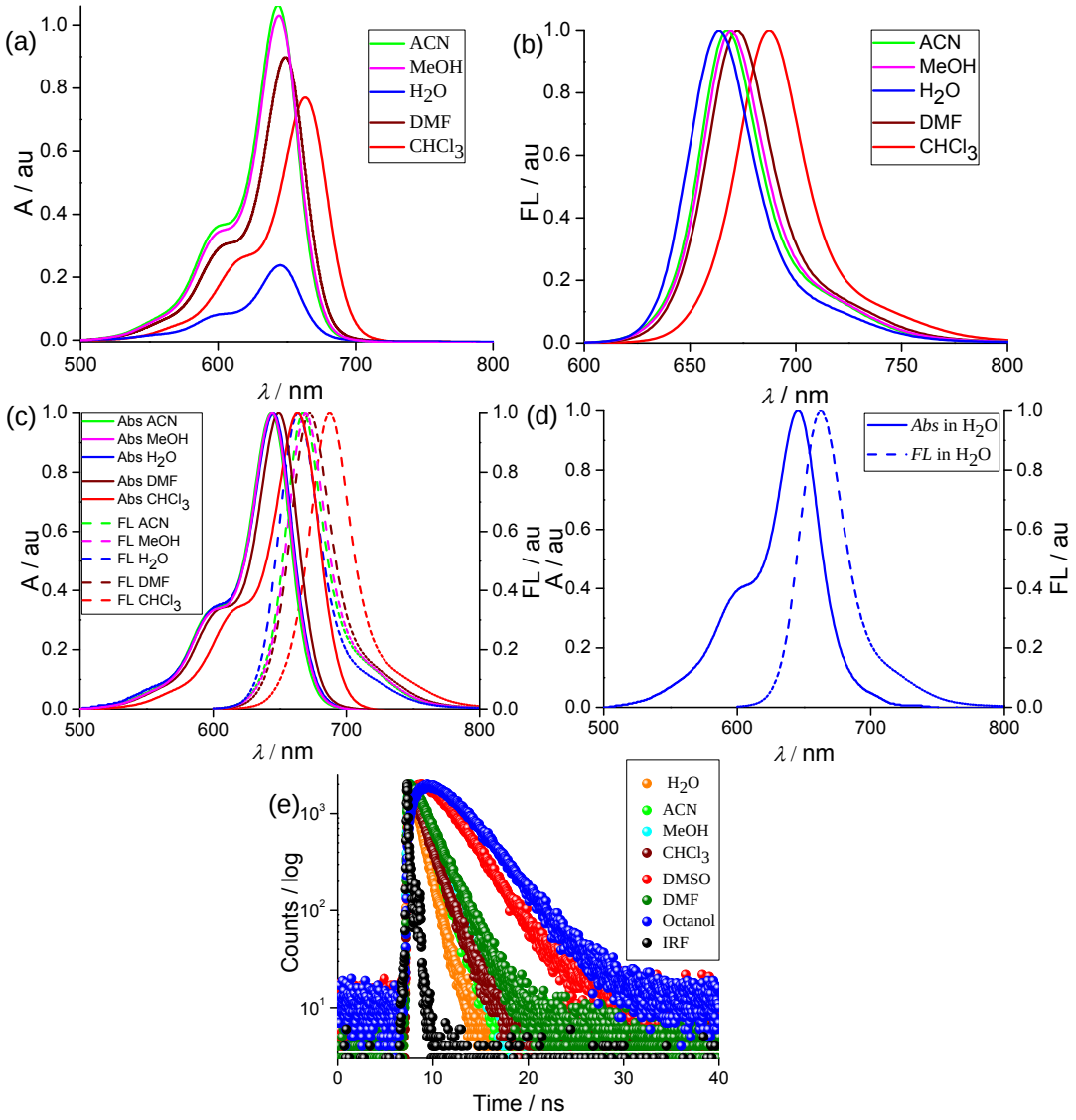

Figure 19. (a) Absorption spectra of Cy-5a (4 μM) in various solvents. (b) Normalized fluorescence emission spectra of Cy-5a dye in various solvents (4 μM). (c) Normalized absorption (solid line) and emission spectra (dashed line) of Cy-5a dye in various solvents. (d) Normalized absorption (blue solid line) and emission spectra (blue dashed line) of Cy-5a dye in H_2O (4 μM). (e) Absorption spectra of Cy-5a dye in H_2O at various concentrations. (f) TCSPC plots of Cy-5a dye in various solvents using excitation with delta diode laser at 650 nm.

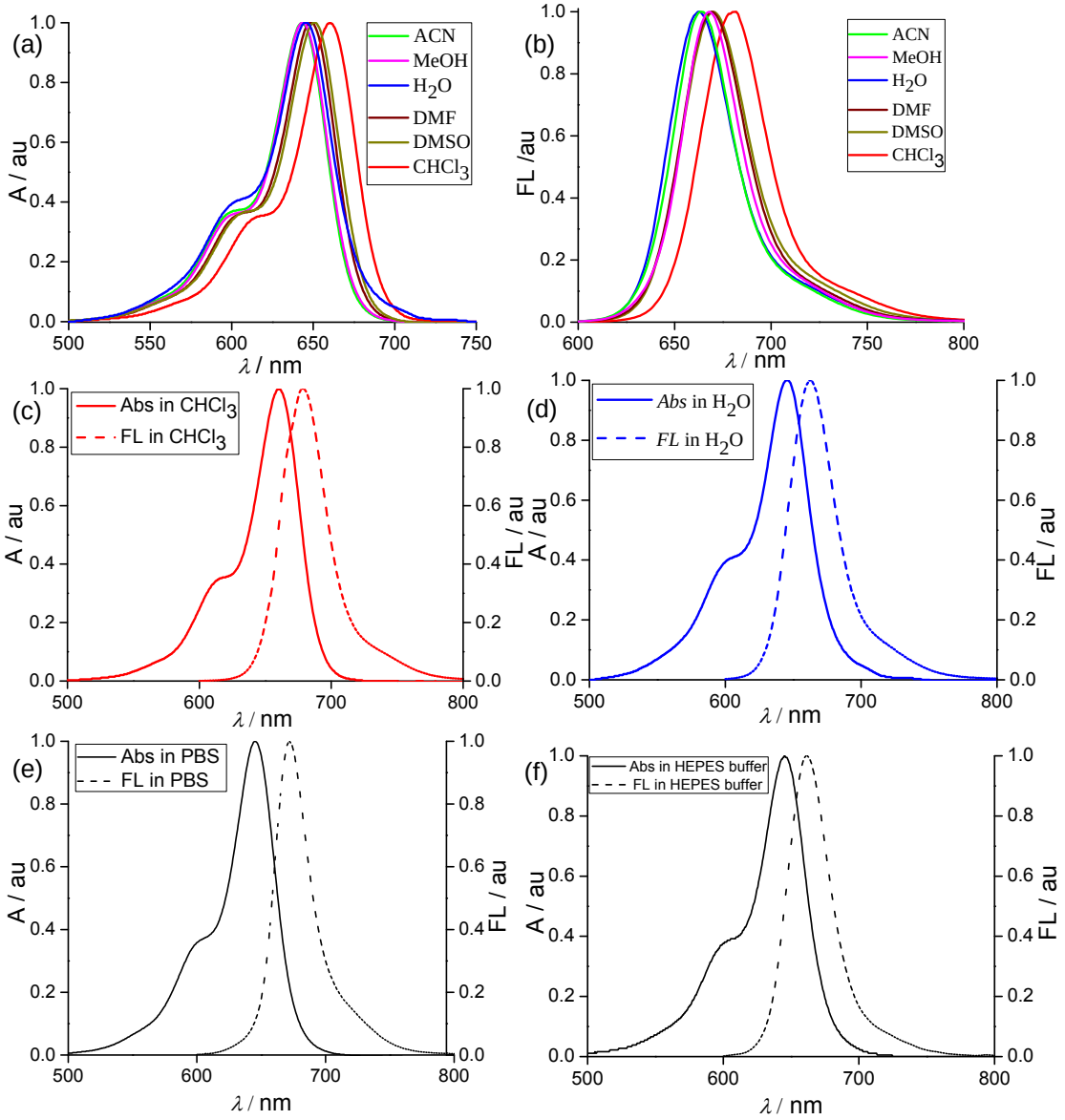

Figure 20. (a,b) Normalized absorption and fluorescence emission plots of Cy-5b in various solvents (4 μM). (c) Normalized absorption (red solid line) and emission spectra (red dashed line) of Cy-5b dye in $CHCl_3$ (4 μM). (d) Normalized absorption (blue solid line) and emission spectra (blue dashed line) of Cy-5b dye in H_2O (4 μM). (e,f) Normalized absorption (solid line) and emission spectra (dashed line) of Cy-5b dye in PBS at pH = 7.4, 37°C (4 μM) and HEPES buffer at pH = 7.4, 37°C (4 μM) respectively.

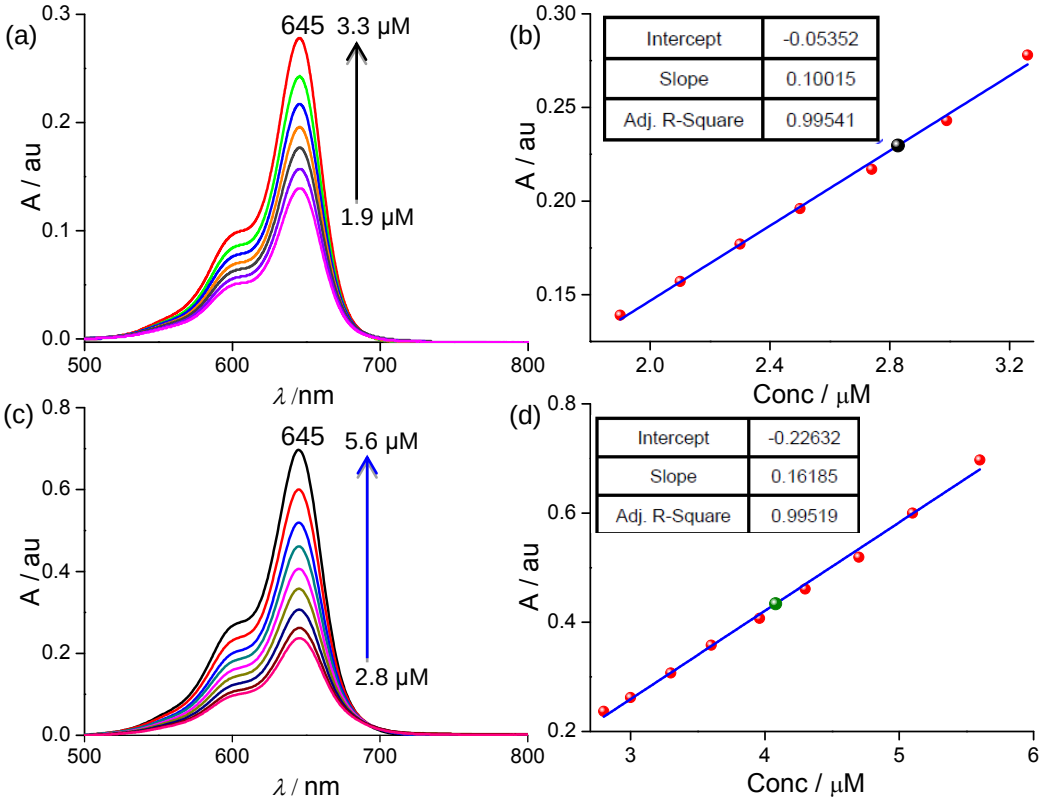

Figure 21. (a) Absorption spectra of Cy-5a dye in H_2O at various concentrations (1.9 μM, 2.1 μM, 2.3 μM, 2.5 μM, 2.7 μM, 3.0 μM, 3.3 μM). (b) Linear relationship obtained in absorbance at 645 nm versus concentration plots of Cy-5a dye in H_2O. Saturated stock solution of Cy-5a is diluted 20 times to check the absorbance and after plotting it on the calibration curve (black spot) the concentration is found to be 2.83 μM. Hence the concentration of the stock solution as well as solubility of Cy-5a is 56.6 μM. (c) Absorption spectra of Cy-5b dye in H_2O at various concentrations (2.8 μM, 3.0 μM, 3.3 μM, 3.6 μM, 3.9 μM, 4.3 μM, 4.7 μM, 5.1 μM, 5.6 μM). (d) Linear relationship observed in absorbance at 645 nm versus concentration plots of Cy-5b dye in H_2O. Saturated stock solution of Cy-5b is diluted 2 times to check the absorbance and after plotting it in calibration curve (olive spot) the concentration is found to be 4.08 μM. Hence the concentration of the stock solution as well as solubility of Cy-5b is 8.16 μM.

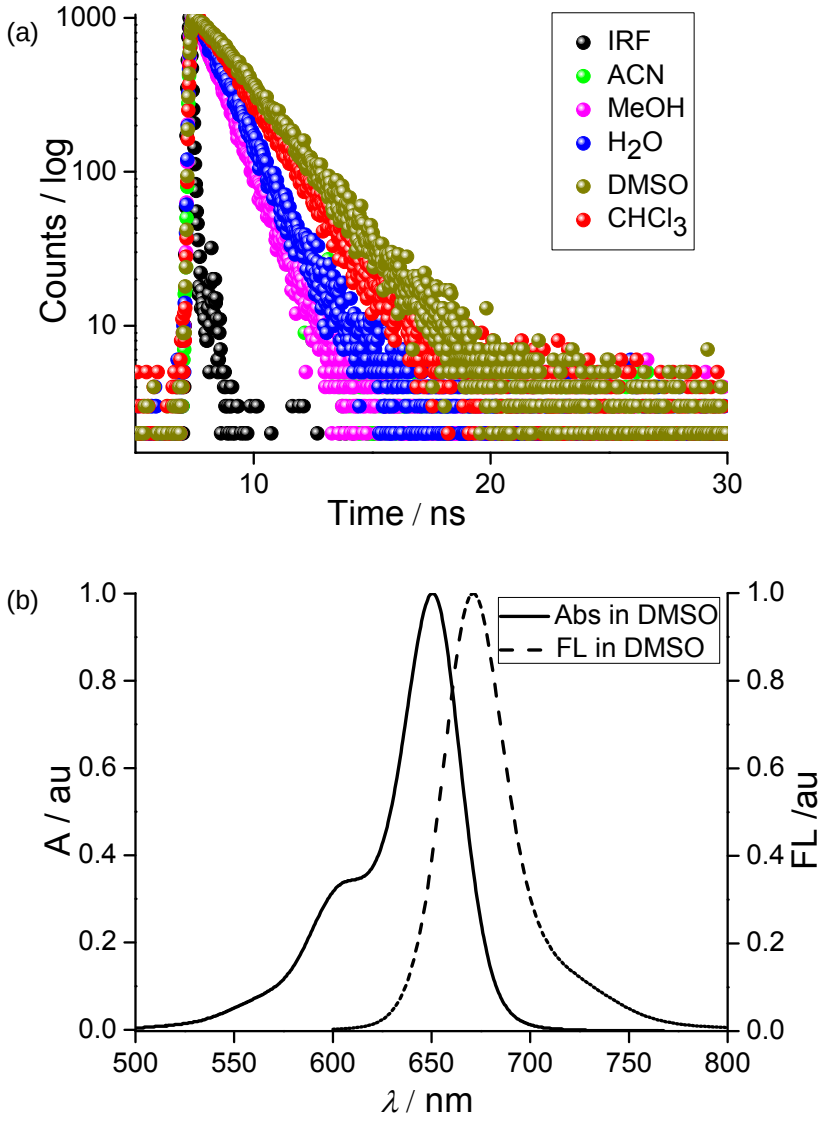

Figure 22. (a) TCSPC plots of Cy-5b dye in various solvents using excitation with delta diode laser at 650 nm. The black dotted line corresponds to the instrument response function (IRF). (b) Normalized absorption (solid line) and emission plots (dashed line) of Cy-5c dye in DMSO (4 μM).

Table 1. Photophysical data of (a) Cy-5a and (b) Cy-5b in various solvents.[c]

(a)

Solvent	Dielectric constant (ϵ) of Solvent	Refractive Index (η) of Solvent	λ_{max} (nm)	λ_{em} (nm)	Stokes shift ($\Delta\lambda$)	$\varepsilon \times 10^5$ ($M^{-1} cm^{-1}$)
H_2O	80.1	1.333	644	663	19	1.19
CH_3CN	37.5	1.341	644	669	25	2.67
DMF	36.7	1.4282	649	671	22	1.85
MeOH	32.6	1.326	644	668	24	2.55
$CHCl_3$	4.81	1.443	663	687	24	1.91

(b)

Solvent	Dielectric constant (ϵ) of Solvent	Refractive Index (η) of Solvent	λ_{max} (nm)	λ_{em} (nm)	Stokes shift ($\Delta\lambda$)	$\varepsilon \times 10^5$ ($M^{-1} cm^{-1}$)
H_2O	80.1	1.333	645	663	18	1.29
CH_3CN	37.5	1.341	643	664	21	2.71
DMF	36.7	1.4282	649	669	20	1.97
MeOH	32.6	1.326	644	668	24	2.59
DMSO	46.7	1.479	651	670	19	1.79
$CHCl_3$	4.81	1.443	660	682	22	1.90

[c] λ_{max}: absorption maximum wavelength, λ_{em}: emission maximum wavelength, ε: molar extinction coefficient.

Table 2. Comparison of λ_{ex}, $\lambda_{em}$and fluorescence quantum yields (QYs) of Cy-5a and Cy-5b with other NIR imaging agent.

Compound	λ_{ex} (nm)	λ_{em} (nm)	QY	Solvent
Cy-5a	651	671	0.30	DMSO
Cy-5b	651	671	0.24	DMSO
Zinc phthalocyanine	650	679	0.20	DMSO
Oxazine 1	645	663	0.14	EtOH
Cryptocyanine	710	721	0.01	EtOH
IR-125	785	818	0.13	EtOH

Table 3. Fluorescence lifetimes of (a) Cy-5a and (b) Cy-5b in solvents with different polarities.

(a)

Solvent	Lifetime (τ / ns)	Chi-square χ^2
H_2O	1.003±0.014	1.223
CH_3CN	1.388±0.017	1.124
DMF	1.831±0.252	1.224
MeOH	1.236±0.147	1.232
$CHCl_3$	1.452±0.016	1.058
DMSO	1.948±0.096	1.068
Octanol	2.488±0.052	1.127

(b)

Solvent	Lifetime (τ / ns)	Chi-square χ^2
H_2O	1.211±0.022	1.139
CH_3CN	1.096±0.028	1.154
MeOH	0.988±0.0187	1.022
$CHCl_3$	1. 757±0.025	1.043
DMSO	1.769±0.296	0.965

Determination of lipophilicity of Cy-5a and Cy-5b dyes:

The lipophilicity of Cy-5a and Cy-5b is determined by octanol/PBS partition coefficient measurements using $P_{octanol/PBS}$ = $[C]_{octanol\ layer}$ /$[C]_{PBS\ layer}$.[37,38] Cy-5b with two –$(CH_2)_6$– linkers is found more lipophilic (P = 7.12, log P = +0.85) than Cy-5a with two –$(CH_2)_4$– linkers (P = 2.88, log P = +0.46) (**Figure 23**). Furthermore, it is expected that the higher log P should lower the activation energy for transport of the cationic Cy-5b molecule from membrane-water interface to lipid bilayer, and greater would be the accumulation of the compound on the matrix side of mitochondria. To scrutinize our hypothesis, biological experiments are designed and performed.

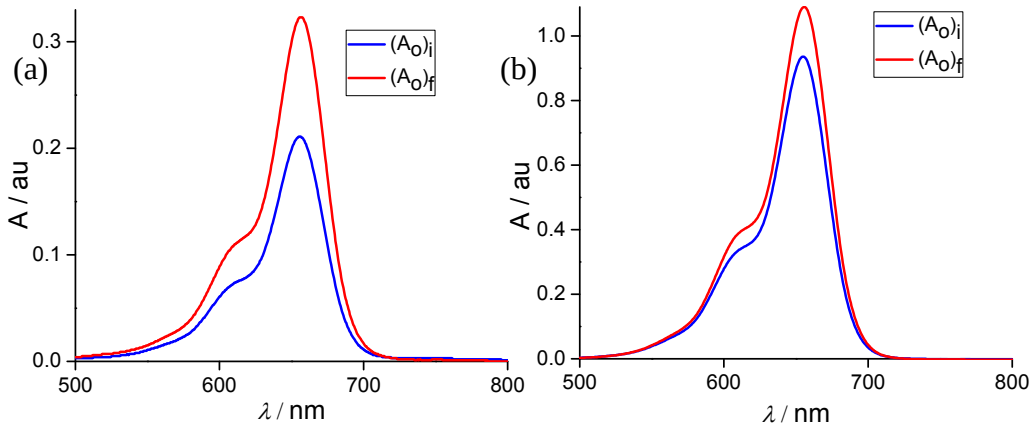

Figure 23. Absorption spectra of (a) Cy-5a and (b) Cy-5b dye in octanol before mixing (red) and after equilibrated with PBS (blue) at 37ºC. Partition coefficient (P) of Cy-5a and Cy-5b dyes are found 2.88 and 7.12, respectively and corresponding log P values are 0.46 and 0.85, respectively.

Stability of Cy-5a and Cy-5b in Physiological pH:

UV/vis experiment shows that Cy-5a and Cy-5b are highly stable in PBS (pH 7.4, 37°C) over 24 h (**Figure 24a,b**). The probable interferences of a

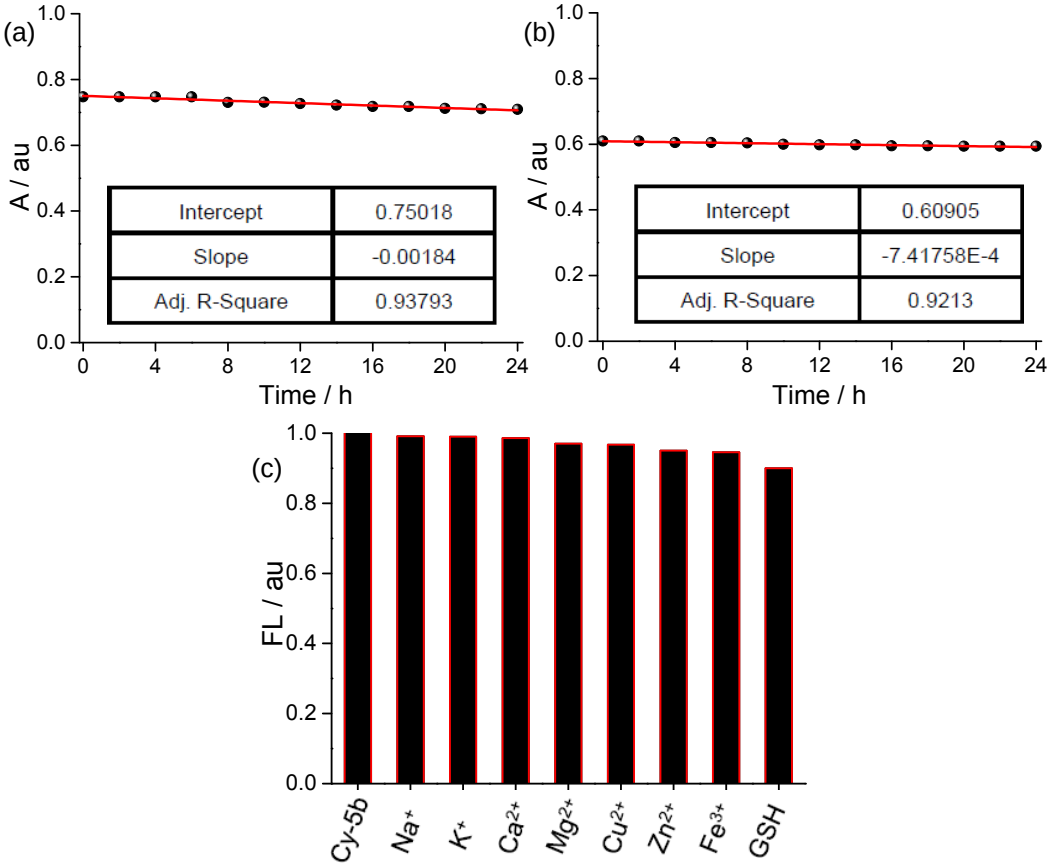

Figure 24. (a) Absorption change of Cy-5a dye in PBS (pH=7.4, 37ºC) at various time intervals. (b) Absorption change of Cy-5b dye in PBS (pH=7.4, 37ºC) at various time intervals. (c) Negligible change in fluorescence response of Cy-5b in the presence of various metal ions (10 mM for Na^+, K^+, and 200 μM for Ca^{2+} , Mg^{2+}, Cu^{2+}, Zn^{2+}, and Fe^{3+}) as chloride salts and bioactive small molecule glutathione (GSH) (5 mM) in PBS (pH=7.4 at 37ºC).

range of biological analytes are examined. The fluorescence experiment of Cy-5b is performed in presence of different crucial metal ions (Na^+, K^+, Ca^{2+}, Mg^{2+}, Cu^{2+}, Zn^{2+}, Fe^{3+} as their chloride salts), and redox substances related with oxidative stress, including glutathione under physiological conditions (PBS, pH 7.4, 37°C) (**Figure 25c**). No obvious changes are observed in the fluorescence spectra of Cy-5b in the presence of biological interferants.

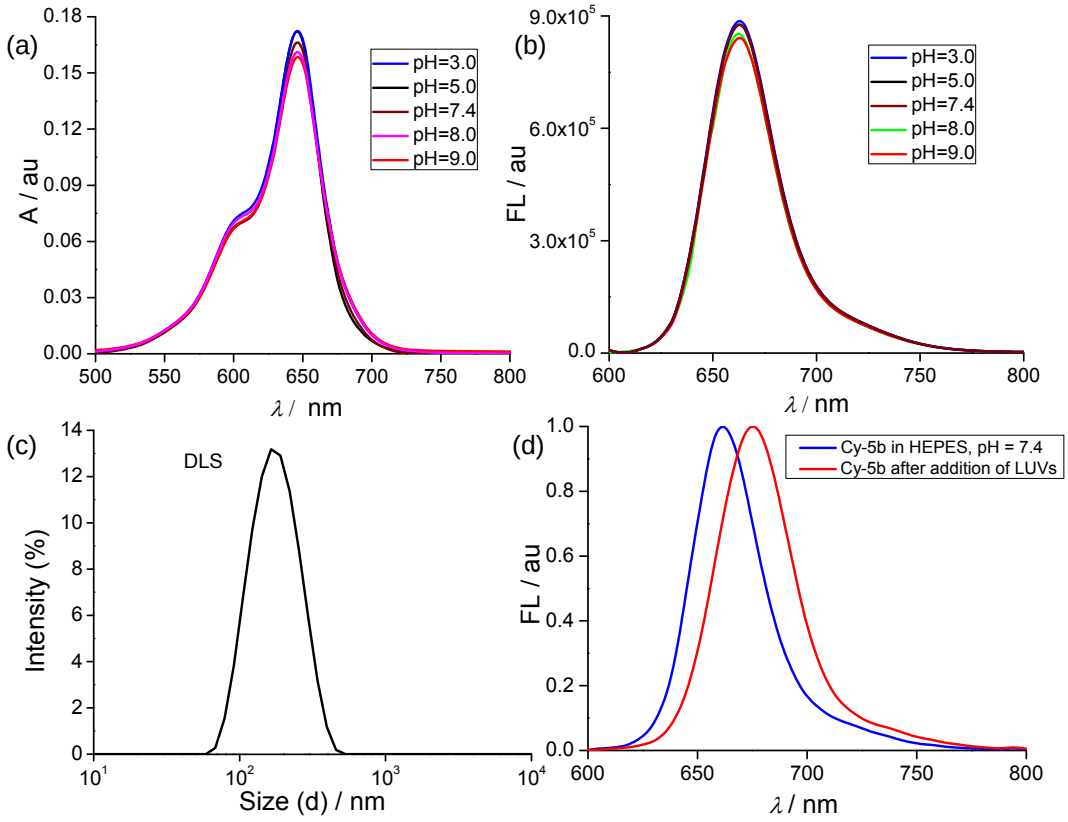

Figure 25. (a) UV/Vis plot of Cy-5a over a wide range of pH (3.0–9.0). (b) Fluorescence emission plots of Cy-5b at various pH (3.0–9.0). (c) Dynamic light scattering (DLS) experiment shows a monodisperse population (PDI = 0.115) with hydrodynamic diameter of 168 nm of the liposome (DOPC:Cholesterol 80:20) in HEPES buffer at pH 7.4. (d) Normalized fluorescence spectra of Cy-5b dye in HEPES buffer at pH 7.4 before (blue) and after (red) addition of LUVs. Bathochromic shift of 14 nm has been observed after addition of LUVs indicates transportation of the Cy-5b dye from water to the lipid membrane.

Moreover, these dyes are stable over a wide range of pH (**Figures 25a,b**). As a proof of concept for transportation of the Cy-5 dye from aqueous buffer to lipid membrane, we prepared large unilamellar vesicles (LUVs) made of 1,2-

dioleoyl-sn-glycero-3-phosphocholine (DOPC):cholesterol (80:20) in HEPES buffer at pH 7.4 using the extrusion technique (hydrodynamic diameter = 168 nm, PDI = 0.115) (**Figure 25c**). λ_{em} of Cy-5b is observed at 661 nm in HEPES buffer at pH 7.4, and when this buffer solution of the dye is added to the LUVs, a 14 nm red shift in λ_{em} is observed which indicates transportation of the dye from buffer to the membrane (**Figure 25d**).

Cellular uptake, localization, and multicolour imaging using confocal laser scanning microscopy:

Cell viability studies using MTT assay shows that the probe Cy-5a and Cy-5b have negligible cytotoxicity against human noncancerous [peripheral blood mononuclear cells (PBMC), human embryonic kidney (HEK293), and lung fibroblast (WI38)] and cancerous [human pancreatic (MIA PaCa-2) and lung (A549)] cell lines at different concentrations over 24 h (**Figure 26**). Flow cytometric titration using Cy-5b at various concentrations for A549 cells indicates cellular uptake and internalization (**Figure 27**). Cellular imaging experiments are carried out using confocal microscopy at 0.7 μM concentration of the Cy-5 dye with short incubation time (10 min) on fixed A549 carcinoma cell line, resulting in bright NIR fluorescence and fast cellular internalization (**Figure 28**). Both Cy-5a and Cy-5b dyes corroborate good photostability and allow prolonged confocal imaging without significant photobleaching. In order to confirm the mitochondrial target specificity, colocalization experiments involving Cy-5a and Cy-5b ($\lambda_{ex}/\lambda_{em}$ 650/675) are performed in fixed A549 carcinoma cell line using a commercially available mitochondrion-tracking probe MitoTracker Red [MTR] ($\lambda_{ex}/\lambda_{em}$ 579/599).[41,42] The fluorescence image produced using more lipophilic Cy-5b (log *P* = 0.85) exhibits high levels of colocalization with that of MTR [Pearson's correlation (PC) coefficient: 0.91 in

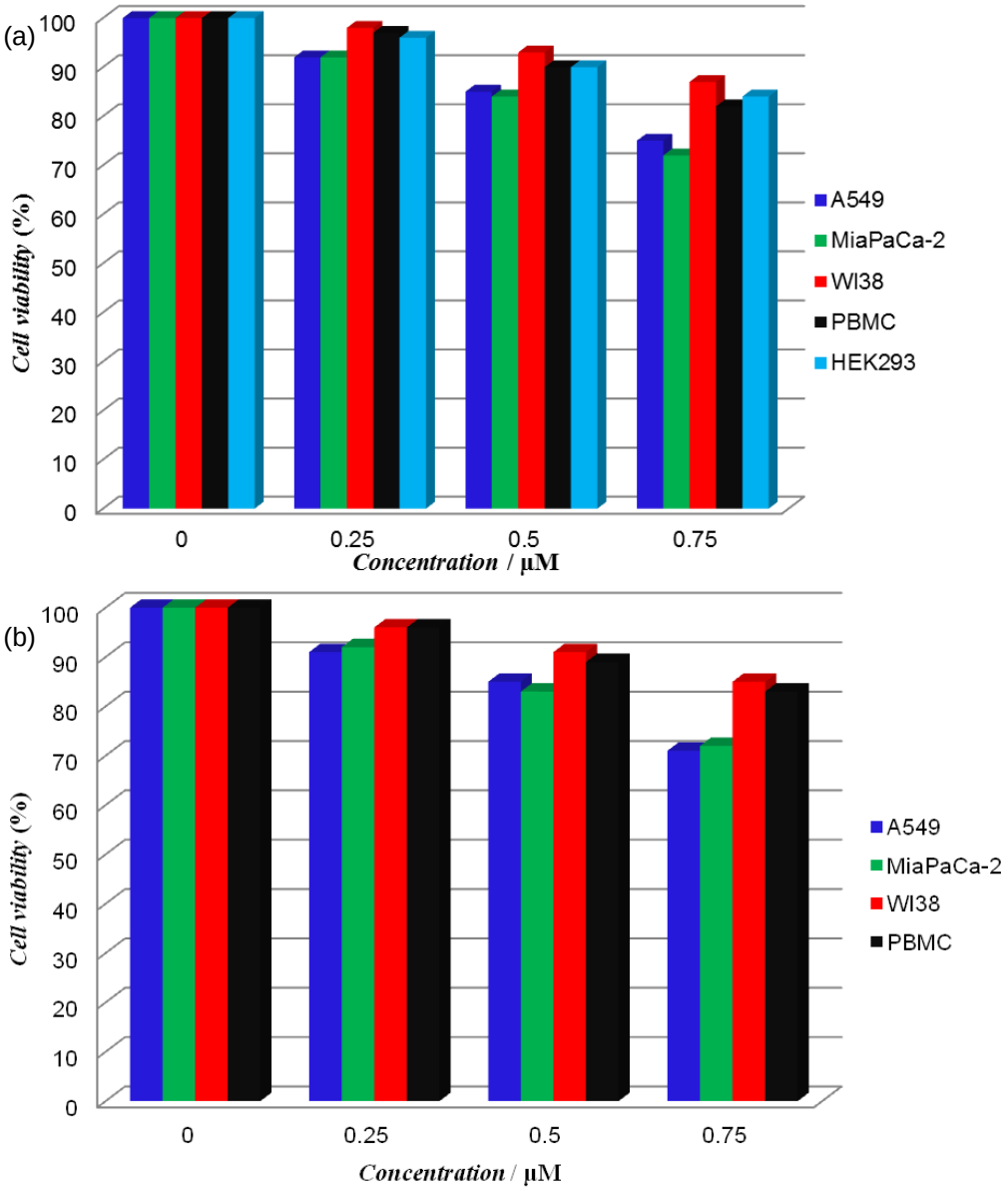

Figure 26. Cell viability studies using MTT assay against human carcinoma cell lines [A549 and MIA PaCa-2] and human noncancerous cell lines [lung fibroblast (WI38) cell, peripheral blood mononuclear cells (PBMC), and human embryonic kidney (HEK293) cell line] over 24 h at various concentrations for (a) Cy-5a dye and (b) Cy-5b dye.

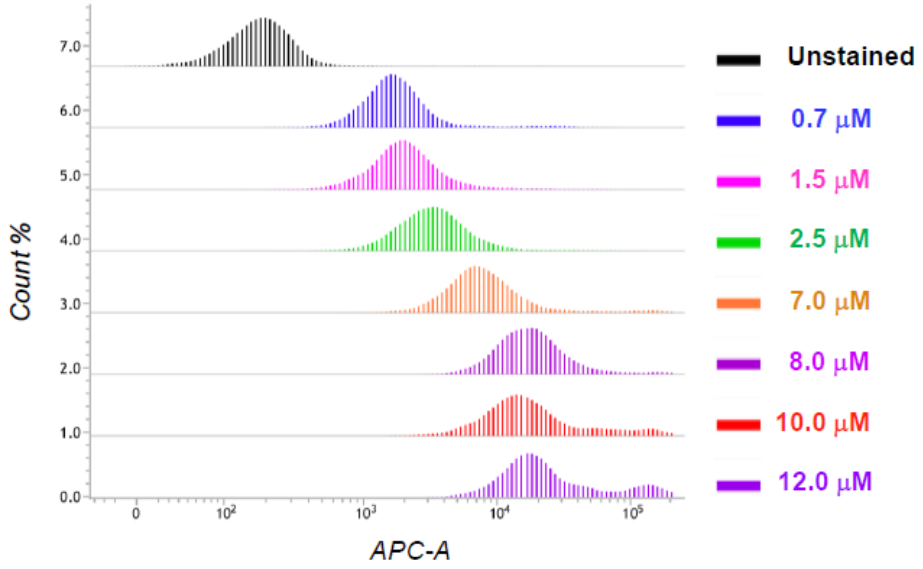

Figure 27. Flow cytometric titration of the Cy-5b dye at various concentrations for 10^4 numbers of A549 cells indicates cellular uptake and internalization.

A549 cells (**Figure 28b**). For Cy-5a (log *P* = +0.46), PC coefficient: 0.86 in A549 cells is found (**Figures 28a**). The observed high PC coefficient established the mitochondrial specificity of the two probes. Cy5a and Cy-5b are compared with a control dye Cy-5c ($\lambda_{ex}/\lambda_{em}$ 650/671 in DMSO, (**Figure 22b**), lacking the mitochondriatargeting TPP^+ moiety and exhibit weaker and nonselective staining in confocal microscopy (PC coefficient: 0.56 in A549 cells) (**Figure 29a**). In order to confirm the mitochondrial selectivity of Cy-5a and Cy-5b over lysosome, colocalization experiments are performed using a commercially available green-fluorescent lysosome-tracking probe, LysoTracker Green DND-26 ($\lambda_{ex}/\lambda_{em}$ 504/511), which exhibits poorer overlap in confocal microscopy (PC coefficient: 0.25 and 0.24 in A549 cells for Cy-5a and Cy-5b, respectively) (**Figures 29b-d**). This suggests that tethering to target-specific lipophilic TPP^+ cation with NIR Cy-5 chromophore is an efficient strategy for selective mitochondrial targeting and staining.

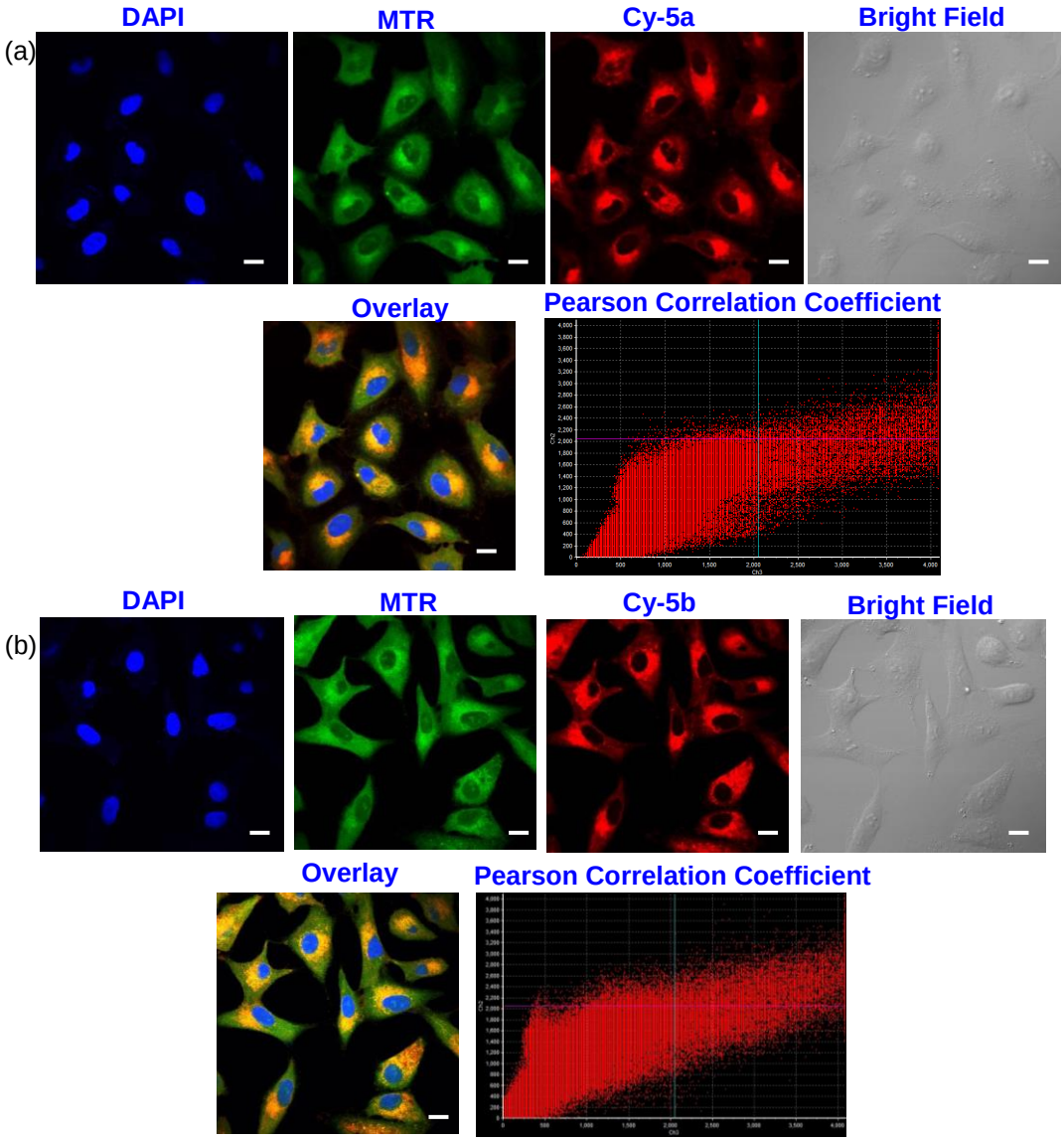

Figure 28. Confocal microscopic images of (a) Cy-5a and (b) Cy-5b colocalized with MitoTracker Red (MTR) in fixed A549 carcinoma cells (scale bar = 10 μM). DAPI, MTR, and Cy-5 dyes are recorded using laser excitation wavelengths at 405 nm, 561 nm, and 635 nm, respectively. Colocalization scatter plots of the overlay pictures show PCC = 0.86 for Cy-5a; and PCC = 0.91 for Cy-5b.

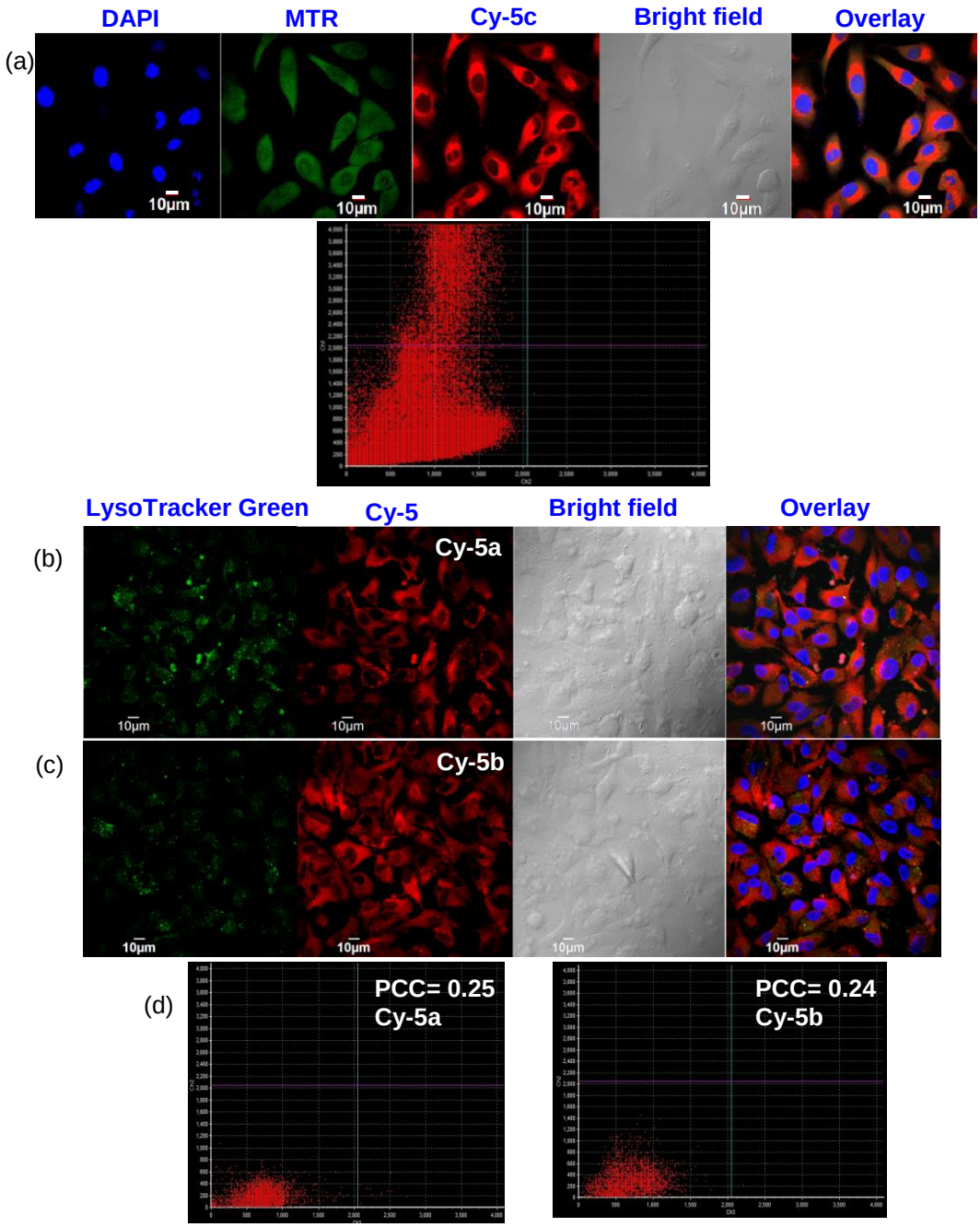

Figure 29. (a) Confocal microscopic images of Cy-5c colocalized with MitoTracker Red (MTR) in fixed A549 carcinoma cells. Confocal microscopic images of (b) Cy-5a and (c) Cy-5b colocalized with Lysotracker Green DND-26 (LTG) in fixed A549 carcinoma cells. (d) Colocalization scatter plots.

The TPP^+ containing Cy-5 dyes can target mitochondria of both normal cells and cancer cells. The flow cytometric experiment demonstrates that the Cy-5b dye penetrates the human lung cancer cells, A549, as well as the noncancerous WI38 cells (**Figure 30**). However, a 2-fold enhancement in the fluorescence intensity of Cy-5b is found inside the A549 cancer cells compared to WI38 noncancerous cells (**Figure 30**). Flow cytometric analysis corroborates our hypothesis that the dye is more attracted and accumulated in the mitochondria of cancer cells compared to normal healthy cells due to higher potential gradient of the former.[20]

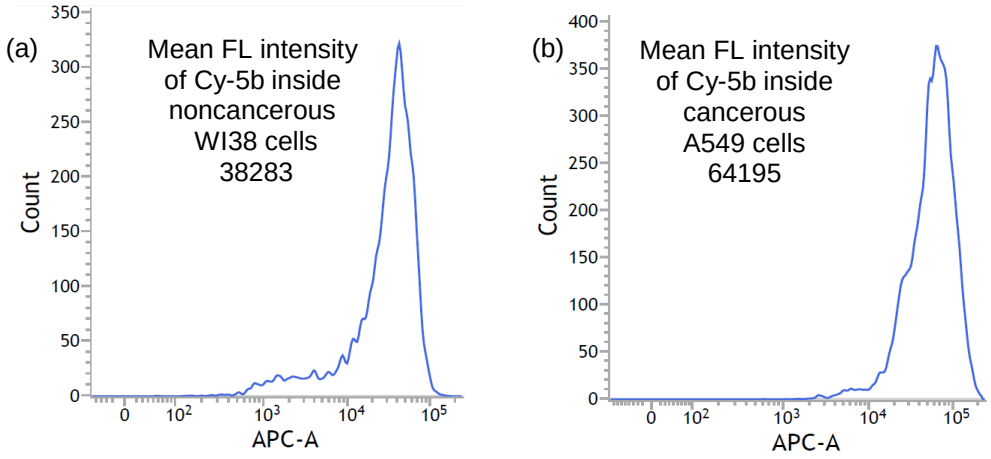

Statistics

Name	% Parent	APC-A Median
A549	97.95	64195
W138	95.19	38238

Figure 30. Flow cytometric analysis shows that Cy-5b dye penetrates inside the (a) noncancerous lung fibroblast WI38 cells and (b) lung cancer cells A549. The mean fluorescence intensity of the Cy-5b dye inside the WI38 and A549 cells are found 38283 and 64195, respectively. A 2-fold increase in the fluorescence intensity is observed in cancer cells compared to the normal fibroblast cells at same incubation time and same concentration of the dye.

Multicolor imaging and tracking of cellular organelles in the same cell remains challenging because of the lack of suitable target-specific fluorescent probes with well-separated excitation and emission bands. Narrow NIR absorption and emission bands of mitochondria-targeting Cy-5 prompted us for the multicolor imaging of cellular organelles using a combination of suitable targeting dyes with distinct excitation and emission.[29-34] Three-color fluorescence A549 cell staining highlighting the plasma membrane (green color), nucleus (blue color), and mitochondria (red color) is achieved by using lipophilic green emitting styryl dye, FM 1-43FX to selectively stain the plasma membrane, blue-fluorescent DAPI to label the nucleus, and Cy-5b to selectively target and stain the mitochondria of A549 cells (**Figure 31**).

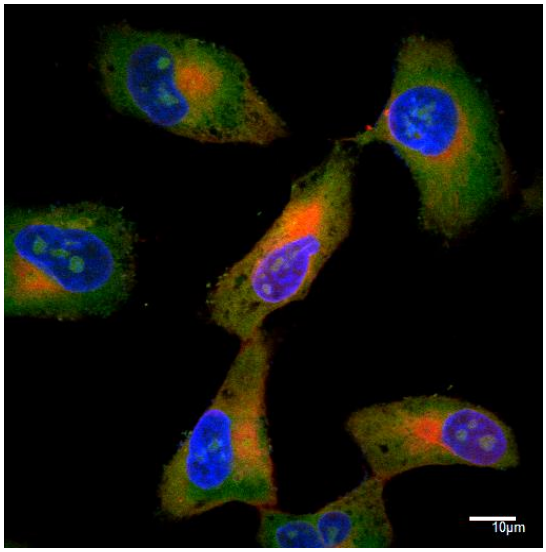

Figure 31. Multicolor confocal microscopic image of A549 cell labeled with lipophilic green emitting FM 1-43FX (laser ex/em 488/590 nm) to stain the plasma membrane (green color), blue-fluorescent DAPI (laser ex/em 405/461 nm) to target nucleus (blue color), and NIR Cy-5b (laser ex/em 635/668 nm) to selectively stain mitochondria (red color). This multicolor imaging of cellular organelles in the same cell is acquired using appropriate filter sets in confocal microscopy.

Determination of mitochondrial potential:

The tricationic Cy-5b is expected to depolarize mitochondrial membrane potential after internalization. To decipher our hypothesis of mitochondrial targeting and depolarization by tricationic Cy-5b dye, mitochondrial membrane potential changes are examined using a JC-1 dye.[44,45] A considerable depolarization in the mitochondrial membrane potential in A549 cells is observed after treatment with Cy-5b. At 0.5 μM and 0.7 μM concentration of Cy-5b the percentage of cells with depolarized mitochondria increases to 21.7% and 26.2%, respectively (**Figure 33**).

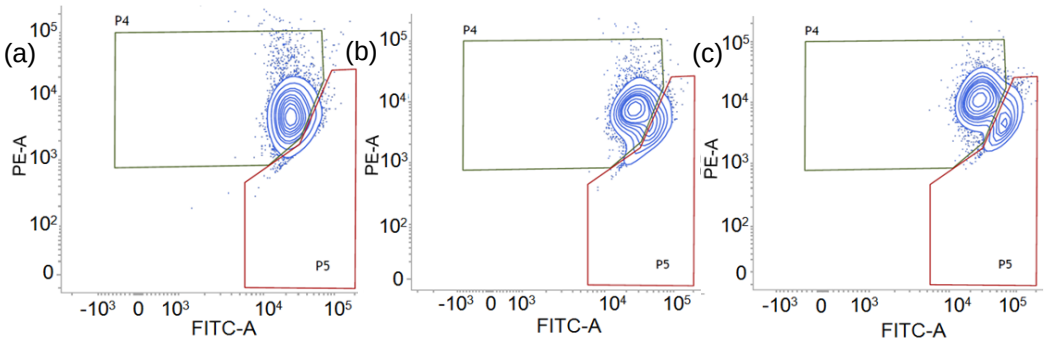

Statistics

Name	% Parent
Cy-5b:P4	71.67
Cy5b:P5	26.16

Figure 32. Determination of mitochondrial membrane potential depolarization in A549 cancer cells using JC-1 dye. After cellular staining with JC-1 dye (1 mg mL^{-1}), the fluorescent signal is analysed in the FITC and PE channels using a 494 nm laser. (a) JC-1 staining of control A549 cells without Cy-5 dye. (b,c) JC-1 staining of A549 cells after incubation with Cy-5b at 0.5 μM and 0.7 μM concentration, respectively. The percentage of cells with depolarized mitochondria increases from 6.63% (control) to 21.7% (0.5 μM Cy-5b) to 26.2% (0.7 μM Cy-5b).

Conclusions:

In summary, we report some unique design concepts for the development of NIR Cy-5 molecules that have the ability to selectively target and stain mitochondria. Submicromolar concentration of the targeting dye is enough to localize and stain mitochondria within minutes. Narrow absorption and emission bands permit the acquisition in multicolor imaging application of the cells. Moreover, these symmetrical NIR cyanine dyes are also useful for determination of mitochondrial membrane potential via monitoring the mitochondrial membrane depolarization process.

References:

[1] Kaloyanova, S.; Zagranyarski, Y.; Ritz, S.; Hanulova, M.;´ Koynov, K.; Vonderheit, A.; Müllen, K.; and Peneva, K. *J. Am. Chem. Soc.* **2016**, *138*, 2881−2884.

[2] Jung, H. S.; Lee, J.-H.; Kim, K.; Koo, S.; Verwilst, P.; Sessler, J. L.; Kang, C.; and Kim, J. S. *J. Am. Chem. Soc.* **2017**, *139*, 9972−9978.

[3] Lee, M. H.; Park, N.; Yi, C.; Han, J. H.; Hong, J. H.; Kim, K. P.; Kang, D. H.; Sessler, J. L.; Kang, C.; and Kim, J. S. *J. Am. Chem. Soc.* **2014**, *136*, 14136−14142.

[4] Leung, C. W. T.; Hong, Y.; Chen, S.; Zhao, E.; Lam, J. W. Y.; and Tang, B. Z. *J. Am. Chem. Soc.* **2013**, *135*, 62−65.

[5] Zielonka, J.; Joseph, J.; Sikora, A.; Hardy, M.; Ouari, O.; Vasquez-Vivar, J.; Cheng, G.; Lopez, M.; and Kalyanaraman, B. *Chem. Rev.* **2017**, *117*, 10043−10120.

[6] Biswas, S.; and Torchilin, V. P. *Adv. Drug Delivery Rev.* **2014**, *66*, 26−41.

[7] Hoye, A. T.; Davoren, J. E.; Wipf, P.; Fink, M. P.; and Kagan, V. E. *Acc. Chem. Res.* **2008**, *41*, 87−97.

[8] Zhu, H.; Fan, J.; Du, J.; and Peng, X. *Acc. Chem. Res.* **2016**, *49*, 2115−2126.

[9] Thomas, A. P.; Palanikumar, L.; Jeena, M. T.; Kim, K.; and Ryu, J.-H. *Chem. Sci.* **2017**, *8*, 8351−8356.

[10] Fulda, S.; Galluzzi, L.; and Kroemer, G. *Nat. Rev. Drug Discovery* **2010**, *9*, 447−464.

[11] Weinberg, S. E.; and Chandel, N. S. *Nat. Chem. Biol.* **2015**, *11*, 9−15.

[12] Pan, G.-Y.; Jia, H.-R.; Zhu, Y.-X.; Wang, R.- H.; Wu, F.-G.; and Chen, Z. *ACS Biomater. Sci. Eng.* **2017**, *3*, 3596−3606.

[13] Pan, G.-Y.; Jia, H.-R.; Zhu, Y.-X.; Sun, W.; Cheng, X.-T.; and Wu, F.-G. *ACS Appl. Nano Mater.* **2018**, *1*, 2885−2897.

[14] Joza, N.; Susin, S. A.; Daugas, E.; Stanford, W. L.; Cho, S. K.; Li, C. Y. J.; Sasaki, T.; Elia, A. J.; Cheng, H.-Y. M.; Ravagnan, L.; Ferri, K. F.; Zamzami, N.; Wakeham, A.; Hakem, R.; Yoshida, H.; Kong, Y.- Y.; Mak, T. W.; Zuń̃iga-Pflücker, J. C.; Kroemer, G.; and Penninger, J. M. *Nature* **2001**, *410*, 549−554.

[15] Danial, N. N.; and Korsmeyer, S. J. Cell Death. Cell 2004, 116, 205−219.

[16] Cory, S.; and Adams, J. M. *Nat. Rev. Cancer* **2002**, *2*, 647−656.

[17] Galluzzi, L.; Blomgren, K.; and Kroemer, G. *Nat. Rev. Neurosci.* **2009**, *10*, 481−494.

[18] Huang, Y.; Zhou, Q.; Feng, Y.; Zhang, W.; Fang, G.; Fang, M.; Chen, M.; Xu, C.; and Meng, X. *Chem. Commun.* **2018**, *54*, 10495−10498.

[19] Davis, S.; Weiss, M. J.; Wong, J. R.; Lampidis, T. J.; and Chen, L. B. *J. Biol. Chem.* **1985**, *260*, 13844−13850.

[20] Chen, L. B. *Annu. Rev. Cell Biol.* **1988**, *4*, 155−181.

[21] Hyun, H.; Park, M. H.; Owens, E. A.; Wada, H.; Henary, M.; Handgraaf, H. J. M.; Vahrmeijer, A. L.; Frangioni, J. V.; and Choi, H. S. *Nat. Med.* **2015**, *21*, 192−197.

[22] Choi, H. S.; Gibbs, S. L.; Lee, J. H.; Kim, S. H.; Ashitate, Y.; Liu, F.; Hyun, H.; Park, G.; Xie, Y.; Bae, S.; Henary, M.; and Frangioni, J. V. *Nat. Biotechnol.* **2013**, *31*, 148−153.

[23] Baumes, J. M.; Gassensmith, J. J.; Giblin, J.; Lee, J.-J.; White, A. G.; Culligan, W. J.; Leevy, W. M.; Kuno, M.; and Smith, B. D. *Nat. Chem.* **2010**, *2*, 1025−1030.

[24] Miao, Q.; Yeo, D. C.; Wiraja, C.; Zhang, J.; Ning, X.; Xu, C.; and Pu, K. *Angew. Chem., Int. Ed.* **2018**, *57*, 1256−1260.

[25] Li, X.; Gao, X.; Shi, W.; and Ma, H. *Chem. Rev.* **2014**, *114*, 590− 659.

[26] Hyun, H.; Owens, E. A.; Wada, H.; Levitz, A.; Park, G.; Park, M. H.; Frangioni, J. V.; Henary, M.; Choi, H. S. *Angew. Chem., Int. Ed.* **2015**, *54*, 8648−8652.

[27] Wang, C.; Wang, G.; Li, X.; Wang, K.; Fan, J.; Jiang, K.; Guo, Y.; and Zhang, H. *Anal. Chem.* **2017**, *89*, 11514−11519.

[28] Pisoni, D. S.; Todeschini, L.; Borges, A. C. A.; Petzhold, C. L.; Rodembusch, F. S.; and Campo, L. F. *J. Org. Chem.* **2014**, *79*, 5511−5520.

[29] Lukinavicius, G.; Reymond, L.; Umezawa, K.; Sallin, O.;ˇ D'Este, E.; Gottfert, F.; Ta, H.; Hell, S. W.; Urano, Y.; Johnsson, K. Fluorogenic Probes for Multicolor Imaging in Living Cells. J. Am. Chem. Soc. 2016, 138, 9365−9368.

[30] Johnson, J. R.; Fu, N.; Arunkumar, E.; Leevy, W. M.; Gammon, S. T.; Piwnica-Worms, D.; and Smith, B. D. *Angew. Chem., Int. Ed.* **2007**, *46*, 5528−5531.

[31] Collot, M.; Fam, T. K.; Ashokkumar, P.; Faklaris, O.; Galli, T.; Danglot, L.; and Klymchenko, A. S. *J. Am. Chem. Soc.* **2018**, *140*, 5401−5411.

[32] Chen, X.; Zhang, X.; Wang, H.-Y.; Chen, Z.; and Wu, F.-G. *Langmuir* **2016**, *32*, 10126−10135.

[33] Wang, H.-Y.; Hua, X.-W.; Jia, H.-R.; Li, C.; Lin, F.; Chen, Z.; and Wu, F.-G. *ACS Biomater. Sci. Eng.* **2016**, *2*, 987−997.

[34] Jia, H.- R.; Wang, H.-Y.; Yu, Z.-W.; Chen, Z.; and Wu, F.-G. *Bioconjugate Chem.* **2016**, *27*, 782−789.

[35] Modica-Napolitano, J. S.; and Aprille, J. R. *Adv. Drug Delivery Rev.* **2001**, *49*, 63−70.

[36] Hickey, J. L.; Ruhayel, R. A.; Barnard, P. J.; Baker, M. V.; Berners-Price, S. J.; and Filipovska, A. *J. Am. Chem. Soc.* **2008**, *130*, 12570−12571.

[37] Ross, M. F.; Da Ros, T.; Blaikie, F. H.; Prime, T. A.; Porteous, C. M.; Severina, I. I.; Skulachev, V. P.; Kjaergaard, H. G.; Smith, R. A. J.; and Murphy, M. P. *Biochem. J.* **2006**, *400*, 199−208.

[38] Leo, A.; Hansch, C.; and Elkins, D. *Chem. Rev.* **1971**, *71*, 525−616.

[43] Zhang, Q. M.; Wang, W.; Su, Y.-Q.; Hensen, E. J. M.; and Serpe, M. J. *Chem. Mater.* **2016**, *28*, 259−265.

[44] Brouwer, A. M. *Pure Appl. Chem.* **2011**, *83*, 2213−2228.

[39] Kawazoe, Y.; Shimogawa, H.; Sato, A.; and Uesugi, M. *Angew. Chem., Int. Ed.* **2011**, *50*, 5478−5481.

[40] Kubi, G. A.; Qian, Z.; Amiar, S.; Sahni, A.; Stahelin, R. V.; and Pei, D. *Angew. Chem., Int. Ed.* **2018**, *57*, 17183−17188.

[41] Salvioli, S.; Ardizzoni, A.; Franceschi, C.; and Cossarizza, A. *FEBS Lett.* **1997**, *411*, 77−82.

[42] Liu, T.; Roh, S. E.; Woo, J. A.; Ryu, H.; and Kang, D. E. *Cell Death Dis.* **2013**, *4*, No. e476.

[45] Yang, S.-H.; Liu, R.; Perez, E. J.; Wen, Y.; Stevens, S. M., Jr.; Brun-Zinkernagel, A.-M.; Prokai, L.; Will, Y.; Dykens, J.; Koulen, P.; Simpkins, J. W.; and Simpkins, J. W. *Proc. Natl. Acad. Sci. U.S.A.* **2004**, *101*, 4130− 4135.

Chapter 4

Amyloid-β Peptide Fragment Conjugated Unsymmetrical NIR Chromophore for Selective Targeting, Imaging, and Dysfunction of Mitochondria

Introduction

Self-assembled peptides play an important role in the development of therapeutics and diagnostics.[1–3] Local concentration of the self-assembling peptide inside a definite cellular organelle can be augmented by transporting them with an organelle-specific targeting group.[4–6] The Design of organelle selective self-assembling peptide tethered with a near-infrared (NIR) chromophore to monitor their interaction with cellular organelles and to regulate cellular function and fate is an emerging field of current research.[7–9] NIR fluorescent dyes (650–900 nm) are imperative in comparison with visible fluorescent dyes.[10–12] NIR light has strong tissue penetration and offers an important bioimaging methodology with minimum autofluorescence background and less photodamaging. However, it is tricky to work in an intracellular location due to the complexity in biological environment. Development of an effective synthetic procedure for the labelling of amyloid-β (Aβ) peptide fragment with NIR fluorescent dye anchoring with organelle targeting moiety is in great demand.[13–15] Amyloid fibrils composed of a cross-β-sheet structure are the characteristic of a range of diseases including Alzheimer's disease.[16–18] Amongst the various cellular organelles, mitochondria are an important target.[19–23] Mitochondrial targeting, imaging, and its dysfunction are the key steps for the design of drug molecules.[19–23] We particularly selected the core recognition motif of Aβ, the Lys-Leu-Val-Phe-Phe (KLVFF, parts of A$\beta_{16\text{-}20}$) pentapeptide, because it self-assemble to form β-sheet structure.[24,25] The KLVFF peptide conjugated with an unsymmetrical NIR cyanine (Cy-5) chromophore containing mitochondria selective lipophilic cationic triphenylphosphonium (TPP^+) targeting moiety is synthesized by a microwave (MW) assisted Fmoc solid phase peptide synthesis (SPPS) protocol

on 2-chlorotrityl chloride (2-CTC) resin.[26–29] The synthesized KLVFF/Cy-5 conjugate is used for the selective targeting and staining of mitochondria in epithelioid cervix carcinoma HeLa cells and lung carcinoma A549 cells, which is monitored through confocal microscopy and compared with a control molecule KLVFF/Cy-5c lacking the TPP^+ functionality. Selective mitochondria targeting and its dysfunction initiates programmed cell death such as apoptosis.[30,31] We hypothesized that the supramolecular β-sheet motif containing KLVFF/Cy-5 can be attracted and accumulated preferentially within the negatively charged mitochondrial matrix [Inner mitochondrial membrane potential, $(\Delta\Psi_m)_{cancer}$ ~ –220 mV] and reached the critical aggregation concentration (CAC) to form amyloid fibrils inside the malignant mitochondria of and cause cell death.[32,33]

Experimental Methods

General Methods and Materials

Synthesis, Purification, and Characterization of Unsymmetrical Cyanine Dyes Cy-5 and Cy-5c:

Unsymmetrical Cy dyes and their precursor molecules were synthesized by an efficient way using microwave (MW) assisted protocol with reasonable overall yield from easily available inexpensive starting materials. Analytical thin layer chromatography (TLC) was performed on silica gel coated aluminium sheets (TLC silica gel 60 F_{254}) with suitable solvent system and detected by naked eye or UV lamp. The compounds were purified via column chromatography using silica gel 100-200 mesh. The solvents for column chromatography were distilled prior to their use.

Malonaldehyde bis(phenylimine) monohydrochloride and (6-Bromohexyl)triphenylphosphonium bromide were synthesized following our previously discussed procedures in Chapters 3 and 4.[34] The three-carbon spacer precursor malonaldehyde bis(phenylimine) monohydrochloride for the synthesis of activated intermediate (plenylamino buta-1,3-dienyl indolium salt) of Cy-5 is prepared by the condensation reaction between the commercially available 1,1,3,3-tetramethoxypropane and aniline, under acidic condition.[34] Syntheses of NIR unsymmetrical cyanine dyes, KLVFF/Cy-5, KLVFF/Cy-5c conjugate, and their precursors were illustrated in **Scheme 1** and **2**. All the compounds were characterised by 1D (^{1}H, ^{13}C and ^{31}P) and 2D (^{1}H-^{1}H DQF-COSY) NMR spectroscopy, as well as high resolution ESI-MS.

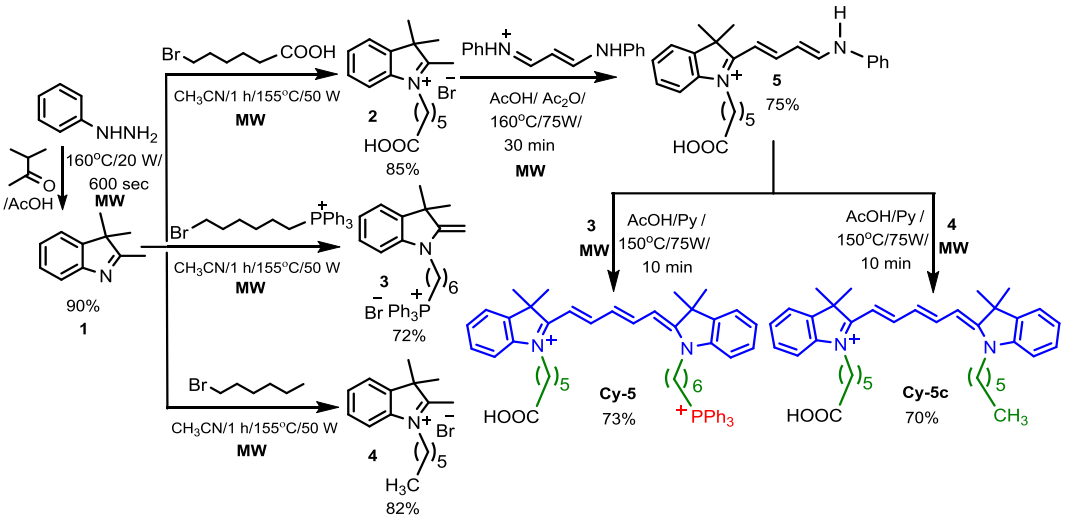

Scheme 1. Synthesis of unsymmetrical NIR Cy-5 and Cy-5c and their related precursor molecules using MW conditions.

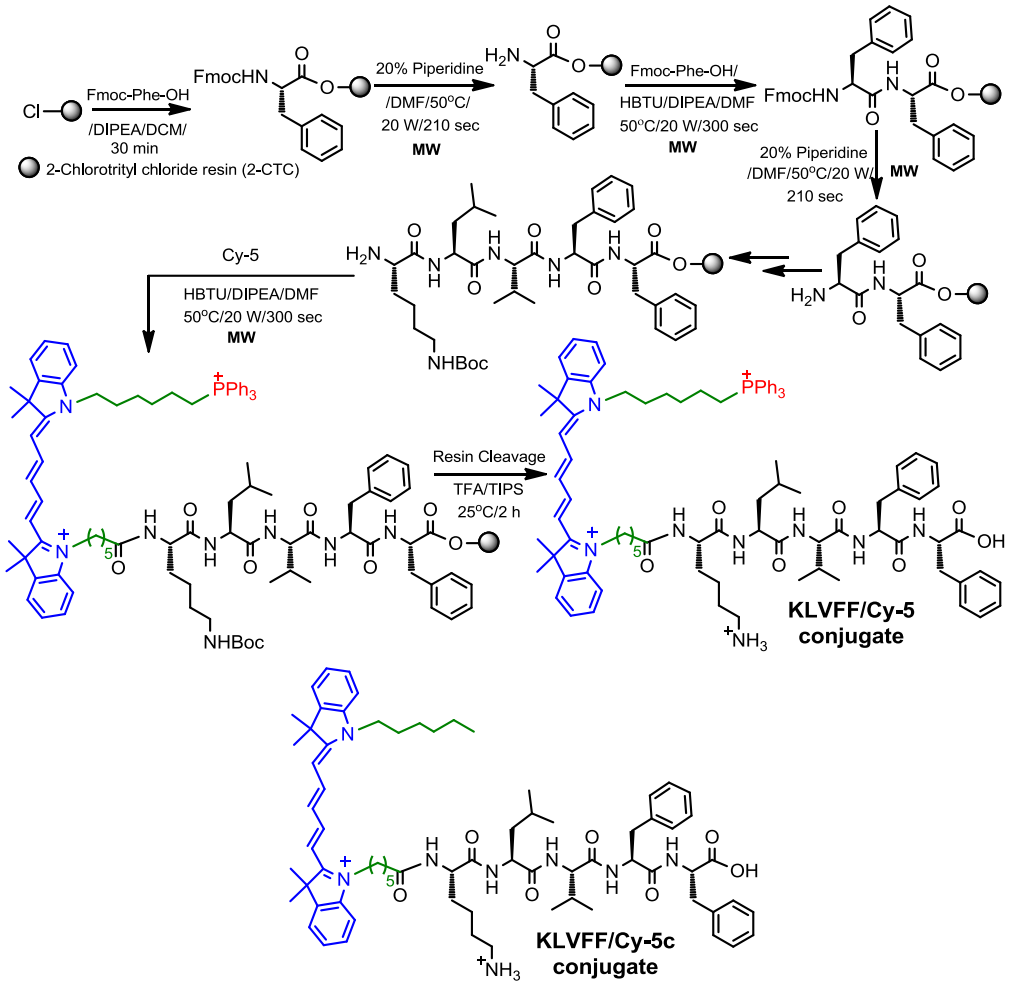

Scheme 2. Synthesis of KLVFF/Cy-5 conjugate and a control KLVFF/Cy-5c molecule (lacking TPP^+ functionality) using MW assisted Fmoc SPPS protocol on 2-CTC resin.

Synthesis of 2,3,3-Trimethylindolenine: The heterocyclic 2,3,3-trimethylindolenine ring is constructed by the Fischer indole synthesis from phenylhydrazine hydrochloride (2.46 g, 17 mmol) and 3-methyl-2-butanone (5 mL, 46.8 mmol) in glacial AcOH (30 mL) in a MW vessel equipped with a magnetic stir bar. The reaction mixture was sealed with a cap and subjected to

MW irradiation at 160ºC for 10 m. The solvent was removed under reduced pressure and the residue was extracted with Et_2O and water and the aqueous phase was washed again with petroleum ether (2 × 30 mL). The combined organic layer were washed with brine (2 × 30 mL), dried over anhydrous Na_2SO_4, filtered, and concentrated under reduced pressure to obtain 2,3,3-trimethylindolenine [R_f = 0.5, Hexane:EtOAc (2:1)] as a brown orange liquid.

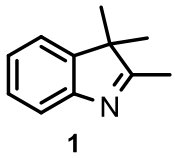

1

Yield: 3.68 g (91%)

^{1}H NMR (400 MHz, $CDCl_3$, 25°C): δ = 7.53 (1H, d, J = 7.7 Hz), 7.32–7.24 (2H, m), 7.22–7.14 (1H, m), 2.27 (3H, s), 1.29 (6H, s) ppm.

13C NMR (100 MHz, $CDCl_3$, 25°C): δ = 188.1, 153.8, 145.8, 127.7, 125.2, 121.4, 120.0, 53.7, 23.2, and 15.5 ppm. HRMS (ESI +ve) m/z: Observed for $C_{11}H_{13}N$ $[M]^+$ = 159.1039 $[M]^+_{calcd}$ = 159.1048.

Synthesis of Quaternary Heterocyclic Indolium Salt:

The synthesis of quaternary heterocyclic indolium salt is generally carried out with an excess of alkylating agent with and without solvent over several hours or days.[34,35] The flexibility in synthetic routes allowed us to covalently conjugate N of 2,3,3-trimethyl indolenine with alkyl chain, triphenylphosphonium (–PPh_3^+), and carboxylic (–COOH) functionality with suitable alkylating agents such as (6-bromohexyl)triphenylphosphonium bromide and 6-bromohexanoic acid using MW conditions.[36] The influence of temperature and time are scrutinized on the yield of the reaction, maintaining the indolenine/alkylating agent mole ratio constant (**Table 1**). MW heating at 155°C for 60 m gave the best result. Compared to the conventional heating process, MW assisted quaternization method afforded the desired products 2 and 3 in higher yields, radically shortening reaction times from day(s) to 60 m.

This method works well with a variety of alkylating agents including the sensitive functional groups like –COOH and $-PPh_3^+$.

Table 1. Synthesis of quaternary heterocyclic indolium salt under conventional and microwave conditions.

Compound	Temperature (ºC)	Time (min)	Method	Yield (%)
2	85	4320	A	65
2	155	10	B	35
2	155	20	B	58
2	155	30	B	70
2	155	60	B	85
3	85	4320	A	43
3	155	60	B	72
4	85	432	A	53
4	155	60	B	82

A: Conventional method ACN/reflux, 72h.

B: Microwave method in ACN.

(1-(5-Carboxypentyl)-2,3,3-trimthyl-3H-indolium bromide (2): 2,3,3-Trimethylindolenine (0.318 g, 2.0 mmol) and 6-bromohexanoic acid (1.17 g, 6.0 mmol) were taken in a MW vessel and dissolved in 4 mL CH_3CN. The reaction mixture was sealed with a cap and heated in MW system at 155ºC for 60 m. The reaction mixture was allowed to cool to room temperature and the solvent was evaporated under reduced pressure. The residue was washed

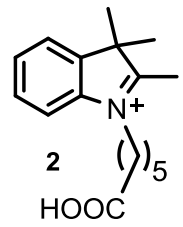

with EtOAc and cold Et_2O several times to get a grey solid. The crude product was purified by column chromatography [R_f = 0.28, DCM:MeOH (4:1)] to obtain the desired compound 2 as a grey solid.

Yield: 0.60 g (85%)

^{1}H NMR (300 MHz, DMSO-d_6, 25°C): δ = 8.02–7.99 (1H, m), 7.88–7.84 (1H, m), 7.65–7.59 (2H, m), 4.47 (2H, t, J = 7.5 Hz), 2.87 (3H, s), 2.23 (2H, t, J = 7.2 Hz), 1.91–1.81 (2H, m), 1.61–1.56 (2H, m), 1.55 (6H, s), 1.54–1.35 (2H, m) ppm. ^{13}C NMR (75 MHz, DMSO-d_6, 25°C): δ = 196.9, 174.8, 142.3, 141.5, 129.8, 129.4, 124.0, 116.0, 54.6, 48.0, 33.8, 27.4, 25.8, 24.1, 22.5, and 14.3 ppm. HRMS (ESI +ve) m/z: Observed for $C_{17}H_{24}NO_2$ $[M]^+$ =274.1829 $[M]^+_{calcd}$ = 274.1802.

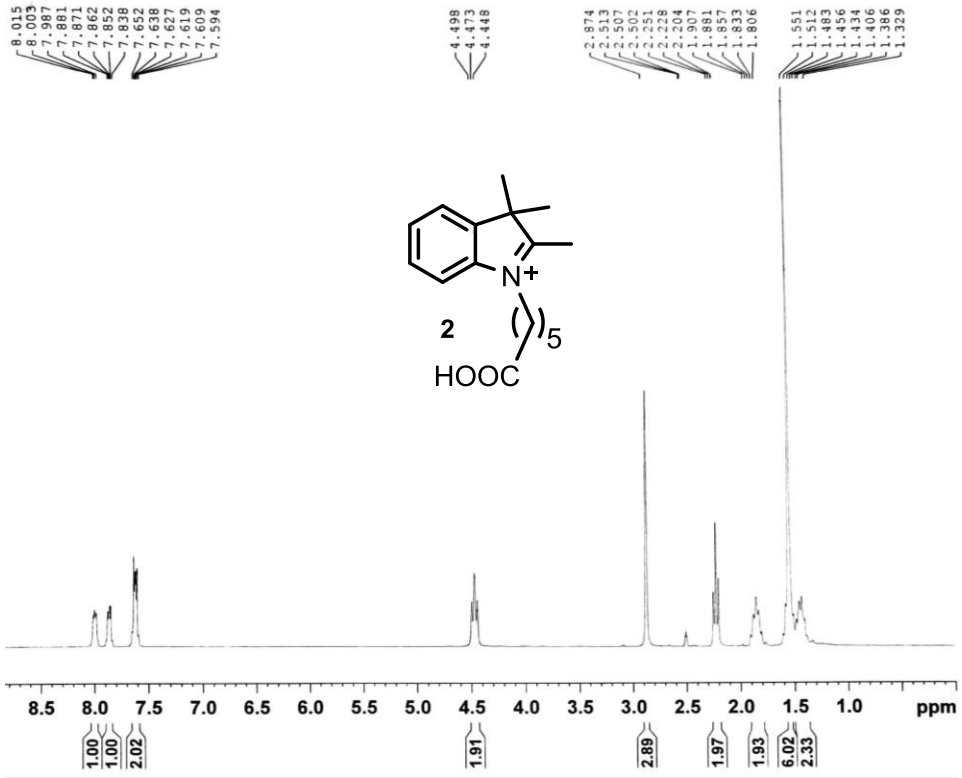

Figure 1. ^{1}H NMR (300 MHz, DMSO-d_6, 25°C) spectrum.

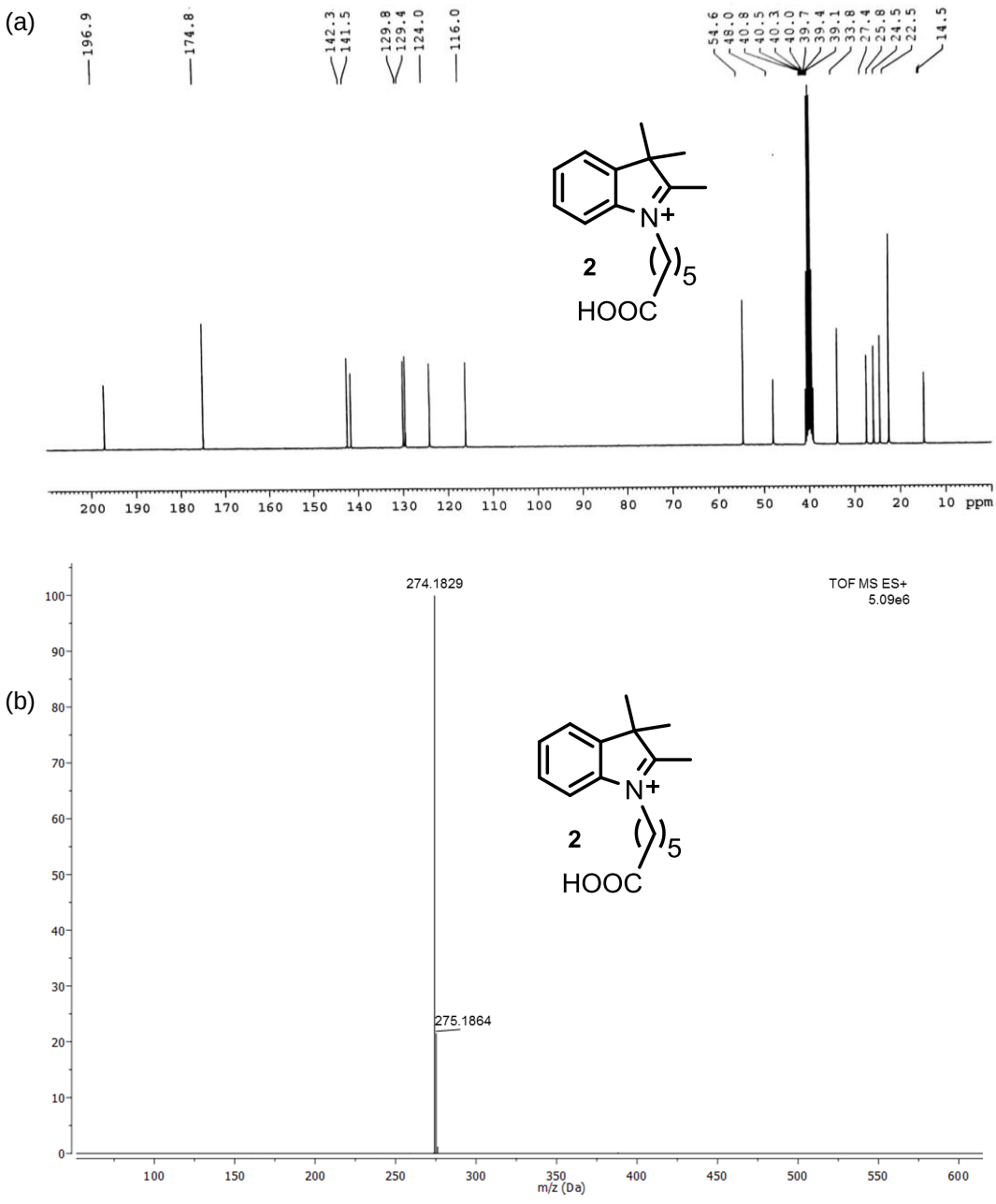

Figure 2. (a) ^{13}C NMR (75 MHz, DMSO-d_6, 25°C) spectrum and (b) HRMS (ESI +ve) spectrum of of compound 2.

(6-(3,3-dimethyl-2-methyleneindolin-1-yl)hexyl)triphenylphosphonium bromide (3): 2,3,3-Trimethylindolenine (0.32 g, 2.0 mmol) and (6-bromohexyl)triphenylphosphonium bromide (3.04 g, 6.0 mmol) were taken in a MW vessel and dissolved in 4 mL CH_3CN. The reaction solution was sealed with a cap and heated in a MW system at 155ºC for 60 m. The reaction mixture was allowed to cool to room temperature. The solvent was removed under reduced pressure to get reddish brown residue. The residue was washed with hexane:$CHCl_3$ (4:1) followed by Et_2O wash (3 × 10 mL) to acquire the desired compound 3 as a reddish brown solid [R_f = 0.40 DCM:MeOH (95:5)].

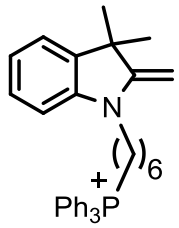

3

Yield: 0.84 g (72%).

^{1}H NMR (400 MHz, $CDCl_3$, 25°C): δ = 7.81–7.67 (15H, m), 7.05 (2H, t, *J* = 8.4 Hz) , 6.69 (1H, t, *J* = 7.2 Hz), 6.49 (1H, d, *J* = 7.2 Hz), 3.77 (2H, br), 3.67–3.60 (2H, m), 3.43 (2H, t, *J* = 6.8 Hz), 1.78–1.64 (6H, m), 1.26 (6H, s) ppm. ^{13}C NMR (101 MHz, $CDCl_3$, 25°C): δ = 161.6, 146.1, 137.5, 135.1, 133.8, 130.6, 127.6, 121.8, 118.6, 118.2, 117.8, 105.3, 73.2, 44.2, 42.1, 30.1, 29.7, 26.7, 25.9, 23.4, 22.9, and 22.4 ppm.

HRMS (ESI +ve) m/z: Observed for $C_{35}H_{39}NP^+$ $[M]^+$ = 504.2821, $[M]^+_{calcd}$ = 504.2820.

1-Hexyl-2,3,3-trimethyl-3H-indol-1-ium bromide (4):

Compound 1 (0.48 g, 3.0 mmol) and 1-bromo hexane (1.49 g, 9.0 mmol) were taken in a MW vessel and dissolved in 6 mL CH_3CN. The reaction mixture sealed with a cap and heated in MW system at 155ºC for 60 m. The reaction mixture was allowed to cool to room temperature. The resulting solution was decanted from the solid and the solvent was removed under reduced pressure to get a reddish brown residue. The residue was washed with Hexane:EtOAc

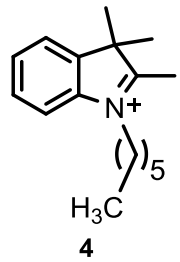

4

mixture (4:1) for several times and followed by Et_2O wash (3 × 10 mL) and dried under vacuum to get the pure compound 4 as a brown solid [R_f = 0.75, DCM:MeOH (97:3)].

Yield: 0.80 g (82%).

^{1}H NMR (400 MHz, $CDCl_3$, 25°C): δ = 7.65–7.50 (4H, m), 4.65 (2H, t, J = 7.7 Hz), 3.11 (3H, s), 1.94–1.89 (2H, m), 1.65 (6H, s), 1.48–1.42 (2H, m), 1.36–1.29 (4H, m), 0.87 (3H, t, J = 7.1 Hz) ppm.^{13}C NMR (100 MHz, $CDCl_3$, 25°C): δ = 195.7, 141.7, 141.0, 130.2, 129.6, 123.5, 115.4, 54.8, 50.2, 31.2, 28.0, 26.5, 23.3, 22.4, 17.1, and 13.9 ppm. HRMS (ESI +ve) m/z: Observed for $C_{17}H_{26}N^+$ [M]+ = 244.2057, $[M]^+_{calcd}$ = 244.2060.

The figures showing ^{1}H and ^{13}C NMR as well as HRMS spectrum for compound 3 and 4 are already given in chapter 3 (**Figures 7-10**).

Synthesis of the intermediate for Cy-5:

The influence of temperature and time are scrutinized on the yield of the reaction, maintaining indolium salt/malonaldehyde bis(phenylimine) monohydrochloride mole ratio constant for the synthesis of Cy-5 intermediate (**Table 2**).

Table 2. General synthesis of Intermediate for Cy-5

Compound	Temperature (ºC)	Time (min)	Yield (%)
5	120	15	20
5	120	30	40
5	160	15	42
5	160	30	75

1-(5-carboxypentyl)-3,3-dimethyl-2-((1E,3E)-4-(phenylamino)buta-1,3-dien-1-yl)-3H-indol-1-ium bromide (5, intermediate of Cy-5 and Cy-5c): Compound 2 (0.71 g, 2.0 mmol) and malonaldehyde bis(phenylimine) monohydrochloride (1.55 g, 6.0 mmol) were dissolved in Ac_2O:AcOH (1:1, 5 mL) in a MW vessel equipped with a magnetic stir bar. The reaction mixture was sealed with a cap and irradiated for 30 m at 160ºC. The reaction mixture was allowed to cool to room temperature and the solvent was removed under reduced pressure. To the reaction mixture cold Et_2O was added to get a dark green precipitate. The resulting dark green residue was extracted with DCM and H_2O and the organic layer was concentrated under reduced pressure. The residue was purified via column chromatography using DCM:MeOH (98:2) to get the intermediate 5 as a scurf green solid.

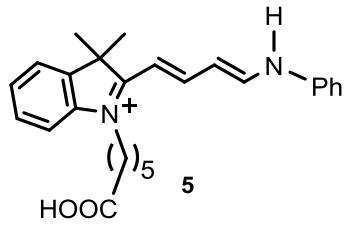

5

Yield: 0.725 g (75%).

^{1}H NMR (400 MHz, DMSO-d_6, 25°C): δ = 11.89 (1H, br), 8.84–8.82 (1H, d, J = 15.0 Hz), 8.37 (1H, t, J = 13.6), 7.63 (1H, d, J = 7.2 Hz), 7.49–7.39 (5H, m), 7.28–7.21 (2H, m), 7.03–6.99 (1H, m), 6.45–6.35 (2H, m), 4.12 (2H, t, J = 6.8 Hz), 3.74 (1H, br), 2.20 (2H, t, J = 7.1 Hz), 1.67 (6H, s), 1.56–1.52 (2H, m), 1.42–1.29 (4H, m) ppm. ^{13}C NMR (101 MHz, DMSO-d_6, 25°C): δ = 175.2, 174.3, 158.2, 155.3, 141.7, 141.2, 139.1, 129.9, 128.6, 125.4, 123.2, 122.5, 121.3, 119.0, 117.3, 111.6, 110.3, 107.9, 101.8, 49.3, 43.5, 34.4, 31.5, 29.4, 28.6, 27.9, 26.7, 24.2, and 22.1 ppm. HRMS (ESI +ve) m/z: Observed for $C_{26}H_{31}N_2O_2^+$ $[M]^+$ = 403.2296, $[M]^+_{calcd}$ = 403.2381.

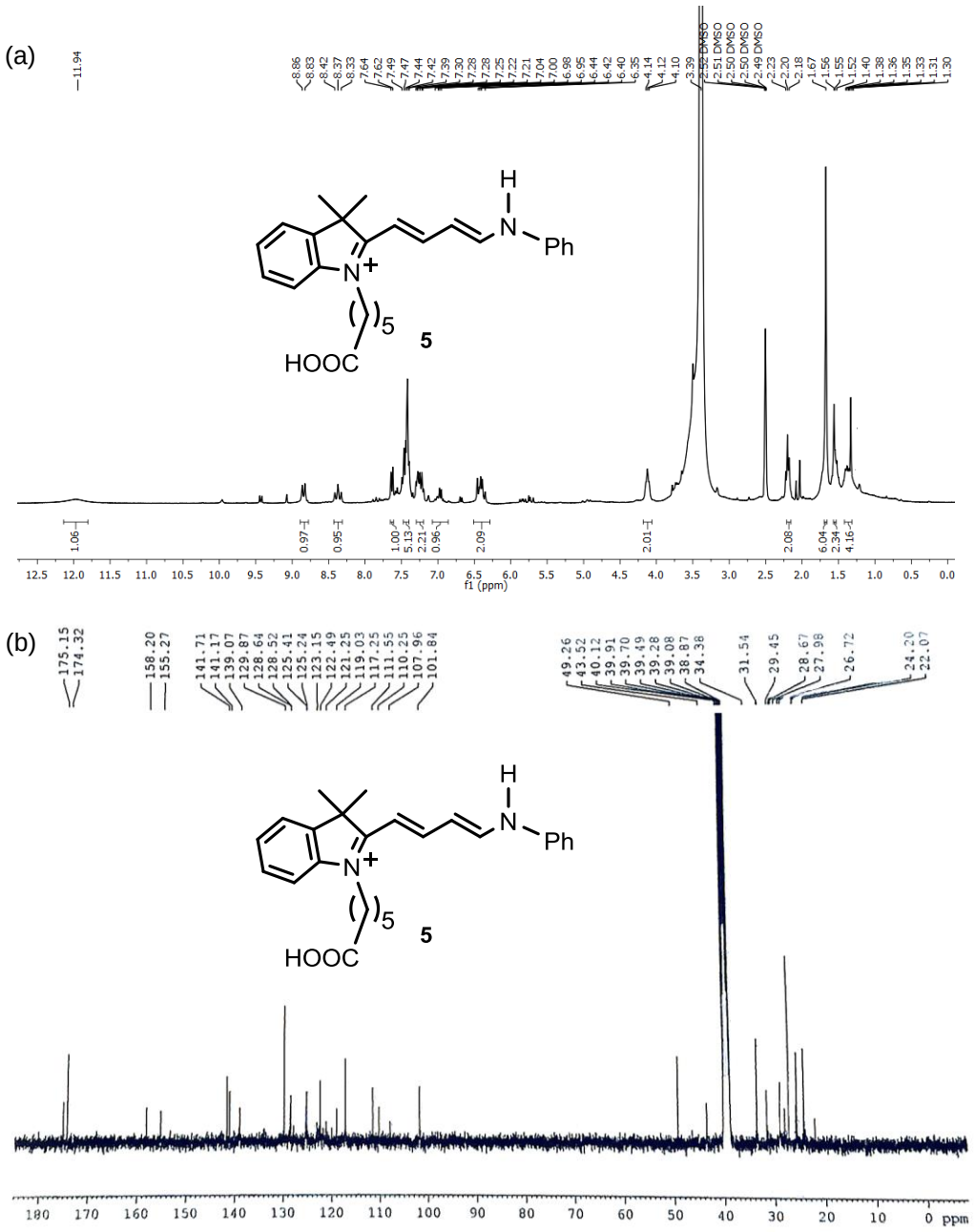

Figure 3. (a) ^{1}H NMR (400 MHz, DMSO-d_6, 25°C) spectrum and (b) ^{13}C NMR (101 MHz, DMSO-d_6, 25°C) spectrum of compound 5.

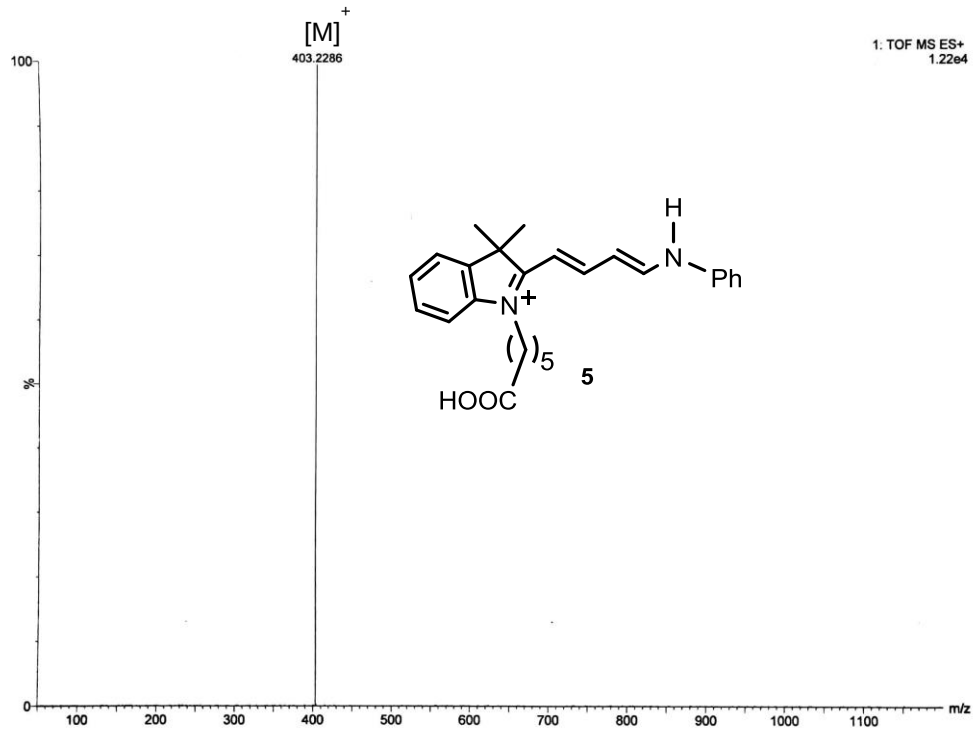

Figure 4. HRMS (ESI +ve) spectrum of compound 5.

Synthesis of Cy-5 and Cy-5c:

The influence of temperature and time are scrutinized on the yield of the reaction, maintaining indolium salt/intermediate 5 mole ratio constant for the synthesis of Cy-5 and Cy-5c (**Table 3**).

Table 3. General synthesis of unsymmetrical Cy-5 and Cy-5c under conventional and microwave conditions.

Compound	Temperature (ºC)	Time (min)	Method	Yield (%)
Cy-5	130	360	A	33
Cy-5	120	5	B	35
Cy-5	120	10	B	60
Cy-5	150	5	B	55
Cy-5	150	10	B	73
Cy-5c	130	360	A	37
Cy-5c	150	10	B	70

A: Conventional method (a) Ac_2O/AcOH, 4h, reflux; (b) AcOH/ Py, 2h, reflux

B: Microwave Method

Unsymmetrical Cy-5 dye:

The intermediate 5 (0.15 g, 0.30 mmol) was dissolved in pyridine:AcOH (1:1, 1.5 mL each) in a MW vessel equipped with a magnetic stir bar. Compound 3 (0.19 g, 0.33 mmol) was added to it and and the MW vessel was sealed with a cap and subjected to MW irradiation for 10 m at 150°C. The reaction mixture was allowed to cool to room temperature and Et_2O was added to get a blue colored

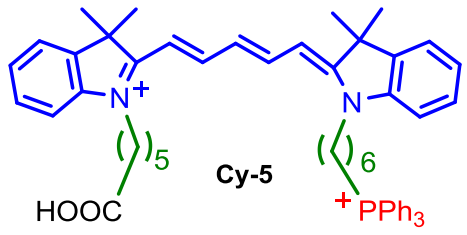

Cy-5

residue and was kept overnight in the refrigerator. The blue solid was collected by filtration and washed with Et_2O (3×5 mL). The crude product was purified by silica gel column chromatography using DCM:MeOH (90:10) (R_f = 0.42, visible without staining, blue color) to obtain the desired unsymmetrical compound Cy-5 as a blue solid.

Yield: 0.213 g (73%).

^{1}H NMR (500 MHz, DMSO-d_6, 25°C): δ = 12.00 (1H, br), 8.35 (2H, t, J = 12.8 Hz), 7.91–7.74 (15H, m), 7.63 (2H, d, J = 7.0 Hz), 7.40–7.38 (4H, m), 7.26–7.25 (2H, m), 6.62 (1H, t, J = 12.3 Hz), 6.29 (2H, d, J = 13.7 Hz), 4.10–4.07 (4H, m), 3.62–3.56 (2H, m), 2.19 (2H, t, J = 6.7 Hz), 1.69 (6H, s), 1.68 (6H, s), 1.63–1.52 (10H, m), 1.42–1.39 (4H, m) ppm.

^{13}C NMR (125 MHz, DMSO-d_6, 25°C): δ = 174.2, 172.5, 171.9, 153.9, 141.9, 141.0, 134.8, 133.4, 130.2, 128.4, 125.5, 124.6, 122.4, 118.9, 118.0, 111.0, 103.0, 48.9, 48.5, 43.3, 33.4, 29.4, 29.2, 27.1, 26.6, 25.6, 25.0, 24.1, 21.5, 21.0, 20.5, and 20.0 ppm.

HRMS (ESI +ve) *m*/*z*: Observed for $C_{55}H_{63}N_2O_2P^{2+}$ $[M]^{2+}$ = 407.2655, $[M]^{2+}$calcd = 407.2308.

Photophysical properties in DMSO λ_{abs}= 650 nm, λ_{em}= 671 nm, Stokes shift ($\Delta\lambda$) = 21 nm, ε = 2.23 ×10^5 M^{-1} cm^{-1}, Φ_f = 0.30 in DMSO (Zinc pthalocyanine dye as a reference, Φ_f of Zinc pthalocyanine = 0.20 in DMSO).

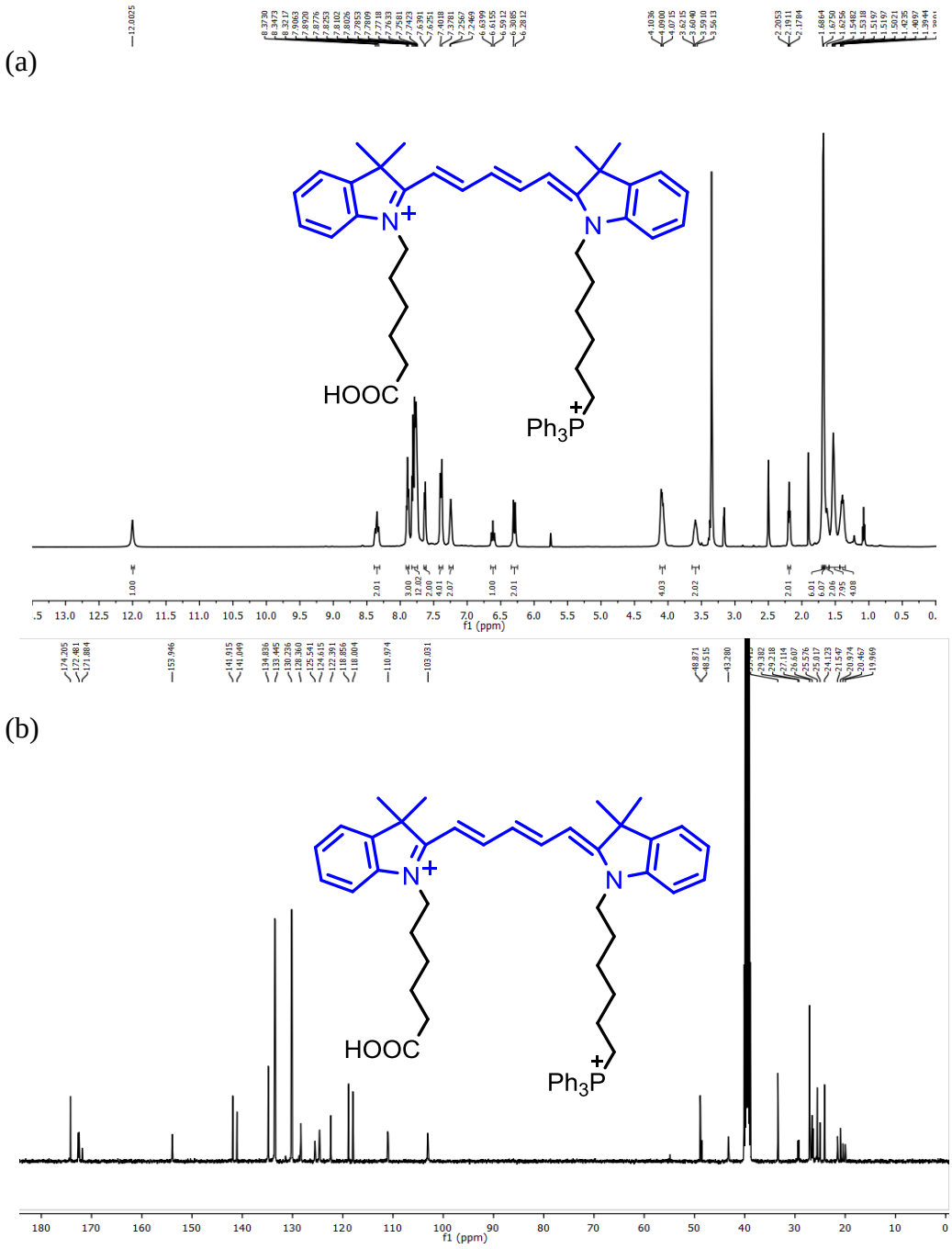

Figure 5. (a) ^{1}H NMR (500 MHz, DMSO-d_6, 25°C) spectrum and (b) ^{13}C NMR (125 MHz, DMSO-d_6, 25°C) spectrum of Cy–5-TPP (Cy–5-TPP or Cy-5).

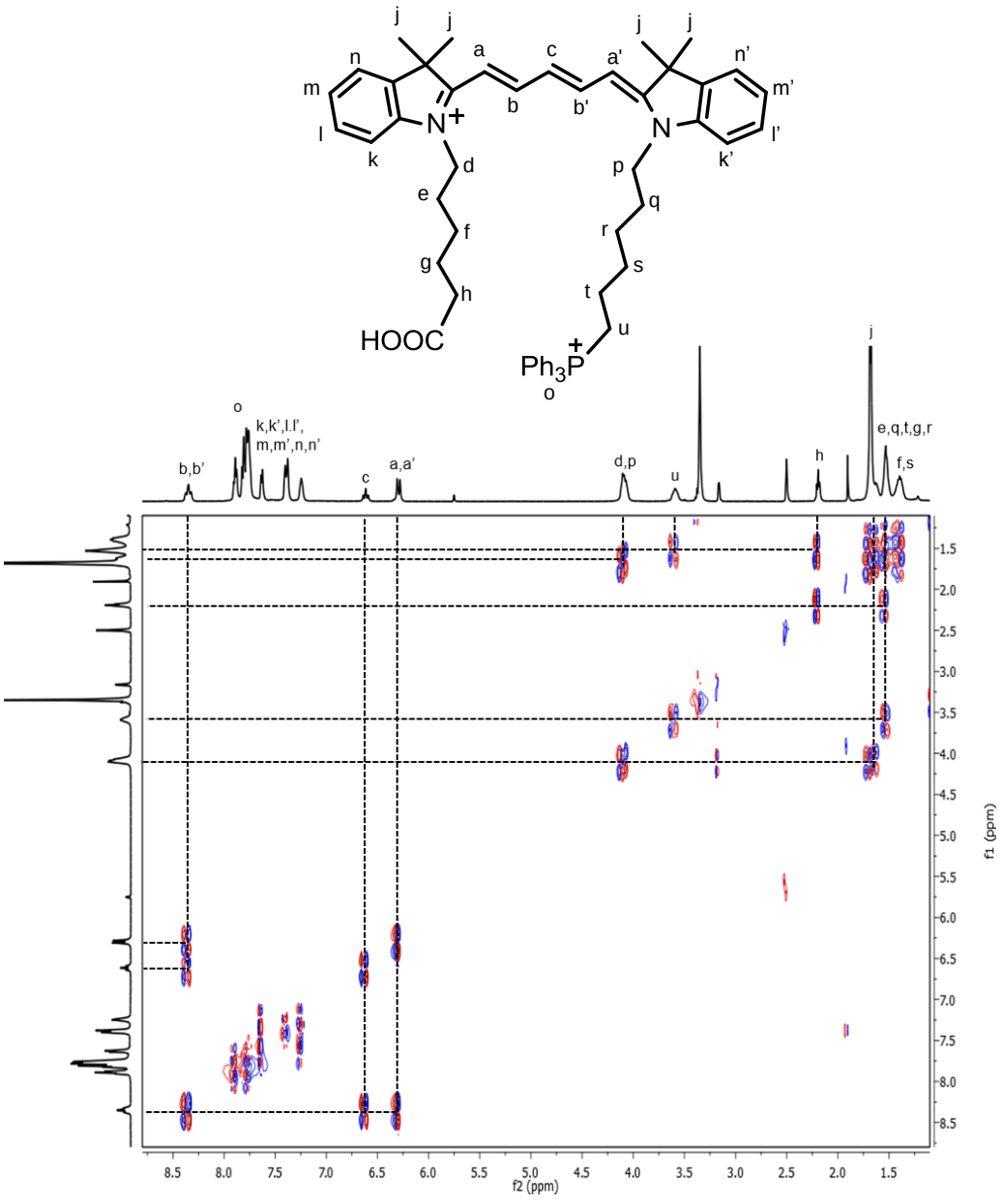

Figure 6. ^{1}H-^{1}H DQF COSY NMR spectrum of Cy-5 (500 MHz, DMSO-d_6, 25°C).

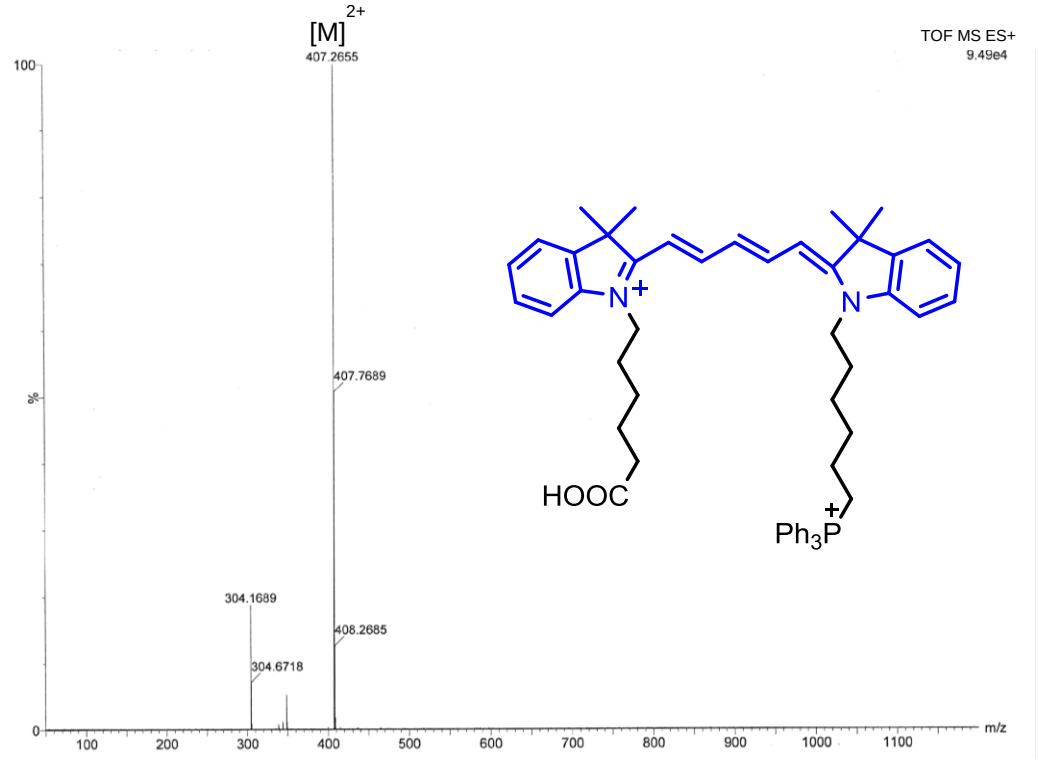

Figure 7. HRMS (ESI +ve) spectrum of Cy–5.

Synthesis of Cy-5c dye: The intermediate 5 (0.15 g, 0.30 mmol) was dissolved in pyridine:AcOH (1:1, 1.5 mL each) in a MW vessel equipped with a magnetic stir bar. Compound 4 (0.11 g, 0.33 mmol) was added to it and the MW vessel was sealed with a cap and subjected to MW irradiation for 10 m at 150°C. The reaction mixture was allowed to cool to room temperature and Et_2O was added to get a blue colored residue and was kept overnight in the refrigerator. The blue solid was collected by filtration and

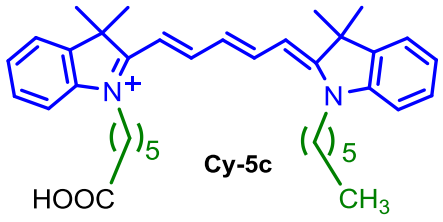

washed with Et_2O (3×5 mL). The crude product was purified by silica gel column chromatography using DCM:MeOH (93:7) (R_f = 0.60, visible without staining, blue color) to obtain the desired compound Cy-5c as a blue solid.

Yield: 0.13 g (70%).

^{1}H NMR (400 MHz, DMSO-d6, 25°C): δ = 8.32 (2H, t, J = 13.1 Hz), 7.61 (2H, d, J = 7.2 Hz), 7.42–7.38 (4H, m), 7.27–7.21 (2H, m), 6.57 (1H, t, J = 13.4 Hz), 6.30 (2H, d, J = 13.6 Hz), 4.15–4.08 (4H, m), 2.18 (2H, t, J = 7.1 Hz), 1.67 (12H, s), 1.61–1.58 (2H, m), 1.55–1.52 (2H, m), 1.44–1.22 (10H, m), 0.84 (3H, t, J = 6.4 Hz) ppm.

^{13}C NMR (101 MHz, DMSO-d6, 25°C): δ = 174.3, 172.6, 153.9, 141.9, 141.1, 128.4, 125.5, 124.6, 122.4, 121.6, 111.0, 103.1, 48.8, 43.3, 35.7, 33.5, 30.8, 27.1, 26.8, 26.6, 25.6, 24.2, 21.9, and 13.7 ppm.

HRMS (ESI +ve) m/z: Observed for $C_{37}H_{49}N_2O_2^+$ $[M]^+$ = 553.3753, $[M]^+_{calcd}$ =553.3789.

Photophysical properties in DMSO λ_{abs}= 650 nm, λ_{em}= 672 nm, Stokes shift ($\Delta\lambda$) = 22 nm, ε = 1.85 ×105 M^{-1} cm^{-1}, Φ_f = 0.28 in DMSO (Zinc pthalocyanine dye as a reference, Φ_f of Zinc pthalocyanine = 0.20 in DMSO).

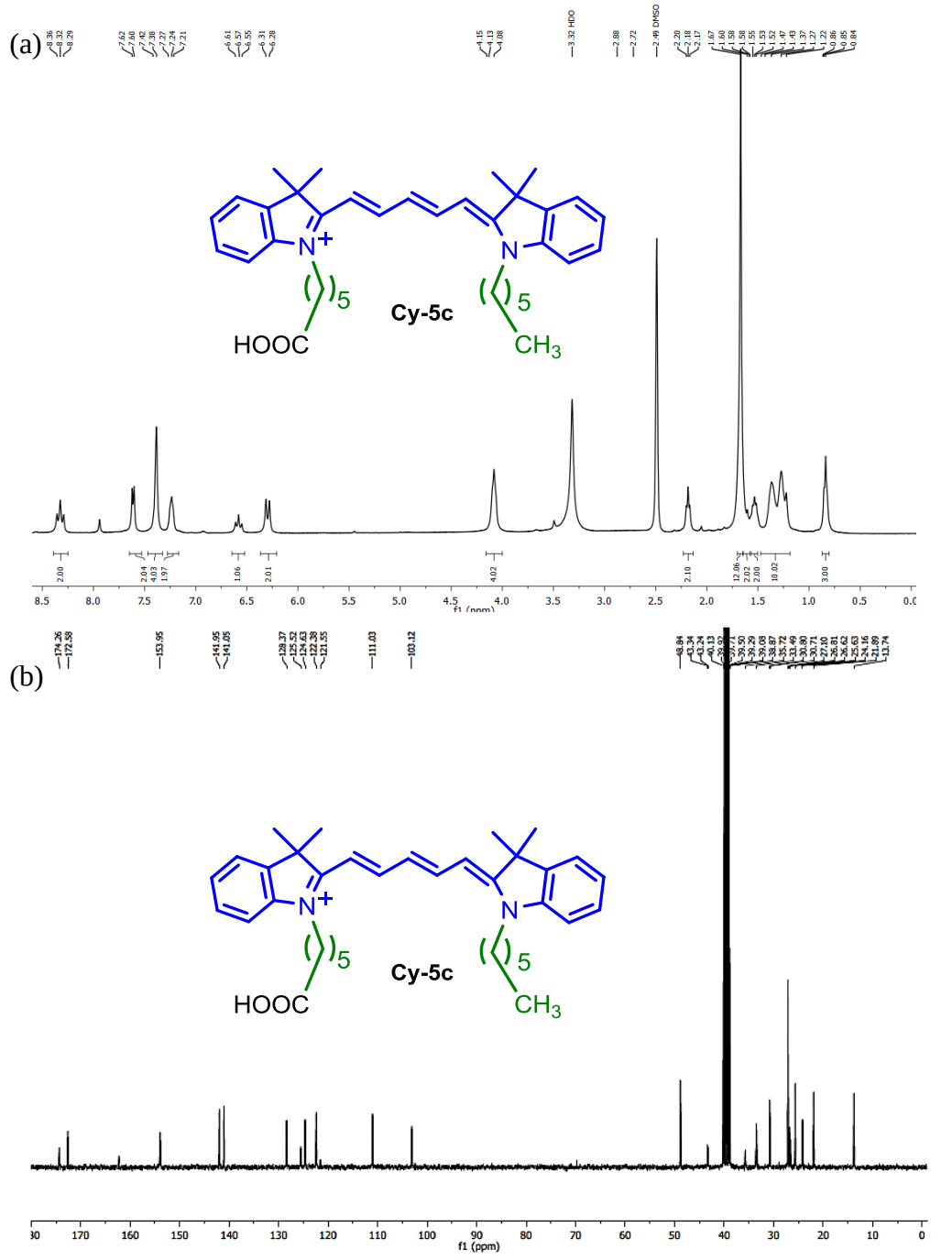

Figure 8. (a) ^{1}H NMR (400 MHz, DMSO-d_6, 25°C) spectrum and (b) ^{13}C NMR (101 MHz, DMSO-d_6, 25°C) spectrum of Cy-5c.

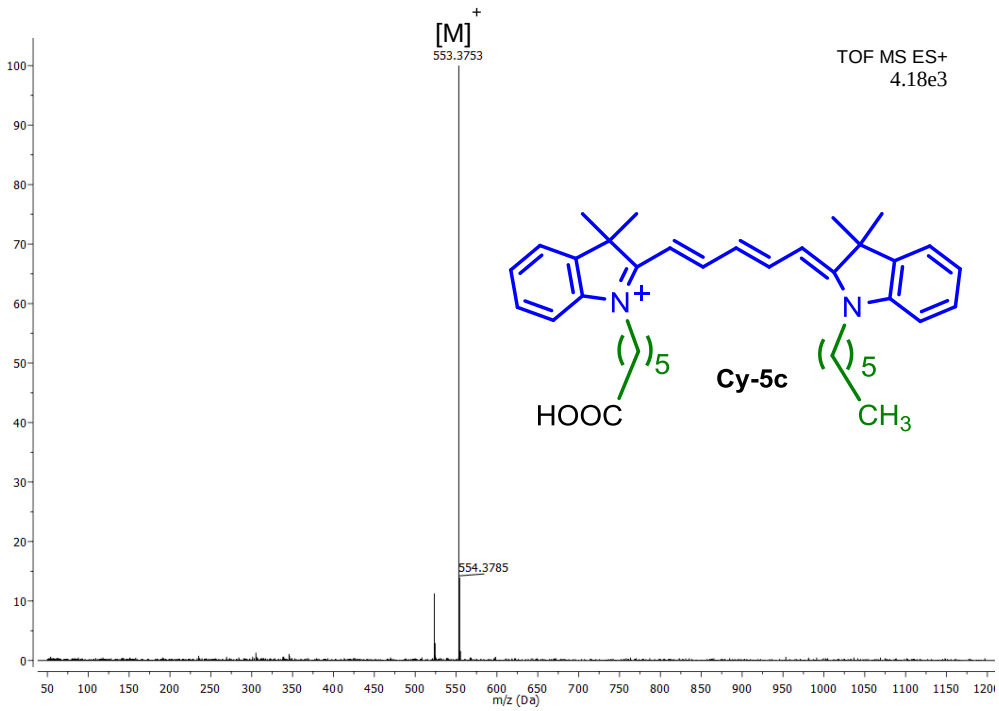

Figure 9. HRMS (ESI +ve) spectrum of Cy-5c.

Synthesis of KLVFF peptide, KLVFF/Cy-5, and KLVFF/Cy-5c conjugate using manual MW Peptide Synthesizer on 2-CTC resin:

Lys-Leu-Val-Phe-Phe (KLVFF) peptide was synthesized by manual microwave-assisted Fmoc-SPPS protocol on a microwave peptide synthesizer (*CEM, Discover Bio*). We use 2-CTC (2-chloro tritylchloride) resin (LL, 0.85 mmol/g loading density) to synthesize KLVFF peptide and KLVFF/Cy-5 conjugate. The following Fmoc-amino acid building blocks were used: Fmoc-Leu-OH, Fmoc-Lys(Boc)-OH, Fmoc-Phe-OH, and Fmoc-Val-OH.

First amino acid (Fmoc-Phe-OH) loading on 2-CTC resin: Fmoc-Phe-OH (0.66 g, 1.2 mmol, 2 eq), DCM (10 mL), and DIPEA (0.59 mL, 3.4 mmol, 4 eq) were taken in a solid phase extraction (SPE) cartridge with frit. The mixture was shaken to dissolve under N_2 atm. 1.0 g 2-CTC resin (LL, 0.85 mmol/g,

1eq) was added into the Fmoc-Phe-OH solution and shaken for 4 h under N_2 bubbling. 2 ml HPLC grade MeOH was added into the resin solution and it was shaken for 30 min for the capping of any unreacted 2-CTC resin and then washes with DCM (2×), DMF (2×), MeOH (3×).

After first amino acid loading on resin, the loading density was estimated by UV-analysis of the Fmoc- dibenzofulvene deprotection product.

Estimation of the First Amino Acid Loading: The resin loading was estimated by measuring the absorption using UV/vis spectroscopy. The resin (5 mg) was taken in a 10 mL graduated flask and 1,8-diazabicyclo[5.4.0]undec-7-en (DBU) in NMP (2 mL, 2 % in NMP) was added. It was shaken for 30 min then the flask was filled to 10 mL with CH_3CN. The solution was further diluted with CH_3CN (1/12.5) and transferred to an UV cuvette (cuvette path length = 1 cm). The absorption of the cleaved dibenzofulvene was detected at 304 nm (ε_{304} = 7624 L $mol^{-1}cm^{-1}$) and corrected against reference. The resin loading was calculated based on Lambert-Beer's law.

$\rho(\text{mmol/g}) = 163.96\times(A - A_0)/\text{m}$

ρ is the loading density of the resin, A is the absorption of a sample, A_0 is the absorption of reference and m is the mass of the analyzed resin in mg.

Microwave-assisted SPPS: The synthesis of KLVFF peptide was performed using microwave assisted solid-phase peptide synthesizer at a 1 mmol scale using SPPS protocol. Special care was taken for the coupling using 2-CTC resin. The temperature was reduced to 50°C and no HOBt was added to the coupling and the deprotection steps using 2-CTC resin. Fmoc-deprotection (20% piperidine/DMF; 210 sec, 50°C, 20 W) and coupling (0.5 M HBTU/2 M DIPEA/DMF; 300 sec, 50°C, 20 W) were performed under MW condition. After the final coupling cycle, Fmoc-deprotection was performed to get a

Fmoc-deprotected *N*-terminus of the peptide. The resin was transferred into a SPE cartridge with frit and washed manually with DMF (5×), DCM (5×), MTBE (5×), and finally with MeOH (5×). The resins were dried in vacuum and stored at −18°C.

Washing after Fmoc-deprotection: DMF (4×), DCM (4×), DMF (4×) to remove the dibenzofulvene by-product. Test cleavage of peptide from 2-chlorotrityl chloride resin: A pinch of resin was taken in a sample vial and 20% HFIP in DCM was added and stirred for 20 min at room temperature. Afterward the resin beads were filtered off and evaporate the solvent to get the peptide or peptide/Cy dye conjugate with protecting groups on the amino acid side chains and a free carboxyl (–COOH) at C-terminus.

Microwave-assisted Synthesis of KLVFF/Cy-5 and KLVFF/Cy-5c conjugates: The synthesis of KLVFF/Cy-5 and KLVFF/Cy-5c conjugates was carried out using microwave assisted solid-phase peptide synthesizer at a 5 μmol scale using SPPS protocol.

Protocol for KLVFF/Cy-5 as well as KLVFF/Cy-5c conjugates synthesis

Working Step	Resin	Reagents	Reaction condition
Coupling	2-CTC	HBTU/DIPEA/DMF	300 sec/50°C/20 W
Washing after final coupling	2-CTC	DMF(5×), DCM(5×), MTBE(5×), MeOH(5×)	
Test Cleavage	2-CTC	20% HFIP/DCM	20 min/25°C
Final Cleavage	2-CTC	TFA/TIPS (92.5/5.0 v/v)	2 h/25°C

Standards Protocols for Manual MW-Assisted SPPS using 2-CTC resin:

1. Bubbling during the MW-assisted synthesis for all steps: on 3 sec; off 7 sec

2. Fmoc deprotection: time 210 sec, power 20 W, temperature 50ºC, delta temperature 5ºC

3. Coupling: 2-CTC resin- time 300 sec, power 20 W, temperature: 50ºC, delta temperature: 5ºC

H-K(Boc)LVFF-OH: FTIR: 3295 cm^{-1} (amide A region, N–H stretching,), a sharp peak at 1635 cm^{-1} and a weak shoulder at 1717 cm^{-1} (amide I region, amide CO stretching), 1536 cm^{-1} (amide II region, NH bending).

HRMS (ESI +ve) m/z: Observed for $C_{40}H_{60}N_6O_8$ $[M+H]^+$ = 753.4440, $[M+H]^+_{calcd}$ = 753.4546

KLVFF/Cy-5 conjugate: FTIR: 3278 cm^{-1} (amide A region, N–H stretching,), a sharp peak at 1633 cm^{-1} and a weak shoulder at 1676 cm^{-1} (amide I region, amide CO stretching), 1544 cm^{-1} (amide II region, NH bending).

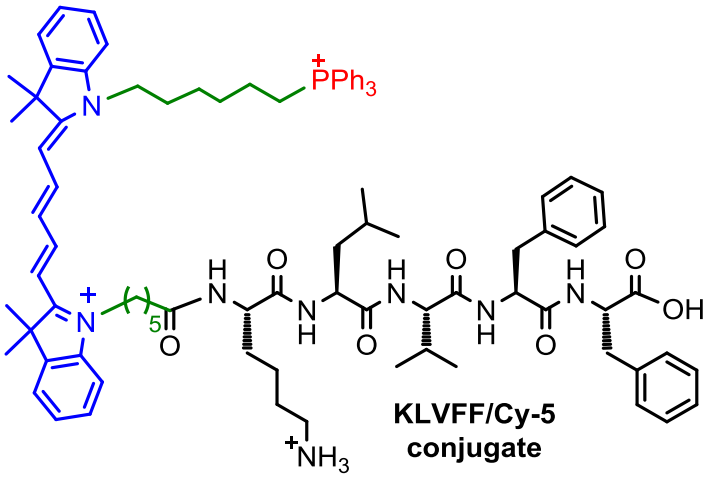

HRMS (ESI +ve) *m/z*: Observed for $C_{90}H_{114}N_8O_7P^{3+}$ $[M]^{3+}$ = 483.3293, $[M]^{3+}$calcd = 483.2844 (*m/z*, *z* = 3).

^{31}P NMR (202 MHz, $CDCl_3$, 25°C): δ = 24.09 ppm.

Photophysical properties in DMSO λ_{abs}= 651 nm, λ_{em}= 672 nm, Stokes shift ($\Delta\lambda$) 21 nm, ε = 2.2 ×105 $M^{-1}cm^{-1}$.

Fluorescence quantum yield, Φ_f = 0.35 in DMSO.

Fluorescence lifetime (τ) = 1.671±0.060 ns in $CHCl_3$, τ = 1.389±0.046 ns in DMSO.

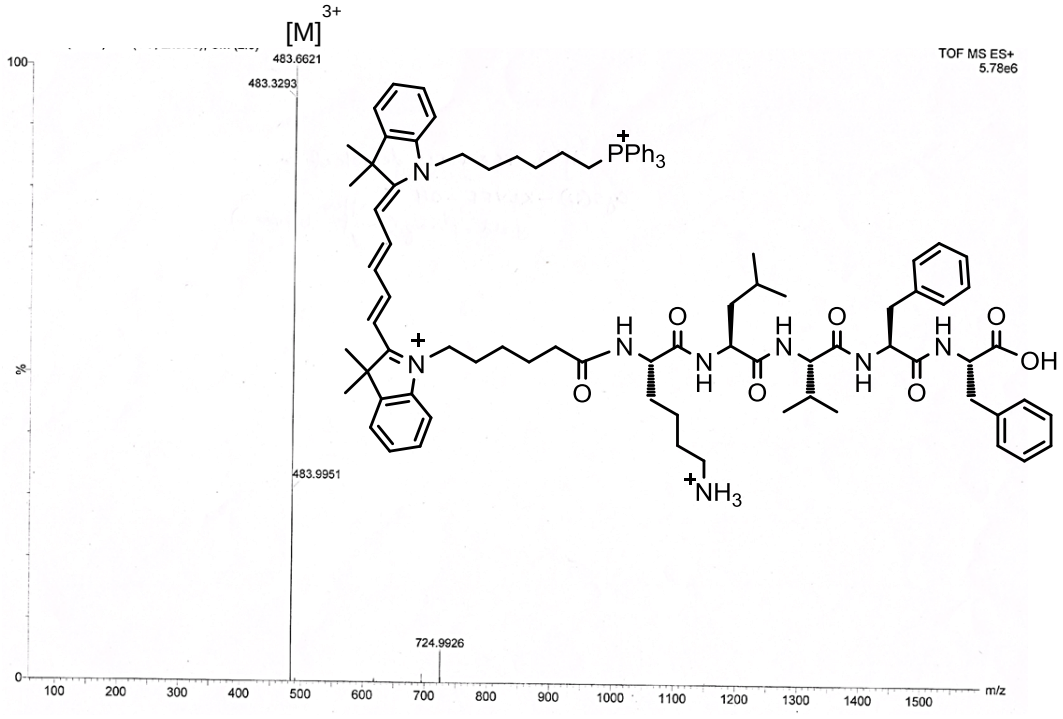

Figure 10. HRMS (ESI +ve) spectrum of KLVFF/Cy-5 conjugate.

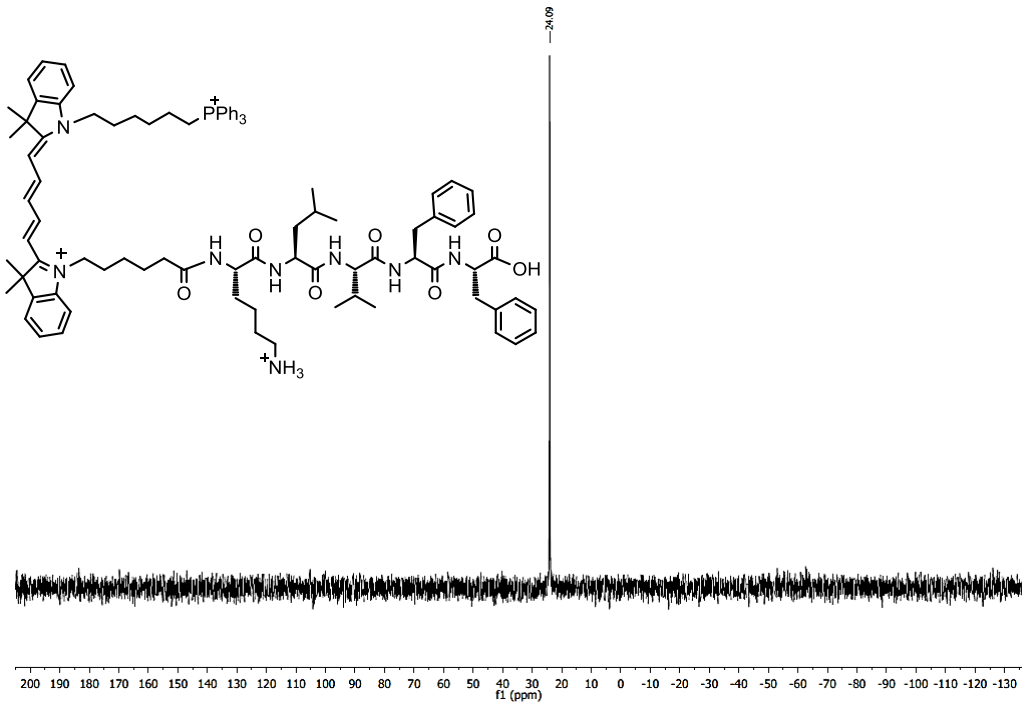

Figure 11. ^{31}P NMR (202 MHz, $CDCl_3$, 25°C) spectrum of KLVFF/Cy-5 conjugate.

KLVFF/Cy-5c conjugate: HRMS (ESI +ve) *m/z*: Observed for $C_{72}H_{100}N_8O_7^{2+}$ $[M]^{2+}$ = 594.3905, $[M]^{2+}$calcd = 594.3852. Photophysical properties in DMSO λ_{abs}= 650 nm, λ_{em}= 672 nm, Stokes shift ($\Delta\lambda$) 22 nm, ε = 1.2 ×10^5 $M^{-1}cm^{-1}$.

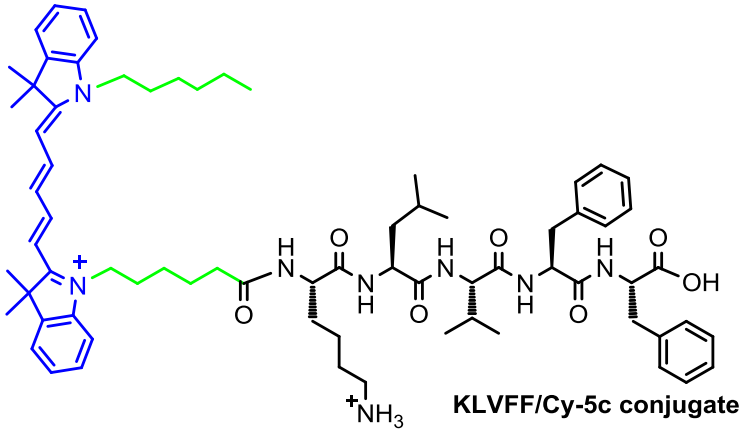

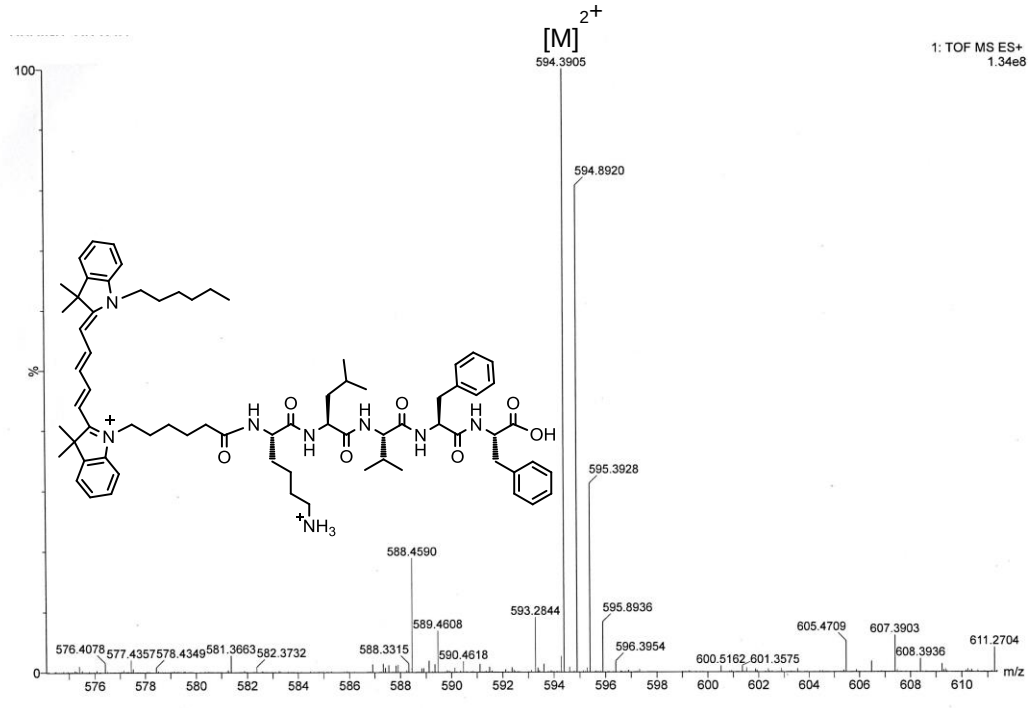

Figure 12. HRMS (ESI +ve) spectrum of KLVFF/Cy-5c conjugate.

METHODS

Microwave Synthesizer: Unsymmetrical Cy-5 dye, KLVFF peptide, KLVFF/Cy-5 and KLVFF/Cy-5c conjugate were synthesized using manual microwave synthesizer (CEM corporation, USA make, model discover bio).

NMR Spectroscopy: 1D (^{1}H, ^{13}C, ^{31}P) and 2D NMR (^{1}H–^{1}H DQF COSY) were recorded on Bruker DPX300 MHz and Bruker DPX500 MHz spectrometers at ambient temperature in appropriate deuterated solvents.

HRMS (ESI): High-resolution electrospray ionisation mass spectrometry (HRMS-ESI) was performed using a Q-TofmicroTM (Waters Corporation) mass spectrometer.

Absorption Spectroscopy: Absorption spectra were recorded using a Shimadzu UV-1800 spectrometer in a quartz cuvette with a path length of 1 cm.

Fluorescence Spectroscopy: Fluorescence measurement was obtained on a Horiba Jobin Yvon FluoroMax-4 spectrofluorometer.

Time-correlated single photon counting (TCSPC) experiment: Fluorescence lifetime (τ) of the KLVFF/Cy-5 conjugate was measured by time-correlated single photon counting (TCSPC) technique on Horiba DeltaFlex lifetime instrument (Horiba Jobin Yvon IBH Ltd, Glasgow, Scotland, UK). A 650 nm delta diode laser excitation source (Model: DD-650L, Horiba Scientific) was used to determine the fluorescence lifetime of KLVFF/Cy-5 conjugate in various solvents. Lifetime measurements and data analysis were obtained using Horiba EzTime decay analysis software.

X-Ray powder Diffraction: The X-ray diffraction from dried film of KLVFF/Cy conjugate was collected with a Bruker D8 Advance X-ray diffractometer using Cu K_α radiation (λ = 1.5418 Å) operating at 40 kV and 40 mA.

FT-IR Spectroscopy: FT-IR spectrum was recorded on a PerkinElmer Spectrum Two FT-IR spectrometer.

CD Spectroscopy: CD spectrum was recorded on a JASCO instrument, Model J-815–150S. Data were collected in a quartz cuvette with a path length of 1 mm at wavelengths between 190 nm to 260 nm with a 0.5 nm step, 1 nm bandwidth, and 2 s collection times per step at 25°C, taking three averages. The CD signal from the solvent as background was subtracted from the CD data of the sample solution. TFE solution of the KLVFF/Cy-5 conjugate (0.03 wt %) was used for the CD experiment.

Atomic Force Microscopy: AFM experiment was performed in AUTOPROBE CP base unit, di CP-II instrument (Model no: AP-0100).

Calculation of relative quantum yield of KLVFF/Cy-5 conjugate: Fluorescence quantum yields (Φ_f) of KLVFF/Cy-5 conjugate was measured by relative method. The integrated fluorescence intensity of the KLVFF/Cy-5 conjugate was compared with fluorescence intensity of a reference compound (Zinc pthalocyanine, Φ_f (st) of Zinc pthalocyanine in DMSO is 0.20) according to the following equation:

$\Phi_f(x) = \Phi_f(st) \times [(A_{st} \times F_x \times \eta_x^2) / (A_x \times F_{st} \times \eta_{st}^2)]$

Φ_f (st) and Φ_f (x): fluorescence quantum yield of the reference and sample compounds respectively

A_{st} and A_x: Absorbance of reference and sample at the excitation wavelength, respectively

F_{st} and F_x: Integrated fluorescence areas under the corrected fluorescence spectra for the reference and sample compound, respectively.

η_{st} and η_x: Refractive indices of the solvent in which the reference and sample compounds were measured, respectively [here, both the reference and sample compounds were dissolved in DMSO; so $(\eta_x^2 / \eta_{st}^2) = 1$].

"st" stands for the standard and "x" refers to the unknown sample.

The relative Quantum yield (Φ_f) of KLVFF/Cy-5 conjugate was measured as 0.35 in DMSO.

Determination of critical aggregation concentration for KLVFF/Cy-5 conjugate: Surface tension of KLVFF/Cy-5 conjugate in PBS (pH 7.4) at various concentrations was measured using KRÜSS-K7 Tensiometer instrument (Germany) by applying Ring-detachment method. To determine the critical aggregation concentration (CAC) of KLVFF/Cy-5 conjugate surface tension values of KLVFF/Cy-5 was plotted against log[C] which gives a

sigmoid curve. After each addition of the KLVFF/Cy-5 conjugate 5 min was given to reach the equilibrium. Increasing the concentrations of KLVFF/Cy-5 gradually lowered the surface tension. The experiment was repeated three times and nearly identical results were obtained. Each data point is the mean value of three measurements. Sharp decline of surface tension value of KLVFF/Cy-5 conjugate give the measure of CAC value.

Cell Culture: HeLa and A549 cells were cultured in DMEM (pH 7.4) containing 10% FBS and antibiotic-antimycotic solution 100×(containing 10000 units penicillin, 10 mg streptomycin, and 25 μg amphotericin B per mL in 0.9% normal saline). The cell lines were maintained at 37°C in an air-jacketed 5% CO_2 incubator and were routinely passaged.

MTT assay for cell viability: The cytotoxicity of KLVFF/Cy-5 conjugate on different cancerous cell lines were determined by MTT assay. HeLa and A549 cancerous cells as well as healthy human cell lines such as lung fibroblast (WI38) and human embryonic kidney (HEK293) were individually plated at a density of ~100 cells in a 96-well plate using DMEM with a 24 h incubation to allow proper cell growth. After 24 h incubation, KLVFF/Cy-5 conjugate was treated at specific concentrations (0.5, 2, 3, 5, 10, and 15 μM per well) for 24 h at 37°C. The cells were then treated with 10 μL of MTT solution (5 mg mL^{-1} in PBS) for 4 h in darkness at 37°C. Dark blue formazan crystals was formed which were dissolved in DMSO and the absorbance (A) was monitored (each data point was measured in triplicate) at 570 nm using an ELISA plate reader. The results were expressed as the percentages of the viable cells by the following equation:

Viable cells (%) = (*A* of treated cells / *A* of untreated cells) × 100

Confocal microscopy: Confocal microscopy was carried out using ZEISS LSM 800 Confocal Laser Scanning Microscope and Leica TCS SP8 Confocal Microscope equipped with a 60× and 100× oil plan apochromatic objective. HeLa cells were seeded on a cover slip and grown in DMEM. Cells were fixed for 30 m with 4% paraformaldehyde and subjected to confocal microscopic experiments. Fixed cells were incubated with 0.5 μM solution of KLVFF/Cy-5 conjugate or KLVFF/Cy-5c conjugate at 37°C for 10 m in darkness and then washed twice using 1x PBS. Then the samples were incubated with 0.2 μM MitoTracker Red and placed in the dark for 15 m, cells were washed three times with 1x PBS. Cells were then incubated with DAPI for 15 m. After washing in the same protocol, cells were mounted with antiquench agent n-propyl gallate for microscopic slide preparation and detected by confocal microscope. High resolution images obtained from ZEISS and Leica microscope were analyzed by ZEN Lite 2.3 and LAS X softwares, respectively. For DAPI: laser excitation wave length = 405 nm, emission wavelength range = 415–461 nm, MitoTracker Red: laser excitation wavelength = 561 nm, emission wavelength range = 578–598 nm, For KLVFF/Cy-5 conjugate: laser excitation wave length = 635 nm, emission wavelength range = 660–700 nm.

Determination of the concentration of KLVFF/Cy-5 conjugate inside the mitochondria: To measure the inner mitochondrial concentration of KLVFF/Cy-5 conjugate, HeLa cells and A549 cells were separately seeded in a 24 well plate and allowed to grow for 24 h at 37°C, 10% CO_2. Then the culture media was discarded and new medium containing 5 μM and 10 μM KLVFF/Cy-5 conjugate was added and incubated for 3 h at 37°C to have enough cellular uptakes. The media was discarded; cells were washed with cold 1X PBS for three times. HeLa cells and A549 cells were then separately harvested with trypsin solution and collected in an eppendorf. Hemocytometer

was used to determine the average cell number. The cells were then centrifuged at 1400 rpm for 5 min, the supernatant was discarded to collect the cells as pellet. Same centrifugation process was repeated twice with PBS and supernatant was discarded. To the collected pellet of cells, 200 µL Ripa lysis buffer was added and waited for 30 min to ensure complete lysis. 200 µL of MeOH was added into the lysate and after centrifugation supernatant was collected and fluorescence emission (λem) at 664 nm (λex = 644 nm) were recorded. Using the fluorescence vs concentration calibration curve corresponding concentration of the KLVFF/Cy-5 was determined. Initially, with known concentrations of KLVFF/Cy-5 conjugate (0.02 µM, 0.10 µM, 0.25 µM, 0.50 µM, and 1.00 µM) in a 1:1 mixture of Ripa buffer and MeOH, fluorescence vs concentration calibration curve was plotted. Concentration of KLVFF/Cy-5 conjugate inside the cell was determined using the following relationship: Intracellular concentration = Cellular uptake (µmol) / (Cell number × Volume of the cell). The average size and cell volume of the HeLa cell was determined as 20 µm and 4000 μm^3, respectively. The average size and cell volume of the A549 cell was 15 µm and 1670 μm^3, respectively. Concentration of KLVFF/Cy-5 conjugate inside the mitochondria was calculated by the following relation: Volume ratio of HeLa cell to the cell mitochondria as 0.06.[37] Volume ratio of A549 cell to the cell mitochondria as 0.04.[38] Fluorescence spectroscopy revealed that the accumulation of KLVFF/Cy-5 molecules inside the mitochondria of HeLa cells are 3.2±0.7 mM and 6.1±0.5 mM; and A549 cells are 5.4±0.4 mM and 10.5±0.6 mM with respect to the original external concentration in the culture medium 5 µM and 10 µM, respectively.

Annexin V-FITC/PI Apoptosis Detection Assay: The magnitude of apoptosis was determined quantitatively by Annexin V-FITC (FITC = fluorescein isothiocyanate) apoptosis detection kit by flow cytometry. Annexin V is a Ca^{2+} dependent phospholipid binding protein and it has a high affinity for negatively charged phosphatidylserine (PS) on the apoptotic cell membrane surface. Annexin V is one of the most sensitive markers to detect early apoptosis. PS is generally found in the inner leaflet of normal healthy cell membrane. In case of early apoptosis, the PS is translocated from inner to outer leaflet of plasma membrane and is exposed. The kit also contains propidium iodide (PI) to stain the cellular DNA in necrotic cells. PI cannot enter the intact cell membrane of healthy or early apoptotic cells. PI can penetrate the cell membrane of late apoptotic and necrotic cells, and stain these cells. A549 cells were cultured in a 25-mL T-flask in DMEM (pH 7.4) containing 10% FBS and antibiotic-antimycotic solution 100×(containing 10000 units penicillin, 10 mg streptomycin, and 25 μg amphotericin B per mL in 0.9% normal saline). The cell lines were maintained at 37°C in an air-jacketed 5% CO_2 incubator and were routinely passaged. The cells were then treated with KLVFF/Cy-5 at various concentration 1.5, 3.0, 10.0 μM for 24h in media. The cells were then trypsinised and washed with cold 1x PBS for 2 times. The cells were then resuspended in 1× annexin-binding buffer and then transfer 100 μL of the solution to a 5 mL culture tube. Following the manufacturer's protocol, the cells were treated with 5 μL of Annexin V-FITC and 5 μL of PI solutions for 15 min incubated period at room temperature in the dark. 400 μL of 1× Binding Buffer was added to each tube. The binding buffer included in the kit contains $CaCl_2$. After the incubation period the samples were kept on ice. The fluorescence was measured on a BD FACSCalibur Flow Cytometer (BD Bioscience). Data were analyzed and the percentage of cells in early and late

apoptosis was estimated using BD CellQuest Pro software (BD Bioscience). A control experiment was performed without the addition of KLVFF/Cy-5.

Results and discussion

Design and synthesis of Cy-5, Cy-5c, KLVFF/Cy-5, KLVFF/Cy-5c conjugate:

Synthesis of unsymmetrical NIR Cy-5 dye is more challenging and important than symmetric Cy-5 dye.[39-44] Construction of unsymmetrical Cy-5 has been reported in the literature using the conventional method which takes days and frequently requires very difficult column chromatographic separation.[42-44] Herein, a MW assisted efficient synthesis of unsymmetrical Cy-5 and its related precursor molecules is illustrated in Scheme 1a. The flexibility in synthetic routes allowed us to covalently conjugate N of 2,3,3-trimethylindolenine with TPP^+(mitochondria targeting group) and carboxylic (–COOH, to couple with amino group of peptides) functionality by suitable alkylating agents using MW conditions (**Table 1**). We have also carried out a screening study under MW conditions to optimize the yield of the activated intermediate 5, maintaining the corresponding indolium salt and malonaldehyde bis(phenylimine) monohydrochloride ratio in Ac_2O/AcOH (1:1) constant (**Table 2**). The unsymmetrical Cy-5 is prepared by condensation between the activated intermediate 5 with the quaternary indolium salt 3 in the presence of AcOH/pyridine (1:1) and under MW irradiation (**Scheme 1, Table 3**). Unsymmetrical Cy-5 is obtained in good yield and characterized by 1D (^1H, ^{13}C) NMR, 2D (^1H-^1H DQF COSY) NMR, and high-resolution ESI-MS (Experimental section and **Figures 5-7**). Moreover, a control molecule Cy-5c (c stands for control) is also synthesized by the MW methodology and

characterized (**Scheme 1**, **Figures 8** and **9**). Cy-5 is further conjugated at the N-terminal position of KLVFF pentapeptide using MW assisted Fmoc SPPS protocol on 2-CTC resin (**Scheme 2**). Here, KLVFF peptide residue acts as a self-assembling β-sheet forming motif, unsymmetrical Cy-5 chromophore serves as NIR imaging agent, and TPP^+ acts as a mitochondria targeting group. The KLVFF/Cy-5 shows one ^{31}P NMR peak at 24.1 ppm due to the presence of one TPP^+ moiety (**Figure 11**). A control molecule KLVFF/Cy-5c lacking the TPP^+ functionality is also constructed. Both the KLVFF/Cy-5 and KLVFF/Cy-5c conjugates were characterized by ESI-MS (**Figures 10** and **12**).

Photophysical characterization:

The photophysical property of KLVFF/Cy-5 is examined in different solvents including buffer at physiological pH 7.4 and mitochondrial pH 8.0 (**Figure 12**). The absorption spectra of KLVFF/Cy-5 displayed a peak at 651 nm in DMSO**,** due to $\pi \rightarrow \pi^*$ transitions (**Figure 12a**). The KLVFF/Cy-5 also exhibited large molar extinction coefficients of ca. 2.2×10^5 M^{-1} cm^{-1} (**Table 4**). KLVFF/Cy-5 fluoresces in the NIR region (λ_{ex} = 651 nm, λ_{em} = 672 nm) in DMSO with 21 nm Stokes shift (**Figure 12c**). The control molecule KLVFF/Cy-5c also absorbs and emits in the NIR region (**Figure 13**). Fluorescence quantum yield, Φ_f = 0.35 is observed in DMSO for KLVFF/Cy-5. Fluorescence lifetime (τ) of KLVFF/Cy-5 is determined in various solvents by TCSPC technique. $\tau \approx 1.67$ ns in $CHCl_3$ is found (**Figure 1f, Table 5**) after excitation with a delta diode laser at 650 nm.

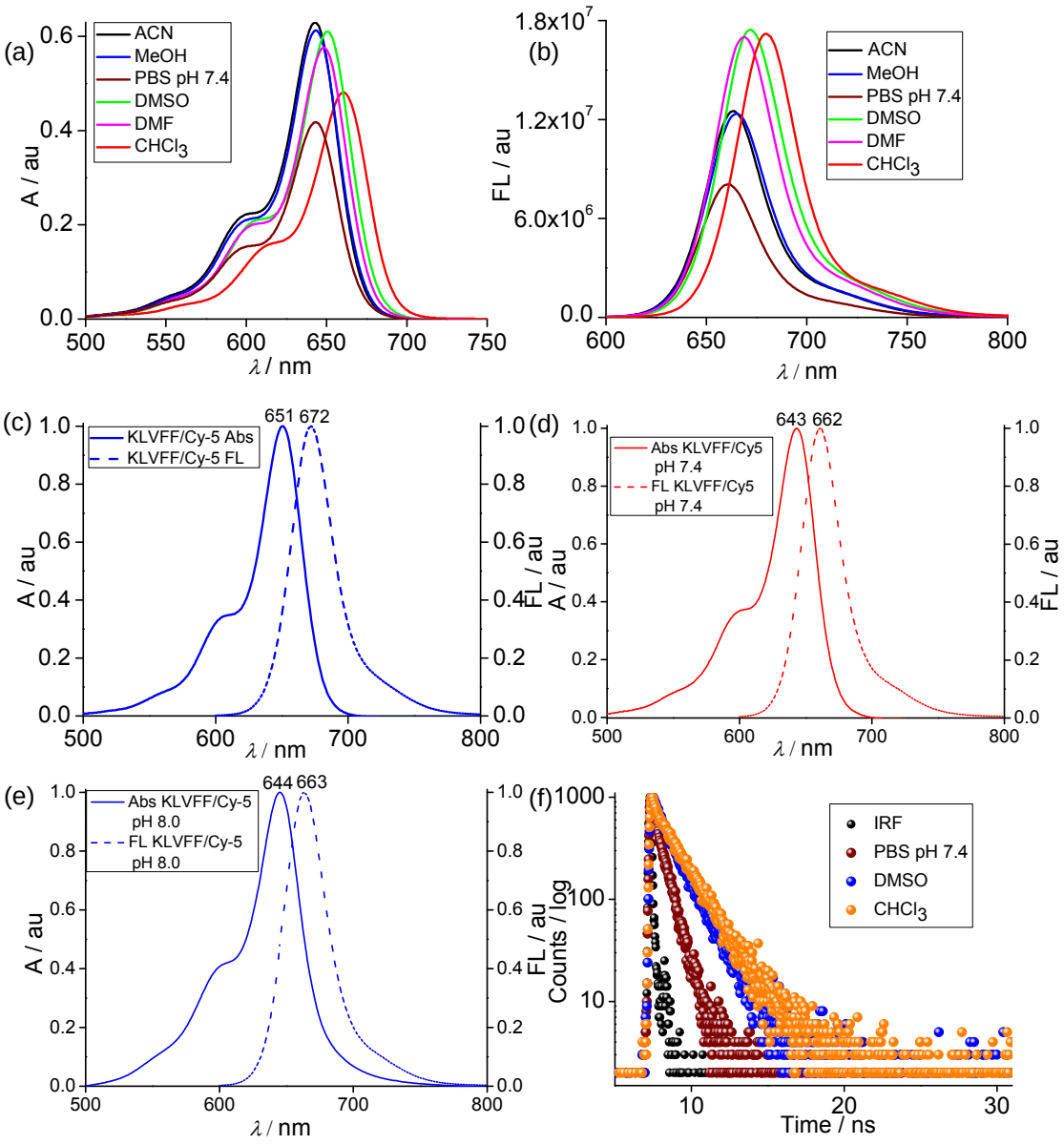

Figure 12. (a) Absorption and (b) Fluorescence plot of KLVFF/Cy-5 in various solvents. (c) Normalized absorption (solid line) and emission (dashed line) spectra of KLVFF/Cy-5 in DMSO. Normalized UV/vis and fluorescence plot of KLVFF/Cy-5 at (d) physiological pH=7.4 and (e) mitochondrial pH=8.0. (e) TCSPC plot of KLVFF/Cy-5 in PBS, DMSO, and $CHCl_3$.

Table 4. Photophysical data of KLVFF/Cy-5 conjugate in different solvents.[d]

[d] ε: molar extinction coefficient., λ_{max}: absorption maximum wavelength, λ_{em}: emission maximum wavelength.

Solvent	Dielectric constant (ϵ) of Solvent	Refractive Index (η) of Solvent	λ_{max} (nm)	λ_{em} (nm)	Stokes shift ($\Delta\lambda$)	$\varepsilon \times 10^5$ (M^{-1} cm^{-1})	Φ_f
PBS	80.1	1.333	643	661	18	1.31	
CH_3CN	37.5	1.341	643	664	21	2.30	
DMF	36.7	1.428	648	669	21	2.10	
MeOH	32.6	1.326	644	665	21	2.24	
DMSO	46.7	1.479	651	672	21	2.20	0.35
$CHCl_3$	4.81	1.443	661	680	19	1.76	

Table 5. Fluorescence lifetimes (τ / ns) of KLVFF/Cy-5 conjugate in various solvents.

Solvent	Lifetime (τ / ns)	Chi-square χ^2
PBS pH 7.4	0.648±0.014	1.113
$CHCl_3$	1.671±0.060	1.228
DMSO	1.389±0.046	1.101

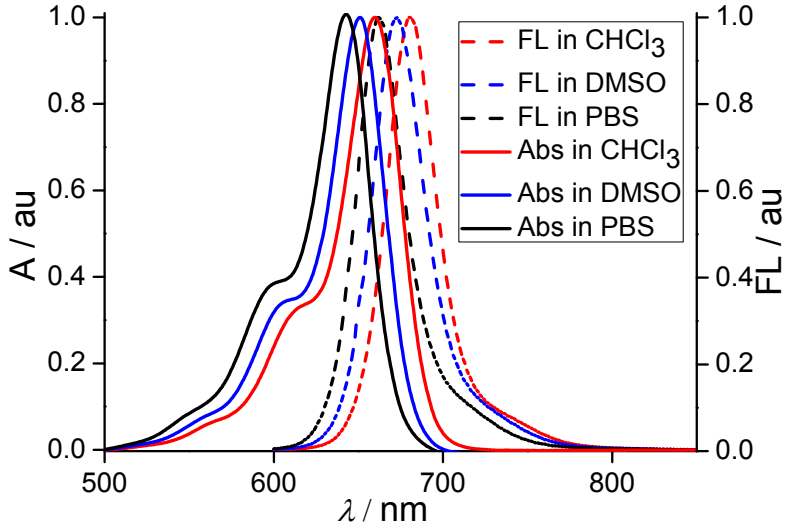

Figure 13. Normalized UV/vis and fluorescence plot of the control molecule KLVFF/Cy-5c (lacking TPP^{+} functionality) in different solvents.

Secondary structure:

To probe the secondary structural information of KLVFF/Cy-5 we performed FT-IR and CD spectroscopy. FT-IR spectrum containing KLVFF/Cy-5 fiber, aged over 2 days, shows a peak at 3278 cm^{-1}, corresponding to the N–H stretching vibrations of the KLVFF residue (amide A), a peak at 1633 cm^{-1} at the amide I region (amide CO stretching), and 1545 cm^{-1} at the amide II region (NH bending), indicating the formation of intermolecularly hydrogen-bonded β-sheet structure (**Figure 14a**). No band at ~3400 cm^{-1} has been observed indicating involvement of all the NHs in hydrogen bonding (No free NH). Moreover, a weak shoulder at 1675 cm^{-1} suggests that the β-sheets are antiparallel in nature.[45] The CD spectrum of KLVFF/Cy-5 in dilute PBS (pH 7.4) solution (0.03 wt %) shows a lower wavelength positive peak at 196 nm and the higher wavelength two positive

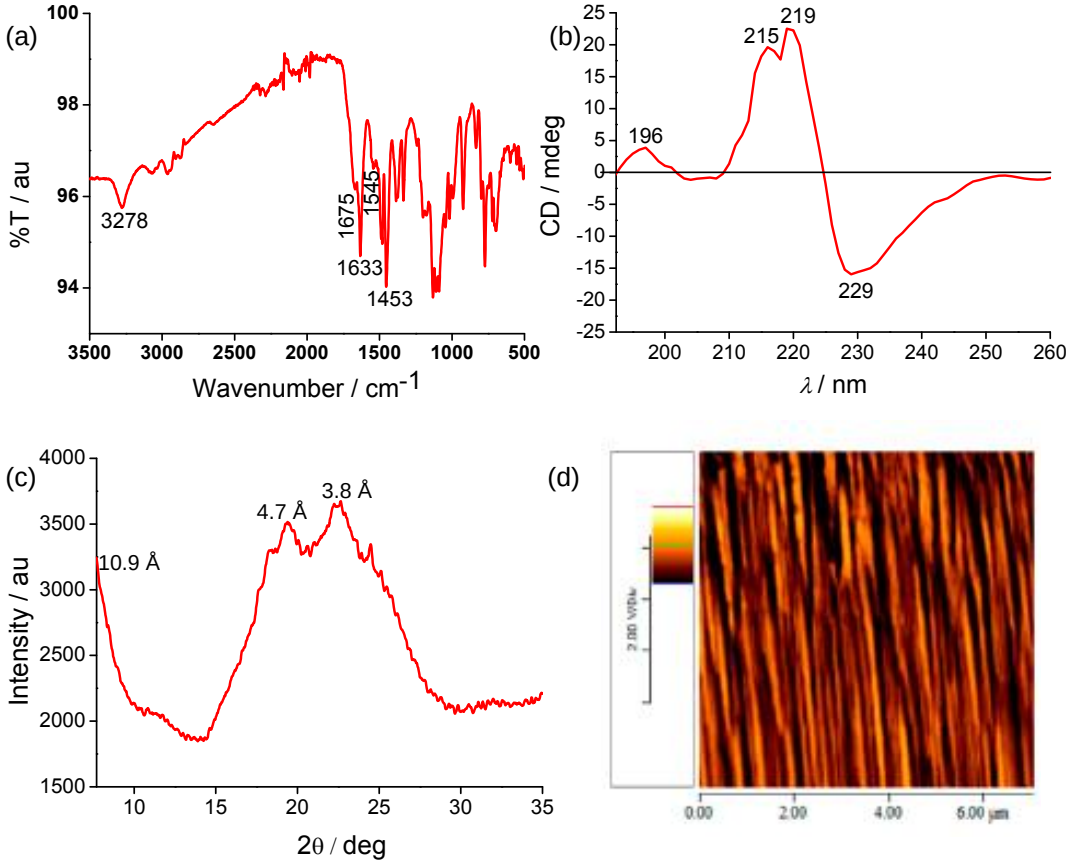

Figure 14. (a) FT-IR spectrum of KLVFF/Cy-5 fiber, aged over 2 days, shows a peak at 3278 cm^{-1} (N–H stretching, amide A), a sharp peak at 1633 cm^{-1} (amide CO stretching, amide I), 1545 cm^{-1} (NH bending, amide II region), indicating the formation of a intermolecularly hydrogen-bonded β-sheet structure related with amyloid fibrils. A weak shoulder at 1675 cm^{-1} suggests that the β-sheets are antiparallel in nature. (b) CD spectrum of KLVFF/Cy-5 in PBS shows lower wavelength positive peak at 196 nm, two higher wavelength positive peaks at 215 and 219 nm, and negative maxima at 229 nm. (c) X-ray diffraction of dried film from KLVFF/Cy-5 fiber shows cross-β-sheet structure due to the presence of 4.7 Å (meridional reflection), 10.8 Å (equatorial reflection), and 3.8 Å (off-meridional reflection) peaks. (d) AFM image indicates that KLVFF/Cy-5 self-assembles to form amyloid fibrils.

peaks at 215 and 219 nm (**Figure 14b**).[46] We also observed negative maxima at 229 nm. The CD spectrum of KLVFF/Cy-5 is strongly influenced by the involvement of π-π stacking of aromatic residues of the phenylalanine side chain which masks the characteristic spectrum of a *β*-sheet structure. X-ray diffraction and AFM provided further support for the *β*-sheet amyloid fibril formation (**Figure 14c,d**). The peaks obtained from X-ray diffraction of dried film from KLVFF/Cy-5 fiber are characteristic of a typical cross-*β*-sheet structure due to the presence of a peak at 4.7 Å (meridional reflection), which corresponds to the separation of *β*-strand within the *β*-sheets and a peak at 10.9 Å (equatorial reflection), which is due to the spacing of β-sheets (**Figure 14c**).[47,48] Moreover, an off-meridional reflection at 3.8 Å is also observed.[48] In the cross-*β* structure, the individual strands of each *β*-sheet run perpendicular to the fibril axis (4.7 Å spacing), whereas the *β*-sheets (10.9 Å spacing) are parallel to the fibril axis. The FT-IR and X-ray diffraction pattern of the fiber reveals that the KLVFF/Cy-5 forms fibrils composed of antiparallel *β*-sheets through hydrogen bonding, characteristic of amyloid fibrils. The intermolecularly hydrogen bonded antiparallel *β*-sheets are packed further through π-π stacking between aromatic residues of the phenylalanine (Phe) units in a cross-*β* arrangement, and these interactions are very important in the formation and stability of amyloid fibrils.[49]

Cellular uptake and confocal laser scanning microscopy:

UV/vis experiment displays that the absorption of KLVFF/Cy-5 is stable in PBS (pH 7.4, 37°C) and mitochondrial pH (pH 8.0, 37°C) (**Figure 15a,b**). The plausible interference from biological environment by various metal ions (Na^+, K^+, Ca^{2+}, etc.) are investigated under physiological conditions

(PBS, pH 7.4, 37°C). No significant fluorescence changes are observed in the presence of these potential biological interferants (**Figure 15c**).

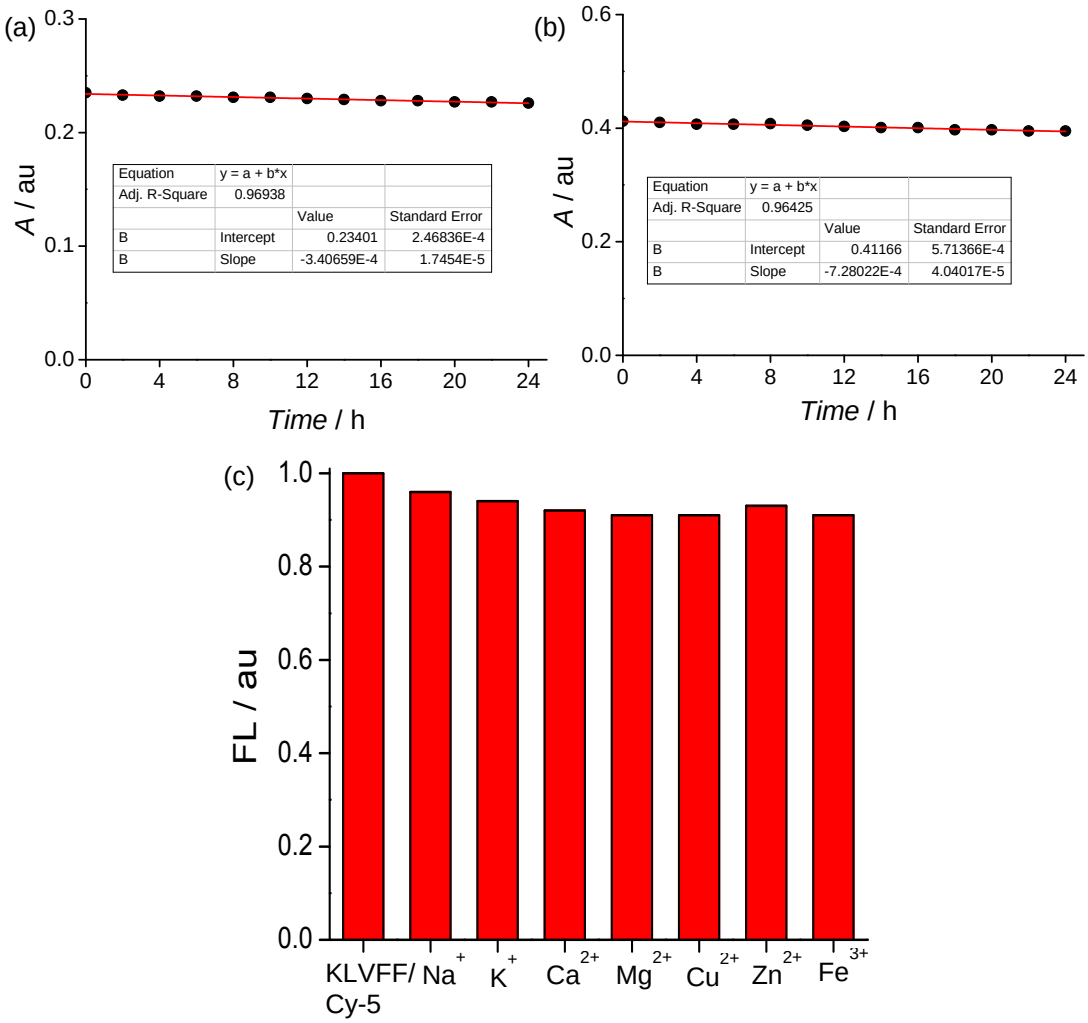

Figure 15. (a) Very negligible absorption changes are detected for KLVFF/Cy-5 conjugate in PBS (pH=7.4, 37ºC) and (b) pH=8.0 (37ºC) at different time intervals. (c) No noticeable fluorescence changes ($\lambda_{ex}/\lambda_{em}$ 644/663 nm) are observed for KLVFF/Cy-5 conjugate in the presence of different metal ions (10 mM for Na^+, K^+, and 200 μM for Ca^{2+} , Mg^{2+}, Cu^{2+}, Zn^{2+}, and Fe^{3+}) as chloride salts in PBS (pH=7.4 at 37ºC).

Cellular uptake and imaging experiments are carried out using a confocal laser scanning microscope on the HeLa and A549 carcinoma cell lines, resulting in bright NIR fluorescence and fast cellular internalization (**Figures 16 and 17**). To verify the mitochondrial selectivity, a colocalization assay involving KLVFF/Cy-5 is performed in fixed carcinoma HeLa and A549 cells with a mitochondria specific fluorescent probe, MitoTracker Red (MTR, $\lambda_{ex}/\lambda_{em}$ 579/599).[50–52] The KLVFF/Cy-5 reveals high levels of colocalization with that of MTR in the confocal fluorescence microscopy with a Pearson's correlation (PC) coefficient: 0.94 and 0.89 for HeLa and A549, respectively (**Figures 16f and 17f**). The KLVFF/Cy-5 is rapidly, extensively and selectively taken up by mitochondria driven by the large negative $\Delta\Psi_m$. Higher magnification confocal laser scanning microscopic image is obtained using 100× objective for the better understanding of mitochondrial selectivity of KLVFF/Cy-5 conjugate (**Figure17g,h**). Higher magnification confocal image shows linear and curved short rods under the microscope with a sharp outline. Mitochondrial target selectivity of KLVFF/Cy-5 conjugate is compared with the control KLVFF/Cy-5c molecule lacking lipophilic cationic TPP^+ functionality, which shows weaker mitochondrial colocalization in confocal microscopy (PC coefficient: 0.63 and 0.65 in HeLa and A549 cells, respectively, **Figure 18**). This suggests that tethering to a target-specific lipophilic cationic TPP^+ containing a NIR Cy-5 chromophore anchored with KLVFF peptide is an efficient strategy for selective mitochondrial targeting and imaging.

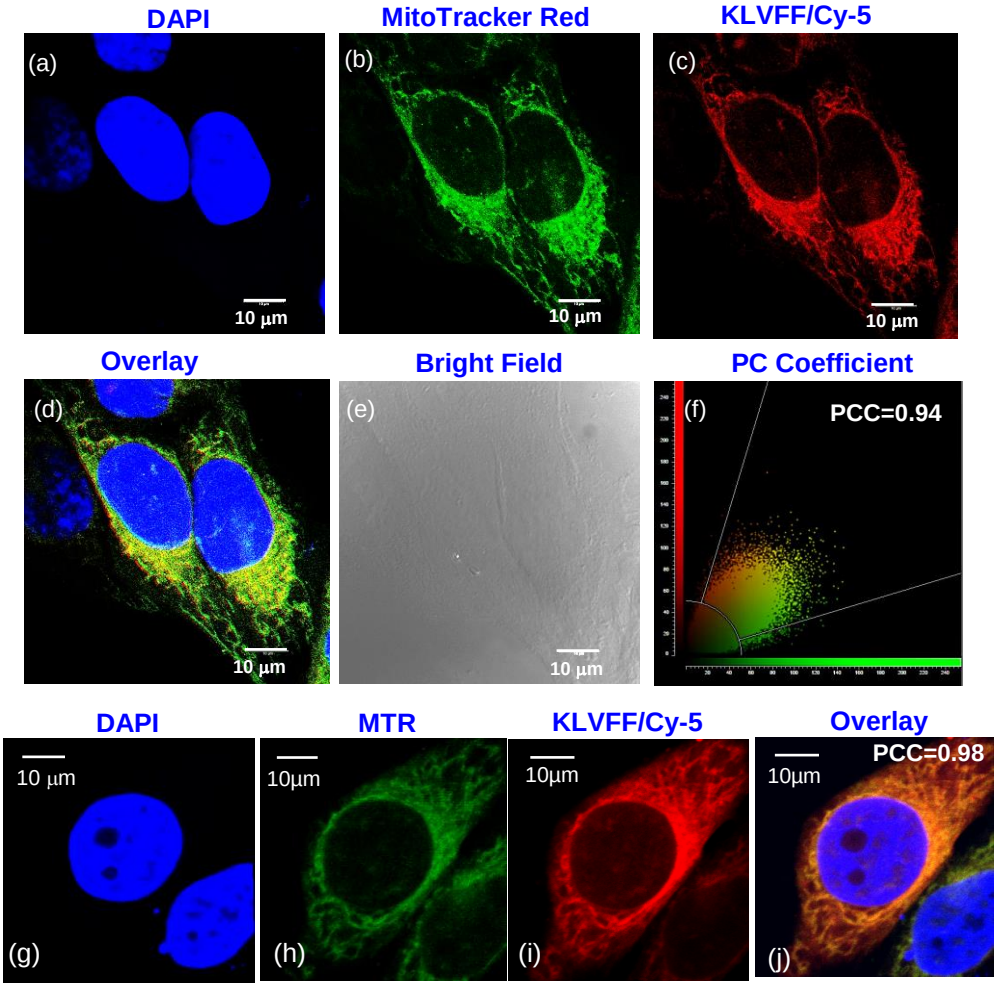

Figure 16. (a-e, g-j) Confocal microscopic images of KLVFF/Cy-5 conjugate colocalized with MitoTracker Red (MTR) in fixed HeLa carcinoma cells. DAPI (blue channel), MTR (green channel), and KLVFF/Cy-5 (red channel) are recorded using laser excitation wavelengths at 405 nm, 561 nm, and 635nm, respectively. (f) Colocalization scatter plot shows Pearson's correlation coefficient (PCC) 0.94.

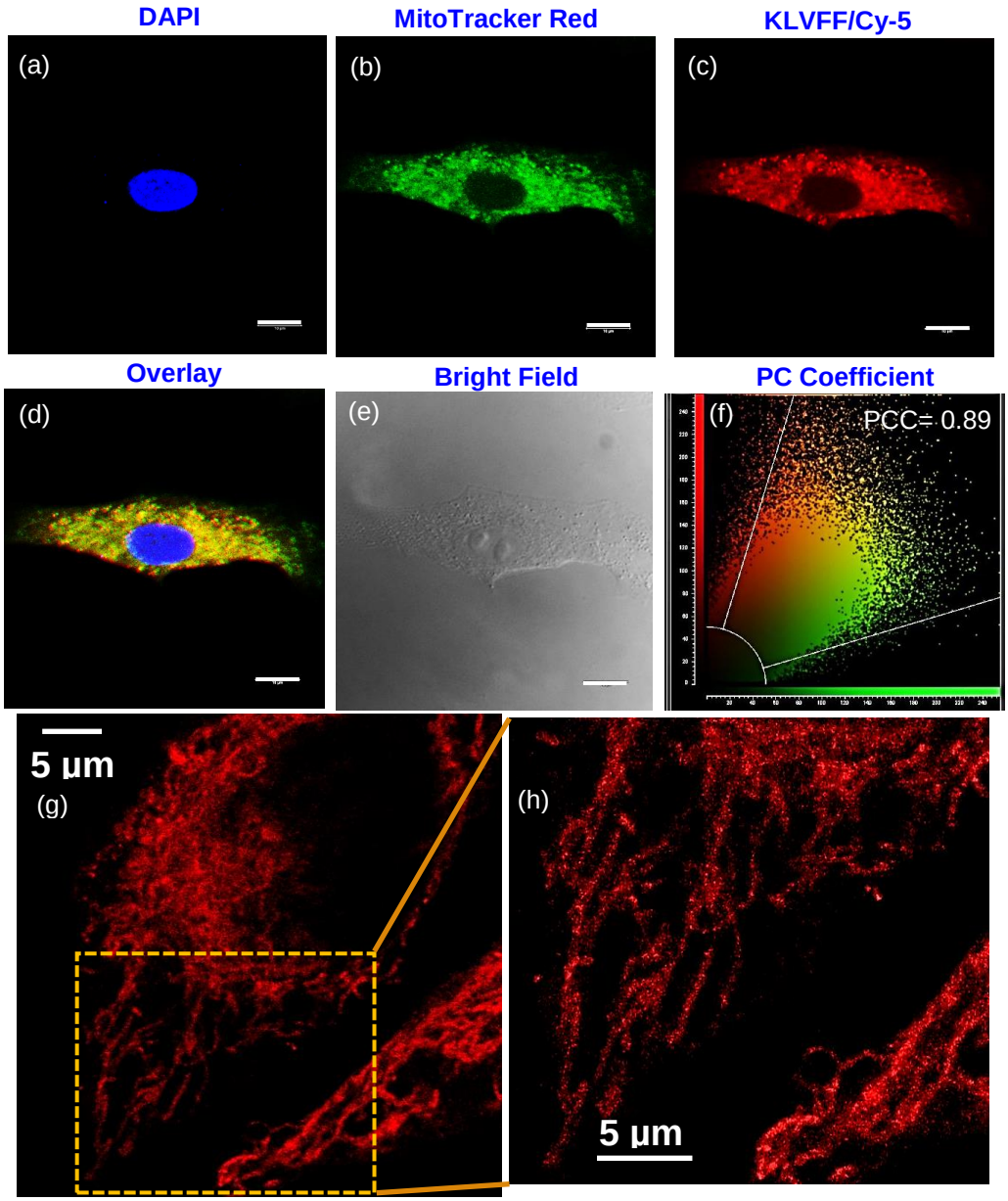

Figure 17. (a-e) Confocal microscopic images of KLVFF/Cy-5 colocalized with MTR in fixed A549 carcinoma cells (scale bar 10 µm). (f) Colocalization scatter plot displays Pearson's correlation (PC) coefficient: 0.89. (g,h) Higher magnification confocal microscopic images of fixed HeLa cell treated with KLVFF/Cy-5 (λ_{ex} 645 nm) indicates mitochondrial staining.

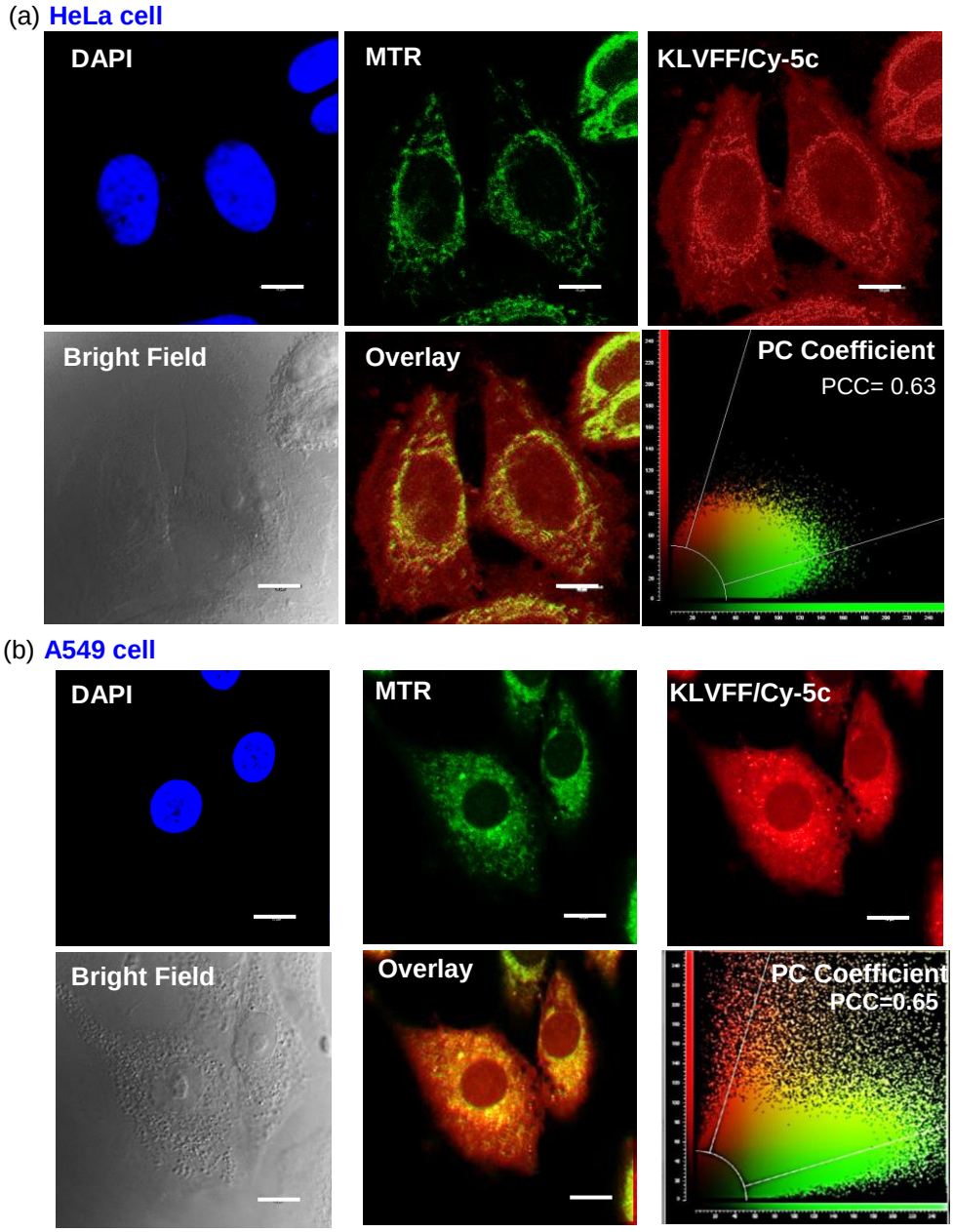

Figure 18. Confocal microscopic images of a control molecule KLVFF/Cy-5c colocalized with MitoTracker Red (MTR) in fixed (a) HeLa and (b) A549 cells (scale bar 10 μm) shows weaker mitochondrial colocalization in CLSM.

Cellular Dysfunction:

Targeting of malignant mitochondria and activation of the cell death machinery by modulating $\Delta\Psi_m$ and stimulating mitochondrial membrane permeabilization is one of the most promising approaches for the development of anticancer agents. The accumulation of KLVFF/Cy-5 molecules inside the mitochondria is expected to be 500–1000 times higher than that of extracellular space because $(\Delta\Psi_m)_{cancer} \sim -220$ mV in comparison with plasma membrane potential, $\Delta\Psi_p$ – 30 to –60 mV.[53] Cell viability studies using MTT assay shows that the KLVFF/Cy-5 exhibits cytotoxicity against human epithelioid cervix carcinoma HeLa cells and lung carcinoma A549 cells (**Figure 19a**). The IC_{50} values for KLVFF/Cy-5 against HeLa and A549 cells is determined at a dosage-dependent manner and are found 4.0 μM and 3.0 μM, respectively at 24 h. For a control experiment using HeLa and A549 cell lines without the addition of KLVFF/Cy-5 we observed abnormally fast cell growth over time. Fluorescence assay revealed that the accumulation values of KLVFF/Cy-5 molecules inside the mitochondria of HeLa cells are 3.2 ± 0.7 mM and 6.1 ± 0.5 mM (for A549 cells 5.4 ± 0.4 mM and 10.5 ± 0.6 mM) compared to the original external concentration in the culture medium of 5 μM and 10 μM, respectively (**Figure 19b,c**).The CAC of KLVFF/Cy-5 is found to be 3.7 μM using surface tension analysis (**Figure 19d**). Cytotoxicity study using healthy human cell lines such as lung fibroblast (WI38) and human embryonic kidney (HEK293) is performed. These normal healthy cells are separately treated with KLVFF/Cy-5 at various concentrations over 24 h. At 4.0 μM concentration (IC_{50} dose for carcinoma cells), ca. 17% of normal cell death occurred after 24 h, which signifies that the KLVFF/Cy-5 conjugate is comparatively more toxic for cancer cell than normal cell. KLVFF/Cy-5 molecule is expected to

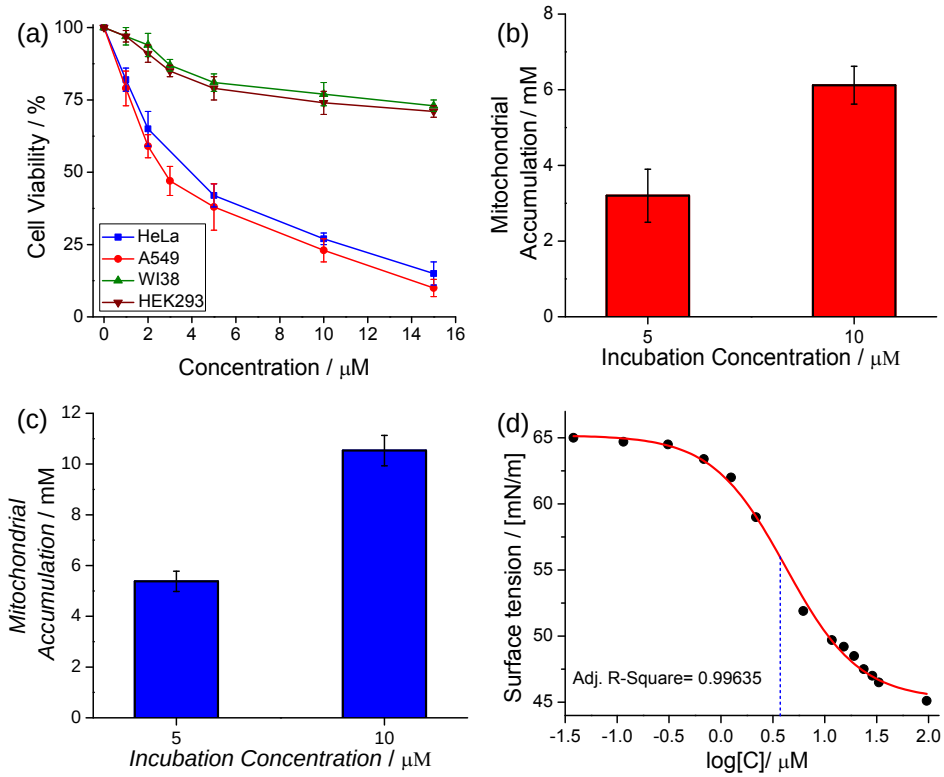

Figure 19. (a) Cell viability studies against HeLa and A549 carcinoma cell lines and WI38 and HEK293 normal cell lines over 24 h. (b,c) Concentration of KLVFF/Cy-5 inside the mitochondria of HeLa and A549 cells respectively after incubation with 5 μM and 10 μM. (d) Surface tension values as a function of log [KLVFF/Cy-5 concentration] to determine CAC.

accumulate more in the cancer cell mitochondria than noncancerous cell mitochondria due to more hyperpolarized $\Delta\Psi_m$ [$(\Delta\Psi_m)_{cancer}$ –220 mV] of cancer cells compared to normal healthy cells [$(\Delta\Psi_m)_{normal}$ –150 to –180 mV]. We proposed that after selective mitochondrial internalization of KLVFF/Cy-5 molecules in HeLa and A549 cancer cells, the CAC reached and self-assemble to form amyloid fibrils via cross-β-sheet structure inside the malignant mitochondria leading to mitochondrial dysfunction and cytotoxicity (**Figure**

20). Moreover, the noncovalent interaction of the KLVFF/Cy-5 fibrils with malignant mitochondrial proteins may also help to induce mitochondrial dysfunction. This suggests that the KLVFF/Cy-5 based target specific supramolecular system not only extremely hampers the growth of the HeLa and A549 carcinoma cell lines but also efficiently induces cytotoxicity. After cellular internalization and selective mitochondrial accumulation, the self-assembling KLVFF residue plays an important role in controlling the cellular function and fate.

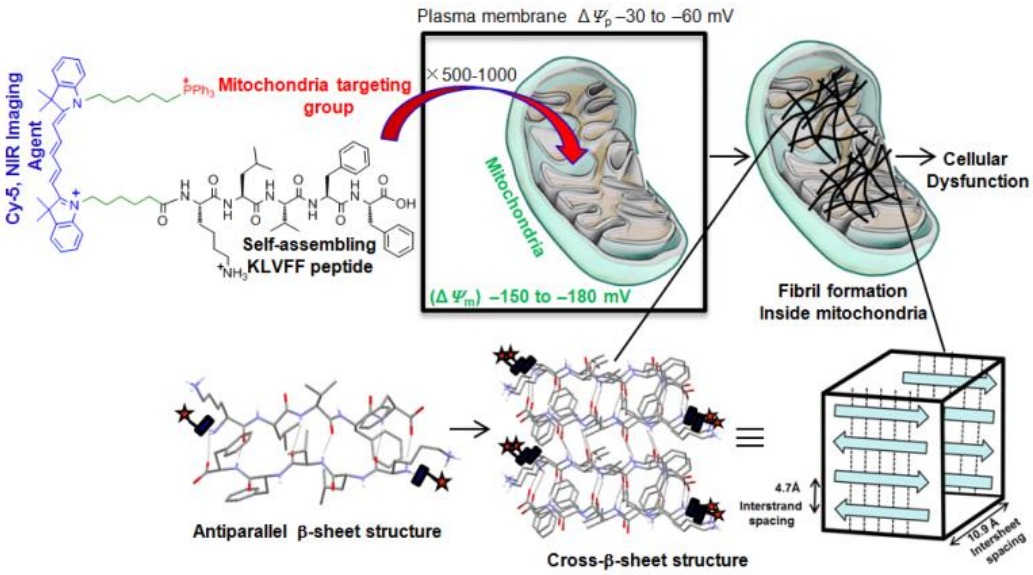

Figure 20. Schematic representation of selective mitochondrial internalization of the KLVFF/Cy-5 molecule and self-assembly to form amyloid fibrils via cross-*β*-sheet inside the mitochondria that leads to mitochondrial dysfunction and cytotoxicity.

Annexin V-FITC/PI Apoptosis Detection Assay:

Both early and late stages of apoptosis are determined using Annexin V-FITC/PI apoptosis assay by fluorescence-activated cell sorting (FACS) with

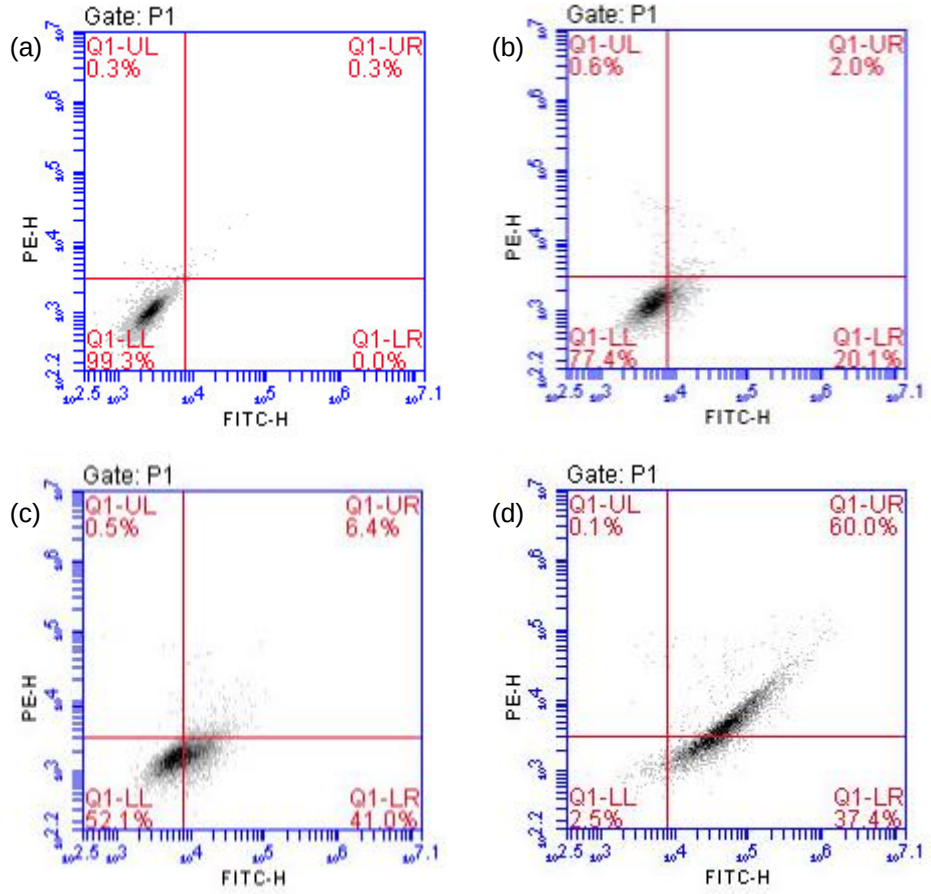

Figure 21. Dose-dependent effect of KLVFF/Cy-5 on apoptosis in A549 cells. (a) Untreated control experiment; (b) cells treated with 1.5 μM, (c) 3 μM, and (d) 10 μM of KLVFF/Cy-5. Lower left quadrant indicates viable cell, both Annexin V and PI −Ve; lower right quadrant: Annexin V +Ve and PI −Ve; upper right quadrant: Annexin V +Ve and PI +Ve; upper left quadrant: Annexin V –Ve and PI +Ve.

varying concentrations of KLVFF/Cy-5.[49] In the untreated control experiment, 99.3% of cells are considered viable [both Annexin V and PI –Ve] (**Figure 21**). In contrast, with increasing doses of KLVFF/Cy-5 (1.5 μM, 3 μM) there are an increase in A549 cells undergoing early apoptosis (Annexin V +Ve and PI

–Ve) (**Figure 21**). Annexin V staining is observed through exposed phosphatidylserine (PS, normally present in the inner leaflet of the healthy plasma membrane) recognition on the apoptotic cell, which signifies early apoptosis. After incubation with a high dose (10 μM) of KLVFF/Cy-5, the membrane ruptures and both Annexin V and PI are positive, suggesting late stages of apoptosis (**Figure 21d**).

The Targeted cationic KLVFF/Cy-5 molecule has been selectively incorporated inside the mitochondria [large negative $(\Delta \Psi_m)_{cancer} \sim -220$ mV]. It reaches the CAC and self-assembles to form amyloid fibrils via cross-β-sheet structure inside the malignant mitochondria. Hence mitochondrial membrane depolarizes, PS exposed on the cell surface, consequently, the mitochondrial transition pores are open, membrane is ruptured, and mitochondrial content such as cytochrome c and other pro-apoptotic proteins is leaked into the cytosol, which triggers cell death via apoptotic cascade.

Conclusions

In conclusion, we have used a MW assisted SPPS method for the rapid and effective synthesis of unsymmetrical NIR KLVFF/Cy-5 conjugate. This KLVFF/Cy-5 system holds significant potential for selective targeting and NIR imaging of mitochondria. Here, mitochondria targeted supramolecular chemistry is utilized to trigger programmed cell death. Supramolecular chemistry at the target site may be used for cancer-selective therapy with NIR imaging diagnostics.

REFERENCES

[1] Zhou, J., Du, X., and Xu, B. *Angew. Chem., Int. Ed.* **2016**, 55, 5770−5775.

[2] Acar, H.; Srivastava, S.; Chung, E. J.; Schnorenberg, M. R.; Barrett, J. C.; LaBelle, J. L.; and Tirrell, M. *Adv. Drug Delivery Rev.* 2017, *110−111*, 65−79.

[3] Wang, Q.; Jiang, N.; Fu, B.; Huang, F.; and Liu, J. *Biomater. Sci.* **2019**, *7*, 4888−4911.

[4] Ulijn, R. V.; and Smith, A. M. *Chem. Soc. Rev.* **2008**, *37*, 664−675.

[5] Wang, H.; Feng, Z.; Wang, Y.; Zhou, R.; Yang, Z.; and Xu, B. *J. Am. Chem. Soc.* **2016**, *138*, 16046−16055.

[6] Zhan, J.; Cai, Y.; He, S.; Wang, L.; and Yang, Z. *Angew. Chem., Int. Ed.* **2018**, *57*, 1813−1816.

[7] Tanaka, A.; Fukuoka, Y.; Morimoto, Y.; Honjo, T.; Koda, D.; Goto, M.; and Maruyama, T. *J. Am. Chem. Soc.* **2015**, *137*, 770−775.

[8] Pires, R. A.; Abul-Haija, Y. M.; Costa, D. S.; Novoa-Carballal, R.; Reis, R. L.; Ulijn, R. V.; and Pashkuleva, I. *J. Am. Chem. Soc.* **2015**, *137*, 576−579.

[9] Gao, Y.; Shi, J.; Yuan, D.; and Xu, B. *Nat. Commun.* **2012**, *3*, 1−8.

[10] Baumes, J. M.; Gassensmith, J. J.; Giblin, J.; Lee, J.-J.; White, A. G.; Culligan, W. J.; Leevy, W. M.; Kuno, M.; and Smith, B. D. *Nat. Chem.* **2010**, *2*, 1025−1030.

[11] Zhao, J.; Chu, H.; Zhao, Y.; Lu, Y.; and Li, L. A. *J. Am. Chem. Soc.* **2019**, *141*, 7056−7062.

[12] Yan, R.; Hu, Y.; Liu, F.; Wei, S.; Fang, D.; Shuhendler, A. J.; Liu, H.; Chen, H.-Y.; and Ye, D. *J. Am. Chem. Soc.* **2019**, *141*, 10331−10341.

[13] Jungbauer, L. M.; Yu, C.; Laxton, K. J.; and LaDu, M. J. *J. Mol. Recognit.* **2009**, *22*, 403−413.

[14] Salveson, P. J.; Haerianardakani, S.; Thuy-Boun, A.; Yoo, S.; Kreutzer, A. G.; Demeler, B.; and Nowick, J. S. *J. Am. Chem. Soc.* **2018**, 140, 11745−11754.

[15] Lee, J. K.; Wang, K.; Park, M. H.; Kim, N.; Lee, J. Y.; Jin, H. K.; Kim, I.-S.; Lee, B.-H.; and Bae, J. *Brain Res.* **2016**, *1646*, 514−521.

[16] Soto, C. *Nat. Rev. Neurosci.* **2003**, *4*, 49−60.

[17] Aguzzi, A.; and O'Connor, T. *Nat. Rev. Drug Discovery* **2010**, *9*, 237−248.

[18] Chiti, F.; and Dobson, C. M. *Annu. Rev. Biochem.* **2017**, *86*, 27−68.

[19] Jung, H. S.; Lee, J.-H.; Kim, K.; Koo, S.; Verwilst, P.; Sessler, J. L.; Kang, C.; and Kim, J. S. *J. Am. Chem. Soc.* **2017**, *139*, 9972−9978.

[20] Zielonka, J.; Joseph, J.; Sikora, A.; Hardy, M.; Ouari, O.; Vasquez-Vivar, J.; Cheng, G.; Lopez, M.; and Kalyanaraman, B. *Chem. Rev.* **2017**, *117*, 10043−10120.

[21] Thomas, A. P.; Palanikumar, L.; Jeena, M. T.; Kim, K.; and Ryu, J.-H. *Chem. Sci.* **2017**, *8*, 8351−8356.

[22] He, H.; Wang, J.; Wang, H.; Zhou, N.; Yang, D.; Green, D. R.; and Xu, B. *J. Am. Chem. Soc.* **2018**, *140*, 1215−1218.

[23] Han, X.; Wang, R.; Song, X.; Yu, F.; Lv, C.; and Chen, L. *Biomaterials* **2018**, *156*, 134−146.

[24] Qu, A.; Huang, F.; Li, A.; Yang, H.; Zhou, H.; Long, J.; and Shi, L. *Chem. Commun.* **2017**, *53*, 1289−1292.

[25] Hamley, I. W. *Chem. Rev.* **2012**, *112*, 5147−5192.

[26] Mason, S. J.; and Balasubramanian, S. *Org. Lett.* **2002**, *4*, 4261−4264.

[27] Barbero, N.; Magistris, C.; Park, J.; Saccone, D.; Quagliotto, P.; Buscaino, R.; Medana, C.; Barolo, C.; and Viscardi, G. *Org. Lett*. **2015**, 17, 3306−3309.

[28] Kappe, C. O.; Pieber, B.; and Dallinger, D. *Angew. Chem., Int. Ed.* **2013**, *52*, 1088−1094.

[29] Polshettiwar, V.; and Varma, R. S. *Acc. Chem. Res.* **2008**, *41*, 629−639.

[30] Danial, N. N.; and Korsmeyer, S. J. *Cell* **2004**, *116*, 205−219.

(31) Noh, I.; Lee, D. Y.; Kim, H.; Jeong, C.-U.; Lee, Y.; Ahn, J.-O.; Hyun, H.; Park, J.-H.; and Kim, Y.-C. *Adv. Sci.* **2018**, *5*, 1700481.

.[32] Jeena, M. T.; Palanikumar, L.; Go, E. M.; Kim, I.; Kang, M. G.; Lee, S.; Park, S.; Choi, H., Kim; C., and Jin, S.-M., et al. *Nat. Commun.* **2017**, *8*, 1−10.

[33] Jeena, M. T.; Jeong, K.; Go, E. M.; Cho, Y.; Lee, S.; Jin, S.; Hwang, S.-W.; Jang, J. H.; Kang, C. S.; Bang, W.-Y.; et al. *ACS Nano* **2019**, *13*, 11022−11033.

[34] Saha, P. C., Chatterjee, T., Pattanayak, R., Das, R. S., Mukherjee, A., Bhattacharyya, M., and Guha, S. *ACS Omega* **2019**, *4*, 14579−14588.

[35] Thomas, A. P., Palanikumar, L., Jeena, M. T., Kim, K., and Ryu, J.-H. *Chem. Sci*. **2017**, *8*, 8351−8356.

[36] Barbero, N., Magistris, C., Park, J., Saccone, D., Quagliotto, P., Buscaino, R., Medana, C., Barolo C., and Viscardi, G. *Org. Lett*. **2015**, *17*, 3306–3309.

[37] Jeena, M. T., Palanikumar, L., Go, E. M., Kim, I., Kang, M. G., Lee, S., Park, S., Choi, H., Kim, C., Jin, S.-M., et al. *Nat. Commun.* **2017**, *8*, 1– 10.

[38] Jiang, R.-D., Shen, H., and Piao, Y.-J. *Rom. J. Morphol. Embryol.* **2010**, *51*, 663–667.

[39] Mitra, K.; Lyons, C. E.; and Hartman, M. C. T. *Angew. Chem., Int. Ed.* 2018, 57, 10263−10267.

[40] Jiang, Q.; Xu, X.; Yin, P.-A.; Ma, K.; Zhen, Y.; Duan, P.; Peng, Q.; Chen, W.-Q.; and Ding, B. *J. Am. Chem. Soc.* **2019**; *141*, 9490−9494.

[41] Sun, W.; Guo, S.; Hu, C.; Fan, J.; and Peng, X. *Chem. Rev.* **2016**, *116*, 7768−7817.

[42] Tan, X.; Constantin, T. P.; Sloane, K. L.; Waggoner, A. S.; Bruchez, M. P.; and Armitage, B. A. *J. Am. Chem. Soc.* **2017**, *139*, 9001−9009.

[43] Mishra, A.; Behera, R. K.; Behera, P. K.; Mishra, B. K.; and Behera, G. B. *Chem. Rev.* **2000**, *100*, 1973−2012.

[44] Pisoni, D. S.; Todeschini, L.; Borges, A. C. A.; Petzhold, C. L.; Rodembusch, F. S.; and Campo, L. F. *J. Org. Chem.* **2014**, *79*, 5511−5520.

[45] Reches, M.; and Gazit, E. *Science* **2003**, *300*, 625−627.

[46] Krysmann, M. J.; Castelletto, V.; Kelarakis, A.; Hamley, I. W.; Hule, R. A.; and Pochan, D. J. *Biochemistry* **2008**, *47*, 4597−4605.

[47] Balbach, J. J.; Ishii, Y.; Antzutkin, O. N.; Leapman, R. D.; Rizzo, N. W.; Dyda, F.; Reed, J.; and Tycko, R. *Biochemistry* **2000**, *39*, 13748−13759.

[48] Malinchik, S. B.; Inouye, H.; Szumowski, K. E.; and Kirschner, D. *A. Biophys. J.* **1998**, *74*, 537−545.

[49] Hamley, I. W. *Angew. Chem., Int. Ed.* **2007**, *46*, 8128−8147.

[50] Appiah Kubi, G.; Qian, Z.; Amiar, S.; Sahni, A.; Stahelin, R. V.; and Pei, D. *Angew. Chem., Int. Ed.* **2018**, *57*, 17183−17188.

[51] Kawazoe, Y.; Shimogawa, H.; Sato, A.; and Uesugi, M. *Angew. Chem., Int. Ed.* **2011**, *50*, 5478−5481.

[52] Ning, J.; Huang, B.; Wei, Z.; Li, W.; Zheng, H.; Ma, L.; Xing, Z.; Niu, H.; and Huang, W. *Mol. Med. Rep.* **2017**, *15*, 3761−3766.

[53] Weinberg, S. E.; and Chandel, N. S. *Nat. Chem. Biol.* **2015**, *11*, 9−15.

[54] Liu, T.; Roh, S. E.; Woo, J. A.; Ryu, H.; and Kang, D. E. *Cell Death Dis.* **2013,** *4*, e476.

Chapter 5

Self-Assembly of Dipeptide-Based Near-Infrared Fluorescent Nanotubes for Cellular Mitochondria Targeted Imaging and Early Apoptosis

Introduction

Targeting of specific cellular organelle by self-assembly of biological building blocks such as peptides using the "bottom-up" approach is an emerging field of current research.[1–11] Development of one-dimensional nanotubes through noncovalent interactions from self-assembling peptides have been widely used in biomedical sciences including glucose transporters, artificial ion channels, antibiotics, storage of drugs, and in other fields of bionano science.[12–17] Phe-Phe (FF, portion of amyloid β, A$\beta_{19–20}$) dipeptide is a bioinspired supramolecular building block that self-assemble to form nanotubes which possess unique mechanical as well as electrical properties and has been widely used in the fabrication of electrochemical biosensors, production of nanowires, development of nanocables, and delivery of oligonucleotides.[18–24] However, there is a genuine need for the design of visible to near-infrared (NIR) emitting self-assembling nanotubes with biological function that can selectively target and accumulate at a specific cellular organelle. NIR light emitting self-assembling peptide biomarkers (650–900 nm) are superior over the visible light emitting peptides for biological imaging application because NIR light has strong tissue penetration with the least autofluorescence background.[25–29] However, the precise control of the self-assembly processes of peptide biomarkers to form uniform nanotubes is a challenging task. Among the innumerable cellular organelles, mitochondria are a key target.[30–33] Mitochondria are the powerhouse of cells, regulate cellular function, and control programmed cell death such as apoptosis.[34–37] Selective targeting and imaging of malignant mitochondria are the fundamental steps for early detection, diagnosis, and design of drug molecules. However, in contrast to other intracellular organelles, mitochondria

are challenging to target due to their unique double layer membrane as well as extremely negative potential of inner mitochondrial membrane (IMM) [$(\Delta\Psi_m)_{cancer} \approx -220$ mV] which act as a fence for the uptake of molecules.[38] We exploited the unusual biophysical membrane property of malignant mitochondria to target IMM. The FF dipeptide anchored with unsymmetrical visible Cy–3 and NIR Cy–5 chromophores comprising a mitochondria specific triphenylphosphonium (TPP^+) group are constructed using a microwave (MW) aided Fmoc solid phase peptide synthesis (SPPS) procedure on the Wang resin. Cy–3-TPP/FF as well as Cy–5-TPP/FF molecules self-assemble to form visible and NIR nanotubes, respectively, in solution. The synthesized visible and NIR dipeptide-based molecules are used for selective targeting and imaging of mitochondria in human HeLa epithelioid cervix carcinoma as well as A549 lung carcinoma living cells, which is monitored through confocal laser scanning microscopy (CLSM). The mitochondria-targeting TPP^+ group is effective for transporting the supramolecular peptide building block with NIR imaging functionality into the mitochondrial interior.[39,40] These lipophilic delocalized cationic dipeptide-based fluorescent molecules penetrate cells facilely, accumulate specifically at the negatively charged malignant mitochondrial site, attain the critical aggregation concentration (CAC) inside the mitochondria, and induce early apoptosis.

Experimental Methods

General Methods and Materials

Synthesis, Purification, and Characterization of Unsymmetrical Cy–3-TPP and Cy–5-TPP Dyes:

Unsymmetrical Cy–3-TPP and Cy–5-TPP dyes and their associated precursor molecules were constructed using microwave (MW) method outlined

in **Scheme 1**. TLC was performed on silica gel coated aluminium sheets (TLC silica gel 60 F_{254}) using appropriate solvent system and identified by naked eye or UV lamp. The products were purified by column chromatographic technique using silica gel (100-200 mesh) as a stationary phase. The solvents were distilled using appropriate drying agent and used for column chromatography. (6-Bromohexyl)triphenylphosphonium bromide, 1-[5-Carboxypentyl)-2,3,3-trimthyl-3H-indolium] bromide (compound 1), and [6-(3,3-Dimethyl-2-methyleneindolin-1-yl)hexyl]triphenylphosphonium bromide (compound 2) were synthesized by the reported procedure that mentioned in chapter 4.[27]

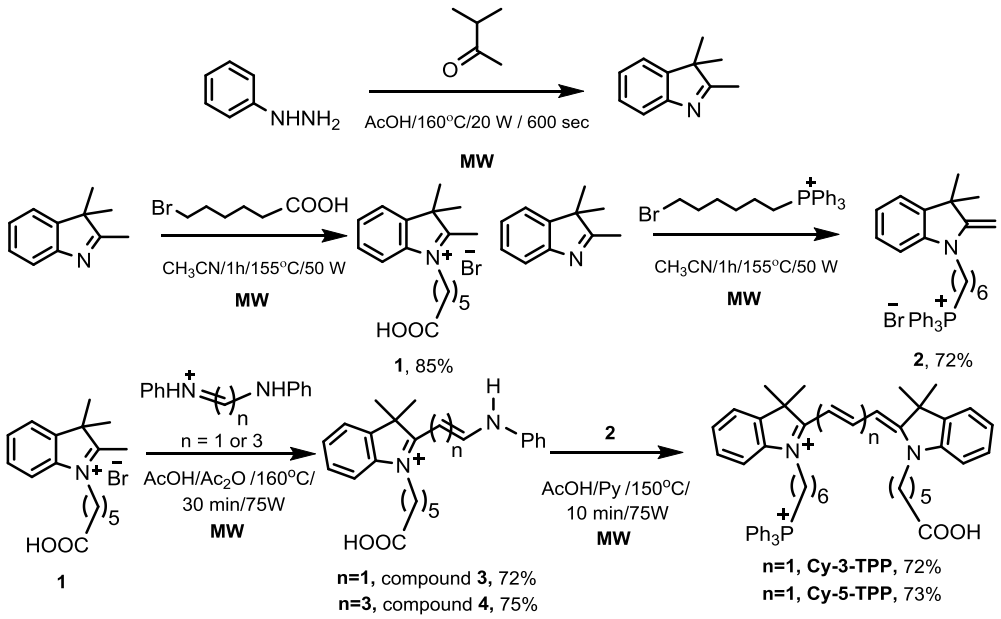

Scheme 1. Synthesis of Cy–3-TPP, Cy–5-TPP, and their associated precursor molecules using MW method.

The one-carbon spacer precursor *N*,*N*′-diphenylformamidine for the synthesis of Cy–3-TPP was prepared from the commercially available triethyl orthoformate and aniline under acidic condition. The three-carbon spacer

precursor malonaldehyde bis(phenylimine) monohydrochloride for the construction of Cy–5-TPP was synthesized by condensation between 1,1,3,3-tetramethoxypropane and aniline, under acidic condition.[41] 2,3,3-trimethylindolenine was synthesized by the Fischer indole synthesis from phenylhydrazine hydrochloride and 3-methyl-2-butanone in glacial AcOH under MW irradiation for 10 min at 160°C, 20 W.[27]

Intermediate for Cy–3-TPP and Cy–5-TPP Synthesis: The influence of temperature and time are scrutinized on the yield of the reaction, maintaining indolium salt/*N*,*N*′-diphenylformamidine and indolium salt/malonaldehyde bis(phenylimine) monohydrochloride mole ratio constant, for Cy–3-TPP and Cy–5-TPP, respectively (**Table 1**). Compound **4** (intermediate of Cy–5-TPP) was synthesized following the same MW synthesized protocol that was already mentioned in chapter 4.[27]

Table 1. Synthesis of the intermediates **3** and **4**

Compound	Temperature (ºC)	Time (min)	Yield (%)
3	120	15	25
3	120	30	45
3	150	15	33
3	150	30	61
3	160	15	40
3	160	30	72
4	120	15	20
4	120	30	40
4	150	15	35
4	150	30	64
4	160	15	42
4	160	30	75

(*E*)-1-(5-carboxypentyl)-3,3-dimethyl-2-(2-(phenylamino)vinyl)-3*H*-indol-1-ium bromide (3, intermediate of Cy–3-TPP): Compound 1 (0.71 g, 2.0 mmol) and *N*,*N*′-diphenylformamidine (1.18 g, 6.0 mmol) were dissolved in Ac_2O:AcOH (1:1, 5 mL) and heated in the MW system for 30 m at 160ºC. The reaction mixture was allowed to cool to room temperature and the solvent was removed under reduced pressure. To the reaction mixture cold Et_2O was added to get a dark orange precipitate. The resulting dark orange residue was extracted with DCM and H_2O and the organic layer was concentrated. The resulting residue was purified via column chromatography using DCM:MeOH (98:2) to get the intermediate **3** as dark orange colored solid.

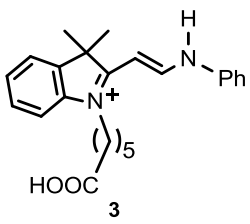

3

Yield: 0.66 g (72%).

^{1}H NMR (300 MHz, DMSO-d_6, 25°C): δ = 12.01 (1H, br), 8.36 (1H, t, J = 13.5 Hz), 7.65 (1H, d, J = 7.5 Hz), 7.56 (1H, d, J = 6.9 Hz), 7.49–7.39 (4H, m), 7.33–7.27 (2H, m), 7.09–6.98 (1H, m), 6.54 (1H, d, J = 13.5 Hz), 4.13 (2H, t, J = 6.3 Hz), 3.98–3.94 (1H, m), 2.22 (2H, t, J = 7.2 Hz), 1.70 (6H, s), 1.61–1.52 (4H, m), 1.47–1.42 (2H, m) ppm.

^{13}C NMR (75 MHz, DMSO-d_6, 25°C): δ = 174.9, 174.5, 158.0, 145.1, 142.5, 141.3, 129.3, 125.8, 123.1, 113.1, 103.0, 49.5, 34.1, 28.1, 27.4, 26.3, and 24.9 ppm.

HRMS (ESI +ve) *m*/*z*: Observed for $C_{24}H_{29}N_2O_2^+$ $[M]^+$ = 377.2227, $[M]^+$calcd = 377.2224.

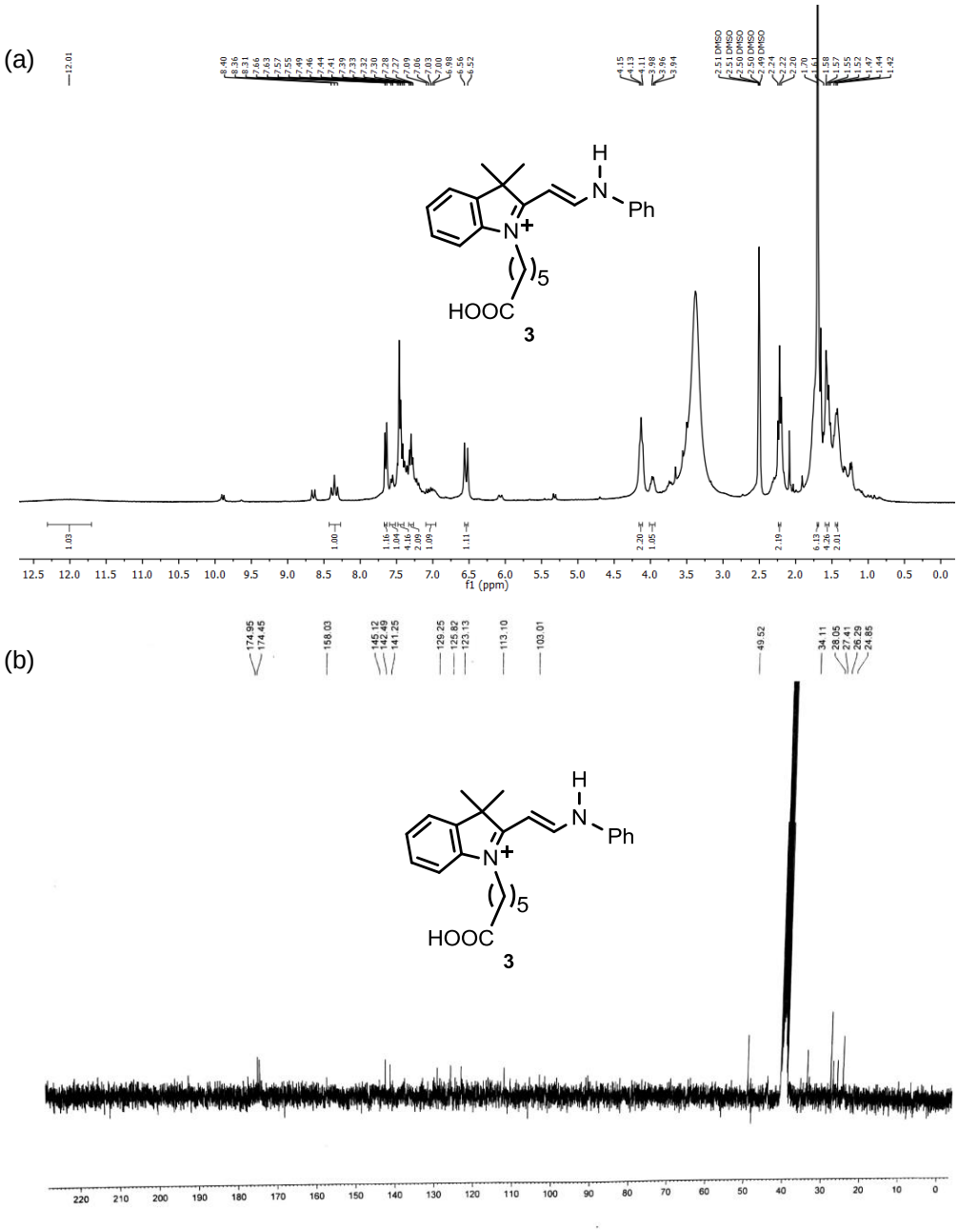

Figure 1. (a) ^{1}H NMR (300MHz, DMSO-d_6, 25°C) spectrum and (b) ^{13}C NMR (75 MHz, DMSO-d_6, 25°C) spectrum of compound 3 (intermediate of Cy–3-TPP).

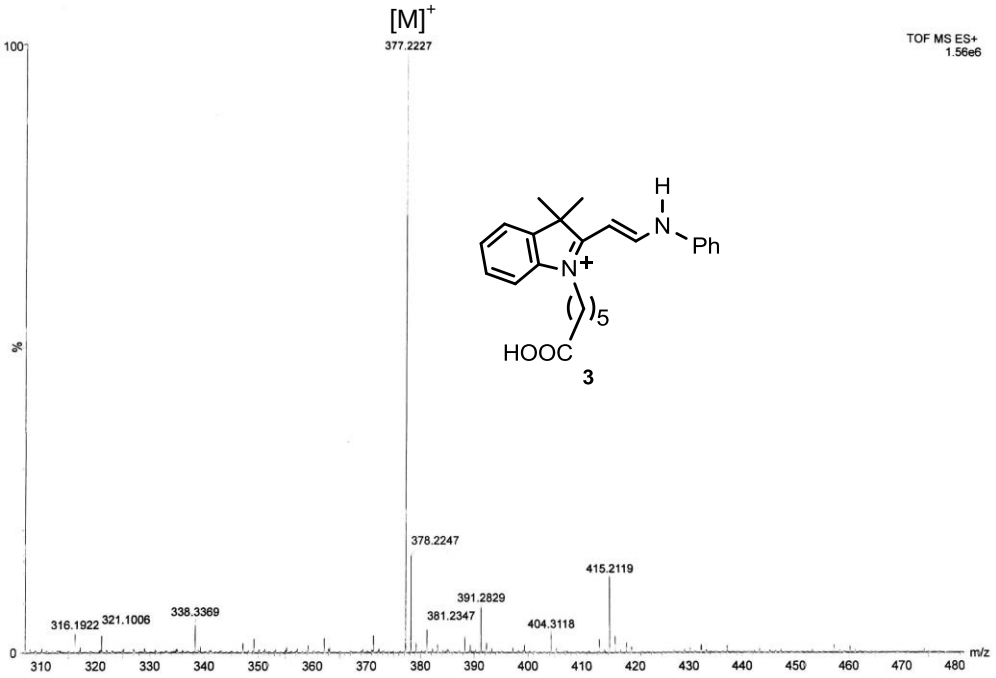

Figure 2. HRMS (ESI +ve) spectrum of compound 3 (intermediate of Cy–3-TPP).

1-(5-carboxypentyl)-3,3-dimethyl-2-((1*E*,3*E*)-4-(phenylamino)buta-1,3-dien-1-yl)-3*H*-indol-1-ium bromide (4, intermediate of Cy–5-TPP): Compound **1** (0.35 g, 1.0 mmol) and malonaldehyde bis(phenylimine) monohydrochloride (0.78 g, 3.0 mmol) were taken in a MW vessel equipped with a magnetic bar and dissolved in Ac_2O:AcOH (1:1, 4 mL). The reaction mixture was capped and irradiated at 160ºC for 30 m. The reaction mixture was cooled to room temperature and the solvent was removed under reduced pressure. To the resulting solution cold Et_2O was added to obtain a dark green precipitate. This dark green residue was extracted with DCM and H_2O and the organic layer was collected and concentrated under reduced pressure. The dark green residue was

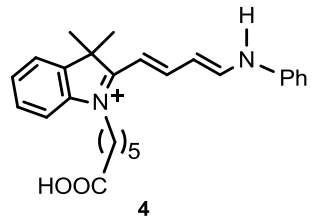

purified via column chromatography using DCM:CH_3OH (98:2) to obtain the intermediate **4** as a scurf green solid.

Yield: 0.36 g (75%).

Synthesis of unsymmetrical Cy–3-TPP and Cy–5-TPP dyes: Time and temperature are optimized on the yield of the reaction, keeping indolium salt/compound **3** and indolium salt/compound **4** mole ratio invariable for the development of Cy**–**3-TPP and Cy**–**5-TPP, respectively (**Table 2**). Meanwhile, Cy**–**5-TPP was synthesized following the same literature procedure that described in chapter 4.[27]

Table 2. Synthesis of Cy–3-TPP and Cy–5-TPP using conventional and microwave methods.

Compound	Temperature (ºC)	Time (min)	Method	Yield (%)
Cy–3-TPP	130	360	A	33
Cy–3-TPP	120	5	B	42
Cy–3-TPP	120	10	B	60
Cy–3-TPP	130	5	B	44
Cy–3-TPP	130	10	B	65
Cy–3-TPP	150	5	B	48
Cy–3-TPP	150	10	B	72
Cy–5-TPP	130	360	A	33
Cy–5-TPP	120	5	B	35
Cy–5-TPP	120	10	B	60
Cy–5-TPP	130	5	B	41
Cy–5-TPP	130	10	B	66
Cy–5-TPP	150	5	B	55
Cy–5-TPP	150	10	B	73

A: Conventional method: (a) Ac_2O/AcOH, 4h, reflux,

(b) AcOH/ Py, 2h, reflux; B: Microwave method

Cy–3-TPP: The intermediate **3** (0.14 g, 0.30 mmol) was dissolved in pyridine:AcOH (1:1, 1 mL each) in a MW vessel equipped with a magnetic stir bar. Compound **2** (0.19 g, 0.33 mmol) was added to it and the MW vessel was sealed with a cap and subjected to MW irradiation for 10 m at 150°C. The reaction mixture was allowed to cool to room temperature and Et_2O was added to get a red colored residue and was kept overnight in the refrigerator. The red solid was collected by filtration and washed with Et_2O (3 × 5 mL). The crude product was purified by silica gel column chromatography using DCM:MeOH (90:10) (R_f = 0.55, visible without staining, pink color) to obtain the desired compound Cy–3-TPP as a red solid.

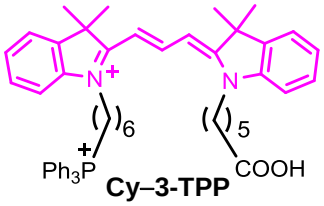

Cy–3-TPP

Yield: 0.21 g (72%).

^{1}H NMR (500 MHz, DMSO-d_6, 25°C): δ = 12.01 (1H, br), 8.35 (1H, t, J = 13.5 Hz), 7.92–7.74 (15H, m), 7.64 (2H, d, J = 7.5 Hz), 7.46–7.42 (4H, m), 7.32–7.29 (2H, m), 6.72 (1H, d, J = 13.0 Hz), 6.57 (1H, d, J = 13.5 Hz), 4.12–4.08 (4H, m), 3.63–3.56 (2H, m), 2.20 (2H, t, J = 6.5 Hz), 1.68 (12H, s), 1.58–1.46 (12H, m), 1.25–1.23 (2H, m) ppm. ^{13}C NMR (125 MHz, DMSO-d_6, 25°C): δ = 182.7, 172.0, 145.9, 145.7, 142.3, 139.4, 134.9, 133.6, 133.5, 130.2, 127.7, 127.5, 122.8, 121.9, 118.8, 118.1, 109.1, 48.1, 42.1, 29.5, 27.4, 25.4, 25.3, 22.4, 21.7, 20.5, and 20.1 ppm.

HRMS (ESI +ve) *m/z*: Observed for $C_{53}H_{61}N_2O_2P^{2+}$ $[M]^{2+}$ = 394.2280, $[M]^{2+}$calcd = 394.2230

Photophysical properties in DMSO λ_{abs} = 555 nm, λ_{em} = 572 nm, Stokes shift ($\Delta\lambda$) = 17 nm, ε = 1.50 ×10^5 $M^{-1}cm^{-1}$, Φ_f = 0.19 in EtOH [Φ_f of Rhodamine-B (reference) in absolute EtOH = 0.49].

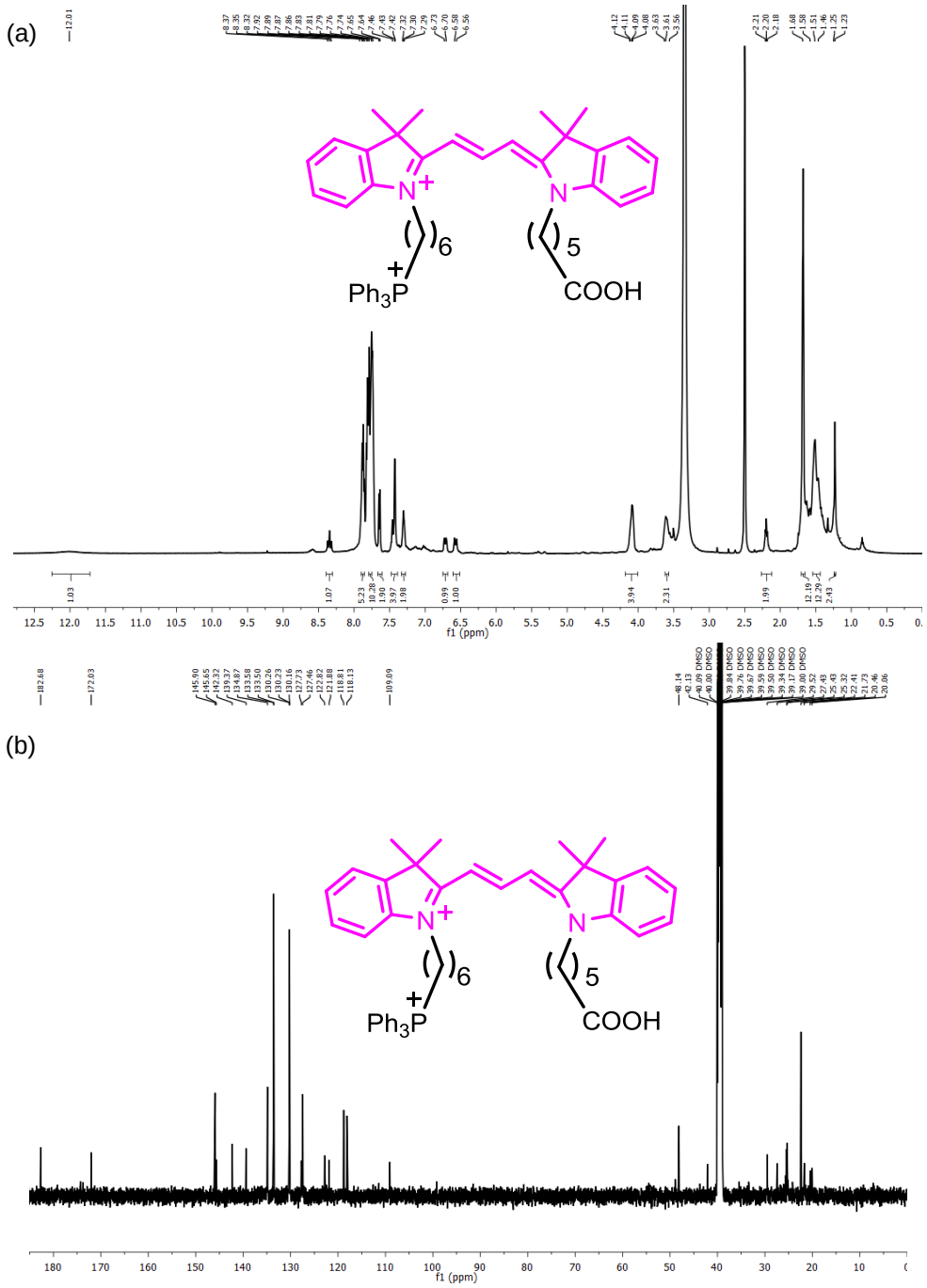

Figure 3. (a) ^{1}H NMR (500 MHz, DMSO-d_6, 25°C) spectrum and (b) ^{13}C NMR (125 MHz, DMSO-d_6, 25°C) spectrum of Cy–3-TPP.

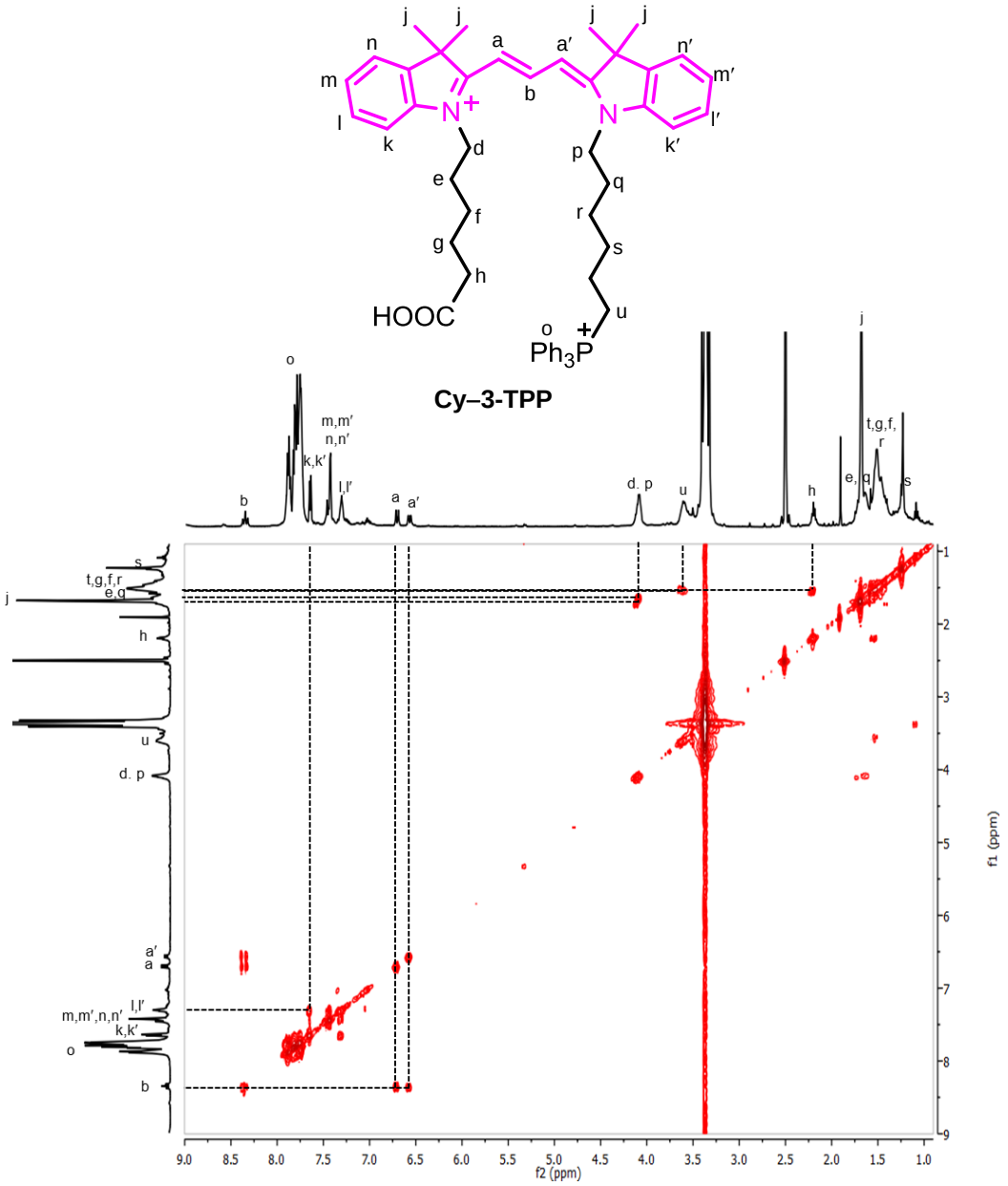

Figure 4. ^{1}H-^{1}H COSY NMR spectrum of Cy–3-TPP (500 MHz, DMSO-d_6, 25°C).

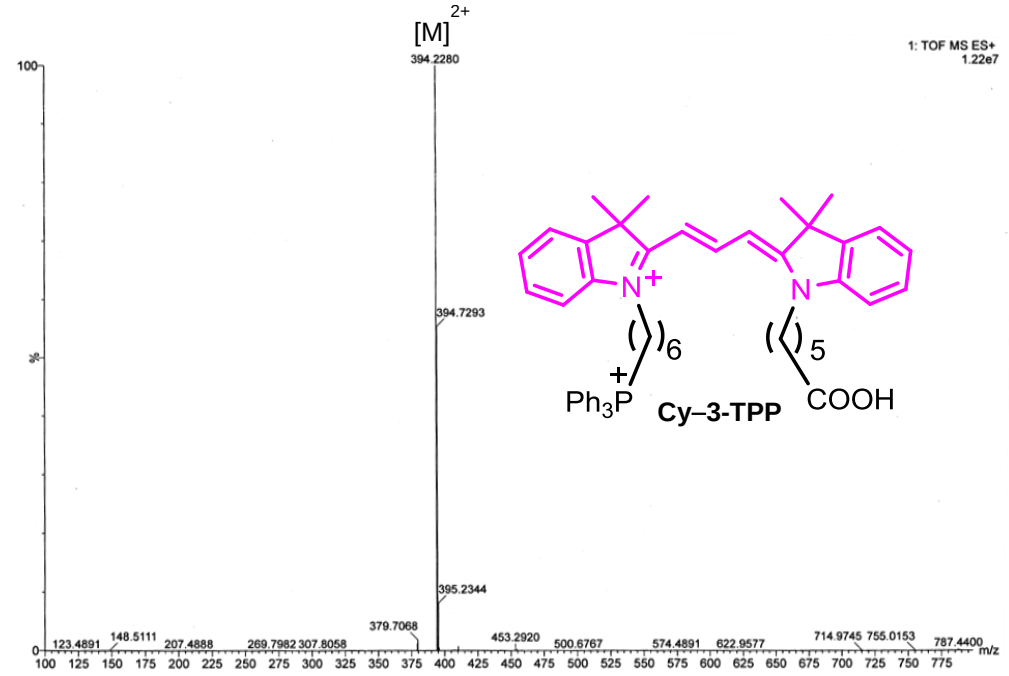

Figure 5. HRMS (ESI +ve) spectrum of Cy–3-TPP.

Cy–5-TPP dye: Compound **4** (0.24 g, 0.50 mmol) was dissolved in pyridine:CH_3COOH (1:1, 2.0 mL each) and taken in a MW vessel furnished with a magnetic stir bar. Compound **2** (0.32 g, 0.55 mmol) was added to the reaction mixture and the MW vessel was capped and subjected to MW irradiation at 150°C for 10 m. The mixture was cooled to room temperature and cold Et_2O was added to obtain a blue colored precipitate and was kept 12 h in the refrigerator. The blue colored residue was filtered and washed with Et_2O (3×10 mL). The crude product was purified by column chromatography using DCM:MeOH (9:1) (R_f = 0.42, blue color) to acquire the pure compound Cy–5-TPP as a blue solid.

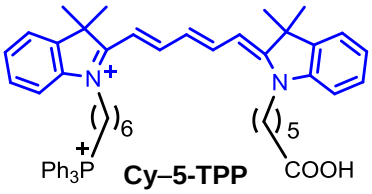

Yield: 0.370 g (76%).

^{1}H NMR (500 MHz, DMSO-d_6, 25°C): δ = 12.00 (1H, br), 8.35 (2H, t, J = 12.8 Hz), 7.91–7.74 (15H, m), 7.63 (2H, d, J = 7.0 Hz), 7.40–7.38 (4H, m), 7.26–7.25 (2H, m), 6.62 (1H, t, J = 12.3 Hz), 6.29 (2H, d, J = 13.7 Hz), 4.10–4.07 (4H, m), 3.62–3.56 (2H, m), 2.19 (2H, t, J = 6.7 Hz), 1.69 (6H, s), 1.68 (6H, s), 1.63–1.52 (10H, m), 1.42–1.39 (4H, m) ppm.

^{13}C NMR (125 MHz, DMSO-d_6, 25°C): δ = 174.2, 172.5, 171.9, 153.9, 141.9, 141.0, 134.8, 133.4, 130.2, 128.4, 125.5, 124.6, 122.4, 118.9, 118.0, 111.0, 103.0, 48.9, 48.5, 43.3, 33.4, 29.4, 29.2, 27.1, 26.6, 25.6, 25.0, 24.1, 21.5, 21.0, 20.5, and 20.0 ppm. HRMS (ESI +ve) *m*/*z*: Observed for $C_{55}H_{63}N_2O_2P^{2+}$ $[M]^{2+}$ = 407.2655, $[M]^{2+}$calcd = 407.2308.

Photophysical properties in $CHCl_3$ λ_{abs} = 660 nm, λ_{em} = 680 nm, Stokes shift ($\Delta\lambda$) = 20 nm, ε = 1.8 ×10^5 $M^{-1}cm^{-1}$, Φ_f = 0.29 in DMSO [Φ_f of Zinc pthalocyanine (reference) in DMSO = 0.20].

Synthesis of Cy–3-TPP/FF and Cy–5-TPP/FF Compounds

Manual MW-Assisted Solid-Phase Peptide Synthesis (SPPS):

Phe-Phe (FF) dipeptide was synthesized by manual microwave (MW)-assisted Fmoc-SPPS procedure on a MW peptide synthesizer (*CEM, Discover Bio*). Wang resin (LL, 0.60 mmol/g loading density) was used to synthesize FF dipeptide, Cy–3-TPP/FF and Cy–5-TPP/FF conjugates.

First Amino Acid (Fmoc-Phe-OH) Loading on Wang Resin: The first amino acid (Fmoc-Phe-OH) loading on Wang resin was performed in a SPE cartridge with frit. The Wang resin (0.1 mmol) was swollen in 2 mL DMF for 1 h, then drains the solvent off and washed with DMF (2×). Fmoc-Phe-OH (5 eq), HBTU (4.9 eq.) and HOBt (5 eq.) was dissolved in 2 mL DCM/DMF (1:1), then DIPEA (10 eq.) was added and the mixture were taken in the SPE

cartridge containing the Wang resin and stirred for 3 h under N_2 bubbling. Drain the solvent and the resin was successively washed with DMF (2×), DCM (2×), MeOH (2×).

After Fmoc-Phe-OH loading on Wang resin, the loading density was calculated by UV/vis analysis of the Fmoc-dibenzofulvene deprotection product.

Estimation of the First Amino Acid Loading: The Fmoc-Phe-Wang resin (5 mg) and 1,8-diazabicyclo[5.4.0]undec-7-en (DBU) in NMP (2 mL, 2 % in NMP) were taken in a 10 mL volumetric flask. It was shaken for 30 min in a shaker then the 10 mL volumetric flask was filled up to the mark with ACN. The solution was diluted with ACN (1/12.5) and transferred to an UV quartz cuvette. The cleaved dibenzofulvene was monitored at 304 nm (ε_{304} = 7624 L $mol^{-1}cm^{-1}$) and corrected against reference. The resin loading was calculated based on Lambert-Beer's law.

$$\rho \text{ (mmol/g)} = 163.96\times(A - A_0)/m$$

ρ = loading density of the resin

A = absorption of a sample

A_0 = absorption of reference

m = mass of the analyzed resin in mg.

MW-Assisted SPPS Synthesis of Cy–3-TPP/FF and Cy–5-TPP/FF Conjugates: The synthesis of Cy–3-TPP/FF and Cy–5-TPP/FF conjugates were carried out using MW-assisted SPPS protocol at a 5 μmol scale outlined in Scheme 2.

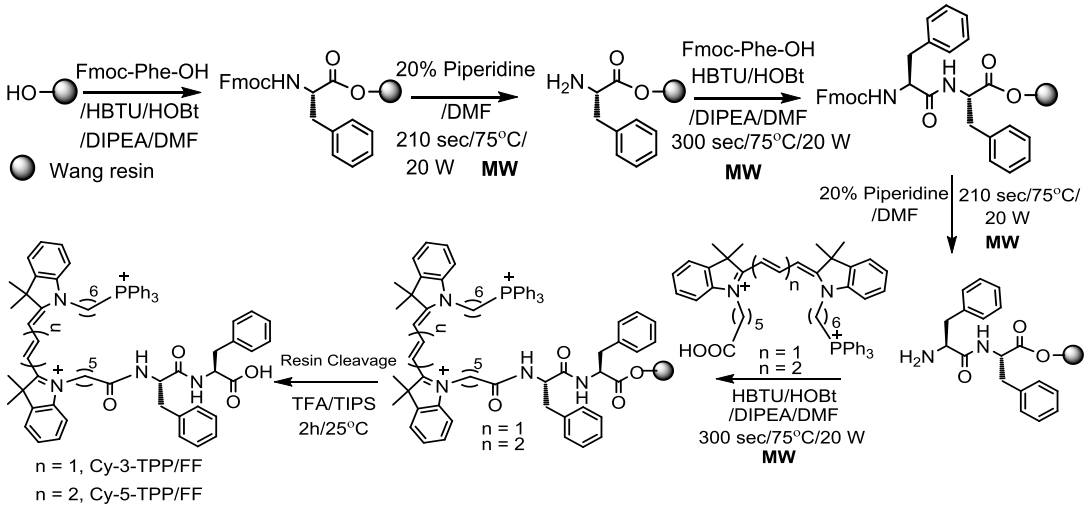

Scheme 2. Synthesis of visible Cy–3-TPP/FF and NIR Cy–5-TPP/FF molecules using MW assisted Fmoc SPPS protocol on Wang resin.

Protocols for MW-Assisted SPPS:

1. Bubbling during the MW-assisted synthesis for all Steps: on 3 sec; off 7 sec.

2. Fmoc deprotection: 20% piperidine/DMF; time 210 sec, power 20 W, temperature 75ºC, delta temperature 5ºC.

Washing after Fmoc-deprotection: DMF (4×), DCM (4×), DMF (4×) to remove dibenzofulvene by-product.

3. **Coupling:** 0.5 M HBTU/0.5 M HOBt/2 M DIPEA/DMF; time 300 sec, power 20 W, temperature: 75ºC, delta temperature: 5ºC.

Washing after coupling: DMF (3×), DCM (3×), DMF (3×)

After the final step, the resin was transferred into a SPE cartridge with frit and washed with DMF (5×), DCM (5×), MTBE (5×), and finally with MeOH (5×). The resins were dried in vacuum and stored at −18°C.

Test Cleavage from Wang Resin: To a pinch of the resin a mixture of TFA/TIS (92.5/5.0 *v*/*v*) was added and the cleavage reaction was performed by shaking the resin for 2 h at room temperature. Afterward the resin beads were

filtered off and the solvents were evaporated under N_2 stream. The Cy–3-TPP/FF or Cy–5-TPP/FF was precipitated by using cold MTBE. The MTBE suspension was centrifuged at –5°C. The supernatant was discarded, and the residue was washed with cold MTBE (3×) and dried to obtain the desired product Cy–3-TPP/FF or Cy–5-TPP/FF with a free carboxy (–COOH) at C-terminus.

Cy–3-TPP/FF: FTIR: 3285 cm^{-1} (amide A region, N–H stretching,), a sharp peak at 1633 cm^{-1} (amide I region, amide CO stretching), 1546 cm^{-1} (amide II region, NH bending).

Cy–3-TPP/FF: ^{1}H NMR (400 MHz, $CDCl_3$, 25 ºC): δ = 8.40 (1H, t, J = 12.8 Hz), 8.09 (1H, br), 7.78–7.67 (15H, m), 7.40–7.34 (4H, m), 7.21–7.11 (14H, m), 6.84 (2H, d, J = 12.3 Hz), 5.79 (1H, br), 4.67–4.58 (2H, m), 4.15–4.02 (4H, m), 3.59–3.51 (2H, m), 3.17–3.05 (4H, m), 2.35–2.30 (2H, m), 1.70 (12H, s), 1.63–1.43 (12H, m), 1.36–1.32 (2H, m) ppm.

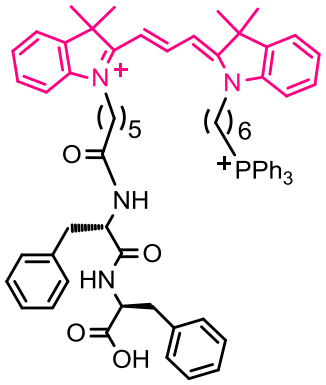

Cy–3-TPP/FF

HRMS (ESI +ve) *m/z*: Observed for $C_{71}H_{79}N_4O_4P^{2+}$ $[M]^{2+}$ = 541.2947, $[M]^+$calcd = 541.2914; observed for $[M\text{-}H+Na]^{2+}$ = 552.2836, $[M\text{-}H+Na]^{2+}$ calcd = 552.2824.

FTIR: 3285 cm^{-1} (amide A region, N–H stretching,), a sharp peak at 1633 cm^{-1} (amide I region, amide CO stretching), 1546 cm^{-1} (amide II region, NH bending). Photophysical properties in DMSO λ_{abs}= 555 nm, λ_{em}= 572 nm, Stokes shift ($\Delta\lambda$) = 17 nm, ε = 1.50 ×10^5 $M^{-1}cm^{-1}$. Φ_f = 0.26 in EtOH [Φ_f of Rhodamine-B (reference) in absolute EtOH = 0.49], Fluorescence lifetime (τ) = 0.674±0.014 ns in DMSO.

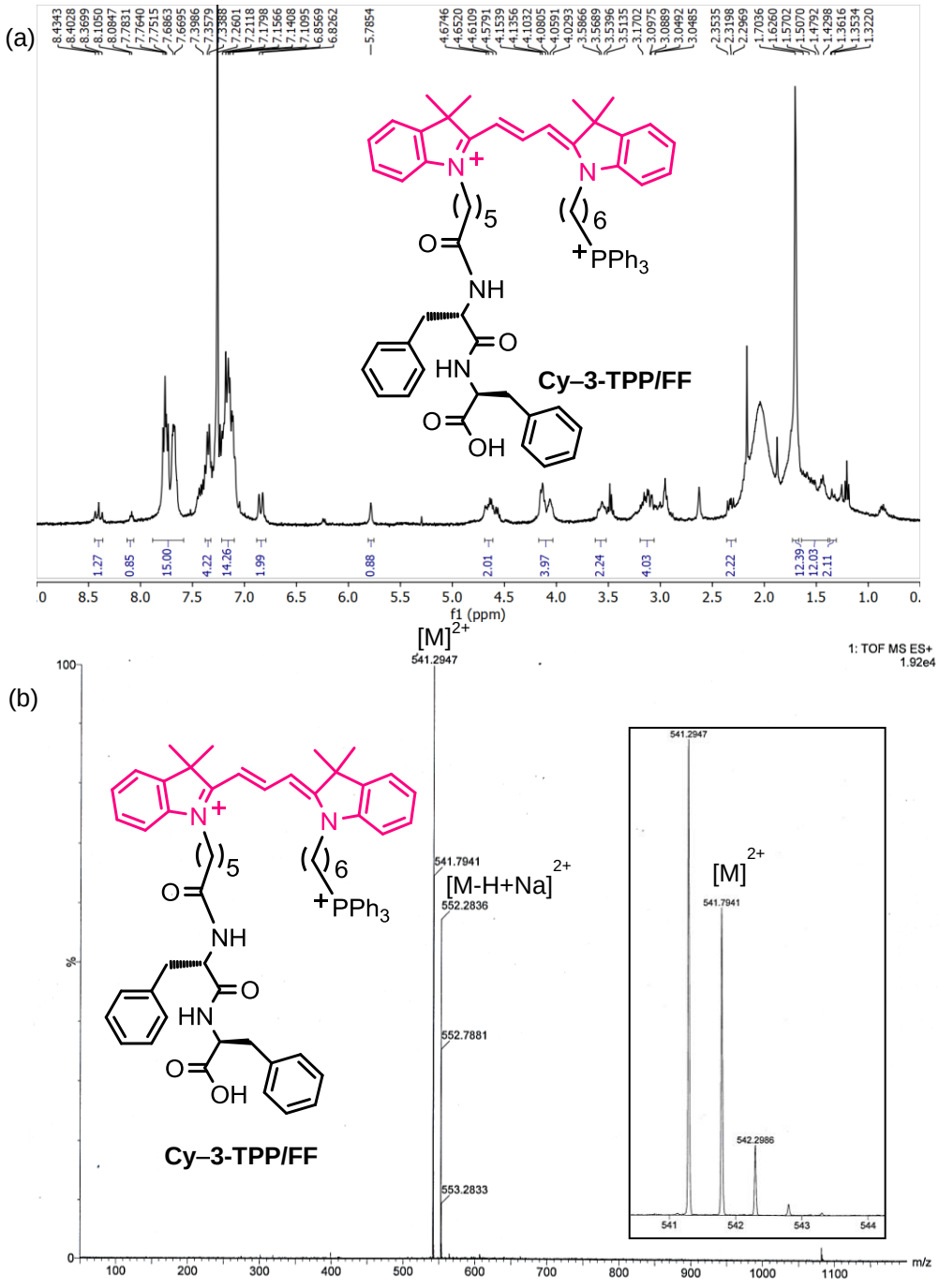

Figure 6. (a) ^{1}H NMR (400 MHz, $CDCl_3$, 25°C) spectrum and (b) HRMS (ESI +ve) spectrum of Cy– 3-TPP/FF. Inset shows isotopic distribution pattern.

Cy–5-TPP/FF: ^{1}H NMR (400 MHz, CDCl3, 25ºC): δ = 8.01 (1H, br), 7.77–7.66 (15H, m), 7.39–7.32 (5H, m), 7.21–7.13 (14H, m), 6.86 (2H, t, J = 12.6 Hz), 6.72 (1H, br), 6.37–6.27 (2H, m), 4.62–4.52 (2H, m), 4.09–4.05 (2H, m), 3.94–3.87 (2H, m), 3.56–3.46 (2H, m), 3.20–3.06 (4H, m), 2.17–2.13 (2H, m), 1.68 (12H, s), 1.63–1.50 (8H, m), 1.39–1.34 (4H, m), 1.29–1.26 (2H, m) ppm. HRMS (ESI +ve) *m*/*z*: Observed for $C_{73}H_{81}N_4O_4P^{2+}$ $[M]^{2+}$ = 554.3512, $[M]^{+}$calcd = 554.2992; observed for $[M\text{-}H+Na]^{2+}$ = 565.3400, $[M\text{-}H+Na]^{2+}$ calcd = 565.2902.

FT-IR: 3300 cm^{-1} (amide A region, N–H stretching,), a sharp peak at 1634 cm^{-1} (amide I region, amide CO stretching), 1537 cm^{-1} (amide II region, NH bending).

Photophysical properties in DMSO λ_{abs}= 651 nm, λ_{em}= 673 nm, Stokes shift ($\Delta\lambda$) = 22 nm, ε = 2.2 ×10^5 $M^{-1}cm^{-1}$. Φ_f = 0.43 in DMSO [Φ_f of Zinc pthalocyanine (reference) in DMSO = 0.20], Fluorescence lifetime (τ) = 2.010±0.026 ns in DMSO.

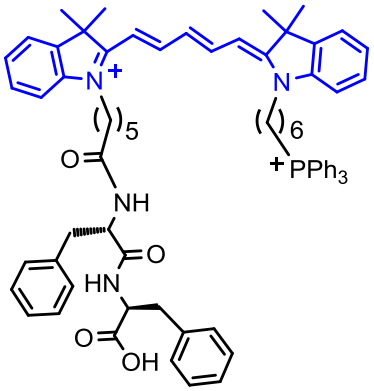

Cy–5-TPP/FF

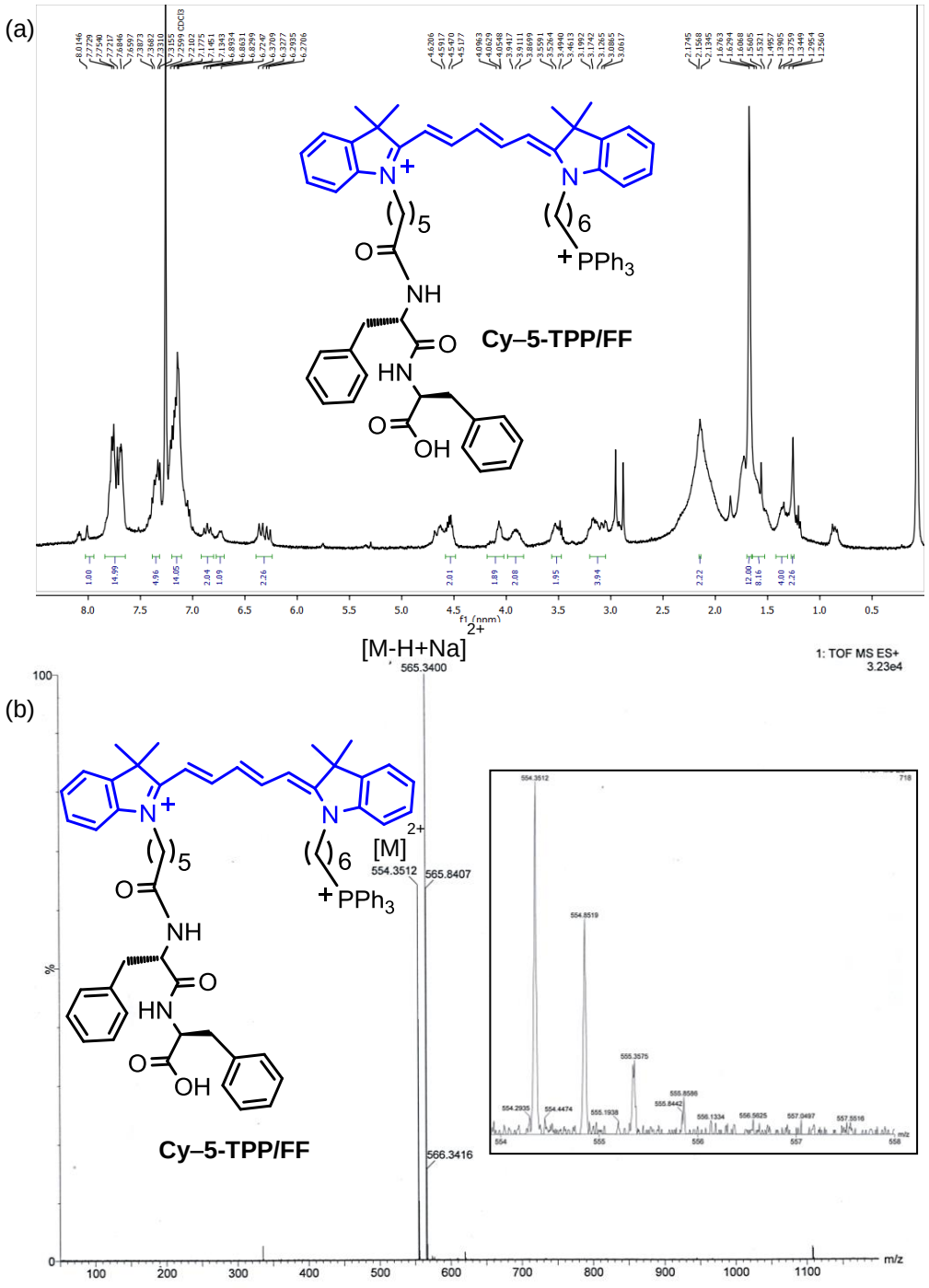

Figure 7. (a) ^{1}H NMR (400 MHz, $CDCl_3$, 25°C) spectrum and (b) HRMS (ESI +ve) spectrum of Cy–5-TPP/FF. Inset shows isotopic distribution pattern.

METHODS

Microwave Synthesizer: Unsymmetrical Cy–3-TPP, Cy–5-TPP chromophores and their associated precursor molecules as well as Cy–3-TPP/FF and Cy–5-TPP/FF conjugates were synthesized by manual microwave solid phase peptide synthesizer (CEM corporation, model discover bio, USA make).

High-Resolution Electrospray Ionization Mass Spectrometry (HRMS-ESI): HRMS-ESI in positive mode was recorded on a Q-TofmicroTM (Waters Corporation) mass spectrometer.

NMR Spectroscopy: 1D as well as 2D NMR was recorded at 298 K on Bruker DPX300 MHz, DPX400 MHz, and DPX500 MHz spectrometers in appropriate deuterated solvents.

UV/vis Spectroscopy: Shimadzu UV-1800 spectrometer was used to record absorption spectra. All the measurements were performed by a quartz cuvette of 1 cm path length.

Fluorescence Spectroscopy: Fluorescence spectra were recorded using Horiba Jobin Yvon FluoroMax-4 spectrofluorometer.

Fluorescence Lifetime Measurement: Time-correlated single photon counting (TCSPC) technique is used to determine the fluorescence lifetime (τ) of Cy–3-TPP/FF and Cy–5-TPP/FF molecules by Horiba DeltaFlex lifetime machine (Horiba Jobin Yvon IBH Ltd, Glasgow, UK). 510 nm (Model: DD-510L, Horiba Scientific) and 650 nm (Model: DD-650L, Horiba Scientific) Delta diode laser excitation source were used to measure the fluorescence lifetime of Cy–3-TPP/FF and Cy–5-TPP/FF, respectively, in DMSO. Fluorescence lifetime (τ) measurements and data analyses were executed by Horiba EzTime decay analysis software.

Fourier Transform Infrared Spectroscopy (FT-IR): FT-IR spectra were recorded using a PerkinElmer Spectrum Two FT-IR spectrometer from 4000 to 400 cm^{-1} at room temperature.

Quantum Yields of Unsymmetrical Cy–3-TPP, Cy–5-TPP, Cy–3-TPP/FF, and Cy–5-TPP/FF: Fluorescence quantum yields (Φ_f) of Cy–3-TPP, Cy–5-TPP, Cy–3-TPP/FF, and Cy–5-TPP/FF were calculated by relative method. Here, the integrated fluorescence intensities of Cy–3-TPP, Cy–5-TPP, Cy–3-TPP/FF, and Cy–5-TPP/FF compounds were compared with fluorescence intensities of reference molecules using the following equation (**Table 5**):

$\Phi_f(x) = \Phi_f(st) \times [(A_{st} \times F_x \times \eta_x^2)/(A_x \times F_{st} \times \eta_{st}^2)]$

$\Phi_f(st)$ and $\Phi_f(x)$: fluorescence quantum yield of the reference and synthesized compounds, respectively

A_{st} and A_x: Absorbance of reference and synthesized compounds at the λ_{ex}, respectively

F_{st} and F_x: Integrated fluorescence areas under the corrected fluorescence spectra for the reference and synthesized compounds, respectively.

η_{st} and η_x: Refractive indices of the solvents in which the reference and synthesized compounds were recorded, respectively [here, $(\eta_x^2 / \eta_{st}^2) = 1$].

"st" signifies to the standard and "x" describes synthesized compound.

$\Phi_f(st)$ of Rhodamine-B in absolute EtOH is 0.49 and used as the reference for Cy–3–TPP and Cy–3-TPP/FF.

$\Phi_f(st)$ of Zinc pthalocyanine in DMSO is 0.20, which is used as the reference for Cy–5-TPP and Cy–5-TPP/FF.

Determination of Critical Aggregation Concentration (CAC): KRÜSS-K7 Tensiometer instrument was used to determine the surface tension values of Cy–5-TPP/FF in deionized water at different concentrations by using ring

detachment method. To obtain the CAC surface tension values of Cy–5-TPP/FF was plotted against log [Concentration of Cy–5-TPP/FF] which provides a sigmoidal curve. 5 min was provided to reach the equilibrium after every addition of the Cy–5-TPP/FF. Increasing the concentrations of Cy–5-TPP/FF progressively dropped the surface tension. The surface tension experiment was repeated three times and almost identical results were achieved and the mean value was taken for each data point. Sharp decrease of surface tension value of Cy–5-TPP/FF at a particular concentration provide the value of CAC.

General Procedure for Preparation of Sample Solution for FE-SEM, TEM, and AFM: 1 mg of both Cy–3-TPP/FF and Cy–5-TPP/FF were dissolved separately in 1 mL DMSO:H_2O (1:10). This solution was diluted with deionized H_2O to make a final concentration of 15 μM each. This solution was stored for 48 h and then used for FE-SEM, TEM, and AFM. To circumvent any pre-aggregation, stock solutions were prepared freshly for each experiment.

Field Emission Scanning Electron Microscopy (FE-SEM): The nanomorphology of the Cy–3-TPP/FF and Cy–5-TPP/FF compounds were characterized using FE-SEM. 10 μL of Cy–3-TPP/FF and Cy–5-TPP/FF stock solution (15 μM) were separately drop casted on a glass cover slip and allowed to dry completely in air at room temperature. Samples were coated with gold and the images were obtained in INSPECT F50 Scanning Electron Microscope instrument with a 10 kV accelerating voltage.

Transmission Electron Microscopy (TEM): 10 μL of Cy–3-TPP/FF and Cy–5-TPP/FF freshly prepared stock solutions (15 μM) were separately drop casted on a carbon coated copper grid (300 mesh) and waited for 2 m followed by blotting with filter paper to remove the excess fluid. Finally, for negative

staining 10 μL of 2 % (w/v) uranyl acetate in H_2O solution was drop casted on the grid and waited for 30 s followed by blotting with filter paper. The grid was allowed to dry completely in air then vacuum drying for 1 day. TEM images of Cy–3-TPP/FF and Cy–5-TPP/FF nanotubes were acquired on JEM-2100F Field Emission Electron microscope (JEOL) instrument with acceleration voltage 200 kV.

Atomic Force Microscopy (AFM): 10 μL of Cy–3-TPP/FF and Cy–5-TPP/FF stock solution (15μM) were separately drop casted on freshly cleaved mica film and allowed to dry completely in air then vacuum dried in a desiccator for 1 day before imaging. AFM images were recorded on an AUTOPROBE CP BASE UNIT di CP-II instrument (model no: AP-0100).

Dynamic Light Scattering (DLS): DLS experiments were accomplished using a Malvern instrument (Malvern, UK) to inspect the hydrodynamic diameters of the nanotubes formed by Cy–3-TPP/FF or Cy–5-TPP/FF in solution. All measurements were performed at a backscattering angle of 173° at 25°C. Three runs were recorded per measurement and the average values were obtained. A monodisperse population of the Cy–3-TPP/FF nanotubes with hydrodynamic diameter = 167 134 nm and PDI = 0.434 was observed in deionized water. For Cy–5-TPP/FF nanotubes, hydrodynamic diameter = 134 nm and PDI = 0.375 was obtained in deionized water (**Figure 16**).

Cell Culture: HeLa human cervix adenocarcinoma epithelial cells and A459 lung carcinoma cells were cultured in Dulbecco's modified Eagle medium (DMEM, pH 7.4) comprising 10% FBS and antibiotic-antimycotic solution 100×(containing 10000 units penicillin, 10 mg streptomycin, and 25 μg amphotericin B per mL in 0.9% normal saline) followed by incubation at 37°C in an air-jacketed 5% CO_2 incubator and was routinely passaged.

MTT Assay: The cytotoxicity of Cy–3-TPP/FF and Cy–5-TPP/FF on HeLa and A549 cancerous cell lines were determined by MTT assay. HeLa and A549 carcinoma cells were separately seeded at a density of ~10^4 cells in a 96-well plate in DMEM and incubated for 24 h. After 24 h incubation, Cy–3-TPP/FF and Cy–5-TPP/FF were separately treated at different concentrations (2, 4, 6, 8, 10, 12, 14, 16, 18, 20, and 25 μM per well) for 24 h at 37°C. HeLa and A549 carcinoma cells were then separately treated with MTT (10 μL) solution (5 mg mL^{-1} in PBS) for 4 h in darkness at 37°C. Formazan crystals (dark blue) was formed which were dissolved in DMSO and the absorbance (*A*) at 575 nm was recorded (measured in triplicate) using an ELISA plate reader. The results were reported by the following equation:

Viable cells (%) = (*A* of treated cells / *A* of untreated cells) × 100

Confocal Microscopy: Confocal laser scanning microscopy (CLSM) was performed by a Leica TCS SP8 confocal microscope using 60× and 100× oil plan apochromatic objectives. Prior to CLSM imaging HeLa and A549 carcinoma cells were individually seeded in 35mm glass bottom confocal dish (SPL Lifesciences, catalogue no. 200350) at a density 10^4 cells/mL and allowed to grow in DMEM for 24h at 37°C in an air-jacketed 5% CO_2 incubator. After that cells were washed two times with 1x PBS. Live cells were incubated with 1.0 μM solution of NIR Cy–5-TPP/FF or visible Cy–3-TPP/FF in media for 10 m at 37°C in 5% CO_2 atmosphere and then washed two times with 1x PBS. The carcinoma cells were then incubated with 0.2 μM MitoTracker Green FM (for Cy–5-TPP/FF) or MitoTracker Deep Red FM (for Cy–3-TPP/FF) and incubated at 37°C in 5% CO_2 atmosphere for 15 m followed by three times washing with 1x PBS. HeLa and A549 cells were finally incubated with DAPI for 15 m and washed in the same procedure. Throughout the CLSM imaging

procedure 37°C temperature and 5% CO_2 atmosphere was maintained. Higher magnification confocal images were investigated by LAS X software.

MitoTracker Green FM: laser λ_{ex} = 488 nm, λ_{em} = 516 nm; MitoTracker Deep Red FM: laser λ_{ex} = 635nm, λ_{em} = 665 nm; Cy–3-TPP/FF: laser λ_{ex} = 561 nm, λ_{em} = 565 nm; Cy–5-TPP/FF: laser λ_{ex} = 635 nm, λ_{em} = 664 nm; DAPI: laser λ_{ex} = 405 nm, λ_{em} = 461 nm.

Determination of the Concentration of Cy–5-TPP/FF Inside the Mitochondria of A549 Cell: To determine the inner mitochondrial concentration of Cy–5-TPP/FF, a 24 well plate is used to seed A549 carcinoma cells and allowed to grow at 37°C for 24 h in 5% CO_2. The culture media was thrown away and new medium containing Cy–5-TPP/FF (5 μM or 10 μM) was added and incubated at 37°C for 3 h to have adequate cellular uptakes. The media was thrown out and the carcinoma cells were washed with cold 1X PBS (three times). A549 carcinoma cells were harvested with trypsin solution and finally collected in a micro centrifuge tube. The average cell number was counted by Hemocytometer. The A549 cells were then centrifuged for 5 min at 1400 rpm and the supernatant was discarded. Centrifugation process was repeated twice with PBS and the cells were collected as pellet. Ripa lysis buffer (200 μL) was added to the pellet of cells and paused for 30 min to confirm complete lysis. CH_3OH (200 μL) was added into the lysate and centrifuged to collect the supernatant. Fluorescence intensity of the lysate solutions at λ_{em} = 664 nm (λ_{ex} = 644 nm) were measured. From the fluorescence emission intensity vs concentration calibration curve corresponding concentration of the Cy–5-TPP/FF was obtained. Originally, with known concentrations of Cy–5-TPP/FF (0.02 μM, 0.10 μM, 0.25 μM, 0.50 μM, 1.00 μM, 1.5 μM, and 2.0 μM) in Ripa buffer:CH_3OH (1:1), emission intensity vs concentration calibration

curve was plotted. Concentration of Cy–5-TPP/FF inside the cell was calculated using the subsequent relationship:

Intracellular concentration = Cellular uptake (μmol) / (Cell number × Volume of the cell).

The average cell volume and size of the A549 carcinoma cell was 1670 μm^3 and 15 μm, respectively. Concentration of Cy–5-TPP/FF inside the mitochondria was determined by the succeeding relation:

Volume ratio of A549 carcinoma cell to the cell mitochondria is 0.04.[42] The accumulation of Cy–5-TPP/FF molecules inside the mitochondria of A549 cancer cells were found to be 2.1±0.3 mM and 6.5±0.5 mM in comparison to the original exterior concentration in the culture medium of 5 μM and 10 μM, respectively.

Early Stages of Apoptosis Detection Experiment: The extent of apoptosis was investigated quantitatively by Annexin V-FITC/PI (FITC = fluorescein isothiocyanate, PI = propidium iodide) apoptosis detection kit using flow cytometry. FITC conjugated annexin V which is a Ca^{2+}-dependent phospholipid binding protein has a superior affinity for negatively charged phosphatidylserine (PS) located on the apoptotic cell plasma membrane surface. In normal healthy cells, PS is usually found in the inner leaflet of plasma membrane. However, in case of early apoptosis, structural changes of plasma membrane takes place and the PS get exposed via translocation from inner to outer leaflet of plasma membrane. Annexin V is a marker to detect early apoptosis. The PI is used to stain the DNA in necrotic cells where cell membrane integrity was totally lost. PI cannot permeate the live cell membrane or early apoptotic cells, however, PI can enter the membrane of late apoptotic and necrotic cells, and stain these cells. A549 carcinoma cells were cultured in a 25 mL T-flask in DMEM at pH 7.4 having 10% FBS and antibiotic-

antimycotic solution 100×(comprising 10000 units/mL of penicillin, 10 mg/mL of streptomycin, and 25 μg/mL of Amphotericin B in 0.9% normal saline) followed by incubation at 37°C in an air-jacketed 5% CO_2 incubator and were routinely passaged. The cells were then treated with Cy–5-TPP/FF at different doses (3.0 μM, 7.0 μM, 10.0 μM) in media for 24 h. The cells were trypsinised and washed with cold 1x PBS for two times. Afterwards the cells were suspended in 1× annexin-binding buffer and 100 μL of the solution was transferred to a 5 mL culture tube. Subsequent the manufacturer's instructions, the A549 cells were treated with annexin V-FITC/PI apoptosis kit for 15 m incubation period in the dark at room temperature. 1× Binding Buffer (400 μL) provided in the annexin V-FITC/PI apoptosis detection kit contains $CaCl_2$ was added to each tube. Subsequently the incubation period the samples were kept on ice in dark. Annexin V-FITC/PI-incubated A549 cells were examined using a BD FACSCalibur Flow Cytometer (BD Bioscience) instrument. The percentage (%) of early apoptotic A549 cells were measured using BD CellQuest Pro software (BD Bioscience). A control experiment without the treatment of Cy–5-TPP/FF was also performed.

Results and Discussion

Design and Synthesis:

The structural backbone of the Cy–3 and Cy–5 chromophores are a conjugated polymethine chain consisting of 3- and 5-carbon (odd number) atoms, respectively, flanked between the two N of two heterocyclic indolenine rings with a delocalized positive charge and hence the absorption and emission maxima of Cy dyes can be modulated from the visible (Cy–3) to the NIR (Cy–5) region.[43–46] Construction of unsymmetrical Cy dye is more challenging and essential.[47–50] Unsymmetrical Cy dyes be able to further conjugate with

cellular organelle selective targeting moiety and self-assembling peptides. The unsymmetrical Cy–3-TPP, Cy–5-TPP, and their related precursor compounds are synthesized by an efficient way with decent yield using MW assisted protocol. We have covalently conjugated N of 2,3,3-trimethyl indolenine with triphenylphosphonium (TPP^+) and carboxylic (–COOH) functionality using appropriate alkylating agents such as (6-bromohexyl)triphenylphosphonium bromide and 6-bromohexanoic acid, respectively, by MW conditions. The effect of time and temperature under MW irradiation are modulated to optimize the yield of the quaternary indolium salt, keeping the indolenine/alkylating reactant ratio invariable (discussed in chapter 4). Isolation of the activated intermediates **3** and **4** are crucial for the development of unsymmetrical Cy–3-TPP and Cy–5-TPP chromophores. A screening inspection on temperature and time are performed in MW methods to improve the yield and purity of the activated intermediates **3** and **4** (**Table 1**). The synthesis of the activated intermediate (phenylaminovinylindolium salt, **Table 1**) of Cy–3-TPP is optimized using equimolar amounts of the *N*-alkyl indolium salt **1** and *N*,*N*′-diphenylformamidine in Ac_2O/AcOH (1:1) under MW irradiation for 30 min, at 160°C, 75 W to obtain the product **3** with excellent yield. The optimized settings under MW protocol for the intermediate of Cy–3-TPP synthesis is then transferred to synthesize the activated intermediate (phenylaminobuta-1,3-dienylindolium salt, compound **4**) of Cy–5-TPP (**Table 2**). Here, instead of *N*,*N*′-diphenylformamidine we have used malonaldehydebis(phenylimine) monohydrochloride to obtain the intermediate **4**. The unsymmetrical Cy–3-TPP dye (pink color) is synthesized by condensation among the precursor intermediate **3** with another quaternary indolium salt **2** in pyridine/AcOH (1:1) using MW irradiation for 10 min, at 150°C, 75 W. The unsymmetrical Cy–5-

TPP probe (blue color) is constructed by the same protocol (MW irradiation 10 min, 150°C, 75 W) used for Cy–3-TPP (**Scheme 1, Table 2**). Unsymmetrical Cy–3-TPP and Cy–5-TPP chromophores and their related intermediates are obtained in reasonable yields after purification by chromatography and characterized by numerous spectroscopic techniques (**Figure 1-5**). Moreover, carboxylic (–COOH) functionality of unsymmetrical Cy–3-TPP and Cy–5-TPP dyes are further covalently tethered at the *N*-terminal position of the FF dipeptide using MW aided Fmoc SPPS technique on Wang resin and characterized by ^{1}H NMR, HRMS, FT-IR, UV/vis, and fluorescence (**Scheme 2, Figure 6 and 7**).

Photophysics:

The photophysical property of Cy–5-TPP/FF and Cy–3-TPP/FF is studied with a range of spectroscopic procedures using various solvents including PBS. Extension in the polymethine chain of the Cy chromophore by one additional conjugated double bond from Cy–3-TPP to Cy–5-TPP causes the bathochromic shift (~100 nm red shift) in λ_{abs} as well as in λ_{em} (**Figure 8a-8d**). The absorption spectra of Cy–3-TPP/FF displayed an intense peak at ca. 548 nm in PBS and ~100 nm bathochromic shift (646 nm) is observed for Cy–5-TPP/FF (**Figure 9a,b and Table 3a,b**). The unsymmetrical Cy–3-TPP/FF and Cy–5-TPP/FF showed large molar extinction coefficients (ε) of ca. 1.5×10^5 M^{-1} cm^{-1} and exhibited narrow absorption and emission band in the visible and NIR region, respectively. Cy–3-TPP/FF fluoresces greenish yellow (ca. λ_{ex} = 555 nm; λ_{em} = 572 nm), while Cy–5-TPP/FF fluoresces in the NIR region (ca. λ_{ex} = 651 nm; λ_{em} = 673 nm) in DMSO with ca. 17 nm and 22 nm Stokes shift, respectively. **Table 3a**,**b** lists the observed λ_{abs}, λ_{em}, ε, and Stokes shift values for the unsymmetrical Cy–3-TPP/FF and Cy–5-TPP/FF in a range

of solvents. The excitation spectra of Cy–3-TPP/FF and Cy–5-TPP/FF molecules are fairly comparable to their respective absorption spectra; it ensured that no substantial conformational or electronic variations occurred in the excited state. In comparison with the fluorescence quantum yields of unsymmetrical dye Cy–3-TPP (Φ_f = 0.19) and Cy–5-TPP(Φ_f = 0.29), quantum

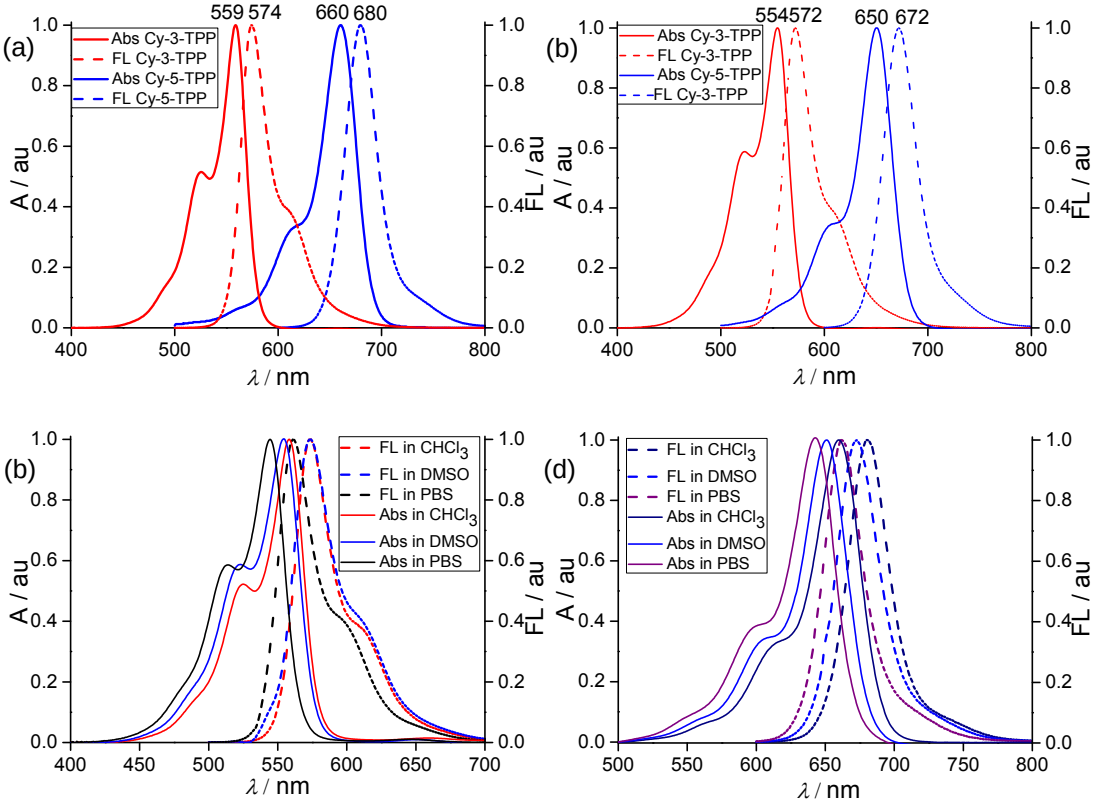

Figure 8. (a, b) Normalized absorption and emission plots of Cy–3-TPP and Cy–5-TPP in $CHCl_3$ and DMSO, respectively. (c) Normalized absorption and fluorescence plots of Cy–3-TPP in different solvents. (d) Normalized absorption and emission plots of Cy–5-TPP in various solvents.

yields of Cy–3-TPP/FF and Cy–5-TPP/FF are found Φ_f = 0.26 and Φ_f = 0.43, respectively (**Table 4a,b**). Fluorescence lifetime (τ) of 0.674±0.014 ns and

2.010±0.026 ns are found for Cy–3-TPP/FF (delta diode laser at λ_{ex} 510 nm) and Cy–5-TPP/FF (delta diode laser, λ_{ex} 650 nm), respectively, in DMSO using TCSPC technique (**Figure 9c**,**d**).

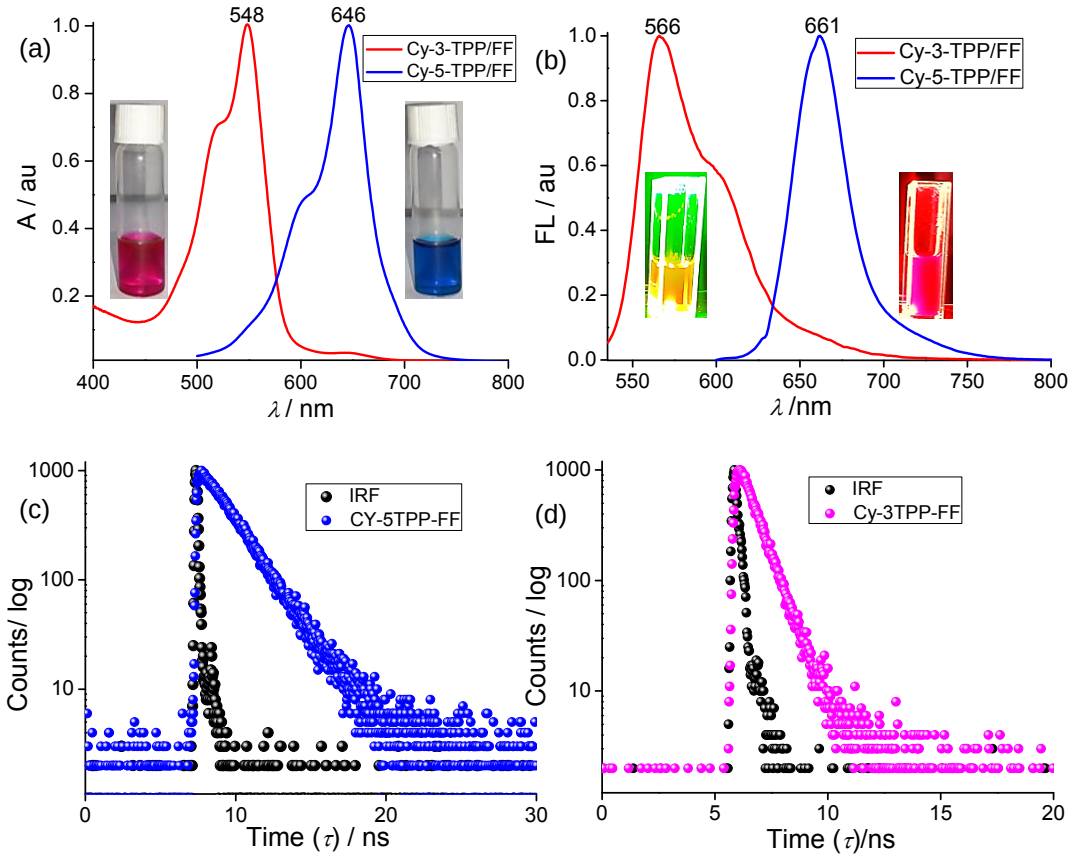

Figure 9. (a) Normalized absorption plots of Cy–3-TPP/FF and Cy–5-TPP/FF in PBS (10 μM). (b) Normalized emission plots of Cy–3-TPP/FF and Cy–5-TPP/FF (10 μM, PBS). (c,d) Fluorescence lifetime (τ) of Cy–5-TPP/FF and Cy-3-TPP/FF in DMSO are found 2.01±0.026 ns and 0.674±0.014 ns after excitation with delta diode laser at 650 nm and 510 nm respectively. (IRF: Instrument Response Function).

Table 3. Photophysical data of (a) Cy–3-TPP/FF and (b) Cy–5-TPP/FF in different solvents.[c]

(a)

Compound	Solvent	λ_{max} (nm)	λ_{em} (nm)	Stokes shift ($\Delta\lambda$)	$\varepsilon \times 10^5$ ($M^{-1} cm^{-1}$)
Cy–3-TPP/FF	PBS	548	566	16	0.82
	DMSO	555	572	17	1.50
	$CHCl_3$	559	574	15	1.76

(b)

Compound	Solvent	λ_{max} (nm)	λ_{em} (nm)	Stokes shift ($\Delta\lambda$)	$\varepsilon \times 10^5$ ($M^{-1} cm^{-1}$)
Cy–5-TPP/FF	PBS	646	661	15	1.10
	DMSO	651	673	22	2.20
	$CHCl_3$	659	681	22	1.63

[c] ε: molar extinction coefficient., λ_{max}: absorption maximum wavelength, λ_{em}: emission maximum wavelength.

Table 4. Quantum yields (QYs) of (a) Cy–3-TPP and Cy–5-TPP (b) Cy–3-TPP/FF and Cy–5-TPP/FF.

(a)

Compound	QY (Φ_f)	Solvent
Cy–3-TPP	0.19	EtOH
Cy–5-TPP	0.29	DMSO

(b)

Compound	QY (Φ_f)	Solvent
Cy–3-TPP/FF	0.26	EtOH
Cy–5-TPP/FF	0.43	DMSO

Fourier Transformed Infrared (FT-IR) Spectroscopy for Secondary Structure Determination:

Fourier-transformed infrared (FT-IR) spectroscopy is used to investigate the secondary structural information of Cy–5-TPP/FF and Cy–3-TPP/FF molecules. FT-IR spectrum of Cy–5-TPP/FF, aged over 48 h, displays a peak at 1634 cm^{-1} in the amide I region (amide CO stretching) and another peak at 1537 cm^{-1} in the amide II region (NH bending), signifying the presence of intermolecularly hydrogen-bonded β-sheet secondary structure (**Figure 10b**).[27] N–H stretching frequency at ~3400 cm^{-1} has not been detected that proposes all the NHs have participated in hydrogen bonding and no free NHs are perceived. Similar type of stretching frequencies is observed for Cy–3-TPP/FF indicating supramolecular β-sheet structure (**Figure 10a**). The absence of a weak band at ~1675 cm^{-1} for both the compounds designates the presence of intermolecularly hydrogen-bonded parallel–β-sheet structures (**Figure 10**).

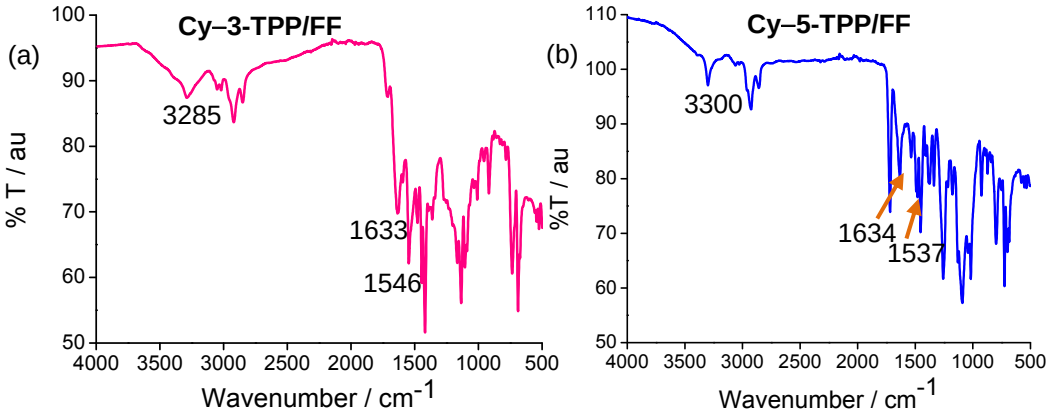

Figure 10. FT-IR spectra of (a) Cy–3-TPP/FF and (b) Cy–5-TPP/FF aged over two days, indicating the formation of intermolecularly hydrogen-bonded parallel β-sheet structures.

Determination of Critical Aggregation Concentration:

The critical aggregation concentration (CAC) of Cy–5-TPP/FF is determined to be 4.5 μM using a tensiometer instrument by applying ring detachment method (**Figure 11**).

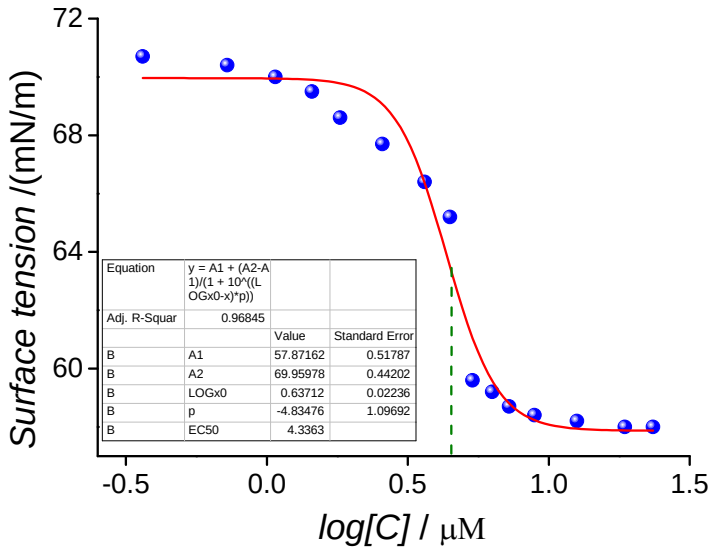

Figure 11. Surface tension values of Cy–5-TPP/FF is determined at various concentrations using a tensiometer instrument by applying ring detachment method.

Sample Preparation for Microscopic Studies:

For microscopic sample preparation 1 mg of Cy–3-TPP/FF and Cy–5-TPP/FF are dissolved separately in 1 mL DMSO:H_2O (1:10). This solution is diluted with deionized H_2O to make a final concentration of 15 μM (higher than the CAC) and it is stored for 48 h before the microscopic analyses.

Field Emission Scanning Electron Microscope (FE-SEM):

FE-SEM images of Cy–3-TPP/FF as well as Cy–5-TPP/FF at 10 kV accelerating voltage provided us with an insight into the nanotubes and revealed their open-ended structures where all the nanotubes are clearly evident

with their full lengths (**Figures 12 and 13**). The statistical analyses of the Cy–3-TPP/FF and Cy-5–TPP/FF nanotube lengths and diameters are shown in the **Figure 12c**,**d** and **Figure 13c**,**d**. The Nanotubes made of Cy–3-TPP/FF or Cy–5-TPP/FF are reasonably homogeneous and discrete with an average diameter and length of 155 nm and 0.6-1.2 μm, respectively, for Cy–3-TPP/FF and 122 nm and 0.4-1.0 μm for Cy–5-TPP/FF.

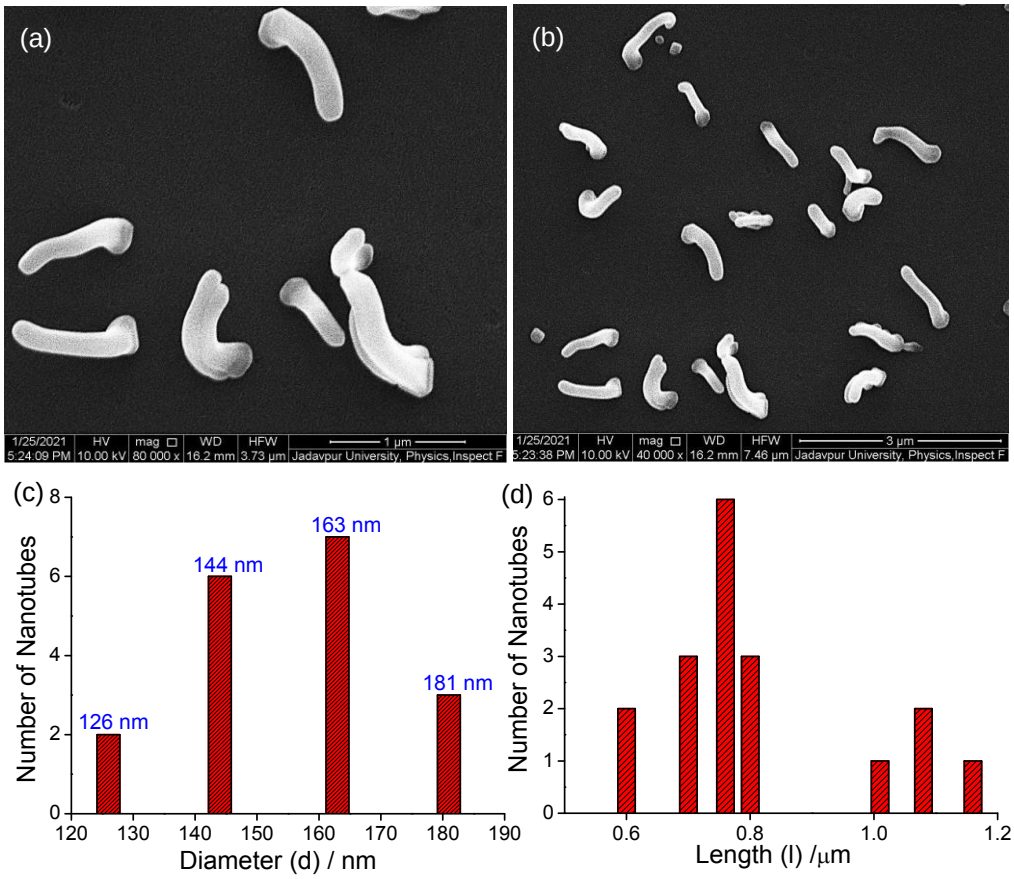

Figure 12. (a) FE-SEM image of Cy–3-TPP/FF indicating nanotubular stuctures. (b) FE-SEM image of Cy–3-TPP/FF nanotubes used for the statistical analyses. (c) Statistical analysis of Cy–3-TPP/FF nanotube diameters and (d) nanotube lengths.

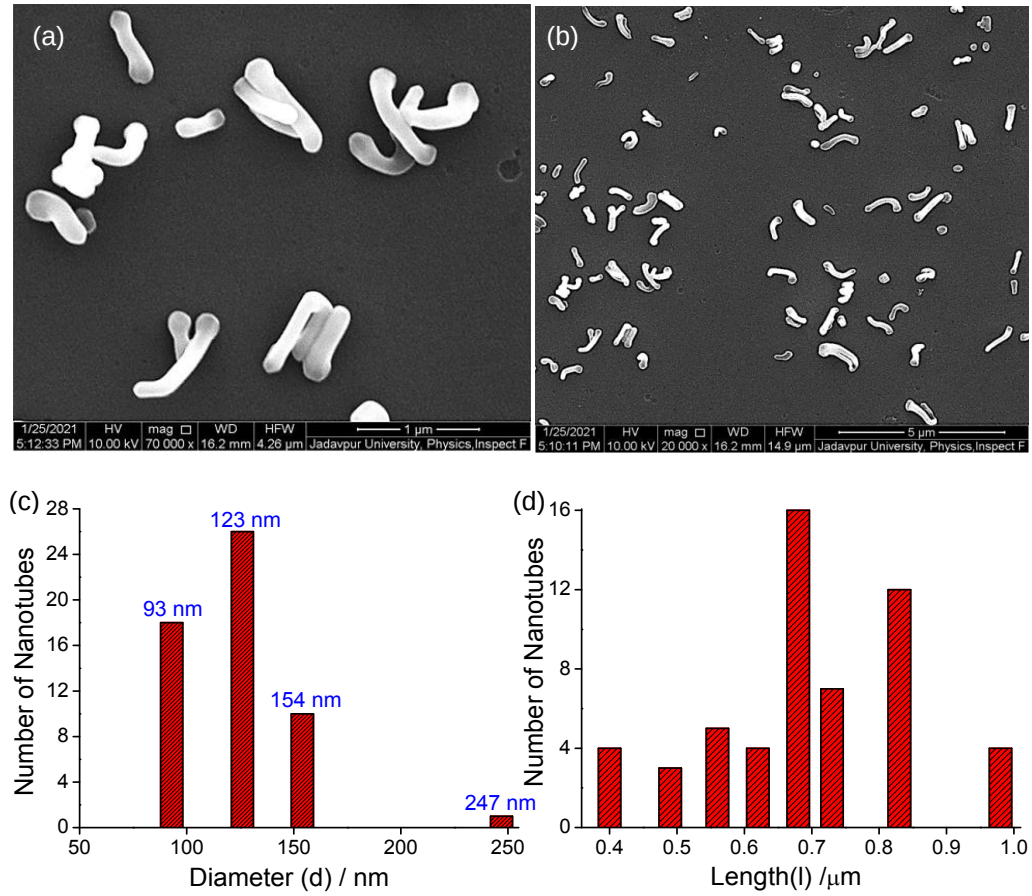

Figure 13. (a) FE-SEM image of Cy-5–TPP/FF indicating nanotubular stuctures. (b) FE-SEM image of Cy–5-TPP/FF nanotubes used for the statistical analyses. (c) Statistical analysis of Cy–5-TPP/FF nanotube diameters and (d) nanotube lengths.

Transmission electron microscopy (TEM):

The TEM images of the Cy–5-TPP/FF and Cy–3-TPP/FF using negative staining show well-ordered supramolecular nanotubes (**Figure 14a,b**). The average diameter of 150 nm with 0.5-1.3 μm length for Cy–3-TPP/FF nanotubes and 124 nm average diameter with 0.4-1.2 μm lengths for Cy–5-TPP/FF nanotubes are observed.

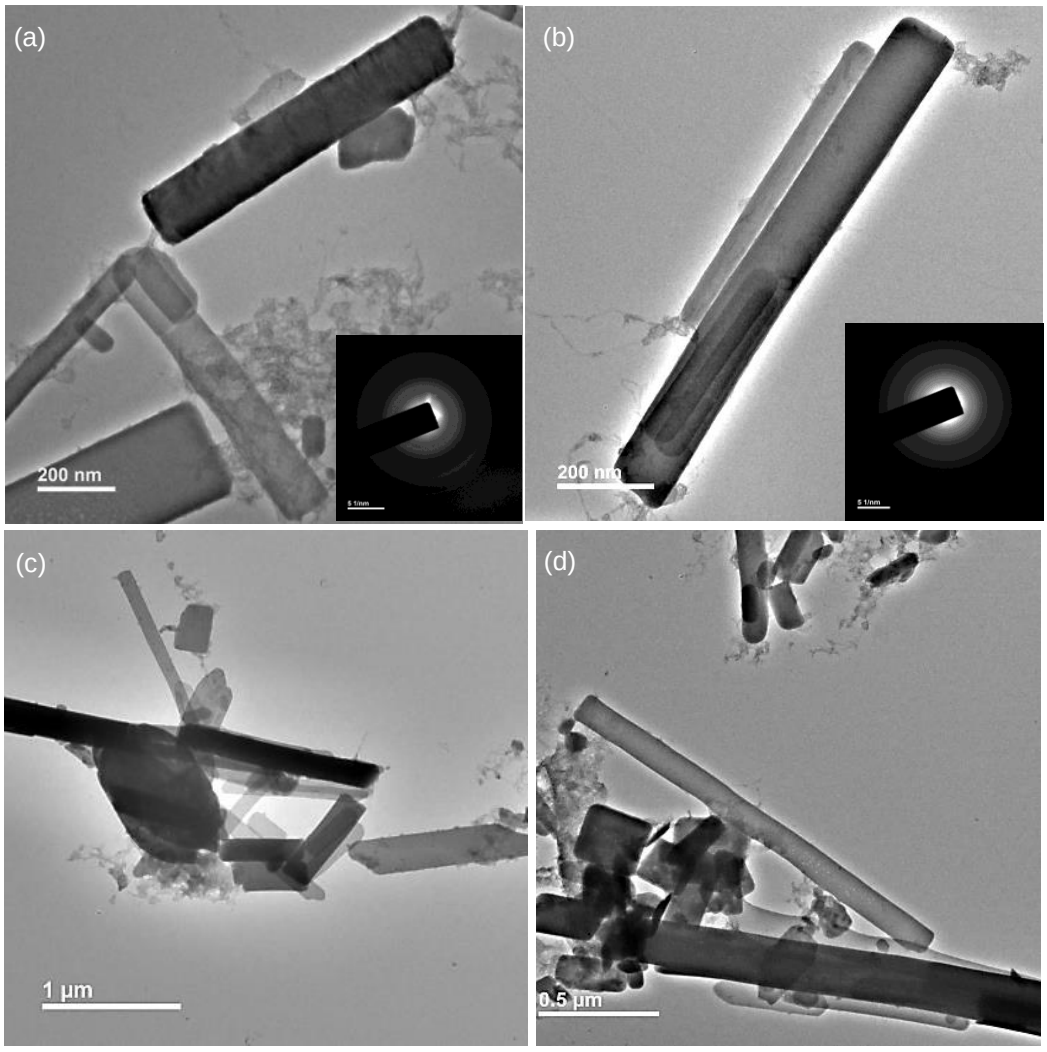

Figure 14. (a,b) TEM images of negatively stained nanotubes composed of Cy–3-TPP/FF and Cy–5-TPP/FF, respectively. SAED pattern are shown in the inset of the respective figures. TEM images of (c) Cy–3-TPP/FF (15 μM) and (d) Cy–5-TPP/FF (15 μM) in mitochondrial pH 8.0, confirm nanotubular morphology.

The selected-area electron diffraction patterns of these nanotubes formed by Cy–5-TPP/FF and Cy–3-TPP/FF are shown in the inset of the **Figure 14a**,**b**, respectively. Moreover, TEM study of the freshly prepared solutions of Cy–5-

TPP/FF (15 μM) as well as Cy–3-TPP/FF (15 μM) in mitochondrial pH 8.0 exhibited homogeneous and discrete nanotubular morphology (**Figure 14c,d**). The supramolecular parallel β-sheet secondary structures formed by Cy–3-TPP/FF or Cy–5-TPP/FF can be folded along single axis of the 2D sheet by intermolecular hydrogen bonding, π-π stacking between aromatic moieties, and hydrophobic interaction to form nanotubular structures in solution.

Atomic Force Microscopy (AFM) study:

To obtain direct topographical information, the freshly prepared stock solution (15μM) of Cy–3-TPP/FF or Cy–5-TPP/FF is deposited on a mica surface and imaged using AFM. AFM experiment revealed the spontaneous organization of Cy–5-TPP/FF or Cy–3-TPP/FF molecules into well-ordered one-dimensional nanotubes with 155 nm average diameter for Cy–3-TPP/FF and 130 nm average diameter for Cy–5-TPP/FF nanotubes (**Figure 15a**,**b**). Furthermore, amorphous aggregation or other morphology has not been detected which is consistent with the FE-SEM and TEM analyses. The height profile obtained from the AFM images are shown in **Figure 15c**,**d**.

Dynamic Light Scattering (DLS) Study:

DLS study is executed to measure the hydrodynamic diameter of the Cy–3-TPP/FF and Cy–5-TPP/FF nanotubes in solution. Monodisperse populations of the nanotubes are observed for Cy–3-TPP/FF and Cy–5-TPP/FF in aqueous solution which suggests the uniform nature of these nanotubes. The hydrodynamic diameters of the nanotubes obtained from self-assembling Cy–3-TPP/FF and Cy–5-TPP/FF are 167 nm and 134 nm, respectively (**Figure 16**) which are marginally larger with respect to SEM and TEM observed average diameters. Obviously, hydrodynamic diameters of the nanotubes including the

water-layer obtained in DLS are slightly larger than that of the non-hydrated diameters obtained in SEM and TEM.

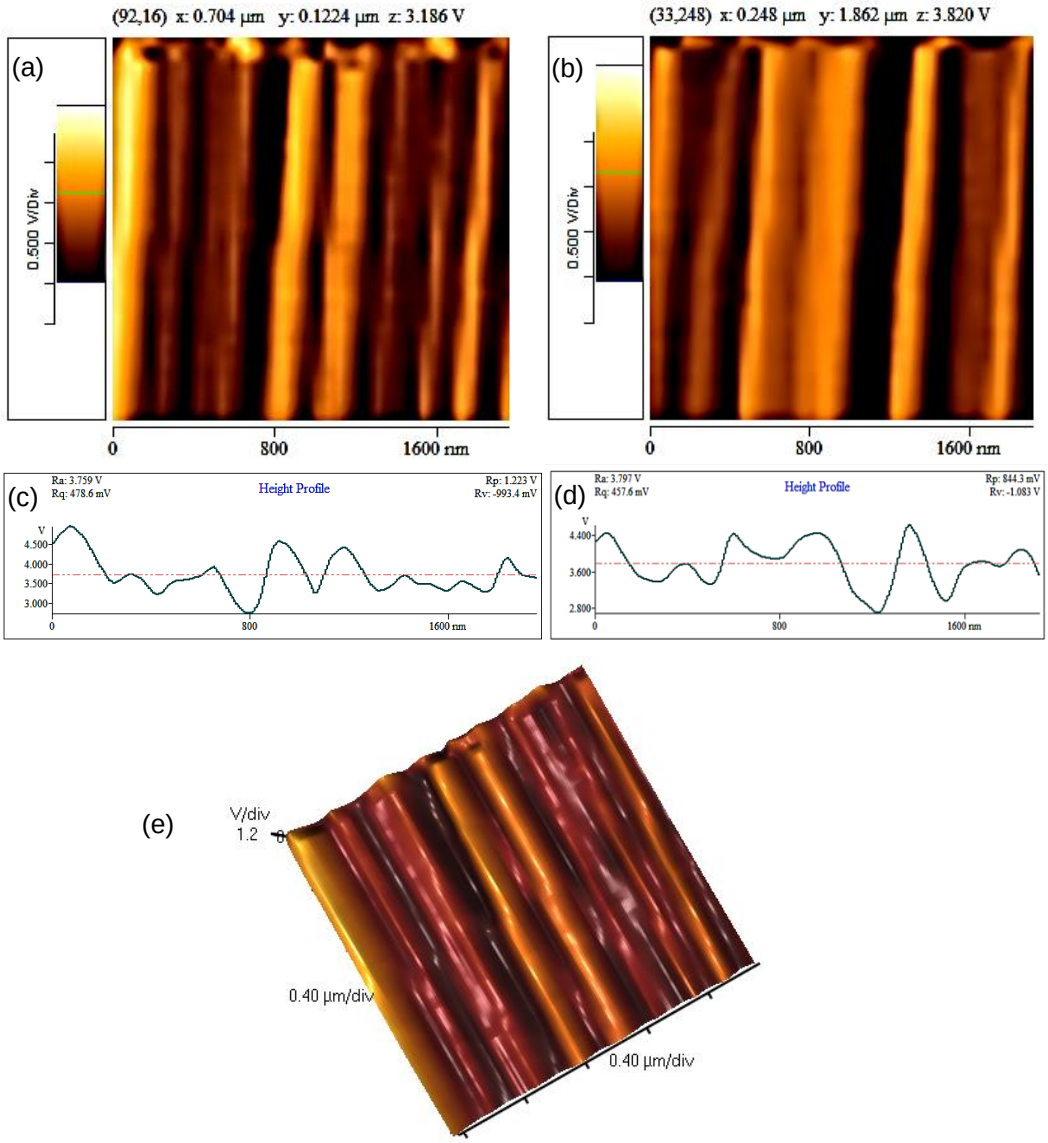

Figure 15. (a,b) AFM image of the nanotubes formed by self-assembling Cy–3-TPP/FF and Cy–5-TPP/FF molecules, respectively. (c,d) Height profile of the Cy–3-TPP/FF and Cy–3-TPP/FF nanotubes, respectively. (e) 3D AFM image of Cy–5-TPP/FF nanotubes.

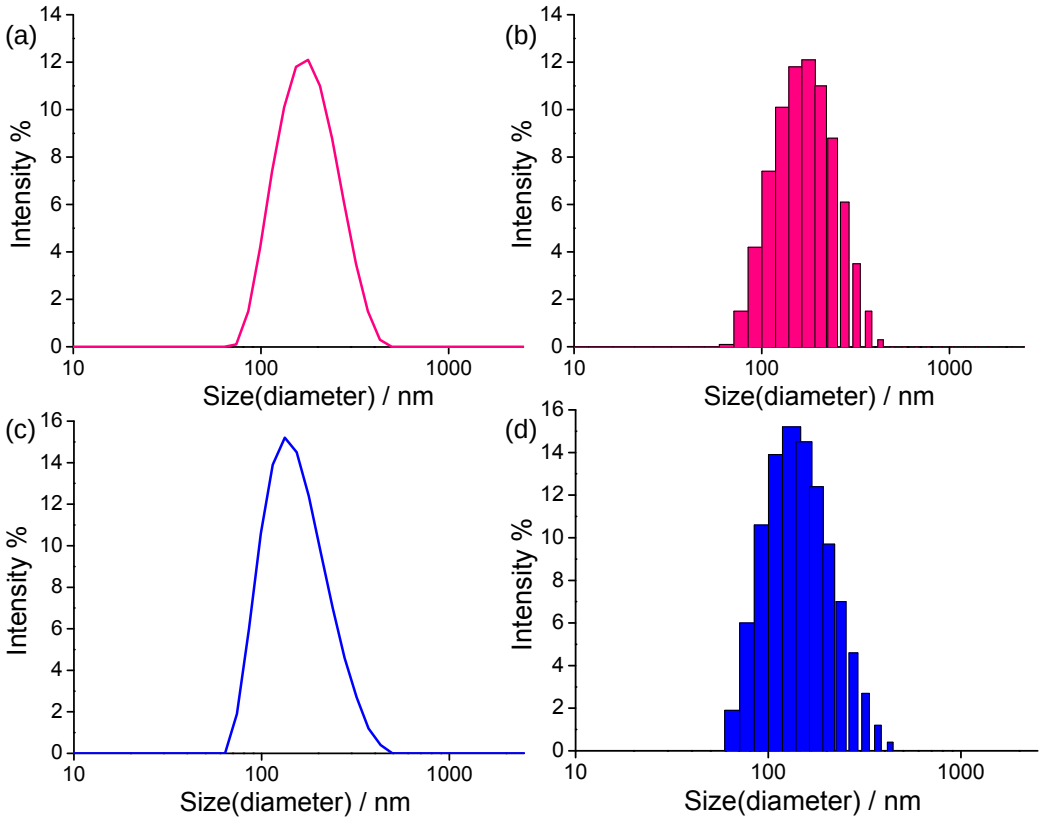

Figure 16. (a,b) Dynamic light scattering (DLS) experiment of the Cy–3-TPP/FF nanotubes in deionized H_2O exhibits a monodisperse population (PDI = 0.334) with hydrodynamic diameter of 167 nm. (c,d) DLS study of the Cy–5-TPP/FF nanotubes displays a monodisperse population (PDI = 0.275) with hydrodynamic diameter of 134 nm in deionized H_2O.

Confocal Laser Scanning Microscopic (CLSM) Image of the Self-Assembled Nanotubes:

CLSM image of the self-assembled nanotubes formed by Cy–3-TPP/FF (15 μM) and Cy–5-TPP/FF (15 μM) is obtained at 561 and 635 nm laser excitation (laser λ_{em} = 664 nm) respectively. CLSM image of Cy–3-

TPP/FF and Cy–5-TPP/FF show the formation of self-assembled NIR bright fluorescent nanotubes with negligible photobleaching (**Figure 17**).

(a)

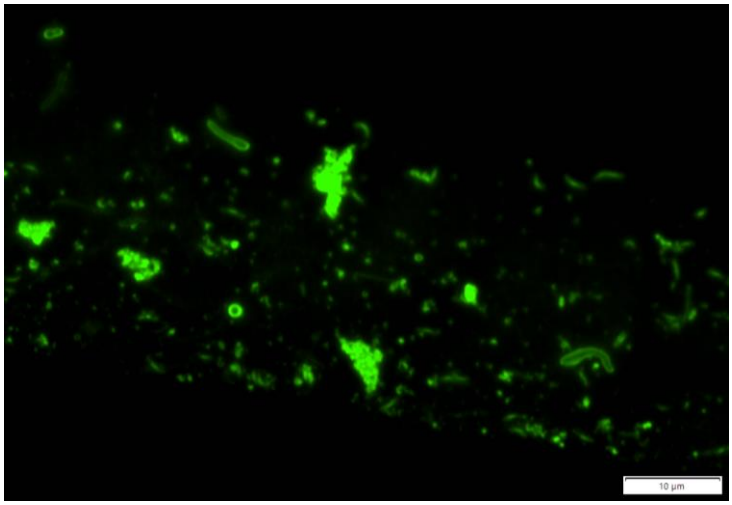

(b)

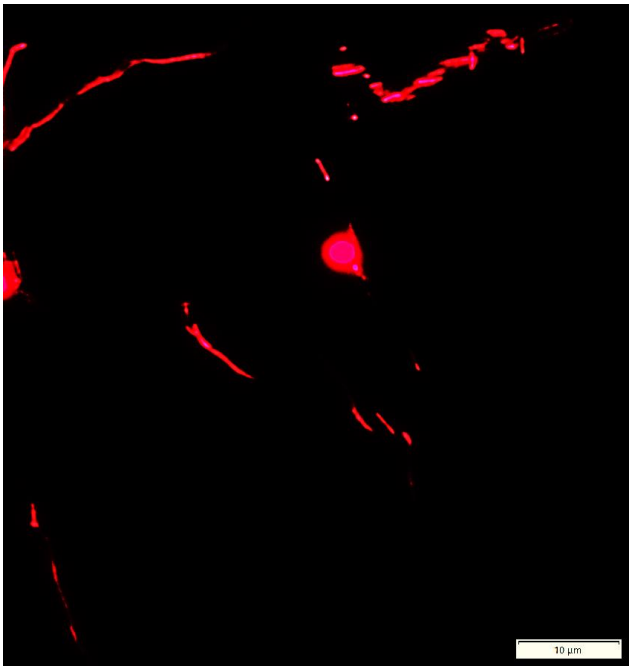

Figure 17. Confocal laser scanning microscopic (CLSM) image of the self-assembled (a) Cy–3-TPP/FF and (b) NIR Cy–5-TPP/FF nanotubes at 561 and 645 nm laser excitation, respectively.

Stability of Cy–3-TPP/FF and Cy–5-TPP/FF in Physiological and Mitochondrial pH:

The fluorescence assay exhibit that the emission of Cy–3-TPP/FF as well as Cy–5-TPP/FF is stable in physiological pH 7.4 and mitochondrial pH 8.0 at 37°C (**Figure 18a-d**). The plausible interfering at the intracellular environment by numerous metal cations (Na^+, K^+, Mg^{2+}, etc.) is scrutinized. No noteworthy fluctuations in emissions have been detected in the presence of these potential cellular interferences (**Figure 19 a**,**b**).

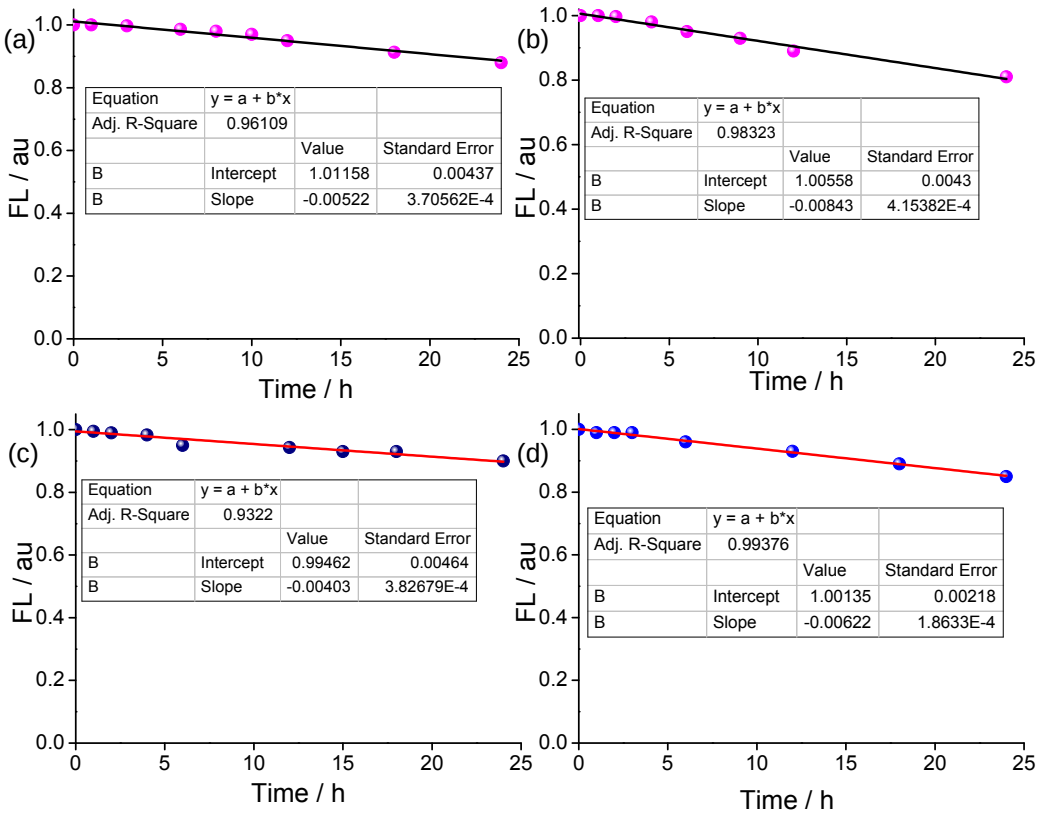

Figure 18. Insignificant fluorescence emission changes are noticed for (a, b) Cy–3-TPP/FF and (c, d) Cy–5-TPP/FF at physiological pH 7.4 (37ºC) and mitochondrial pH 8.0 (37ºC), respectively, at various time intervals.

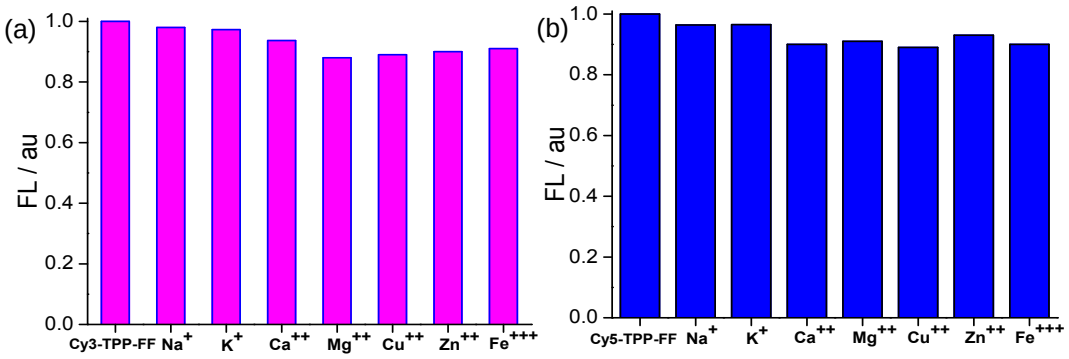

Figure 19. No noteworthy emission variations are observed for (a) Cy–3-TPP/FF and (b) Cy–5-TPP/FF in the presence of various metal cations (10 mM Na^+, K^+, and 200 μM for Ca^{2+} , Mg^{2+}, Cu^{2+}, Zn^{2+}, and Fe^{3+}) as chloride salts in pH=7.4 at 37ºC.

Mitocondrial Accumulation and Cell Viability:

The accumulation of NIR Cy–5-TPP/FF molecules inside the mitochondria [$(\Delta\Psi_m)_{cancer} \approx -220$ mV] is predictable to be 500−1000 times greater with respect to extracellular space [plasma membrane potential, $\Delta\Psi_p$ −0 to −60 mV].[27] The concentrations of Cy–5-TPP/FF molecules inside the mitochondria of A549 carcinoma cells are found to be 2.1 ± 0.3 and 6.5 ± 0.5 mM, respectively, and these values are greater than the external concentrations in the culture medium (5 and 10 μM, respectively) which is determined by fluorescence assay (**Figures 20a**). Cytotoxicity studies using MTT assay display that Cy–3-TPP/FF or Cy–5-TPP/FF at lower concentration (CLSM concentration) is not cytotoxic to healthy human embryonic kidney (HEK293) and A549 carcinoma cell lines which confirm the safe use of Cy–3-TPP/FF and Cy–5-TPP/FF for bioimaging. However, at higher concentration, these molecules exhibit cytotoxicity against HEK293 and A549 cells (**Figure 20b,c**). The IC_{50} values for Cy–5-TPP/FF as well as for Cy–3-TPP/FF against HEK293 and A549 cells are found to be ca. 18.0 and 10.0 μM, respectively, at 24 h.

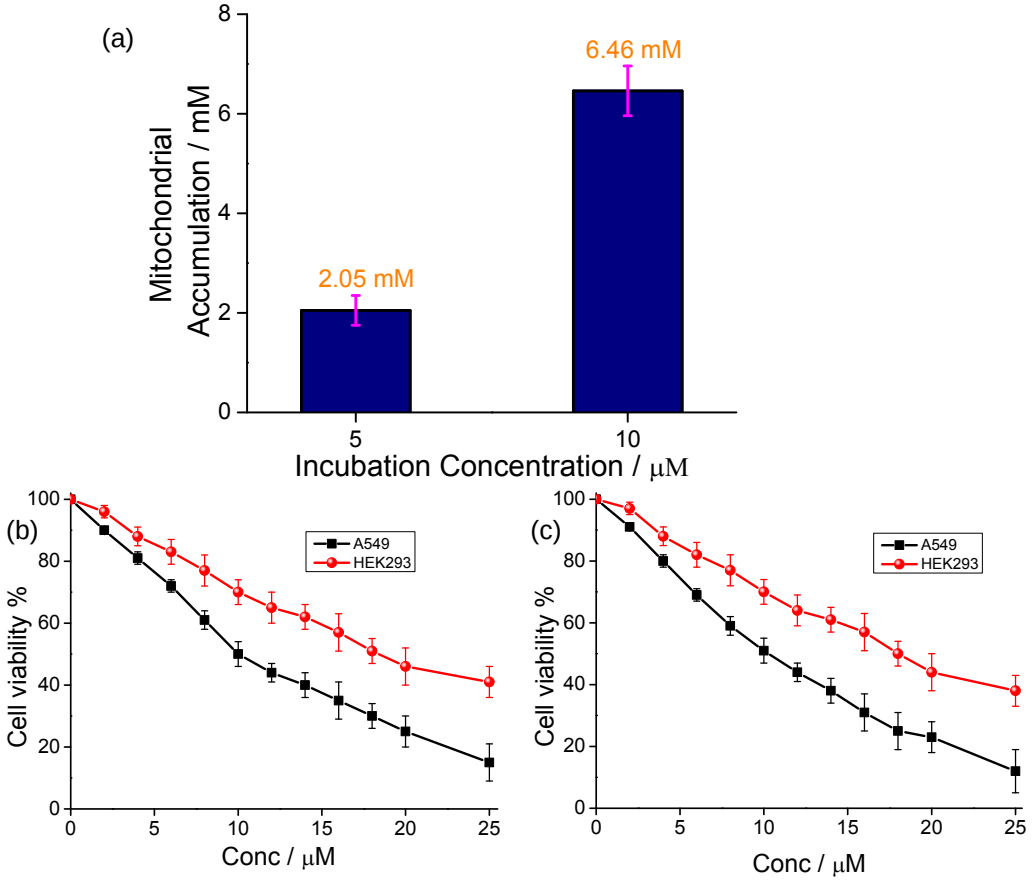

Figure 20. (a) Concentration of Cy–5-TPP/FF molecule inside the mitochondrial of A549 cells after incubation with 5.0 μM and 10.0 μM. Cell viability assay for (b) Cy–3-TPP/FF and (c) Cy–5-TPP/FF in lung adenocarcinoma A549 and healthy human embryonic kidney (HEK293) cell lines.

Live Cell Mitochondrial Imaging:

Narrow NIR absorption/emission bands for Cy–5-TPP/FF, high fluorescence quantum yield, high fluorescence lifetime, delocalized positive charge, as well as sufficient lipophilicity make this NIR molecule a smart choice for live cell mitochondrial imaging. Live cell mitochondrial staining experiment with lipophilic cationic Cy–3-TPP/FF (visible) and Cy–5-TPP/FF (NIR) molecules consist of the mitochondria targeting TPP^+ functional group

and are performed at low concentration (2.0 μM) using a confocal laser scanning microscope on the human HeLa cervix adenocarcinoma epithelial cells and A549 lung adenocarcinoma cells, ensuing fast cellular internalization with bright visible and NIR fluorescence, respectively. Concentration used for live cell CLSM (2.0 μM) is relatively lower than the concentration used for TEM or SEM (15 μM). To validate the mitochondrial target specificity colocalization analyses involving the visible Cy–3-TPP/FF and NIR Cy–5-TPP/FF are executed with the commercially accessible mitochondria tracking fluorescent markers such as MitoTracker Deep Red (MTDR) and MitoTracker Green (MTG), respectively (**Figure 21 and Figure 22**). The remarkable colocalizations have been observed for Cy-3-TPP/FF and Cy–5-TPP/FF with the Pearson's correlation coefficient (PCC) calculated to be 0.87 and 0.91, respectively, for HeLa cells (**Figure 21a,b**). For Cy–3–TPP/FF and Cy–5-TPP/FF molecules PCC is measured to be 0.83 and 0.85, respectively, in A549 cells (**Figure 22a-f, and Figure 22g-k**). All over the CLSM experiment 37°C as well as 5% CO2 incubation is maintained (**Figure 23**). The Cy–3–TPP/FF or Cy–5-TPP/FF molecules are quickly, considerably, and selectively accumulated by the live cell mitochondria directed by the large negative $\Delta\Psi_m$. A higher magnification CLSM image of the NIR Cy–5-TPP/FF molecule in live HeLa carcinoma cell is captured for well understanding of mitochondrial specificity which displays curved and linear short rods under the CLSM. This proposes that tethering to a lipophilic cationic TPP+ group with NIR dipeptide is an effective strategy for selective mitochondrial tracking and imaging (**Figure 22**).

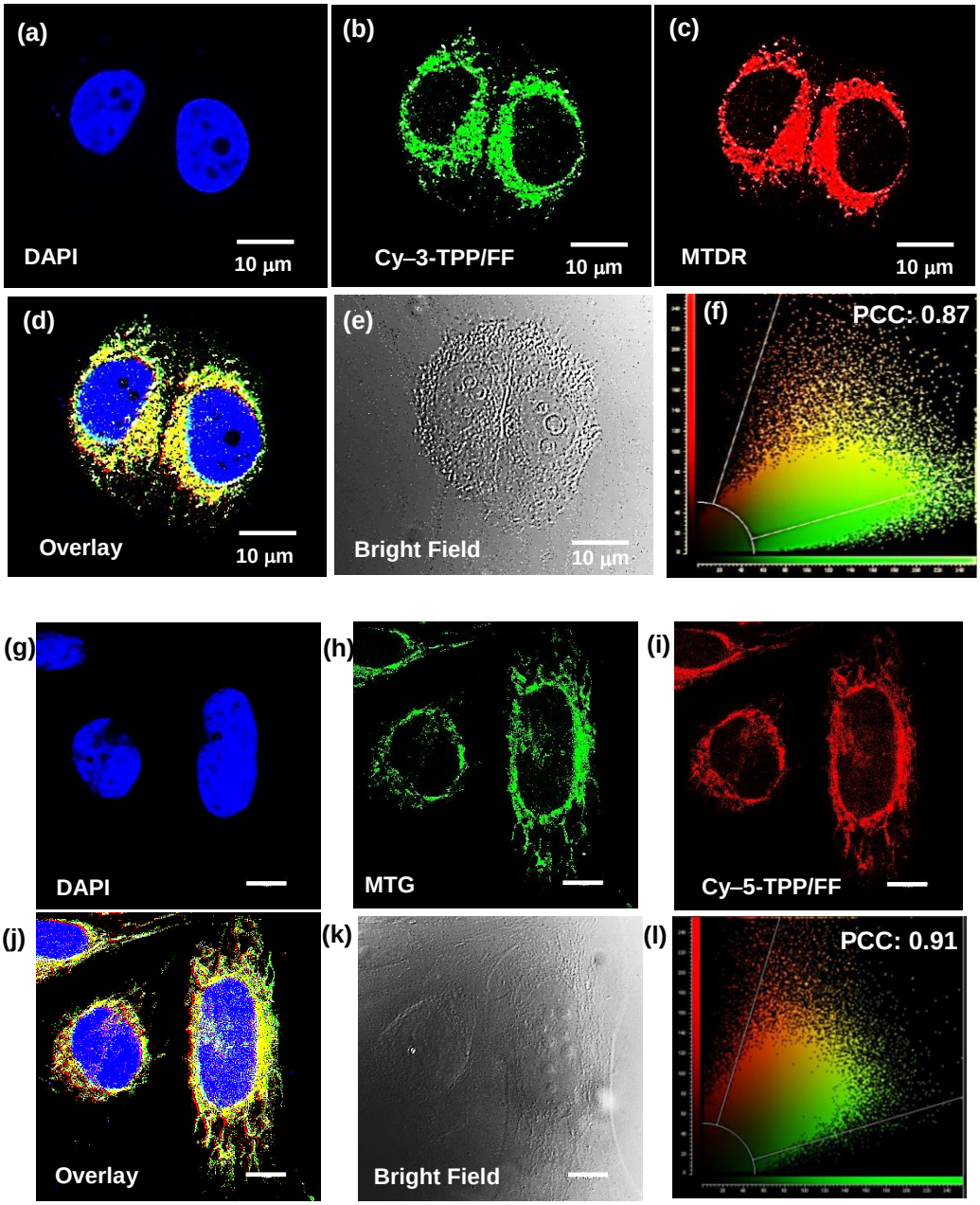

Figure 21. (a-f) CLSM images of Cy–3-TPP/FF colocalized with MTDR in live HeLa cells show high colocalization in mitochondria. (g-l) Live cell CLSM images of NIR Cy–5-TPP/FF molecule in HeLa cells colocalized with MTG display selective mitochondrial staining (scale bar 10 μm).

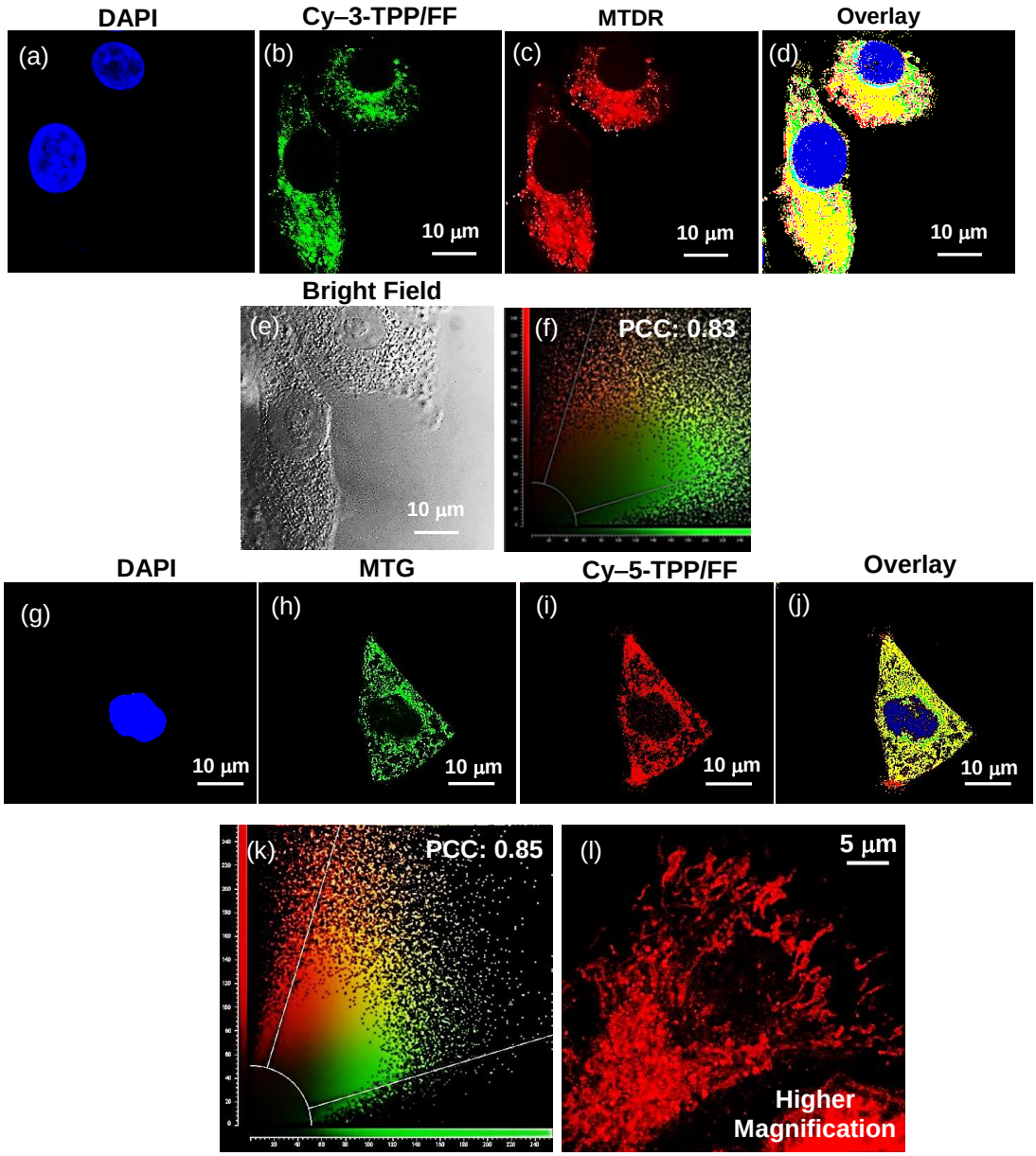

Figure 22. (a-f) CLSM images of Cy–3-TPP/FF colocalized with MTDR in A549 carcinoma cells. Pearson's correlation graph shows remarkable colocalization in mitochondria with PCC of 0.83. (g-k) CLSM images of Cy–5-TPP/FF in A549 cells colocalized with MTG exhibits high colocalization in mitochondria (PCC of 0.85). (l) Higher magnification live HeLa carcinoma cell CLSM image of mitochondria stained with NIR Cy–5-TPP/FF (laser 635 nm).

Live Cell Multicolor Imaging:

Multicolor live cell CLSM imaging in HeLa cells is accomplished by using appropriate target-selective dyes with distinctive λ_{ex} and λ_{em}, e.g., plasma membrane specific green emitting FM 1−43FX, nucleus staining blue-fluorescent DAPI, and selective mitochondria targeting NIR Cy–5-TPP/FF (**Figure 23a,b**). This three-color live cell CLSM imaging of different intracellular organelles in the same live cell is fundamental for understanding intricate cellular processes.

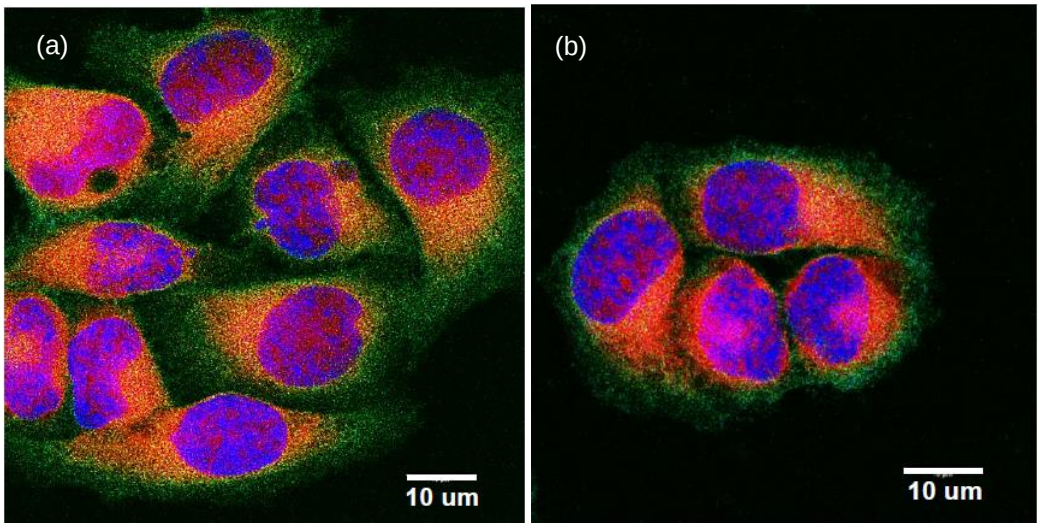

Figure 23. (a,b) Multicolor live cell CLSM imaging in HeLa cells incubated with green emitting plasma membrane specific FM 1−43FX, blue-fluorescent DAPI, and mitochondria specific NIR emitting Cy–5-TPP/FF.

Early Apoptosis Detection Using Annexin V-FITC:

Annexin V-FITC/PI apoptosis finding kit is used to examine the cell death mechanism using fluorescence-activated cell sorting (FACS) with different doses of Cy–5-TPP/FF.[51] Early stage of apoptosis where changes occur at the cell membrane surface and annexin V-FITC conjugated protein is

used as an early apoptosis marker. In a control experiment without the treatment of Cy–5-TPP/FF 99.5% of A549 cells are considered viable [both Annexin V and PI, negative] (**Figure 24a**). However, with increasing doses of Cy–5-TPP/FF (7 and 10 μM) there is an increase in A549 carcinoma cells experiencing early apoptosis (Annexin V, positive and PI, negative) (**Figure 24b,c**).

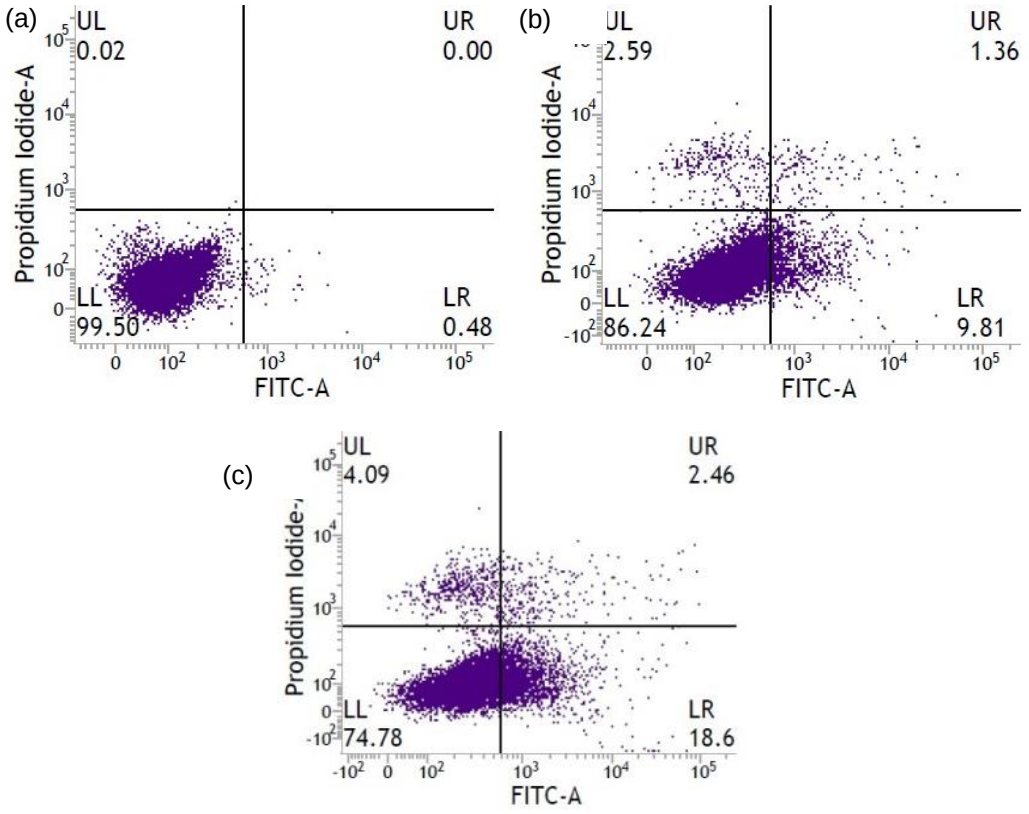

Figure 24. Dose–dependent effect of Cy–5-TPP/FF to determine early apoptosis in A549 carcinoma cells. (a) Control experiment without the treatment of Cy−5-TPP/FF. (b) Cells treated with 7.0 μM and (c) 10.0 μM of Cy−5-TPP/FF. Lower left (LL) quadrant designates viable cell, both Annexin V and PI, negative; lower right (LR) quadrant: Annexin V, positive and PI, negative; upper right (UR) quadrant: Annexin V, positive and PI, positive; upper left (UL) quadrant: Annexin V, negative and PI, positive.

However, the percentage of viable cells is quite high. Moreover, we observe negligible PI staining even at higher concentrations of Cy–5-TPP/FF which nullify the late stages of apoptosis (Annexin V and PI, positive) along with necrosis (Annexin V, negative and PI, positive). The cell membrane integrity excludes PI in early apoptotic cells. PS is translocated from the inner leaflet of the healthy plasma membrane to the outer leaflet during early apoptosis and hence exposed. FITC-labeled annexin V protein binds in a Ca^{2+}-dependent fashion to negatively charged phosphatidylserine (PS) located on the apoptotic cell plasma membrane surface. We proposed that after cellular internalization the targeted lipophilic cationic Cy–5-TPP/FF molecule has been selectively accumulated inside the mitochondria of A549 cells driven by large negative $(\Delta\Psi_m)_{cancer} \approx -220$ mV. At higher concentration it reaches the CAC and self-assembles to form supramolecular nanotubes at malignant mitochondrial site. Here, the PS is exposed on the surface of the cell membrane; subsequently, the transition pores in the mitochondria are open with intact plasma membranes, and mitochondrial caspase activator cytochrome c along with additional pro-apoptotic proteins is seeped into the cytosol that is responsible for the early apoptosis. Furthermore, the noncovalent interaction of the Cy–5-TPP/FF nanotubes with proteins at malignant mitochondria might also aid to induce mitochondria targeted early apoptosis.

Conclusions:

In this study, self-assembling peptide-based molecules forming visible and NIR emitting nanotubes are synthesized by MW-assisted SPPS protocol on Wang resin. The nanotube formation is confirmed by various microscopic techniques. These biomarkers can be used for selective mitochondria targeting and imaging. Moreover, mitochondria targeted early apoptosis is arrested.

These bio-functional nanotubes at the specific intracellular site may be promising approaches to control cellular function and fate. This unique bio-inspired NIR fluorescent peptide-based nanotube may lead to potential methods for image-guided organelle specific delivery, nanobiotechnology in cancer, and targeted nanotheranostic applications. These fluorescent nanotubes can be easily engineered with a variety of targeting functional groups.

REFERENCES:

[1] Tanaka, A.; Fukuoka, Y.; Morimoto, Y.; Honjo, T.; Koda, D.; Goto, M.; and Maruyama, T. *J. Am. Chem. Soc.* **2015**, *137*, 770−775.

[2] Pires, R. A.; Abul-Haija, Y. M.; Costa, D. S.; Novoa-Carballal, R; Reis, R. L.; Ulijn, R. V.; and Pashkuleva, I. *J. Am. Chem. Soc.* **2015**, *137*, 576−579.

[3] He, H.; Lin, X.; Guo, J.; Wang, J.; and Xu, B. *ACS Nano* **2020**, *14*, 6947−6955.

[4] Jeena, M. T.; Jeong, K.; Go, E. M.; Cho, Y.; Lee, S.; Jin, S.; Hwang, S.-W.; Jang, J. H.; Kang, C. S.; Bang, W.-Y.; et al. *ACS Nano* **2019**, *13*, 11022−11033.

[5] Jeena, M. T.; Palanikumar, L.; Go, E. M.; Kim, I.; Kang, M. G.; Lee, S.; Park, S.; Choi, H.; Kim, C.; Jin, S.-M.; et al. *Nat. Commun.* **2017**, *8*, 26.

[6] Liang, G.; Ren, H.; and Rao, J. *Nat. Chem.* **2010**, *2*, 54–60.

[7] Wanga, H.; Fenga, Z.; and Xu, B. *Chem. Soc Rev.* **2017**, *46*, 2421–2436.

[8] Yuan, Y.; Zhang, J.; Qi, X.; Li, S.; Liu, G.; Siddhanta, S.; Barman, I.; Song, X.; McMahon, M. T.; and Bulte, J. W. M. Furin-mediated intracellular self-assembly of olsalazine nanoparticles for enhanced magnetic resonance imaging and tumour therapy. *Nat. Mater.* **2019**, *18*, 1376–1383.

[9] Burgessa, N. C.; Sharp, T. H.; Thomas, F.; Wooda, C. W.; Thomson, A. R.; Zaccai, N. R.; Brady, R. L.; Serpell, L. C.; and Woolfson, D. N.) *J. Am. Chem. Soc.* **2015**, *137*, 10554–10562.

[10] Chen, W.; Li, S.; Lang, J. C.; Chang, Y.; Pan, Z.; Kroll, P.; Sun, X.; Tang, L.; and Dong, H. *Small* **2020**, *16*, 2002780.

[11] Yang, L.; Peltier, R.; Zhang, M.; Song, D.; Huang, H.; Chen, G.; Chen, Y.; Zhou, F.; Hao, Q.,; Bian, L.; et al. *J. Am. Chem. Soc*. **2020**, *142*, 18150−18159.

[12] Ghadiri, M. R.; Granja, J. R.; and Buehler, L. K. *Nature* **1994**, *369*, 301−304.

[13] Montenegro, J.; Ghadiri, M. R.; and Granja, J. R. *Acc. Chem. Res.* **2013**, *46*, 2955−2965.

[14] Sánchez-Quesada, J.; Isler, M. P.; and Ghadiri, M. R. *J. Am. Chem. Soc.* **2002**, *124*, 10004−10005.

[15] Rho, J. Y.; Cox, H.; Mansfield, E. D. H.; Ellacott, S. H.; Peltier, R.; Brendel, J. C.; Hartlieb, M.; Waigh, T. A.; and Perrier, S. *Nat. Commun.* 2019, *10*, 4708.

[16] Méndez-Ardoy, A.; Bayón-Fernández, A.; Yu, Z.; Abell, C.; Granja, J. R.; and Montenegro, J. *Angew. Chem., Int. Ed.*. **2020**, *59*, 6902−6908.

[17] Luo, Y.; Song, Y.; Wang, M.; Jian, T.; Ding, S.; Mu, P.; Liao, Z.; Shi, Q.; Cai, X.; Jin, H.; et al. *Small* 2019, *15*, 1902485.

[18] Reches, M.; and Gazit, E. *Science* **2003**, *300*, 625−627.

[19] Carny, O.; Shalev, D. E.; and Gazit, E. *Nano Lett.* **2006**, 6, 1594–1597.

[20] Görbitz, C. H. *Chem. Commun.* 2006, 2332–2334.

[21] Görbitz, C. H. *Chem. Eur.* **2001**, *J. 7*, 5153–5169.

[22] Sun, B.; Tao, K.; Jia, Y.; Yan, X.; Zou, Q.; Gazit, E.; and Li, J. *Chem. Soc Rev. 48*, **2019**, 4387−4400.

[23] Yan, X.; He, Q.; Wang, K.; Duan, L.; Cui, Y.; and Li, J. *Angew. Chem., Int. Ed. 46*, **2007**, 2431–2434.

[24] Yan, X.; Zhu P.; and Li, J. *Chem. Soc. Rev.* **2010**, *39*, 1877–1890.

[25] Fan, Z.; Chang, Y.; Cui, C.; Sun, L.; Wang, D. H.; Pan, Z.; and Zhang, M. *Nat. Commun.* 2018, *9*, 2605.

[26] An, H.-W., Hou, D., Zheng, R., Wang, M.-D., Zeng, X.-Z., Xiao, W.-Y., Yan, T.-D., Wang, J. Q., Zhao, C.-H., Cheng, L.-M. et al. *ACS Nano* **2020**, *14*, 927–936.

[27] Saha, P. C., Das, R. S., Chatterjee, T., Bhattacharyya, M., and Guha, S. *Bioconjugate Chem.* **2020**, *31*, 1301–1306.

[28] Yan, R., Hu, Y., Liu, F., Wei, S., Fang, D., Shuhendler, A. J., Liu, H., Chen, H.-Y.; and Ye, D. *J. Am. Chem. Soc.* **2019**, *141*, 10331−10341.

[29] Baumes, J. M.; Gassensmith, J. J.; Giblin, J.; Lee, J.-J.; White, A. G., Culligan, W. J., Leevy, W. M., Kuno, M., and Smith, B. D. *Nature Chem. 2*, **2010**, 1025–1030.

[30] Thomas, A. P., Palanikumar, L., Jeena, M. T., Kim, K., and Ryu, J.-H. *Chem. Sci.* **2017**, *8*, 8351−8356.

[31] He, H.; Wang, J., Wang; H., Zhou, N.; Yang, D.; Green, D. R.; and Xu, B. Enzymatic Cleavage **2018**, *J. Am. Chem. Soc. 140*, 1215−1218.

[32] Nash, G. T.; Luo, T.; Lan, G.; Ni, K.; Kaufmann, M.; and Lin, W. *J. Am. Chem. Soc.* **2021**,*143*, 2194−2199.

[33] Kubi, A. G.; Qian, Z.; Amiar, S.; Sahni, A.; Stahelin, R. V.; and Pei, D. *Angew. Chem., Int. Ed.* **2018**, *57*, 17183−17188.

[34] Danial, N. N.; and Korsmeyer, S. J. Cell Death: Critical Control Points. *Cell **2004**, 116*, 205−219.

[35] Noh, I.; Lee, D. Y.; Kim, H.; Jeong, C.-U.; Lee, Y.; Ahn, J.-O.; Hyun, H.; Park, J.-H.; and Kim, Y.-C. *Adv. Sci. 5 **2018***, 1700481.

[36] Liu, T.; Roh, S. E.; Woo, J. A.; Ryu, H.; and Kang, D. E. *Cell* **2013**, *Death Dis. 4*, e476.

[37] Lakhani, S. A.; Masud, A.; Kuida, K.; Porter Jr., G. A.; Booth, C. J.; Mehal, W. Z.; Inayat, I.; and Flavell, R. A. *Science* 2006, *311*, 847–851.

[38] Vyssokikha, M. Y.; Holtzeb, S.; Averinaa, O. A.; Lyamzaeva, K. G.; Panteleevaa, A. A.; Mareyd, M. V.; Zinovkina, R. A.; Severina, F. F.; Skulacheva, M. V.; Faself, N., et al. *Proc. Natl. Acad. Sci. U.S A.* **2020**, *117*, 6491–6501.

[39] Zielonka, J.; Joseph, J.; Sikora, A.; Hardy, M.; Ouari, O.; Vasquez-Vivar, J.; Cheng, G.; Lopez, M.; and Kalyanaraman, B. *Chem. Rev.* **2017**, *117*, 10043−10120.

[40] Jung, H. S.; Lee, J.-H.; Kim, K.; Koo, S.; Verwilst, P.; Sessler, J. L.; Kang, C.; and Kim, J. S. *J. Am. Chem. Soc.* **2017**, *139*, 9972−9978.

Jiang, R.-D., Shen, H., and Piao, Y.-J.

[41] Saha, P. C.; Chatterjee, T.; Pattanayak, R.; Das, R. S.; Mukherjee, A.; Bhattacharyya M.; and Guha, S. *ACS Omega* **2019**, *4*, 14579−14588.

[42] Jiang, R.-D., Shen, H., and Piao, Y.-J. *Rom. J. Morphol. Embryol.* **2010**, *51*, 663–667.

[43] Buckhout-White, S.; Spillmann, C. M.; Algar, W. R.; Khachatrian, A.; Melinger, J. S.; Goldman, E. R.; Ancona, M. G.; and Medintz, I. L. *Nat. Commun.* **2014**, *5*, 5615.

[44] García, M. Á. A.; Estirado, E. M.; Milroy, L.-G.; and Brunsveld, L. *Angew. Chem., Int. Ed.* **2018**, *57*, 4976–4980.

[45] Jia, X.; Chen, Q.; Yang, Y.; Tang, Y.; Wang, R.; Xu, Y.; Zhu, W.; and Qian, X. *J. Am. Chem. Soc.* **2016**, *138*, 10778–10781.

[46] Pisoni, D. S.; Todeschini, L.; Borges, A. C. A.; Petzhold, C. L.; Rodembusch, F. S.; and Campo, L. F. *J. Org. Chem.* **2014**, *79*, 5511−5520.

[47] Silva, G. L.; Ediz, V.; Yaron, D.; and Armitage, A. B. *J. Am. Chem. Soc.* **2007**, *129*, 5710–5718.

[48] Mitra, K.; Lyons, C. E.; and Hartman, M. C. T. *Angew. Chem., Int. Ed.* **2018**, *57*, 10263−10267.

[49] Jiang, Q.; Xu, X.; Yin, P.-A.; Ma, K.; Zhen, Y.; Duan, P.; Peng, Q.; Chen, W.-Q.; and Ding, B. *J. Am. Chem. Soc.* **2019**, *141*, 9490−9494.

[50] Tan, X.; Constantin, T. P.; Sloane, K. L.; Waggoner, A. S.; Bruchez, M. P.; and Armitage, B. A. *J. Am. Chem. Soc.* **2017**, *139*, 9001−9009.

[51] Carneiro, B. A.; and El-Deiry, W. S. *Nat. Rev. Clin. Oncol.* **2020**, *17*, 395–417.

Chapter 6

Near-Infrared Unsymmetrical Cyanine Maleimide Conjugate for Live Cell Mitochondria Targeted Imaging and Labeling of Mitochondrial Thiol Exposed Proteins

Introduction

Living cells can be functionalized in a highly regulated manner by expressing a wide range of proteins and their diverse functionality has immense impact on different biological processes. A variety of internal and external stresses like heat, radiation, toxic chemicals or some internal cell diseases such as cancers can exert significant pressures on living cells, resulting in overproduction of some proteins at high levels. Thus, live-cell protein labeling through site-specific covalent modification with organelle targeting fluorophores has immense importance in the fields of cellular biology, bioimaging, chemical biology, biophysics, biotechnology, as well as development of therapeutics.[1–3] However, bioorthogonal conjugation of proteins and site-specific protein labeling using small functional probes inside the heavily crowded complicated live cells milieu without any alteration or impairing of native protein properties, structures, functions and locations is a challenging task.[4–6] Hence, it is imperative to develop a molecular tool for selective organelle targeted labeling of specific proteins inside a complex live cell environment in a rapid and cost-effective manner at minimal biological disturbance.[7–9] Recently, covalent labeling of proteins with small synthetic molecular probes has attracted greater attention.[10–12] NIR fluorophore (NIR) integrated with bioorthogonal reaction holder and organelle targeted functional group for selectively label the specific protein at particular intracellular location is an emerging bioconjugation technique for live-cell imaging and monitoring of specific cellular organelle function, disease progression along with visualization of structure, dynamics in normal and various pathological conditions.[13,14]

Among all other cellular organelles, mitochondria are unique and indispensable, which not only harness energy through ATP production but also play a pivotal role in regulating cellular protein homeostasis, oxidative metabolism and maintaining intracellular redox balance. Mammalian mitochondria encompass more than 1500 proteins, of which only 13 are encoded by mtDNA for oxidative phosphorylation and rest are by nuclear DNA which is then post-translationally imported into mitochondria with the help of different translocases situated at inner and outer membrane of mitochondria. [15] Mitochondrial molecular chaperones along with some client proteins control the biogenesis, protein import, folding, and quality control processes.[16–17] Perturbation of mitochondrial proteome causes neurodegenerative and metabolic disorders including diabetes, cancer, Alzheimer's, Parkinson, Huntington, and cardiovascular diseases.[18-21] Most importantly, the large fluctuations in the local redox environment experienced by mitochondrial proteins especially, thiol group of cysteine (Cys) residues, respond to these alterations through oxidative modifications.[22–24] Mitochondria contains numerous proteins that have characteristic Cys functionality (till now approximately 1500 Cys residues were identified from nearly 450 mitochondrial proteins) showing high nucleophilicity and also due to Cys paucity throughout the proteome, it is pretty good choice for site-specific labeling to acquire better understanding of proteins expression within mitochondria during various biological and pathological conditions. An attractive approach of organelle targeted site-specific protein labeling methods is the introduction of thiol (SH) reactive groups to the chromophore that already bears an organelle targeting moiety. It would result greater accumulation of the probe within a smaller subcellular region and eventually trigger the formation of thioether linkages. Till date Cys specific labeling has

been carried out with haloacetyl, disulfide, benzyl chloride and maleimide moiety containing fluorophores. However, various studies indicates that thioether bond formation by aforementioned approaches suffer lack of preciseness in organelle selective native protein labeling and their stability in a cellular microenvironment containing elevated concentration of free thiols is also a major concern.[25–31] Maleimides by far are most ubiquitous reagents in bioconjugation, owing to their high reactivity and selectivity for biothiols; particularly reaction with exposed Cys residues in peptides and proteins at neutral conditions (pH 6.5-7.5).[32–35] Maleimides indeed do not react with other amino acids like methionine, histidine or tyrosine, whereas amines generally require higher pH compared to reaction of maleimides with thiols. NIR chromophore conjugated with maleimide functional group as well as organelle selective moiety serves as an excellent combination for exposed thiol-selective organelle specific protein labeling, protein modification, quantification, and bioimaging.

In this chapter we introduced a water soluble lipophilic cationic dual targeting NIR unsymmetrical cyanine-5 probe conjugated with maleimide and triphenylphosphonium (TPP^+) functionalities for selective targeting and labeling of Cys exposed proteins inside the live cell mitochondria. The lipophilic cationic TPP^+ subunit is expected to facilitate the rapid accumulation of Cy-5-Mal/TPP^+ in mitochondria depending on a higher negative membrane potential [$(\Delta\Psi_m)_{normal}$ –150 to –180 mV] of inner mitochondrial membrane (IMM).[36–38] We envisioned that after swift initialization through cell membrane Cy-5-Mal/TPP^+ will accumulates in the inner mitochondrial matrix with elevated concentration where maleimide functionality will selectively label the exposed Cys residue of mitochondrial proteins by undergoing

chemoselective Michael addition reaction with reactive thiols (SH). It is expected that this dual localization effect, would help to retain the probe in the mitochondrial matrix for longer time period even after membrane depolarization and facilitate the tracking and visualization of mitochondrial movement in live cells using confocal laser scanning microscopy (CLSM). The combination of selective organelle targeting probes with immobilisation after covalent attachment with reactive side chain exposed proteins in the subcellular compartments also provides an elegant strategy in live cell multicolour imaging as well as monitoring of disease progression.

Experimental Methods

General Methods and Materials

Synthesis and Characterization of Cy-5a/TPP$^+$, Cy-5-Mal/TPP$^+$, and Cy-5b-Mal dyes:

Syntheses of all the compounds were carried out in dry solvents and under the N_2 atmosphere. Silica gel coated aluminium TLC sheets (TLC silica gel 60 F_{254}) were used to carry out analytical thin layer chromatography (TLC) and respective spots were further detected under UV lamp or naked eye or by developing with I_2. The crude materials were purified by column chromatography by silica gel (100-200 mesh). Prior to usage, the column chromatography solvents were distilled. The intermediate compounds 2,3,3-Trimethylindolenine, 1-(5-Carboxypentyl)-2,3,3-trimthyl-3*H*-indolium bromide (**3**), 1-Hexyl-2,3,3-trimethyl-3*H*-indol-1-ium bromide (**4**) and Malonaldehyde bis(phenylimine) monohydrochloride, for the constructions of unsymmetrical Cy-5a/TPP$^+$ (**8**) and Cy-5b were synthesized following our previously discussed procedures in Chapters 3 and 4.[39–40] Syntheses of Cy-5a/TPP$^+$, Cy-

5-Mal/TPP$^+$, Cy-5b-Mal, and their precursors were illustrated in Scheme 1 and all the compounds were characterised by 1D (^{1}H, ^{13}C , ^{31}P and ^{19}F) and 2D (^{1}H-^{1}H gCOSY) NMR spectroscopy, as well as high resolution ESI-MS.

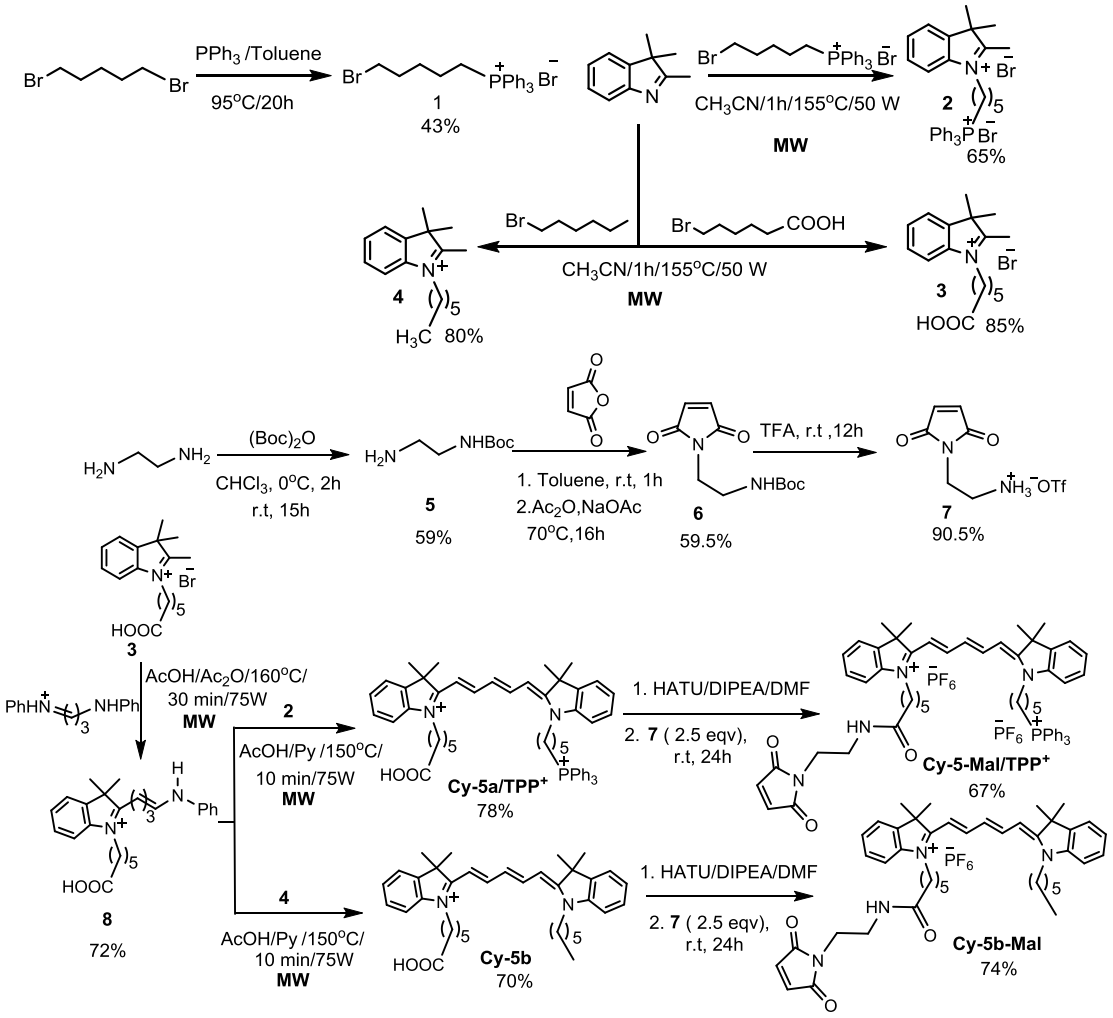

Scheme 1. Synthetic route for the preparation of Cy-5a/TPP$^+$, Cy-5-Mal/TPP$^+$ and Cy-5b-Mal.

(a) (5-Bromopentyl)triphenylphosphonium bromide (1): 1,5-dibromobutane (3.1 mL, 5.29 g, 23 mmol) was slowly added to a solution of

triphenylphosphine (TPP) (3.01 g, 11.5 mmol) in 25 mL toluene at 95°C and the solution was refluxed for 20 h. After cooling the resultant solution to room temperature, it was concentrated under reduced pressure to get a sticky solid, which was washed with ACN:EtOAc (4:1) solvent mixture for several times to get the pure product 1 as a pale-yellow sticky solid.

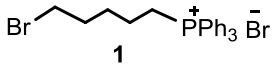

1

Yield: 2.43 g (43%).

^{1}H NMR (500 MHz, DMSO-d_6, 25°C): δ = 7.92–7.73 (15H, m), 3.96–3.81 (2H, m), 3.67–3.59 (2H, m), and 1.55–1.29 (6H, m) ppm. ^{13}C NMR (101 MHz, DMSO-d_6, 25°C): δ = 134.9, 133.6, 133.5, 130.3, 130.1, 119.0, 118.9, 118.7, 118.1, 118.0, 34.9, 32.1, 31.8, 26.7 and 24.7 ppm.

HRMS (ESI +ve) *m*/*z*: Observed for $C_{23}H_{25}BrP^{+}$ $[M]^{+}$ =411.0783, $[M]^{+}$calcd = 411.0872.

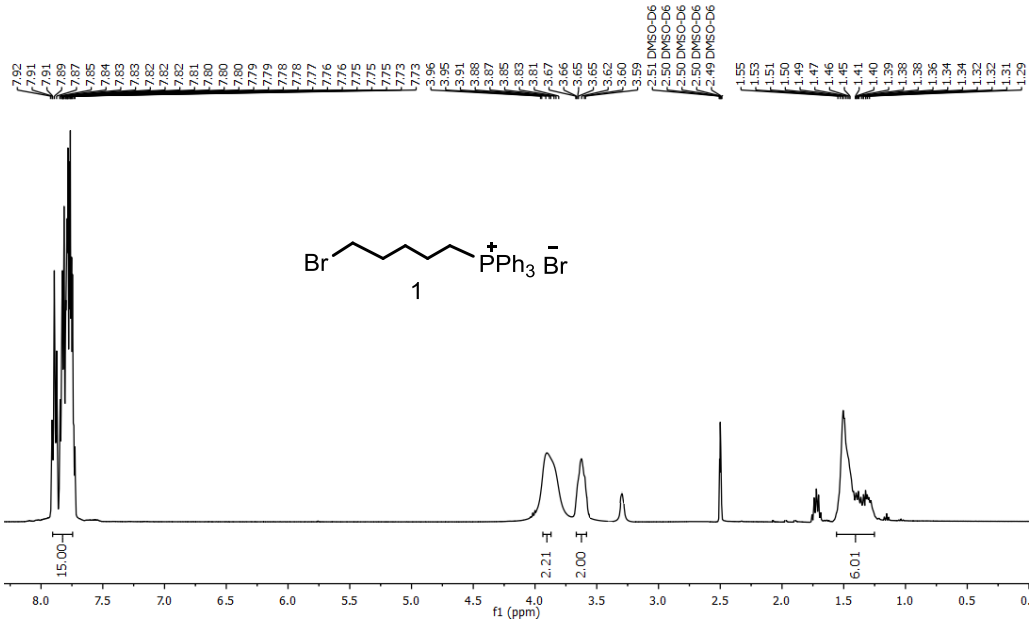

Figure 1. ^{1}H NMR (400 MHz, DMSO-d_6, 25°C) spectrum of (5-bromopentyl)triphenylphosphonium bromide (compound 1).

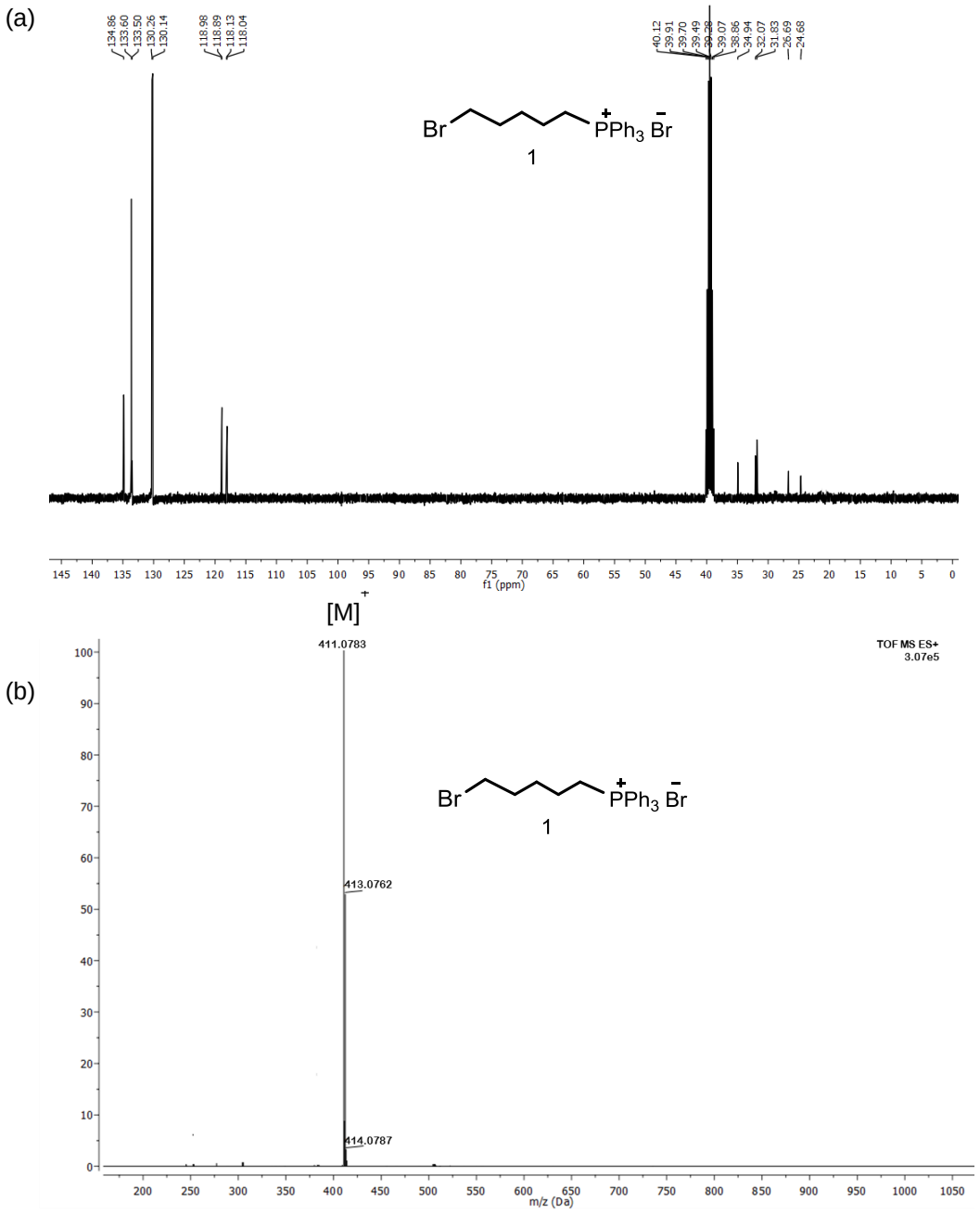

Figure 2. (a) ^{13}C NMR (101 MHz, DMSO-d_6, 25°C) and (b) HRMS (ESI +ve) spectrum of (5-bromopentyl)triphenylphosphonium bromide (compound 1).

Synthesis of Quaternary Heterocyclic Indolium Salt:

N atom of 2,3,3-trimethyl indolenine was covalently attached with alkyl chain, triphenylphosphonium ($–PPh_3^+$), and carboxylic (–COOH) functionality (following our previously reported synthetic approach discussed in chapters 4 and 5) using appropriate alkylating agents such as (5-bromopentyl)triphenylphosphonium bromide and 6-bromohexanoic acid under microwave (MW) conditions.[39–40] The influence of temperature and time are scrutinized on the yield of the reaction, without altering the mole ratio of indolenine and alkylating agent containing TPP^+ moiety (Table 1). MW heating at 155°C for 60 min gave the best result. Compared to the conventional heating process, MW assisted quaternization method afforded the desired products 2, 3 and 4 in higher yields, considerably shortening reaction times from day(s) to 60 min.

Table S1. Synthesis of quaternary indolium salt containing TPP^+ moiety (**2)** by conventional and microwave methods.

Compound	Temperature (ºC)	Time (min)	Method	Yield (%)
2	85	4320	A	45
2	155	10	B	15
2	155	30	B	33
2	155	60	B	65

A: Conventional heating method: ACN/reflux, 72 h.

B: Microwave method: ACN.

(b) 5-(3,3-Dimethyl-2-methyleneindolin-1-yl)pentyltriphenylphosphonium bromide (2): 2,3,3-Trimethylindolenine (0.16 g, 1.0 mmol), 2 [(5-bromopentyl)triphenylphosphonium bromide] (1.48 g, 3.0 mmol) were taken in a microwave tube and CH_3CN (3.0 mL) was added to dissolved the mixture. Then the tube was capped firmly and heated under MW for 1 h at 155°C. The resultant reaction mixture was allowed to cool and concentrated under reduced pressure to get a brown precipitate, which was subsequently washed with $CHCl_3$: Hexane (1:4) solution for 3-4 times and then with ether (3×10 mL) to obtain purple color solid as a desired product.

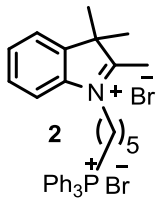

Yield: 0.42 g (65%)

^{1}H NMR (400 MHz, $CDCl_3$, 25°C): δ = 7.76–7.69 (9H, m), 7.67–7.60 (6H, m), 7.58–7.55 (1H, m), 7.50–7.45 (2H, m) , 7.41–7.37 (1H, m), 4.60 (2H, t, *J* = 7.6 Hz), 3.63–3.55 (2H, m), 3.12 (3H, s), 2.21–2.16 (2H, m), 2.01–1.96 (2H, m), 1.81–1.74 (2H, m), 1.57 (6H, s) ppm. ^{13}C NMR (101 MHz, $CDCl_3$, 25°C): δ = 196.0, 141.5, 141.1, 135.4, 135.1, 133.9, 133.8, 133.4, 133.3, 132.1, 132.0, 130.7, 130.6, 130.5, 130.0, 129.8, 128.6, 128.5, 123.1, 119.3, 118.4, 117.5, 116.5, 54.6, 53.6, 49.4, 27.8, 27.4, 23.6, 22.2, and 17.5 ppm.

HRMS (ESI +ve) *m*/*z*: Observed for $C_{34}H_{38}NP^{2+}$ $[M]^{2+}$ = 245.6575, $[M]^{2+}$ calcd = 245.6365, $C_{34}H_{37}NP^{+}$ $[M]^{+}$= 490.3034 $[M]^{+}$ calcd = 490.2658.

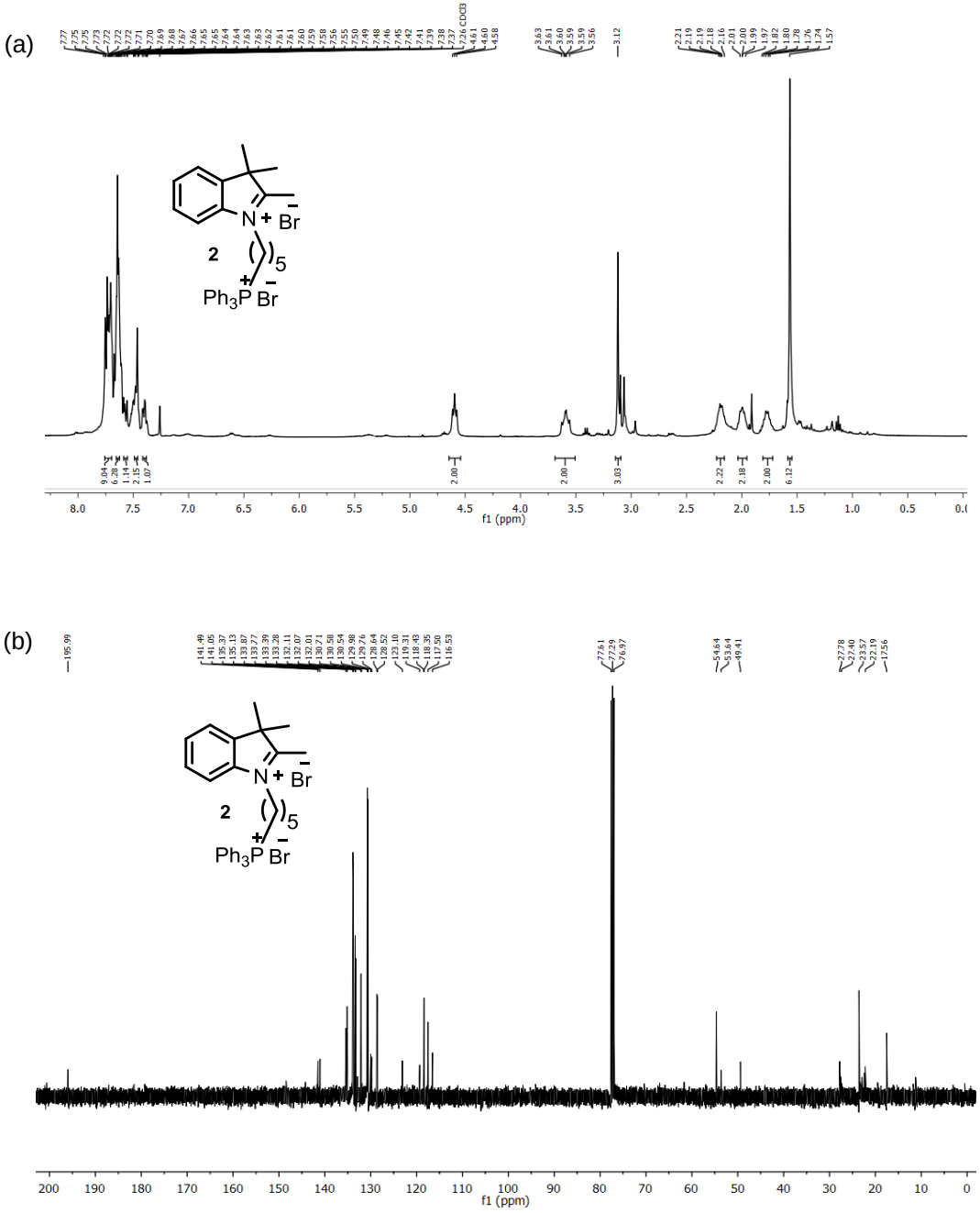

Figure 3. (a) ^{1}H NMR (400 MHz, $CDCl_3$, 25°C) spectrum and (b) ^{13}C NMR (101 MHz, $CDCl_3$, 25°C) spectrum of compound 2.

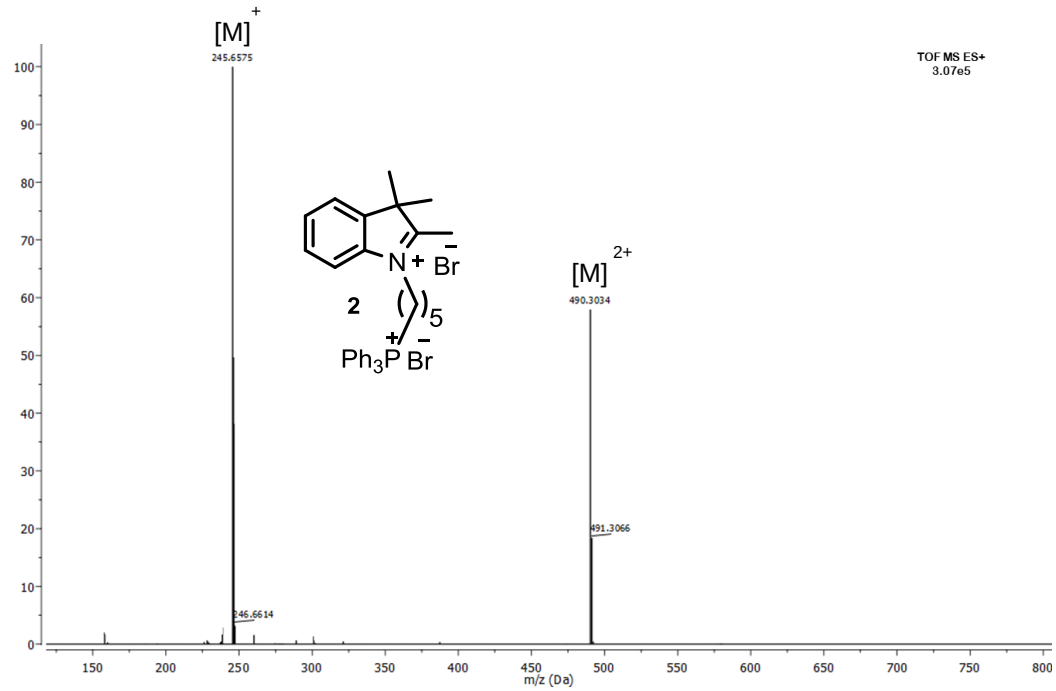

Figure 4. HRMS (ESI +ve) spectrum of compound 2.

Synthesis of N-Maleoyl-ethylenediamine (7):

(c) *N*-Boc-ethylenediamine (5): 1,2-diaminoethane (2.91mL, 43.6mmol) was dissolved in 40 mL $CHCl_3$ and stirred at 0°C. To this solution di-tert-butyldicarbonate (1.0 mL, 4.36mmol.) in 25 mL $CHCl_3$ was added dropwise at 0°C over the duration of 2 h in N_2 atmosphere. Then the resultant mixture was stirred continuously for another 15 h at room temperature. The precipitate obtained was filtered and washed with chloroform (15 mL × 2). Then 40 mL H_2O was added to the filtrate and the organic layer was extracted and subsequently washed with brine (15 mL × 2) followed by drying with anhydrous Na_2SO_4. The combined organic layer was

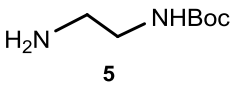

5

collected and $CHCl_3$ was removed under reduced pressure to obtain pure product 5 as a colorless liquid.

Yield: 0.41 g (59%).

^{1}H NMR (400 MHz, $CDCl_3$, 25°C): δ = 4.84 (s, 1H), 3.17 (q, 2H, *J* = 6.2 Hz), 2.77 (t, 2H, *J* = 5.6 Hz), 1.42 (s, 9H) ppm.

HRMS (ESI +ve) *m*/z: Observed for $C_7H_{16}N_2O_2$ $[M+Na]^+$ = 183.1105 $[M+Na]^+$ calcd = 183.1104.

(d) tert-Butyl (2-(2,5-dioxo-2,5-dihydro-1H-pyrrol-1-yl)ethyl)carbamate (6): *N*-Boc-ethylenediamine (0.59 g, 3.67 mmol) was dissolved in 6 mL anhydrous toluene taken in a 25 mL R.B. Maleic anhydride (0.36 g, 3.67 mmol) was added to this solution and stirred for 1 h at 25°C in the N_2 atmosphere. After 1h, reaction mixture was concentrated in rotary evaporator by removing toluene to give crude acid (white amorphous solid R_f = 0.1 in EtOAc). The residue obtained in this process was used in the next cyclisation step without any purification. Then Ac_2O (6 mL) and NaOAc (0.33 g, 4.08 mmol) were added to the residue and warmed to 70°C for 16 h under N_2 atmosphere. The resultant mixture was cooled to r.t. and the residue was poured over ice-cold H_2O and extracted with EtOAc (15 mL × 3). The organic fraction was washed with 25 mL brine, dried with anhydrous Na_2SO_4, filtered and concentrated under reduced pressure to get a brown color crude product. This crude product was purified using column chromatography (EtOAc:Hexane = 7:13) to obtain the desired product 6 as a white solid.

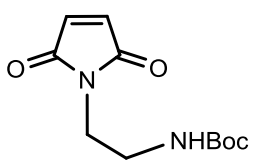

6

Yield: 0.52 g (58.5%).

^{1}H NMR (300 MHz, $CDCl_3$, 25°C): δ = 6.70 (2H, s), 4.75 (1H, br), 3.65 (2H, t, *J* = 5.6Hz), 3.34–3.29 (2H, m), 1.39 (s, 9H) ppm. ^{13}C NMR (101 MHz, $CDCl_3$, 25°C): δ = 170.9, 156.0, 134.2, 79.6, 39.4, 38.1, and 28.4 ppm.

(e) N-(2-Aminoethyl)maleimide (trifluoroacetate salt) (7): Compound 6 (0.48 g, 2.0 mmol) was dissolved in DCM:TFA (1:1) at 0°C and then resulting solution was stirred for 6 h at 25°C. The mixture was concentrated and cold Et_2O was added to get a white precipitate. The precipitate was filtered and washed with Et_2O (3 × 10 mL) to get a white crystalline solid product. Yield: 0.53 g (90.5%).

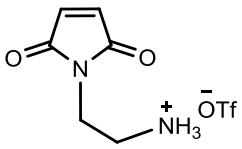

7

^{1}H NMR (400 MHz, DMSO-d_6, 25°C): δ = 7.94 (3H, br), 7.07 (2H, s), 3.66(2H, t, J = 6.0 Hz), 2.99 (2H, t, J = 5.2Hz) ppm. ^{13}C NMR (100 MHz, DMSO-d_6, 25°C): δ =170.8, 134.7, 134.6, 37.4, and 34.7 ppm. HRMS (ESI +ve) m/z: Observed for $C_6H_9N_2O_2$ $[M]^+$ = 141.0671 , $[M]^+$ calcd = 141.0659.

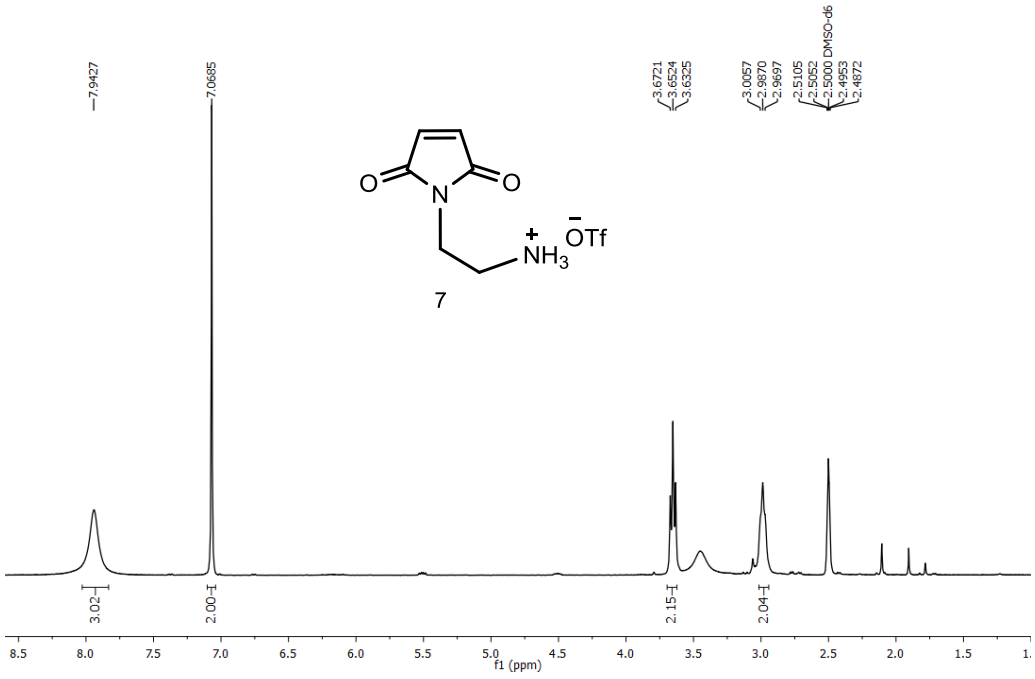

7

Figure 5. ^{1}H NMR (300 MHz, DMSO-d_6, 25°C) of N-(2-Aminoethyl)maleimide (trifluoroacetate salt).

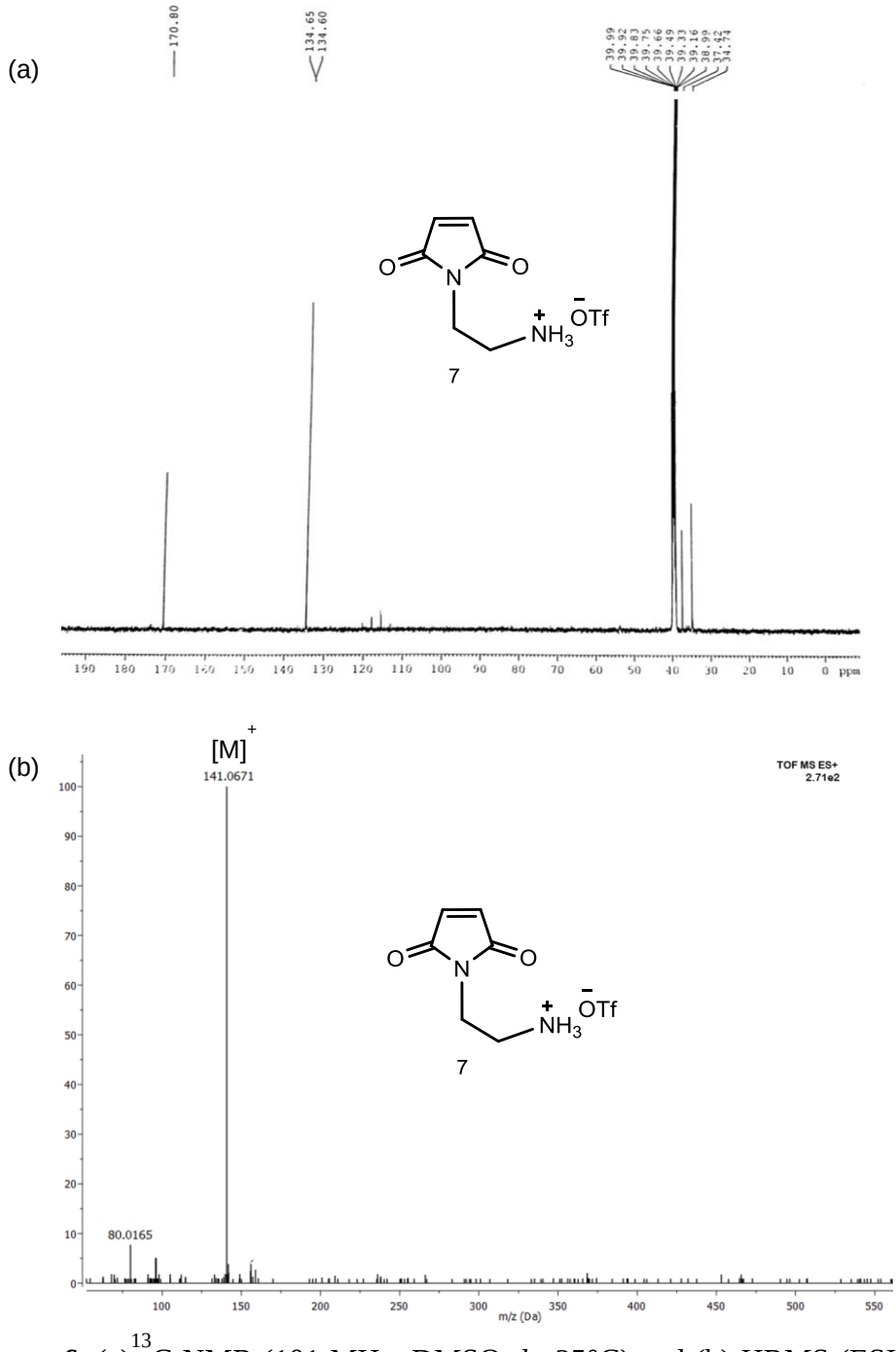

Figure 6. (a) ^{13}C NMR (101 MHz, DMSO-d_6, 25°C) and (b) HRMS (ESI +ve) spectrum of N-(2-Aminoethyl)maleimide (trifluoroacetate salt).

Synthesis of Cy-5a/TPP$^+$, Cy-5-Mal/TPP$^+$, and Cy-5b-Mal dyes and their intermediate:

Intermediate compound 8 for synthesis of both Cy-5a/TPP$^+$ and Cy-5b dyes was prepared following the procedure described in Chapter 4. Further, for the syntheses of Cy-5a/TPP$^+$ and Cy-5b and to get good yield we have also followed the same MW synthetic conditions described in chapter 4. [39]

(f) Cy-5a/TPP$^+$ dye: Intermediate compound **8** (0.24 g, 0.50 mmol) was taken in a MW vessel equipped with a magnetic stir bar and dissolved in pyridine:CH_3COOH (1:1, 2.0 mL each). Compound **2** (0.36 g, 0.55 mmol) was poured into the reaction mixture and the MW tube was capped firmly and exposed to MW irradiation at 150°C for 10 m. The resultant solution was cooled to room temperature and cold Et_2O was added to obtain a blue colored precipitate. The crude compound obtained after filtration was purified by chromatographic separation using DCM:MeOH (9:1) (R_f = 0.43, blue color) to acquire the desired compound Cy–5a/TPP$^+$ as a blue color solid.

Yield: 0.37 g (78%).

^{1}H NMR (400 MHz, DMSO-d_6, 25°C): δ = 8.33 (2H, t, J = 13.0 Hz), 7.89–7.71 (15H, m), 7.63–7.60 (2H, m),7.40–7.32 (4H, m), 7.25–7.22 (2H, m), 6.57–6.54 (1H, m), 6.28 (2H, d, J = 13.4 Hz), 4.09–4.07 (4H, m), 3.58–3.56 (2H, m), 2.17 (2H, t, J = 7.5 Hz), 1.67 (12H, s), 1.54–1.49 (6H, m), 1.38–1.36 (4H, m), 1.21–1.24 (2H, m) ppm. ^{13}C NMR (125 MHz, DMSO-d_6, 25°C): δ = 172.0, 153.5, 141.4, 140.6, 140.5, 134.3, 133.1, 133.0, 129.7, 129.6, 127.8, 125.1, 124.1, 121.9, 118.4, 117.5, 110.5, 102.6, 48.3, 42.8, 42.6, 30.1, 28.4, 26.6, 26.3, 26.1, 25.9, 25.2, 23.8, 21.5, 21.3, and 20.0 ppm.

HRMS (ESI +ve) *m*/*z*: Observed for $C_{54}H_{61}N_2O_2P^{2+}$ $[M]^{2+}$ = 400.2050, $[M]^{2+}$ calcd = 400.2230.

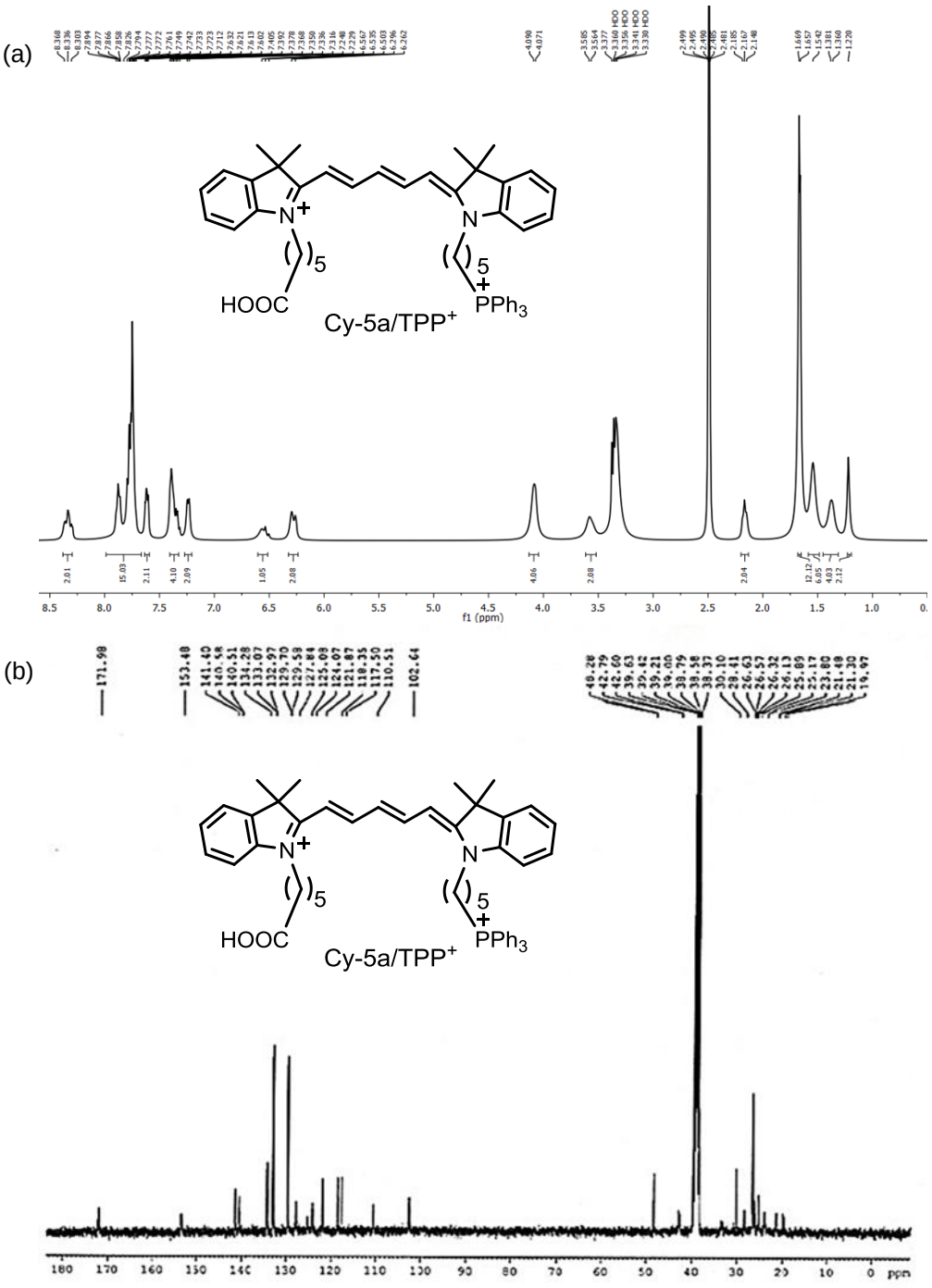

Figure 7. (a) ^{1}H NMR (400 MHz, DMSO-d_6, 25°C) spectrum and (b) ^{13}C NMR (125 MHz, DMSO-d_6, 25°C) spectrum of Cy-5a/TPP^{+}.

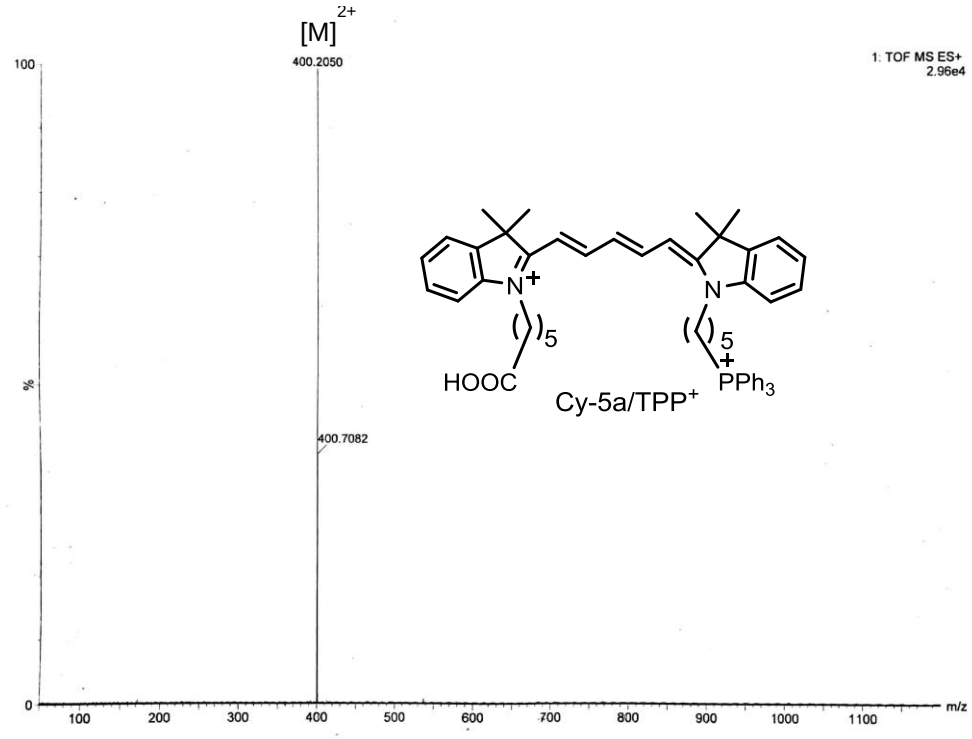

Figure 8. HRMS (ESI +ve) spectrum of Cy-5a/TPP^+.

(g) Cy-5-Mal/TPP^+: Compound Cy-5a/TPP^+ (0.29 g, 0.30 mmol), DIPEA (52 μL, 0.30 mmol), and HATU (0.11 g, 0.30 mmol) were dissolved in 5 mL DMF under N_2 atmosphere and stirred for 30 mins at 25°C. Compound **7** (0.22 g, 0.75mmol) was added to this solution and stirred for 24 h. The resultant solution was concentrated and DMF was evaporated under reduced pressure. Cold Et_2O was added to the residue to obtain blue colored crude product which was collected by filtration. This crude compound was purified by column chromatography using DCM:MeOH (95:5) (R_f = 0.75) to get the blue colored solid pure product Cy-5-Mal/TPP^+.

Yield: 0.25 g (67%).

^{1}H NMR (300 MHz, $CDCl_3$, 25°C): δ = 7.83–7.75 (5H, m), 7.69–7.62 (12H, m), 7.41–7.28 (5H, m), 7.21–7.16 (2H, m), 7.03 (1H, d, *J* = 7.8 Hz), 6.85 (1H, t, *J* = 12.6 Hz), 6.63 (2H, s), 6.34 (1H, t, *J* = 5.8 Hz), 6.30 (1H, d, *J* = 13.5 Hz), 6.17 (1H, d, *J* = 13.2 Hz), 4.00–3.91 (4H, m), 3.61 (2H, t, *J* = 5.8 Hz), 3.38–3.34 (2H, m), 3.25–3.15 (2H, m), 2.22 (2H, t, *J* = 7.0 Hz), 1.82–1.78 (4H, m), 1.73–1.69 (6H, m), 1.67 (6H, s), 1.64–1.58 (6H, m) and 1.51-1.47 (2H, m) ppm.^{13}C NMR (100 MHz, $CDCl_3$, 25°C): δ = 174.0, 173.2, 172.1, 171.1, 153.2, 152.5, 142.3, 142.0, 141.1, 141.1, 135.3, 134.3, 134.3, 133.6, 133.5, 130.8, 130.7, 129.3, 128.8, 127.3, 125.5, 125.0, 122.3, 122.0, 118.5, 117.7, 111.5, 110.5, 104.7, 103.8, 55.9, 49.4, 44.3, 43.8, 38.4, 37.7, 36.1, 29.8, 28.2, 27.5, 27.1, 26.5, 25.1, 22.64, 22.1, and 18.7 ppm.

^{31}P NMR (121 MHz, $CDCl_3$, 25°C): δ = 23.50 (s) and –144.24 (septet, *J* = 710.3 Hz) ppm.

^{19}F NMR (376 MHz, $CDCl_3$, 25°C): δ = –72.14 (d, *J* = 711.0 Hz) ppm.

HRMS (ESI +ve) *m*/*z*: Observed for $C_{60}H_{67}N_4O_3P^{2+}$ $[M]^{2+}$ = 461.2499, $[M]^{2+}$ calcd = 461.2470.

Photophysical properties in H_2O λ_{abs}= 644 nm, λ_{em}= 664 nm, Stokes shift ($\Delta\lambda$) = 20 nm, ε = 1.18 ×10^5 $M^{-1}cm^{-1}$, Φ_f = 0.34 in DMSO [Φ_f of Zinc phthalocyanine (reference) in DMSO = 0.20].

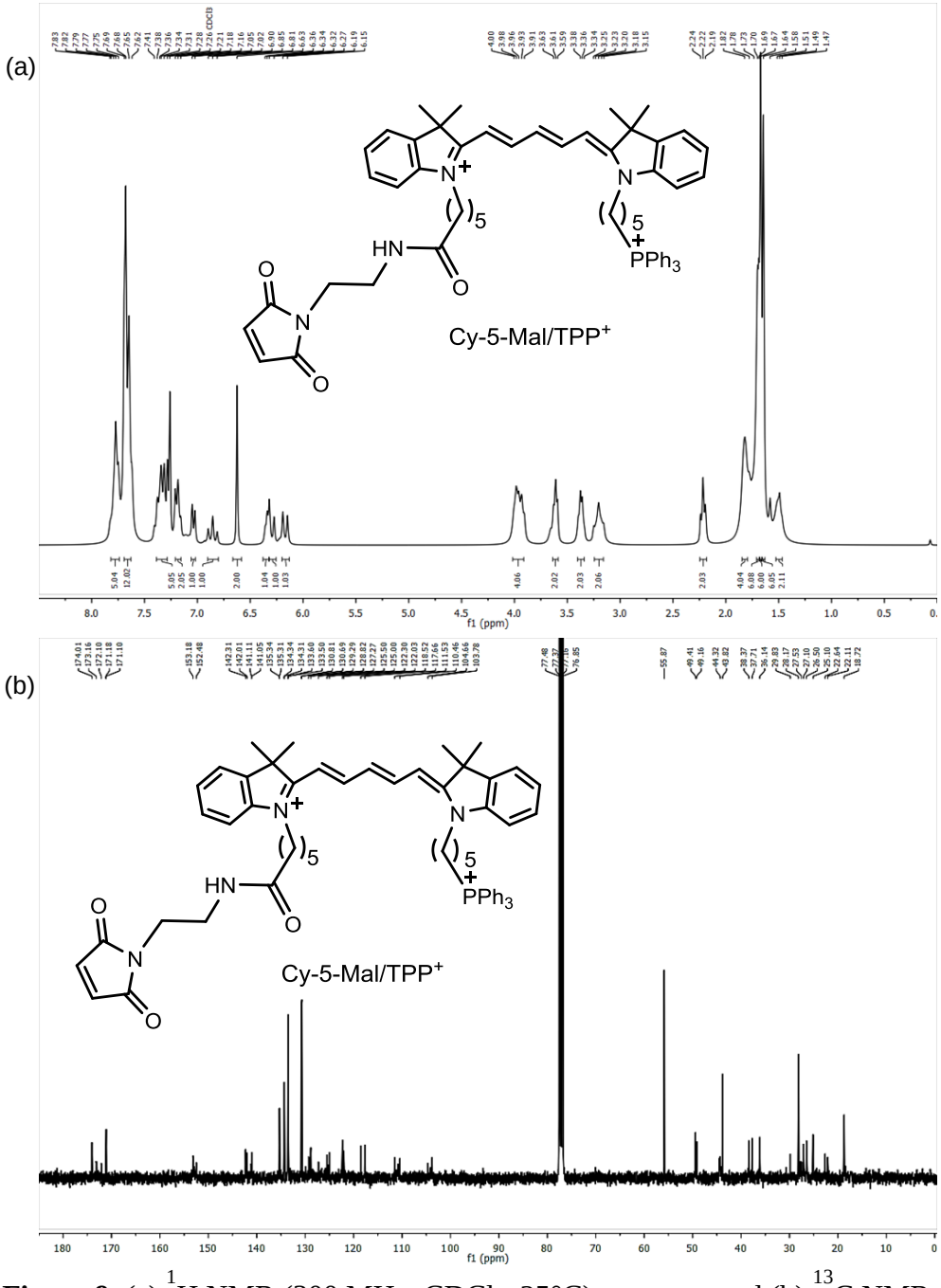

Figure 9. (a) ^{1}H NMR (300 MHz, $CDCl_3$, 25°C) spectrum and (b) ^{13}C NMR (101 MHz, $CDCl_3$, 25°C) spectrum of Cy-5-Mal/TPP^+.

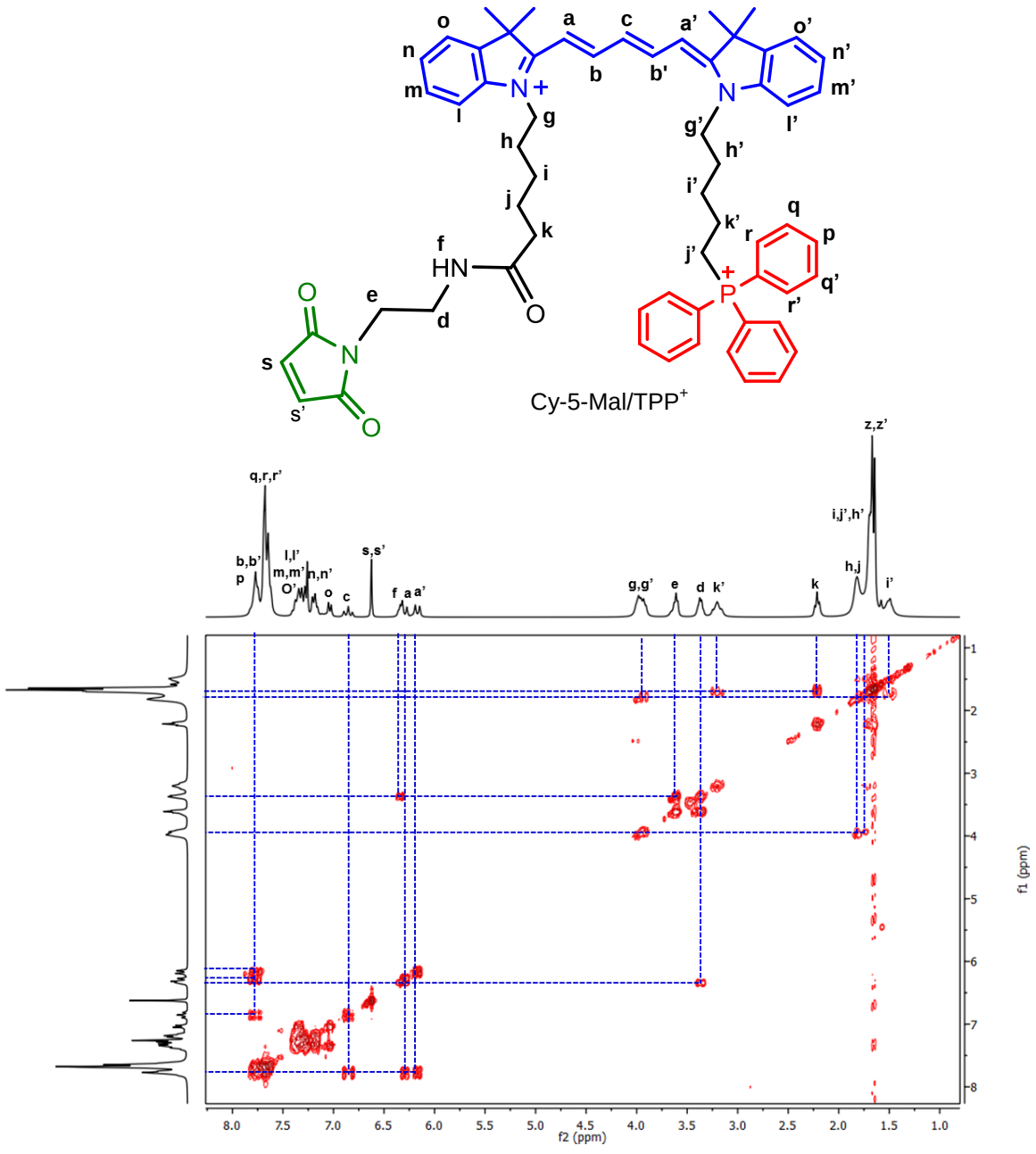

Figure 10. ^{1}H-^{1}H gCOSY NMR spectrum of Cy-5-Mal/TPP^{+} (300 MHz, $CDCl_3$, 25°C).

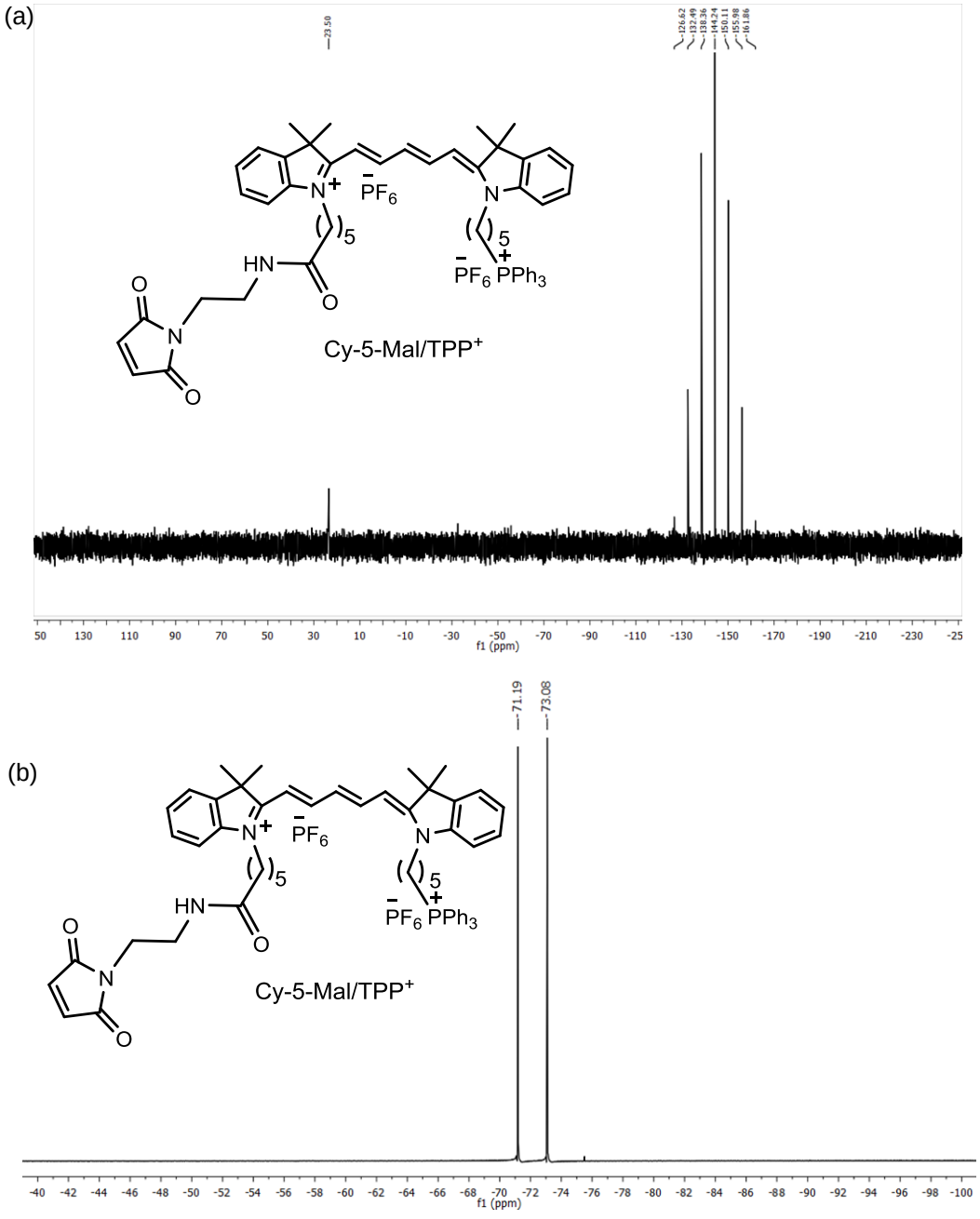

Figure 11. (a) ^{31}P NMR (121 MHz, $CDCl_3$, 25°C) spectrum and (b) ^{19}F NMR (376 MHz, $CDCl_3$, 25°C) spectrum of Cy-5-Mal/TPP$^+$.

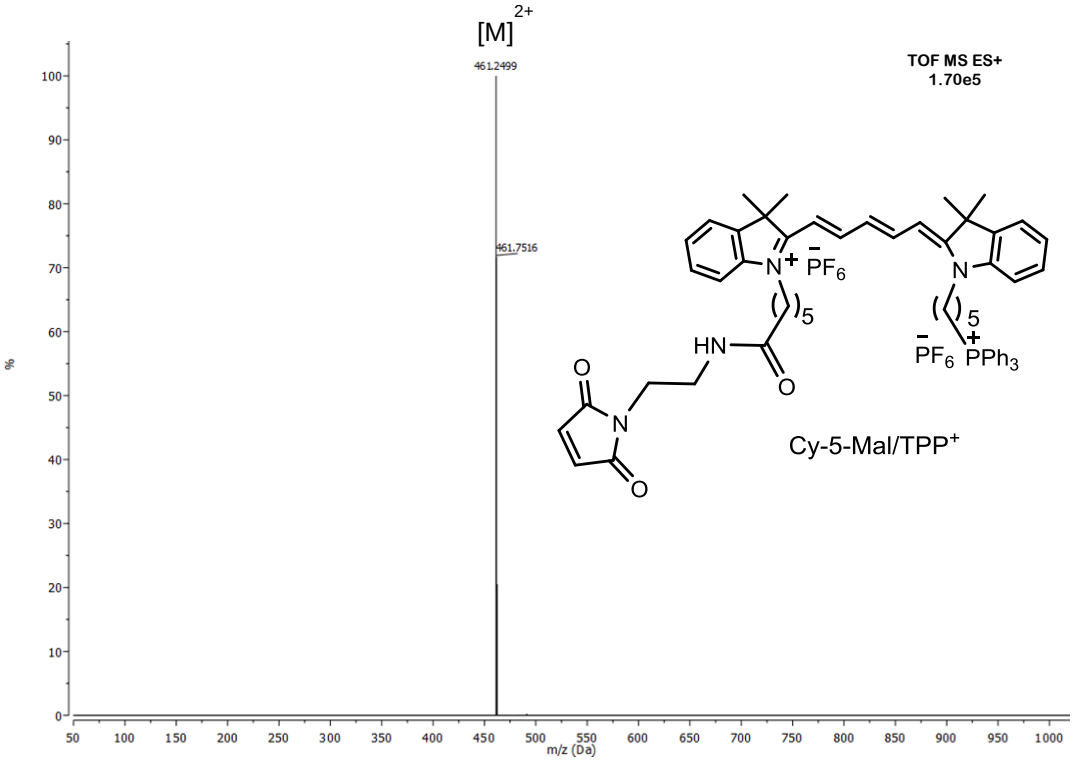

Figure 12. HRMS (ESI +ve) spectrum of Cy-5-Mal/TPP$^+$.

(h) Cy-5b-Mal: Compound Cy-5b (0.11 g, 0.20 mmol), DIPEA (35 µL, 0.20 mmol), and HATU (0.08 g, 0.20 mmol) were dissolved in DMF (4 mL) under N_2 atmosphere and stirred for 30 mins at 25°C. Compound 7 (0.17 g, 0.75 mmol) was added to this mixture and stirred for 24 h. The resultant solution was concentrated and DMF was evaporated under reduced pressure. Et_2O was added to get a dark blue residue which was collected by filtration and further purified by column chromatography using DCM:MeOH (95:5) (R_f = 0.75) to obtain the pure compound Cy-5-Mal/TPP$^+$ as a dark blue solid.

Yield: 0.12 g (74%).

^{1}H NMR (400 MHz, $CDCl_3$, 25°C): δ = 7.83 (2H, t, J = 13.0 Hz), 7.38–7.34 (4H, m), 7.24–7.20 (2H, m), 7. 12–7.04 (2H, m), 6.76–6.68 (3H, m), 6.37 (1H, t, J = 5.2 Hz), 6.22–6.18 (2H, m), 4.00–3.95 (4H, m), 3.67 (2H, t, J = 5.2 Hz),

3.45–3.41 (2H, m), 2.20 (2H, t, J = 7.4 Hz), 1.81–1.76 (4H, m), 1.70 (12H, s), 1.61–1.60 (2H, m), 1.50–1.40 (4H, m), 1.38–1.30 (4H, m) and 0.88 (2H, t, J = 5.2 Hz) ppm. ^{13}C NMR (101 MHz, $CDCl_3$, 25°C): δ = 173.9, 173.0, 172.8, 171.2, 153.10, 142.3, 142.1, 141.7, 134.3, 128.7, 122.3, 110.9, 110.6, 103.9, 103.7, 49.5, 49.4, 44.5, 44.4, 38.5, 37.8, 36.1, 31.5, 28.1, 28.1, 27.4, 27.1, 26.6, 26.4, 25.1, 22.6, and 14.1 ppm.

HRMS (ESI +ve) *m*/*z*: Observed for $C_{43}H_{55}N_4O_3^+$ $[M]^+$ = 675.4239, $[M]^+$ calcd = 675.4269.

Photophysical properties in H_2O λ_{abs}= 643 nm, λ_{em}= 660 nm, Stokes shift ($\Delta\lambda$) = 17 nm, ε = 1.03×10^5 $M^{-1}cm^{-1}$, Φ_f = 0.26 in DMSO [Φ_f of Zinc phthalocyanine (reference) in DMSO = 0.20].

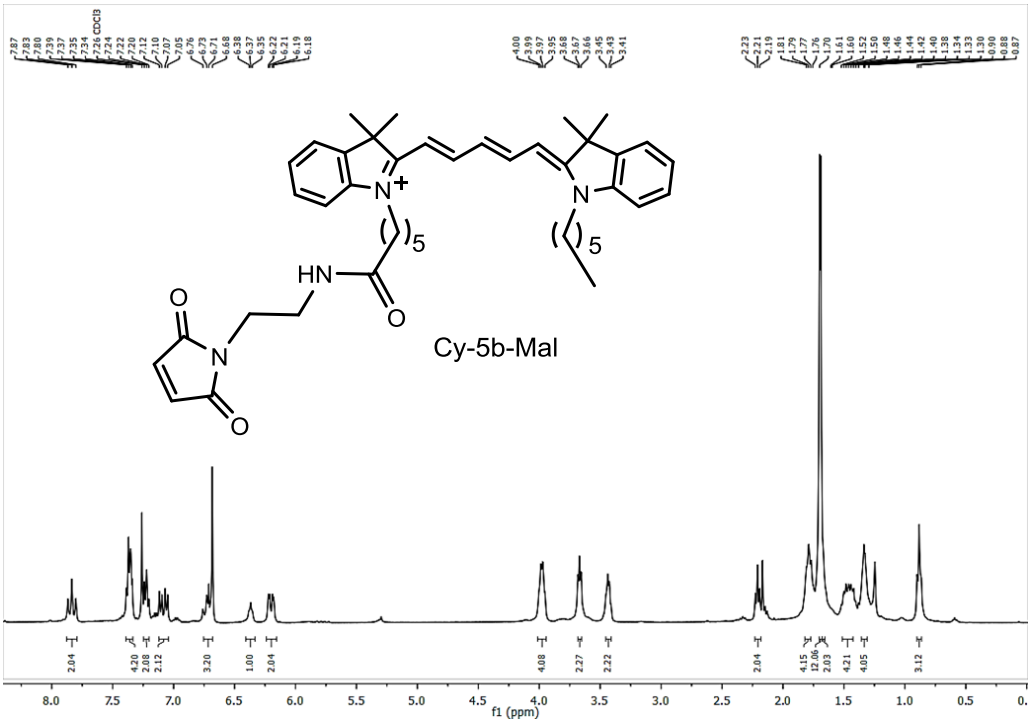

Figure 13. ^{1}H NMR (400 MHz, $CDCl_3$, 25°C) spectrum of Cy-5b-Mal.

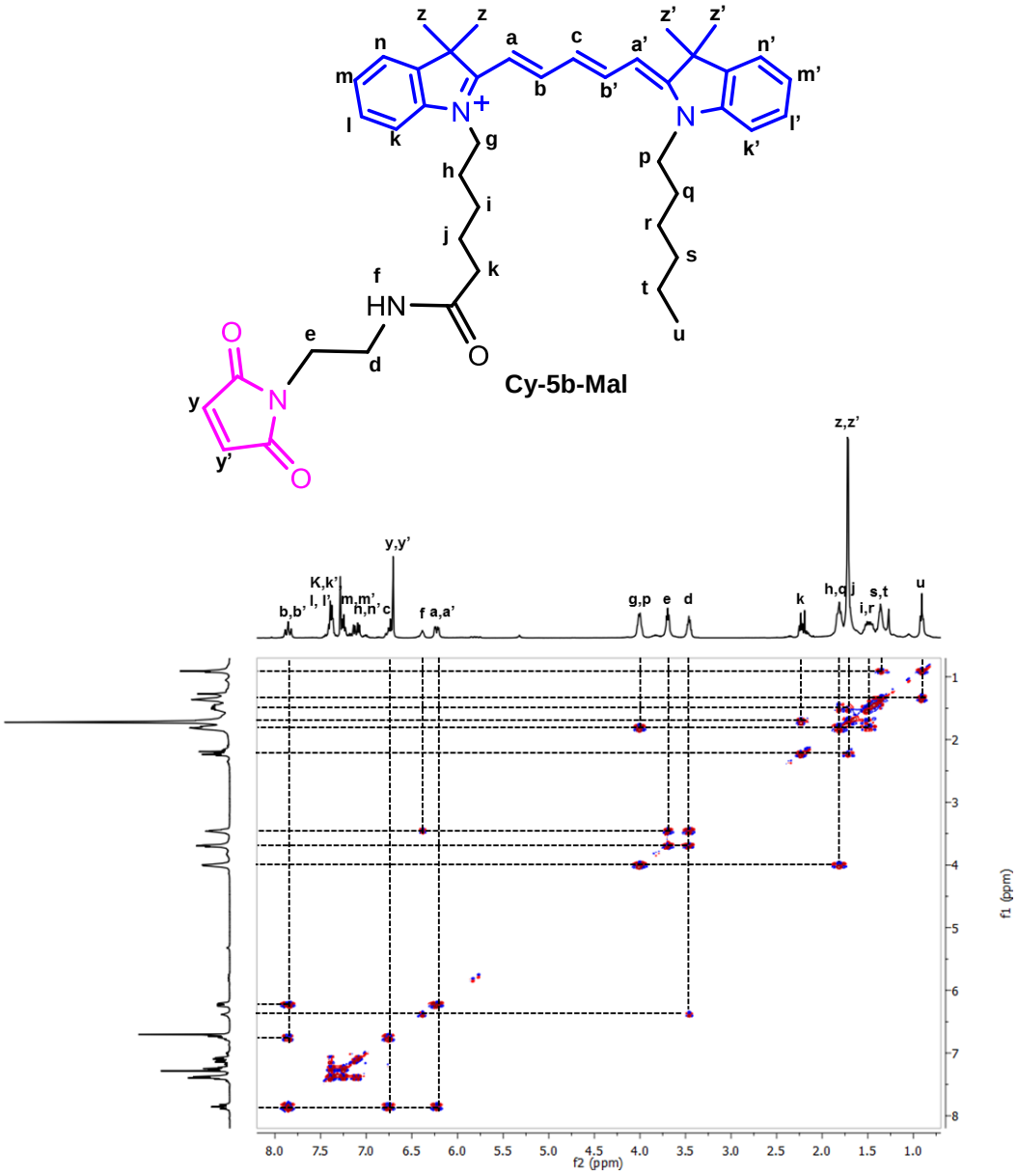

Figure 14. ^{1}H-^{1}H gCOSY NMR spectrum of Cy–5b-Mal (500 MHz, DMSO-d_6, 25°C).

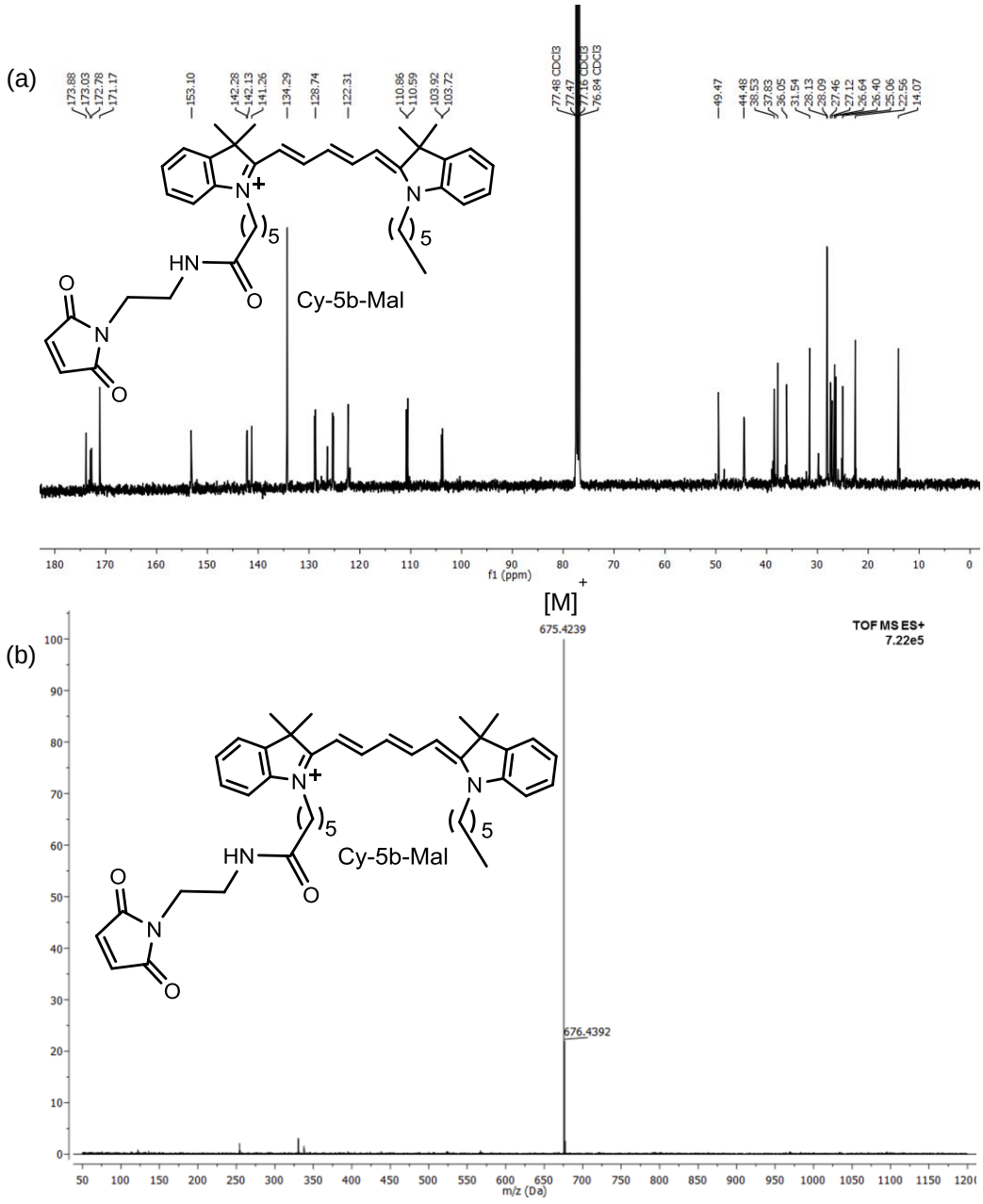

Figure 15. (a) ^{13}C NMR (101 MHz, $CDCl_3$, 25°C) spectrum and (b) HRMS (ESI + ve) spectrum of Cy-5b-Mal.

METHODS

Microwave Synthesizer: Unsymmetrical Cy-5a/TPP^+, Cy-5b-Mal and their precursor molecules were synthesized by manual microwave solid phase peptide synthesizer (CEM corporation, model discover bio, USA make).

NMR Spectroscopy: 1D (^1H, ^{13}C, ^{31}P and ^{19}F NMR) as well as 2D (^1H-^1H gCOSY) NMR spectra were obtained on Bruker DPX300 MHz, Bruker DPX400 MHz and Bruker DPX500 MHz spectrometers at 298 K in appropriate deuterated solvents.

^1H–^1H COSY: The full ^1H NMR assignments including ^1H–^1H correlation of **Cy-5-Mal/TPP^+**, **Cy-5b-Mal**, and **Cy-5-Mal/TPP^+-ME** dyes were done using ^1H–^1H gCOSY experiment (**Figures 10, 14 and 18**).

Mass Spectrometry: High-resolution electrospray ionisation mass spectrometry (HRMS-ESI) results were recorded using a Q-Tofmicro (Waters Corporation) mass spectrometer.

MALDI TOF-MS: To determine mass of Cy-5-Mal/TPP^+ labeled mitochondrial protein complex MALDI TOF-MS were performed using a Bruker Daltonics UltrafleXtreme. Here, for matrix preparation α-cyano-4-hydroxy-cinnamic acid was used.

Absorption Spectroscopy: Shimadzu UV-1800 spectrometer was used to record the absorption spectra in various spectroscopy grade solvents. All measurements were performed in a quartz cuvette having path length of 1 cm. Stability of the Cy-5-Mal/TPP^+ was measured in water, PBS buffer (pH 7.4) and mitochondrial pH=8 at 37°C, over 6 h using peltier temperature controlling unit attached with UV/vis instrument.

Fluorescence Spectroscopy: Horiba Jobin Yvon FluoroMax-4 spectrofluorometer was used to obtain fluorescence spectra in different

spectroscopic grade solvents. Both the excitation and emission bandwidth were fixed at 5 nm.

Time-correlated single photon counting (TCSPC) experiment: Fluorescence lifetimes of the respective fluorophores were measured in different spectroscopic grade solvents using time-correlated single photon counting (TCSPC) method on Horiba DeltaFlex lifetime instrument (Horiba Jobin Yvon IBH Ltd, Glasgow, Scotland, UK). To measure fluorescence lifetimes of Cy-5-Mal/TPP^+ and Cy-5b-Mal 650 nm delta diode laser excitation source (Model: DD-650L, Horiba Scientific) was used. Horiba EzTime decay analysis software was used for data analysis as well as lifetime measurements.

pH Meter: To prepare PBS solutions having different pH values a Mettler Toledo pH meter was used.

Calculation of relative quantum yield of Cy-5-Mal/TPP^+ and Cy-5b-Mal dyes: Relative method was used to measure fluorescence quantum yields (Φ_f) of Cy-5-Mal/TPP^+ and Cy-5b-Mal dyes. Here the integrated fluorescence intensities of the samples were compared with reference compound according to the following equation:

$$\Phi_f(x) = \Phi_f(st) \times [(A_{st} \times F_x \times \eta_x^2) / (A_x \times F_{st} \times \eta_{st}^2)]$$

$\Phi_f(st)$ and $\Phi_f(x)$: fluorescence quantum yields of the reference and synthesized compound, respectively. A_{st} and A_x : absorbance of reference and sample at the excitation wavelength. F_{st} and F_x : the integrated fluorescence area under the corrected fluorescence spectra for the reference and synthesized compound respectively. η_{st} and η_x are the refractive indices of the solvent in which reference and sample compounds, respectively, are measured. Here the reference and sample compounds both were dissolved in DMSO, so (η_x^2 / η_{st}^2) =

1. "st" stands for the standard and "x" refers to the unknown sample. Φ_f (st) of Zinc phthalocyanine in DMSO is 0.20 used as a reference.

The relative Quantum yield (Φ_f) of Cy-5-Mal/TPP$^+$ and Cy-5b-Mal were measured as 0.34 and 0.26, respectively, in DMSO. In water Quantum yield (Φ_f) of Cy-5-Mal/TPP$^+$ was 0.065.

Water solubility of Cy-5-Mal/TPP$^+$ probe: To determine the solubility of Cy-5-Mal/TPP$^+$ in water maximum known amount of this compound was dissolved in water and the solubility was measured by UV/vis spectroscopic method. An absorbance vs concentration calibration curve was obtained by plotting known concentration of Cy-5-Mal/TPP$^+$ against respective absorbance value. Then with proper dilution the absorbance of the saturated solution of the Cy-5-Mal/TPP$^+$ dye was measured using the abs vs conc. calibration curve and corresponding concentration of the dye was determined. This gives the measure of the solubility of Cy-5-Mal/TPP$^+$ in water.

Cell culture: Human cervix adenocarcinoma epithelial cells (HeLa), lung carcinoma (A549), kidney cell (HEK 293), and a mouse myoblast C2C12 cell lines were maintained in growth media containing DMEM (pH 7.4) supplemented with 10% Fetal Bovine Serum (FBS) and antibiotic-(6H, m) antimycotic solution 100× (containing 10,000 units penicillin, 10 mg streptomycin and 25 µg amphotericin B per mL in 0.9% normal saline). All the cell lines were maintained at 37°C in the incubator with routine passage of 5% CO_2.

MTT assay for cell viability: The cytotoxicity of Cy-5-Mal/TPP$^+$ on cancerous HeLa and A549 cell lines as well as noncancerous HEK293 and C2C12 cell lines were determined by MTT assay. All the cells at a population of ~10^4 cells in a 24-well plate were separately seeded in DMEM and incubated for 24 h at 37°C. After 24 h incubation, cells were separately treated at different doses (1,

2, 5, 10, 15, and 20 μM per well) of Cy-5-Mal/TPP^+ and incubated at 37°C for 24 h. MTT (10 μL) solution (5 mg mL^{-1} in PBS) was then added to each well and incubated for 4 h in dark at 37°C. The resultant dark blue formazan crystals formed in this process were dissolved in DMSO and the absorbance (*A*) at 570 nm was recorded (measured in triplicate) using an ELISA plate reader. The results were reported by the following equation:

Viable cells (%) = (*A* of treated cells / *A* of untreated cells) × 100

Similarly, different concentrations of Cy-5b-Mal were also treated with cancerous A549 and normal HEK293 cell lines to measure the cell viability.

Cellular uptake and mitochondrial localization study using confocal microscopy: Confocal laser scanning microscopic (CLSM) images were captured on a Leica STELLARIS 5 platform using HC PL APO 100X/ 1.40 OIL CS2 objective combined with white light laser (WLL) as well as Acousto-Optical Beam Splitter (AOBS) and HyD S detectors. Leica TCS SP8 confocal microscope with 63× and 100× oil plan apochromatic objectives also used in some cases for live cell imaging. For live cell CLSM imaging HeLa and A549 carcinoma cells at a density ~10^3 cells/mL were separately seeded in 35 mm glass bottom confocal dish (SPL Lifesciences, catalogue no. 200350) and allowed to get 70-80% confluency in DMEM for 24 h at 37°C in an air-jacketed 5% CO_2 incubator. After washing with 1x PBS live cells were incubated with 0.7 μM solution of unsymmetrical Cy-5-Mal/TPP^+ in media for 15 min at 37°C in 5% CO_2 atmosphere and then the media was removed carefully and washed gently with 1x PBS. Subsequently cells were incubated first with 0.2 μM MitoTracker Green FM and then with Hoechst (0.1 μg/mL) for 30 and 15 min, respectively at 37°C in 5% CO_2 atmosphere. After the treatment process HeLa and A549 cells were finally washed two times with

media before imaging. Throughout the CLSM imaging procedure 37°C and 5% CO_2 atmosphere was maintained. Higher resolution confocal images were processed by LAS X software. To compare the mitochondrial selectivity of Cy-5-Mal/TPP^+ over the other cellular organelles confocal imaging was also performed with control molecule Cy-5b-Mal following the above mentioned protocol.

For Hoechst: laser excitation wavelength = 405 nm (blue channel, detection range of emission wavelength 415-480 nm); MTG: laser excitation wavelength = 488 nm (green channel, detection range of emission wavelength 499-544 nm); Cy-5 probes: laser excitation wavelength = 638 nm, (Cy-5 channel, detection range of emission wavelength 650-710 nm).

Evidence for immobilisation of Cy-5-Mal/TPP^+ within mitochondria: To verify the immobilization process of Cy-5-Mal/TPP^+ within the inner mitochondrial matrix live cell confocal imaging was performed with Cy-5-Mal/TPP^+ and Cy-5a/ TPP^+ in absence and presence of carbonyl cyanide *m*-chlorophenyl hydrazone (CCCP). First the live HeLa cells were incubated with Cy-5-Mal/TPP^+ and Cy-5a/TPP^+ following the aforementioned live cell staining protocol. After that Cy-5-Mal/TPP^+ and Cy-5a/TPP^+ pre-treated cells were incubated for 20 min with 5 μM CCCP at 37°C. Cells were then washed two times with 1x PBS and imaged under a confocal microscope.

Multicolour confocal imaging: To check the compatibility of Cy-5a-Mal/TPP^+ for multicolour imaging purpose HeLa cells at density of ~10^4 cells/mL were seeded in 35 mm glass bottom confocal dish and allowed to grow for 24 h at 37°C in an air jacketed 5% CO_2 incubator. After gentle washing with 1x PBS live HeLa cells were incubated separately with our mitochondria targeting probe Cy-5-Mal/TPP^+ (0.7 μM for 15 min), nucleus staining dye Hoechst (0.1 μg/mL for 15 min) and plasma membrane highlighting probe CellMask Green

(1 μM for 5-7 min) at 37°C and 5% CO_2 chamber. Then cells were washed with 1x PBS for two times and phenol red free media was added before acquiring the live cell imaging. A real-time video was captured using Leica TCS SP8 confocal microscope (100× oil plan apochromatic objective is used for this purpose) distinctly showing three color confocal image of HeLa cells highlighting the nucleus (blue color), plasma membrane (green color), and mitochondria (red color).

For Hoechst: laser excitation wavelength = 405 nm (blue channel, detection range of emission wavelength 415-480 nm); CellMask Green: laser excitation wavelength = 514 nm (green channel, detection range of emission wavelength 520-570nm); Cy-5 probes: laser excitation wavelength = 638 nm, (Cy-5 channel, detection range of emission wavelength 650-710 nm).

Live cell mitochondria selective protein labeling assay: A549 cells were seeded on 6-well plates ($1x10^5$cells/well) and treated separately with culture media containing various concentrations of Cy-5-Mal/TPP^+ (1, 2, 3, 4, and 5 μM) for 3 h at 37 ^oC humidified with 5% CO_2 incubator. RIPA lysis buffer containing a protease inhibitor cocktail was used to harvest and lyse the cells. The protein concentrations were determined according to Bradford's method.[41] Following lysis, the same volume of 100% acetone was added. Then the samples were vortexed and incubated for 2 h at -20^o C. The samples were centrifuged at 12000 rpm for 10 mins at 4^{o}C and the supernatants were transferred carefully. The pellets obtained in this way were dried by lyophilisation. The lyophilised pellets were reconstituted with 2X Laemmli Sample Buffer (161-0737, Bio-Rad) containing 4% SDS and boiled at 95^{o}C for 5 min. The cell lysates were fractioned in a 10% sodium dodecyl sulphate–polyacrylamide gel electrophoresis (SDS-PAGE). The gel was run for 2 h at

100V. After fixing the gel with MeOH containing 10% AcOH in-gel fluorescent imaging was performed with Amersham Typhoon Biomolecular Imager equipped with NIR excitation laser of 635 nm (emission filter 670 BP30). The protein bands of the gel was then stained by Coomassie blue (0.1% Coomassie Brilliant Blue R-250, 50% MeOH and 10% AcOH) for 1 h at room temperature followed by destaining (40% MeOH and 10% glacial AcOH) overnight at room temperature.

Digestion of fluorescence gel spot for MALDI TOF-MS analysis: Fluorescence gel spots containing mitochondrial proteins labeled with one or more covalently linked Cy-5-Mal/TPP^+ were cut into small pieces and washed two times with *Millipore* ultra-pure water. After dehydrating the gel spots with CH_3CN these fluorescently labeled gel beads were destained with 50 mM NH_4HCO_3:CH_3CN (1:1 v/v) mixture and washed several times with same solution mixture and dried under vacuum centrifuge. Each gel bead was then dissolved in a freshly prepared trypsin solution (final concentration 5 ng/μL in 25 mM NH_4HCO_3) and left at 37^oC for overnight. The digested protein- Cy-5-Mal/TPP^+ complexes were extracted by sonication with aqueous solution containing 1% TFA in 50% CH_3CN. This extraction process followed by sonication repeated several times to ensure complete extraction. Finally these extracts were concentrated under vacuum centrifuge and further analyzed by MALDI-TOF-MS using Bruker Daltonics UltrafleXtreme. α-Cyano-4-hydroxycinnamic acid was used for matrix preparation and matrix was dissolved in 1:1 CH_3CN:H_2O mixture containing 1% TFA.

Protein structure preparation: All the missing atoms and residues of the proteins used in the studies are fixed with the help of homology modelling by Modeller.[42] In this case, 6NHK PDB which correspond to the HSPA9 or mtHSP-70 was used. This PDB file was downloaded from RCSB website. The

position of the binding site in the proteins was found from the atomic coordinate of the bound ligands present in the protein binding site. Obtained protein structure was validated using ProCheck program.[43] Energy minimized structure of the protein was obtained by NAMD 2.3 version on CHARMM General Force Field.[44–45]

Molecular Docking: The molecular docking of **Cy-5-Mal/TPP$^+$** was performed on the HSPA9 protein structure at the natural binding site. For such molecular docking, the energy-minimized structure of the compound was utilized and the energy-minimization was performed through molecular mechanics with the help of MM2 method with 0.0100 minimum RMS Gradient in CHARMM General Force Field. Protein and the compound structures were developed as the .pdbqt files by AutoDockTools which were utilized for docking study with AutoDock4.2.[46] The Auto Dock4.2 was utilized for docking calculations with the help of Lamarckian algorithm inside the grid box having dimensions 60 x 60 x 60 $Å^3$ at the ligand binding pocket. The best docking pose of the compounds was predicted using binding energy, ligand efficiency, inhibition constant, van der Waals forces, intermolecular energy, hydrogen bond; total internal, dissolve energy, torsional energy, and unbound energy. Here, the scoring function can be written as:

$$\Delta G_{binding} = \Delta G_{vdW} + \Delta G_{elec} + \Delta G_{hbond} + \Delta G_{desolv} + \Delta G_{tors}$$

Energy-minimized conformer of the compound in the protein binding site was recorded in the .dlg file which was analysed with the help of AutoDockTools.

Molecular Dynamics: MD simulation of HSPA9 with **Cy-5-Mal/TPP$^+$** were performed using GROMACS with GROMOS96 43a1 force field.[46] In a cubic box, the protein was fitted and charge was neutralized with 0.15 M NaCl. The energy of the system was minimized using the Steepest Descent integrator.

NVT and NPT methods at 1.0 bar pressure and 300K temperature were employed to reach the equilibrium. After this the simulation was performed for 100 ns with 1000 frames/simulation. For the short-range interactions and electrostatic interactions, the cut off value and the PME were 10 Å and 1.0 Å, respectively.

Results and Discussion

Design and characterization of targeting probes:

For selectively target and label mitochondrial proteins we have designed a water soluble NIR small molecular probe equipped with mitochondria-targetable moiety and Cys reactive functional group. Mitochondria maintain a steady pH ~8.0 and 6.8 in the mitochondrial matrix and inter membrane space, respectively, and this serves as impeccable physiological condition to carry out a bioconjugation reaction with thiol group of Cys residue present at the surface of mitochondrial proteins. Selective bioconjugation and labeling of mitochondrial proteins is expected to facilitate by colocalization of the probes with mitochondrial Cys exposed proteins in a smaller subcellular space. These fluorescently modified proteins obtained by such spatially limited chemoselective reactions are then identified by in-gel fluorescent assay and further characterised by MALDI-TOF-MS carried out with Cy-5-Mal/TPP^+ treated A549 cell lysate to confirm their localization in live cells. This selective mitochondria-targeted protein labeling not only ensures retention of Cy-5-Mal/TPP^+ in mitochondria after membrane depolarisation to result long term tracing of single mitochondrial motion but also enables the transfer of dynamically altered mitochondrial proteome information in live cells to a permanent covalent bond. Additionally, high resolution CLSM imaging in live

cells using Cy-5 containing TPP^+ and maleimide functionality demonstrated their efficient mitochondrial targeting ability with excellent biocompatibility.

Our synthesised mitochondria targeted protein labeling compound composed of cyanine-5 (Cy-5) chromophore as NIR signalling unit, a mitochondria localizable lipophilic triphenylphosphonium cation (TPP^+), and a maleimide functionality which can selectively react and covalently bind with thiol group of exposed Cys residues of mitochondrial proteins.[47–48] The construction of unsymmetrical NIR Cy-5 dyes is rather more challenging and demanding than symmetrical Cy-5 dyes.[39] The unsymmetrical Cy-5 dyes are synthesized following an efficient and cost-effective route by isolating and purifying the intermediate to improve the overall yield. Cy-5-Mal/TPP^+ and its related precursor molecules were prepared following our previously standardised microwave assisted synthetic routes outlined in Scheme 1.[39–40] The flexible synthetic routes allowed us to covalently attach mitochondria localizing TPP^+ group and carboxylic (–COOH, that can undergo amidation with amino group of N-aminoethylmaleimide using suitable coupling agent) functionality at the nitrogen atom of 2,3,3-trimethyl indolenine using suitable alkylating agents. To investigate the target specificity and immobilization ability of Cy-5-Mal/TPP^+ in live cell mitochondria, two control molecules Cy-5a/TPP^+ and Cy-5b-Mal, lacking the maleimide and TPP^+ residue, respectively, were also synthesised (scheme 1). All the products obtained were purified by column chromatography and characterised by 1D (^1H, ^{13}C, ^{31}P and ^{19}F) and 2D (^1H-^1H gCOSY) NMR spectroscopy, as well as HRMS (Figures 1-15). ^{19}F NMR of Cy-5-Mal/TPP^+ shows a doublet peak at ~ –72 ppm (J = 711 Hz) suggests the presence of PF_6^- as counter anion. Cy-5-Mal/TPP^+ consists of P

atoms, exhibits two peaks in ^{31}P NMR at ~23.5 ppm (singlet for TPP^+ moiety) and ~ −144.2 ppm (septet, J = 710.3 Hz for PF_6^-) (**Figures 1–15**).

Evidence for thiol cyanine-maleimide conjugation:

To check the thiol selectivity a control molecule Cy-5b-Mal was first treated with 2-mercaptoethanol in $CHCl_3$ in presence of Et_3N and the product was characterised by HRMS (**Figure 16**). Further, to investigate the reactivity of the C=C bond of maleimide functionality of Cy-5-Mal/TPP^+, the targeted molecule was reacted with 2-mercaptoethanol in DMSO/PBS (1/10 v/v, pH=7.0) at 298K for 3 h. The product was purified by column chromatography and characterized using NMR spectroscopy (**Figures 17 and 18**) and mass spectrometry (**Figure 20**). Disappearance of vinylic protons peak of the maleimide functionality at 6.63 ppm and generation of five new peaks between 2.42–7.00 ppm (assigned as t, t′, u, w, x in 2D NMR of Cy-5-Mal/TPP^+-ME **Figure 18**) in ^1H NMR of the Cy-5-Mal/TPP^+-ME indicates the chemoslective addition of thiol group to maleimide unit via Michael reaction. The conjugate was further characterised by ESI-MS (**Figure 19**) and a ^{31}P NMR peak at ~23.5 ppm also confirms to the existence of TPP^+ (**Figure 19**). To confirm biological thiol selectivity, Cy-5-Mal/TPP^+ (1:10 mixture of DMSO/PBS) was added to a degassed aqueous solution (pH=7.0) containing a tripeptide glutathione (GSH), and the final product was identified by ESI-MS (**Figure 20**).

Cy-5b-Mal/ME: 2-Mercaptoethanol (10 μL, 15.0 μmol, 1.5 equiv.) was dissolved in 2 mL $CHCl_3$ containing 0.1 mM Et_3N and taken in a 5 mL glass vial equipped with a tiny magnetic stir bar. The solution was degassed by flushing nitrogen for 20 min. Cy-5b-Mal (8 mg, 10 μmol, 1 equiv.) dissolved in nitrogen-purged $CHCl_3$ (2.5 mL) solution was added dropwise to the 2-mercaptoethanol solution, and the mixer was stirred at r.t. for 24 h. The resultant was concentrated under reduced pressure; residue was dissolved in

DCM and washed with brine. The organic layer was collected and the solvent was evaporated under reduced pressure to obtain a dark blue colored residue. HRMS (ESI +ve) *m*/*z*: Observed for $C_{45}H_{61}N_4O_4S^+$ $[M]^+$ = 753.4416, $[M]^+$ calcd = 753.4408.

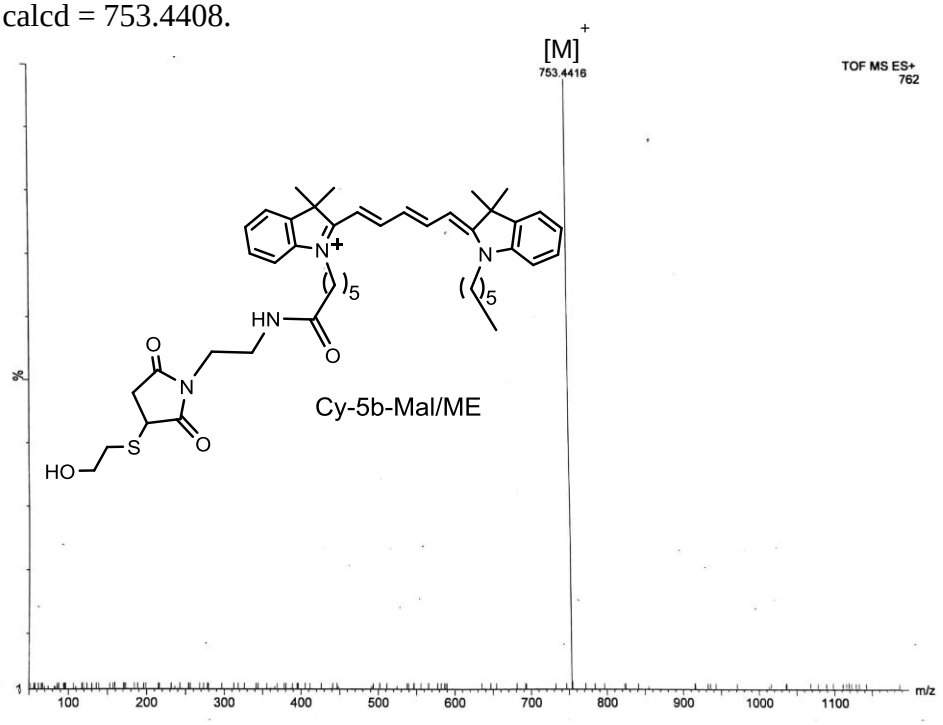

Figure 16. HRMS (ESI +ve) spectrum of Cy-5b-Mal/ME

Cy-5-Mal/TPP$^+$-ME: 2-Mercaptoethanol (16 µL, 22.5 µmol, 1.5 equiv.) was dissolved in 3 mL PBS solution (pH 7.0) and taken in a 10 mL reaction vessel equipped with a magnetic stir bar. The solution was degassed by purging nitrogen for 20 min. Cy-5-Mal/TPP$^+$ (19 mg, 15 µmol, 1 equiv.) dissolved in nitrogen-purged DMSO:PBS (2.5 mL) solution was added dropwise to the 2-mercaptoethanol solution, and the mixer was stirred at r.t. for 3 h. The crude product was extracted from the reaction mixture by shaking with DCM (3×10 mL). The organic layer was combined and washed with brine (2×10 mL). Then

the organic layer was collected and solvent was evaporated under reduced pressure to get a blue solid residue. The crude product was further purified by column chromatography using DCM:MeOH (98:2) (R_f = 0.48) to obtain the pure compound Cy-5-Mal/TPP^+-ME as a dark blue solid.

Yield: 18 mg (94%).

^{1}H NMR (300 MHz, $CDCl_3$, 25°C): δ = 7.80–7.76 (5H, m), 7.73–7.62 (12H, m),7.42–7.29 (5H, m), 7.21–7.16 (2H, m), 7.04 (1H, d, *J* = 8.0 Hz), 6.83 (1H, t, *J* = 13.2 Hz), 6.52 (1H, t, *J* = 5.6 Hz), 6.29 (1H, d, *J* = 13.5 Hz), 6.17 (1H, d, *J* = 13.5 Hz), 4.00–3.89 (5H, m), 3.76 (2H, t, *J* = 5.9 Hz), 3.66–3.61 (2H, m), 3.43–3.37 (2H,m), 3.28–3.17 (3H, m), 2.88 (2H, , t, *J* = 5.7 Hz), 2.50–2.42 (2H, m), 2.22 (2H, t, *J* = 7.2 Hz), 1.84–1.72 (10H, m), 1.67 (6H, s), 1.65 (6H, s), and 1.53–1.49 (2H, m) ppm. ^{13}C NMR (101 MHz, $CDCl_3$, 25°C): δ = 175.2, 173.1, 171.7, 171.0, 142.2, 141.9, 140.8, 135.2, 133.6, 133.4, 130.7, 130.6, 128.6, 126.9, 125.4, 124.8, 122.2, 118.5, 117.4, 110.3, 109.8, 104.7, 104.1, 103.6, 65.9, 61.5, 60.4, 49.3, 48.9, 44.2, 41.3, 39.9, 39.3, 37.3, 36.6, 36.1, 35.5, 29.7, 28.1, 28.0, 27.0, 26.5, 25.0 and 22.7 ppm.

^{31}P NMR (121 MHz, $CDCl_3$, 25°C): δ = 23.57 (s) and –144.26 (septet) ppm.

HRMS (ESI +ve) *m*/*z*: Observed for $C_{62}H_{73}N_4O_4PS^{2+}$ $[M]^{2+}$ = 500.2534, $[M]^{2+}$ calcd = 500.2540.

Cy-5-Mal/TPP^+-GSH: Glutathione (GSH, 4.6 mg, 15.0 µmol, 1.5 equiv.) was dissolved in 3 mL PBS solution (pH 7.0) containing 1 mM TCEP [tris-(2-carboxyethyl)phosphine] and kept in a 10 mL round bottomed flask. The solution was degassed by flushing nitrogen for 20 min. Cy-5-Mal/TPP^+ (13 mg, 10 µmol, 1 equiv.) dissolved in nitrogen-purged DMSO:PBS (2.0 mL) solution was added dropwise to the GSH solution, stirred for 3 h at r.t.. Water was removed from the reaction mixture by freeze drying to get a blue colored solid.

HRMS (ESI +ve) *m*/*z*: Observed for $C_{70}H_{84}N_7O_9PS^{2+}$ $[M]^{2+}$ = 614.7988, $[M]^{2+}$ calcd = 614.7889.

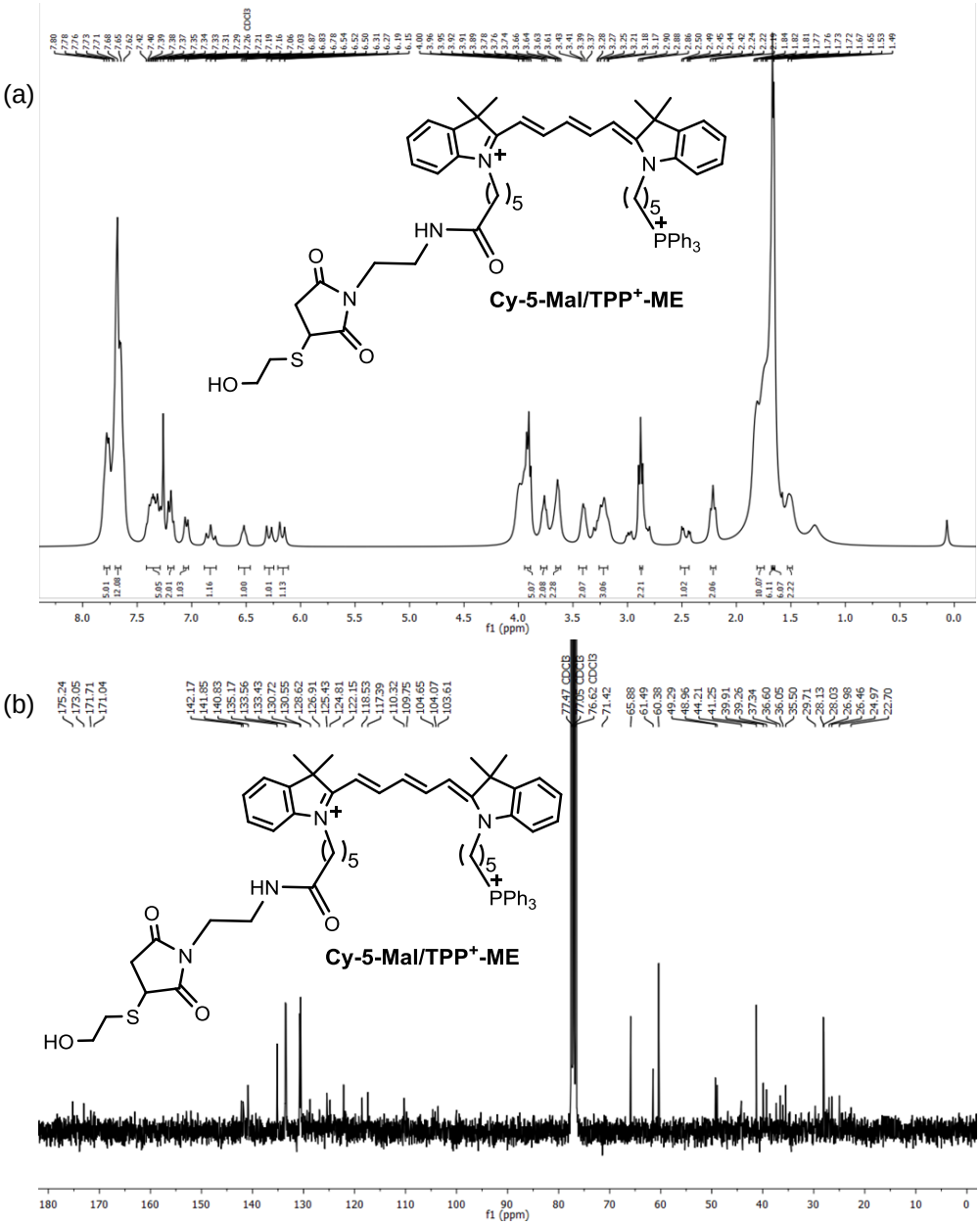

Figure 17. (a) ^{1}H NMR (300 MHz, $CDCl_3$, 25°C) spectrum and (b) ^{13}C NMR (101 MHz, $CDCl_3$, 25°C) spectrum of Cy-5-Mal/TPP^{+}-ME.

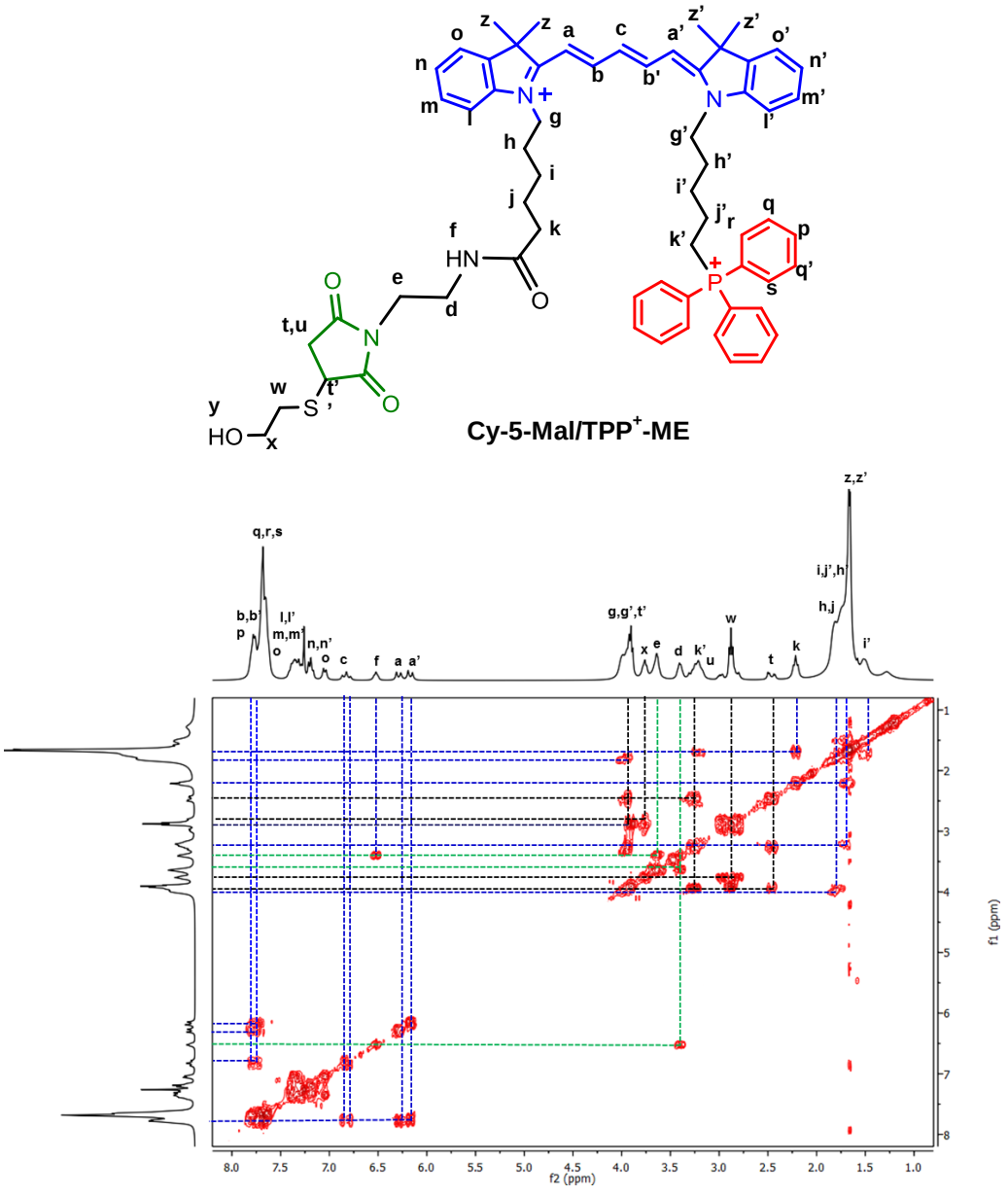

Figure 18. ^{1}H-^{1}H gCOSY NMR spectrum of Cy-5-Mal/TPP^{+}-ME (300 MHz, $CDCl_3$, 25°C).

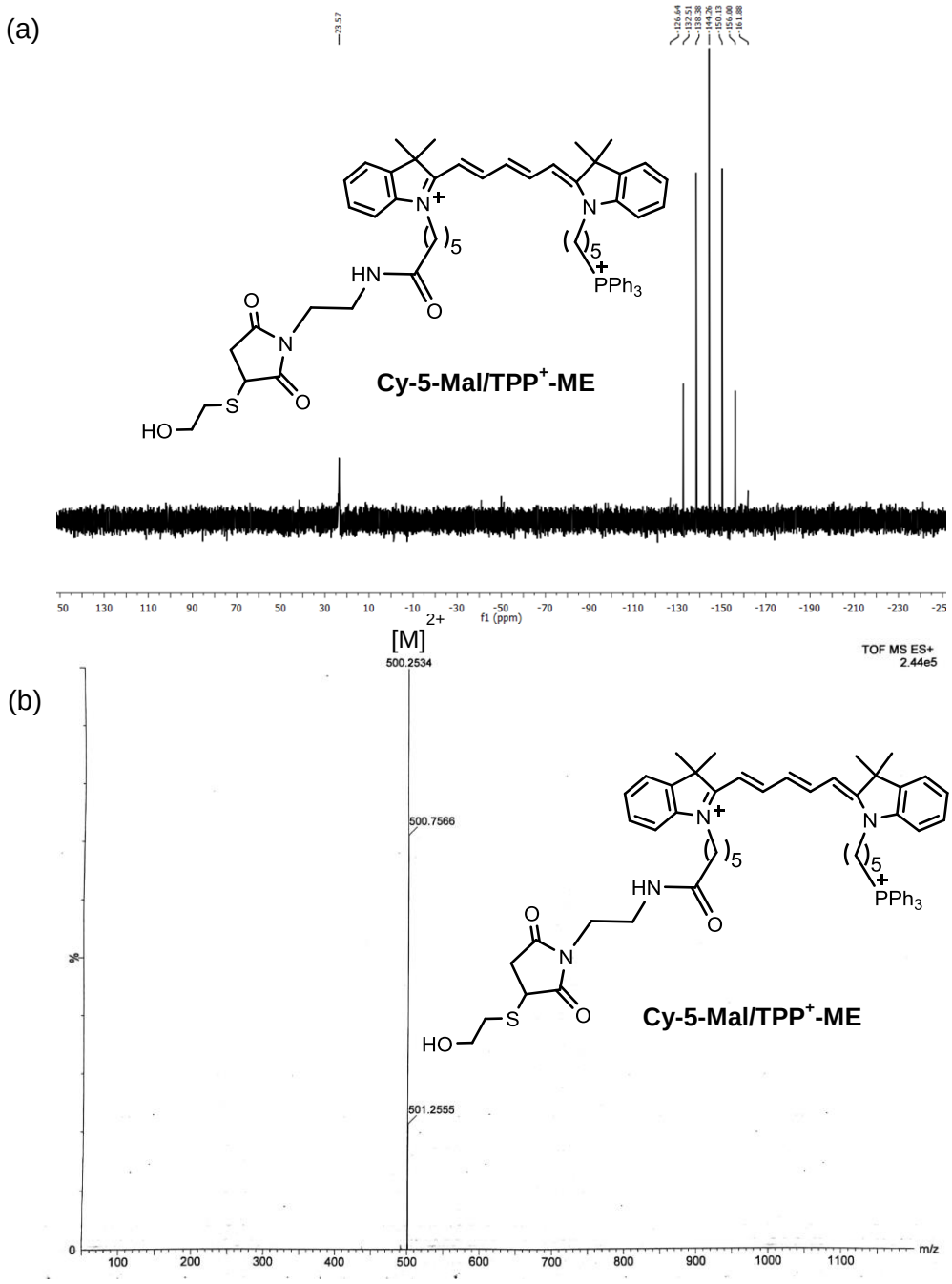

Figure 19. (a) ^{31}P NMR (121 MHz, $CDCl_3$, 25°C) spectrum and (b) HRMS (ESI +ve) spectrum of Cy-5-Mal/TPP^+-ME.

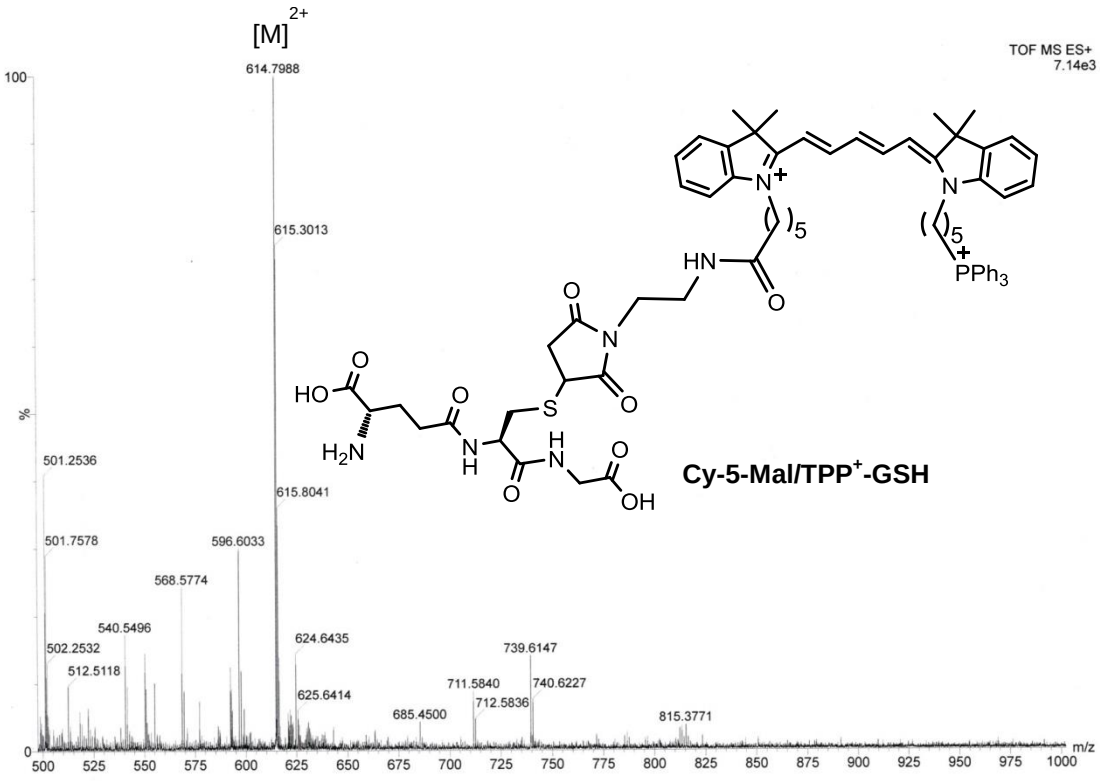

Figure 20. HRMS (ESI +ve) spectrum of Cy-5-Mal/TPP^{+}-GSH.

Photophysical properties and water solubility:

We examined the photophysical properties of both Cy-5-Mal/TPP^{+} and Cy-5b-Mal in various solvents (H_2O, buffer, DMSO, CH_3CN, MeOH, $CHCl_3$) using UV−vis and fluorescence spectroscopy, respectively (**Figures 21** and **23**). Cy-5-Mal/TPP^{+} shows decent water solubility (1.39×10^{-5} mol/L) due to dicationic charge (**Figure 21d**) and maleimide residue. Cy-5-Mal/TPP^{+} displays bright fluorescence owing to its large molar extinction coefficient and good quantum yield. Moreover, Cy-5-Mal/TPP^{+} exhibits extremely narrow absorption and emission bands, which is crucial for multicolor imaging methods where multiple dye combinations with distinctive excitation/emission are often used. The absorption spectra showed an intense peak at 644 nm due to

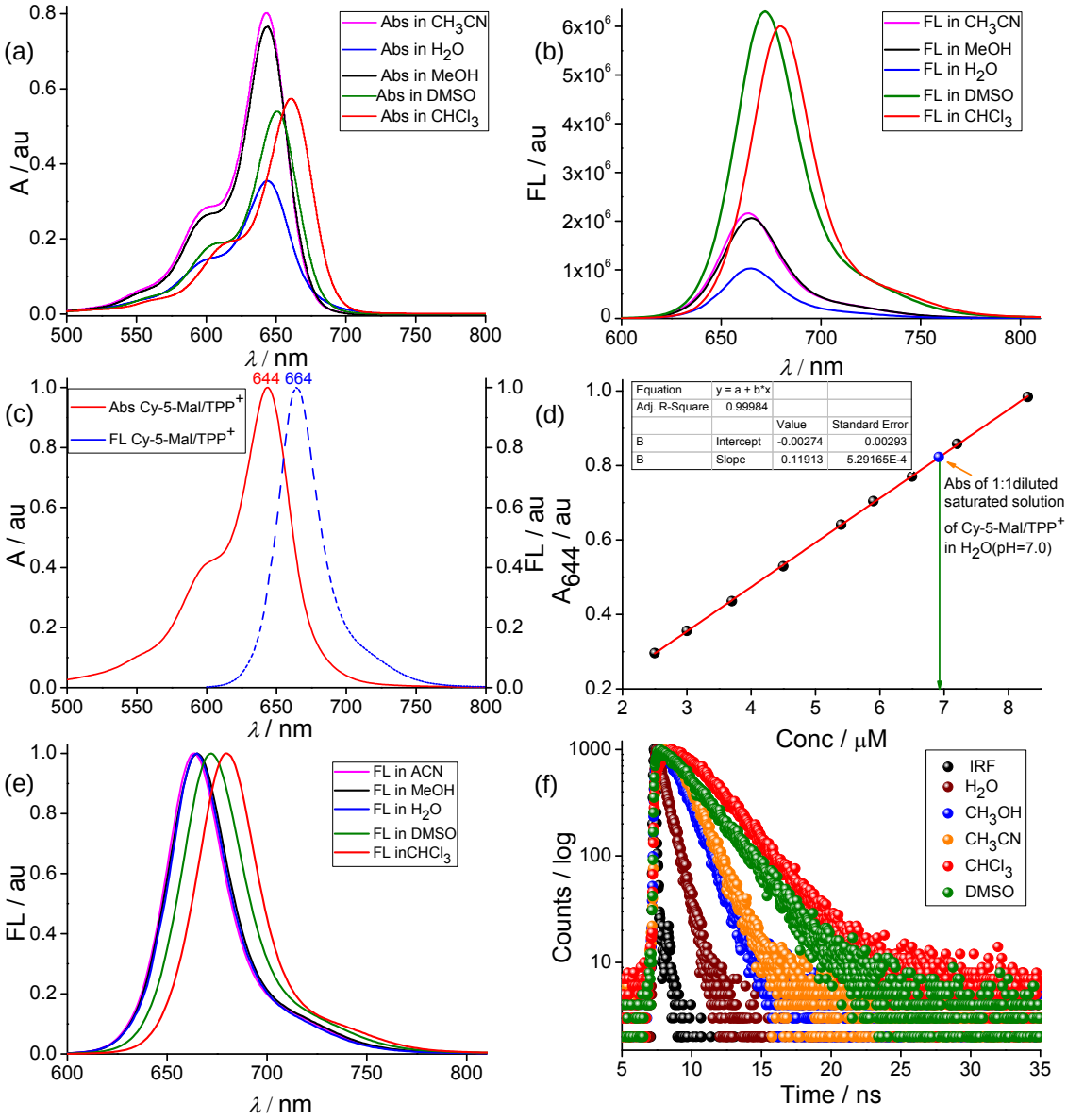

Figure 21. (a) UV-vis absorption and (b) fluorescence emission spectra of Cy-5-Mal/TPP^{+} (3 μM) in various solvents. (c) Normalized absorption and emission plots of Cy-5-Mal/TPP^{+} in PBS (pH=7.4). (d) Linear relationship is observed in absorbance at 644 nm versus concentration plots of Cy-5-Mal/TPP^{+} probe in H_2O (pH=7.0 at 37ºC) and blue sphere represent the absorbance of half

diluted saturated solution of Cy-5-Mal/TPP$^+$ in aqueous solution. (e) Normalized fluorescence intensity plots of Cy-5-Mal/TPP$^+$ showing solvatochromic effect. (f) Variation of fluorescence lifetime of Cy-5-Mal/TPP$^+$ in different solvent polarity after exciting with delta diode laser at 650 nm.

the $\pi \rightarrow \pi^*$ transition with a high molar extinction coefficient of 1.18×10^5 M^{-1} cm^{-1}in water for Cy-5-Mal/TPP$^+$ (**Table 2**). In the case of both probes, the fluorescence maximum was observed at 680 nm (**Figure 21b** and **Figure 23a**) in $CHCl_3$. The high fluorescence QYs of Cy-5-Mal/TPP$^+$ (Φ_f = 0.34) and Cy-5b-Mal (Φ_f = 0.26) are observed in DMSO with respect to zinc phthalocyanines (**Table 2** and **Table 3**). The absorption spectra show a bathochromic shift with decease in solvent polarity. A small solvatochromic effect was observed for both the dyes, in the ground as well as in excited states (~20 nm), which is perhaps due to cooperative effects of refractive indices and dielectric constant of the solvents (**Figures 21e**). Fluorescence lifetime (τ) of Cy-5-Mal/TPP$^+$ is studied in different solvents by TCSPC technique. $\tau \approx 2.093$ ns and $\tau \approx 0.750$ ns are found for Cy-5-Mal/TPP$^+$ in DMSO and water, respectively (**Figure 21f and Table 4**). It is noteworthy to mention that Cy-5-Mal/TPP$^+$ in PBS displayed absorption and fluorescence emission spectra with shapes and maximum positions that were comparable to those seen in organic solvents (**Figure 21c**). UV/vis and fluorescence spectra of Cy-5-Mal/TPP$^+$ in PBS buffer at physiological pH (pH 7.4, 37°C) and mitochondrial pH 8.0 have been checked over a period of 6 h to confirm its stability (**Figures 22a and 22b**). Furthermore, there is negligible change in the fluorescence intensity of Cy-5-Mal/TPP$^+$ in the presence of potential biological interferants such as essential ions (10 mM for Na^+ , K^+ , 200 μM for Ca^{2+}, Mg^{2+}, Zn^{2+}, Fe^{3+}, Fe^{2+}, and Cu^{2+}, as their chloride salts), under physiological conditions (pH 7.4, 37°C) (**Figure 22c**). However, we observed gradual increase of fluorescent intensity, c.a. 1.5

fold increases after 30 min incubation with 25 μM GSH solution (**Figure 22d**). Variation of photophysical properties and fluorescence lifetime of Cy-5b-Mal were listed in **Table 3** and **5**.

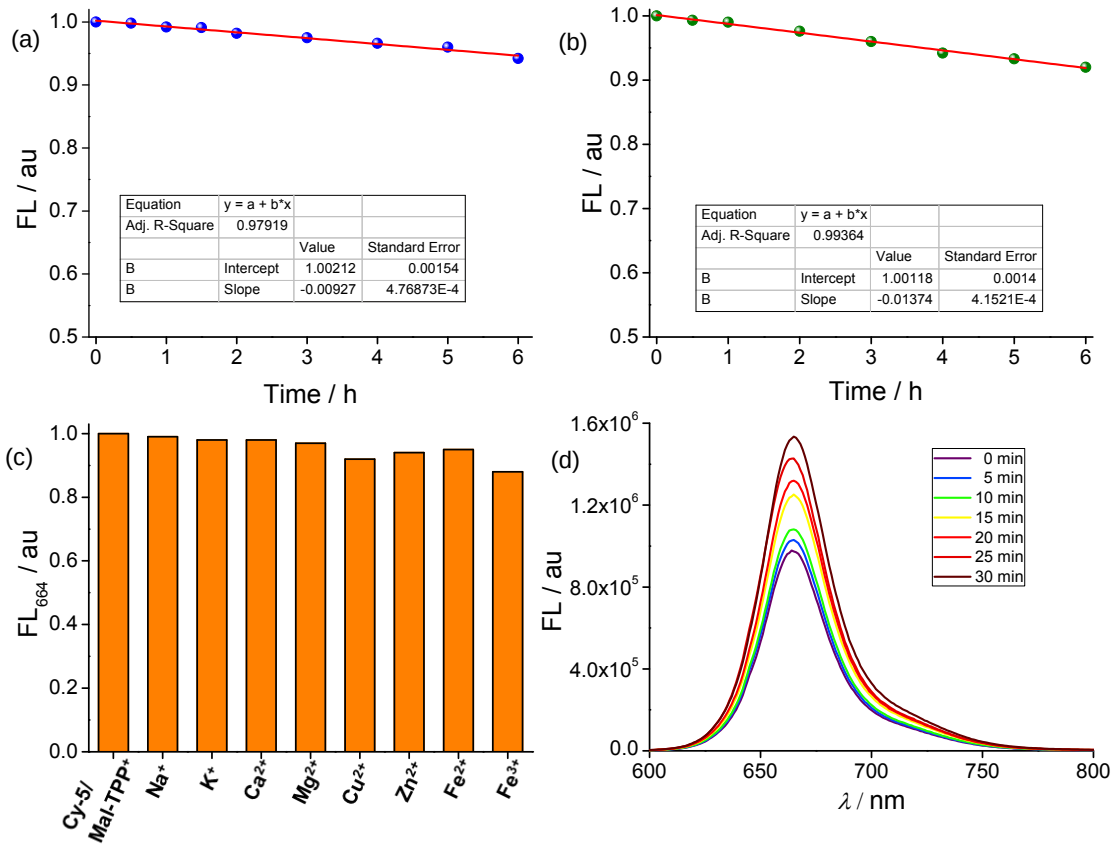

Figure 22. No significant fluorescence intensity changes are noticed for Cy-5a-Mal/TPP^{+} at (a) pH 7.4 and (b) 8.0. (c) Negligible change in fluorescence response (λ_{ex} = 644 nm and λ_{em} = 664 nm) of Cy-5/Mal-TPP^{+} in the presence of various metal ions (10 mM for Na^{+}, K^{+}, and 200 μM for Ca^{2+} , Mg^{2+}, Cu^{2+}, Zn^{2+}, $Fe^{2+}$and Fe^{3+}) as their chloride (Cl^{-}) salts in physiological conditions (PBS, pH=7.4, 37ºC). (d) Variation of fluorescence intensity with time upon addition of GSH (25 μM) in PBS solution of Cy-5a-Mal/TPP^{+} (3 μM) (pH=7.4 at 37ºC).

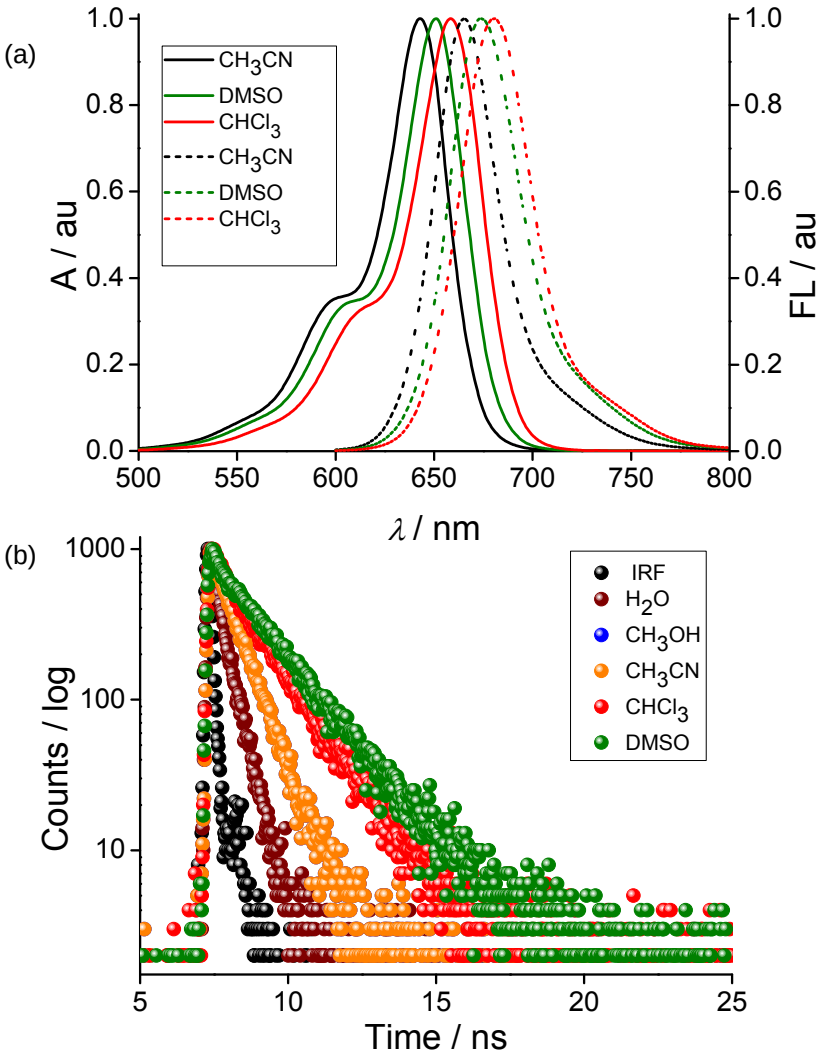

Figure 23. (a) Normalized UV-vis absorption and emission plots of Cy–5b-Mal in different solvents (b) Cy–5b-Mal fluorescence lifetime plots in different solvents following 650 nm delta diode laser excitation.

Table 2. Photophysical data of Cy-5-Mal/TPP^+ in different solvents.[c]

Solvent	Dielectric constant (ϵ) of Solvent	Refractive Index (η) of Solvent	λ_{max} (nm)	λ_{em} (nm)	Stokes shift ($\Delta\lambda$) nm	$\varepsilon \times 10^5$ (M^{-1} cm^{-1})	QY (Φ_f)
H_2O	80.1	1.333	644	664	20	1.18	0.065
CH_3CN	37.5	1.341	643	663	20	2.66	-
MeOH	32.6	1.326	644	664	20	2.57	-
$CHCl_3$	4.81	1.443	661	680	19	1.90	-
DMSO	46.7	1.479	650	672	22	1.80	0.34

Table 3. Photophysical data of Cy-5b-Mal in different solvents.[c]

Solvent	Dielectric constant (ϵ) of Solvent	Refractive Index (η) of Solvent	λ_{max} (nm)	λ_{em} (nm)	Stokes shift ($\Delta\lambda$) nm	$\varepsilon \times 10^5$ (M^{-1} cm^{-1})	QY (Φ_f)
H_2O	80.1	1.333	643	660	17	1.03	-
CH_3CN	37.5	1.341	643	665	22	2.57	
$CHCl_3$	4.81	1.443	660	681	21	1.98	-
DMSO	46.7	1.479	651	673	22	1.81	0.26

[c] ε: molar extinction coefficient, λ_{max}: absorption maximum wavelength, λ_{em}: emission maximum wavelength.

Table 4. Lifetime of Cy-5-Mal/TPP^+

Solvent	Lifetime (τ / ns)	Chi-square χ^2
H_2O	0.750±0.017	1.119
CH_3CN	1.011±0.066	1.244
MeOH	1.006±0.010	1.063
$CHCl_3$	2.093±0.020	1.056
DMSO	1.906±0.013	1.088

Table 5. Lifetime of Cy-5b-Mal

Solvent	Lifetime (τ / ns)	Chi-square χ^2
H_2O	0.385±0.052	1.072
CH_3CN	0.714±0.026	1.150
$CHCl_3$	1.667±0.043	1.068
DMSO	1.346±0.057	1.065

Cellular uptake, localization, and multicolour imaging using confocal laser scanning microscopy:

First we examined the cytotoxicity of Cy-5-Mal/TPP^+ through MTT assay by treating different cancerous cell lines (HeLa and lung adenocarcinoma A549 cells) as well as noncancerous cell lines like human embryonic kidney cell (HEK293) and a mouse myoblast cell (C2C12) with variable doses. We found minimum cytotoxicity of Cy-5-Mal/TPP^+ at very low concentration for all the cell lines. However, at high concentration it showed some toxicity for both cancerous cells with IC_{50} value of ~16 μM, whereas at this concentration normal cell survival rate was much higher (almost 70%) (**Figure 24**).

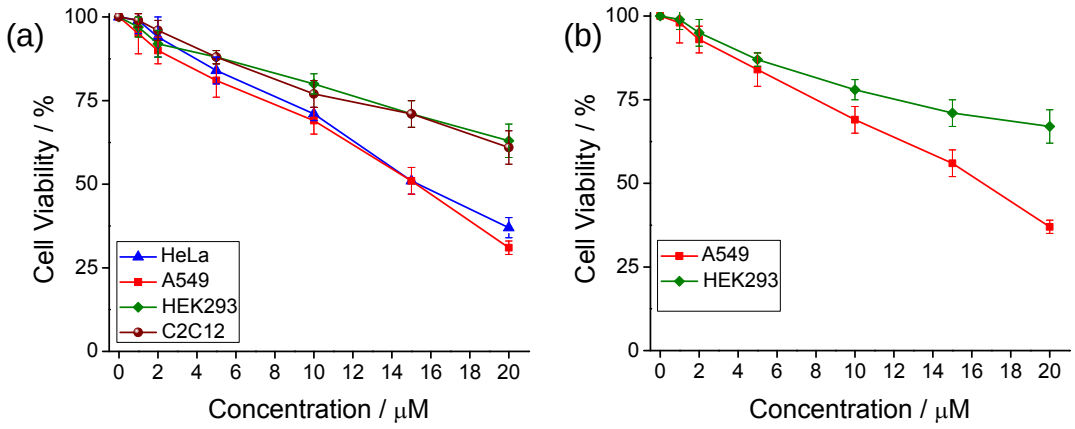

Figure 24. (a) Cell viability assay carried out by treating cancerous HeLa, A549 cells as well as noncancerous HEK293 and C2C12 cells with different doses of Cy-5-Mal/TPP^+ **(**1, 2, 5, 10, 15, and 20 μM per well). (b) MTT assay performed by incubating lung cancerous A549 cell and kidney cell (HEK 293) with different concentrations of Cy-5b-Mal.

To confirm the cellular uptake and mitochondrial localisation HeLa, A549, and H9C2 cells were separately treated with 700 nM Cy-5-Mal/TPP^+ and monitored using CLSM. Living carcinoma HeLa and A549 cells were costained with Cy-5-Mal/TPP^+ and a mitochondria specific fluorescent probe,

MitoTracker Green (MTG) which shows excellent overlap with high Pearson's correlation coefficient (PCC): 0.85 and 0.80, respectively (**Figures 24 and 25**). Additionally, we compared the fluorescence intensity over time for both Cy-5-Mal/TPP^+ and Mitotracker green and we observed higher intensity in the red channel compared to green channel. This proves that Cy-5-Mal/TPP^+ molecules are swiftly, extensively, and selectively uptaken by mitochondria guiding by the strong negative $\Delta\Psi_m$.

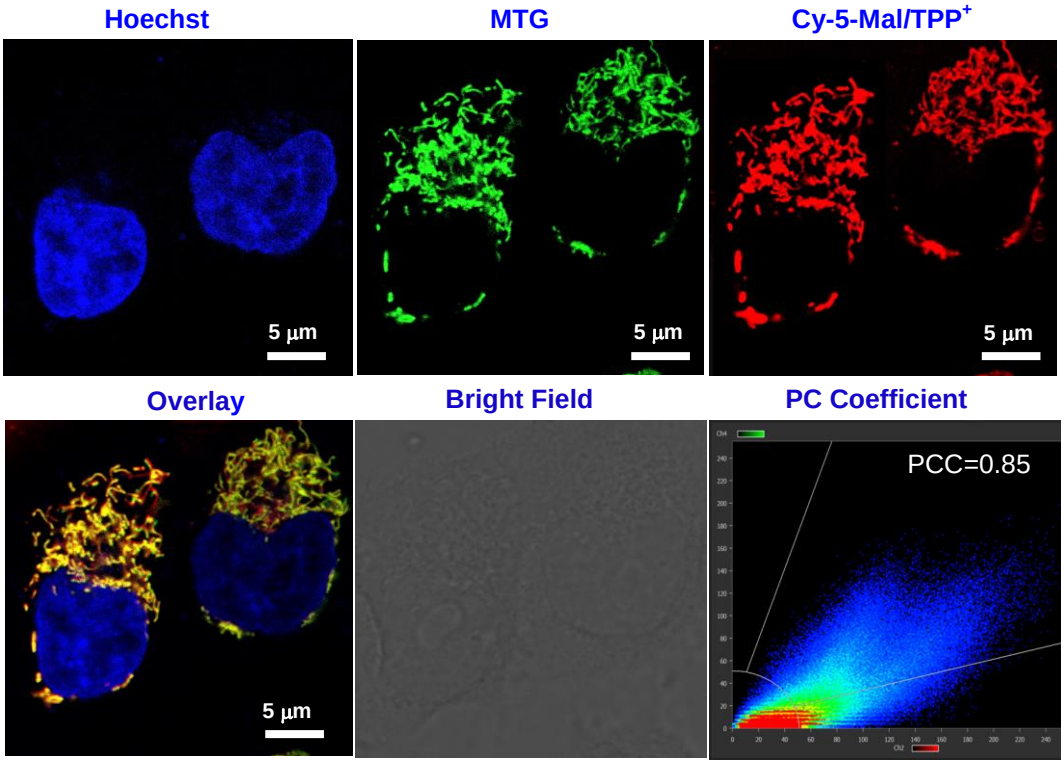

Figure 24. Confocal laser scanning microscopic images of Cy-5-Mal/TPP^+ colocalized with MitoTracker Green FM (MTG) in living HeLa cells display excellent colocalization in mitochondria with Pearson's correlation coefficient (PCC) of 0.85.

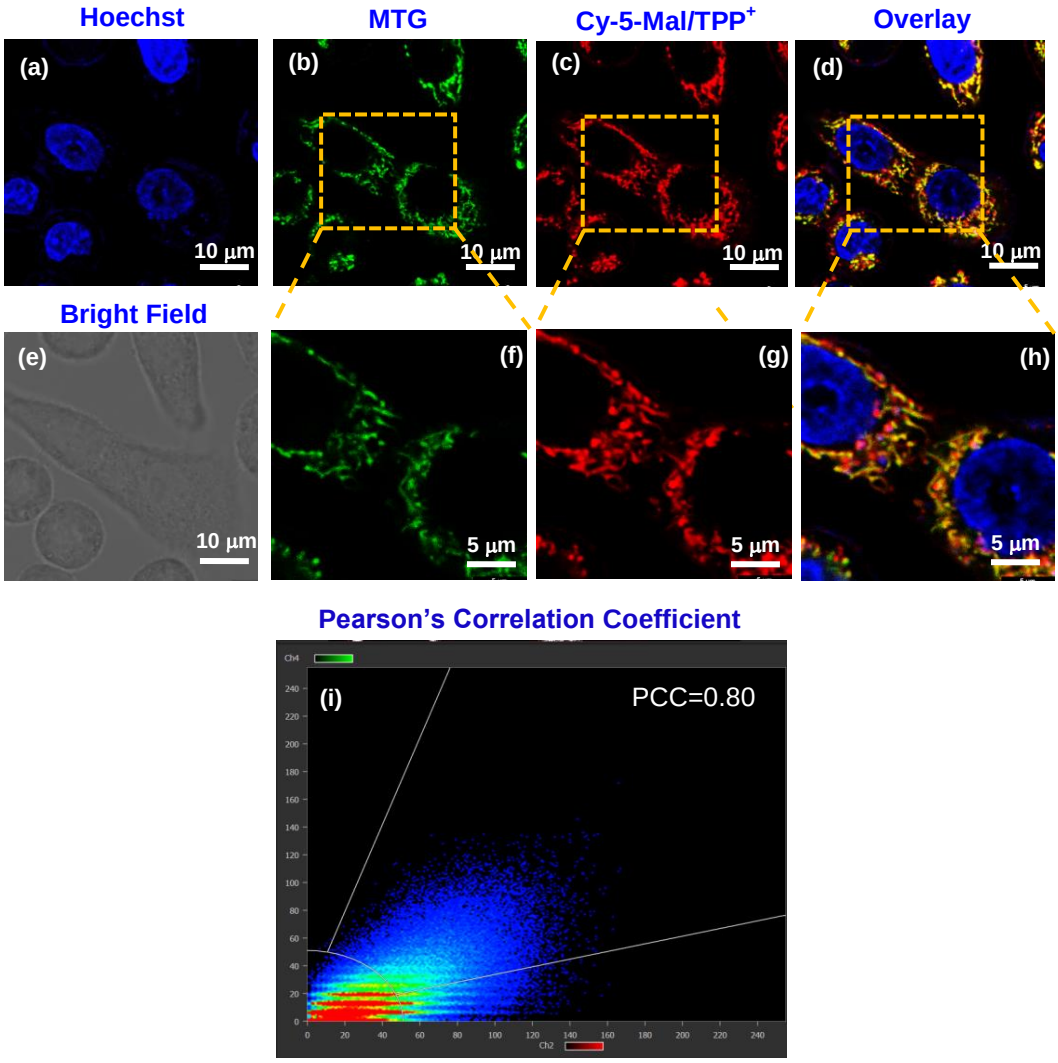

Figure 25. (a-e) Confocal laser microscopic images of Cy-5-Mal/TPP$^+$ colocalized with MitoTracker Green FM (MTG) in living A549 cells. Blue channel, green channel and red channel specify nuclear staining by Hoechst (laser λ_{ex} 405 nm), MitoTracker Green FM (MTG) (laser λ_{ex} 488 nm), and Cy-5-Mal/TPP$^+$ (laser λ_{ex} 638 nm) staining, respectively. (f-h) Higher magnified confocal images of A549 cells colocalized with MTG. (i) Pearson's correlation coefficient scatter plot.

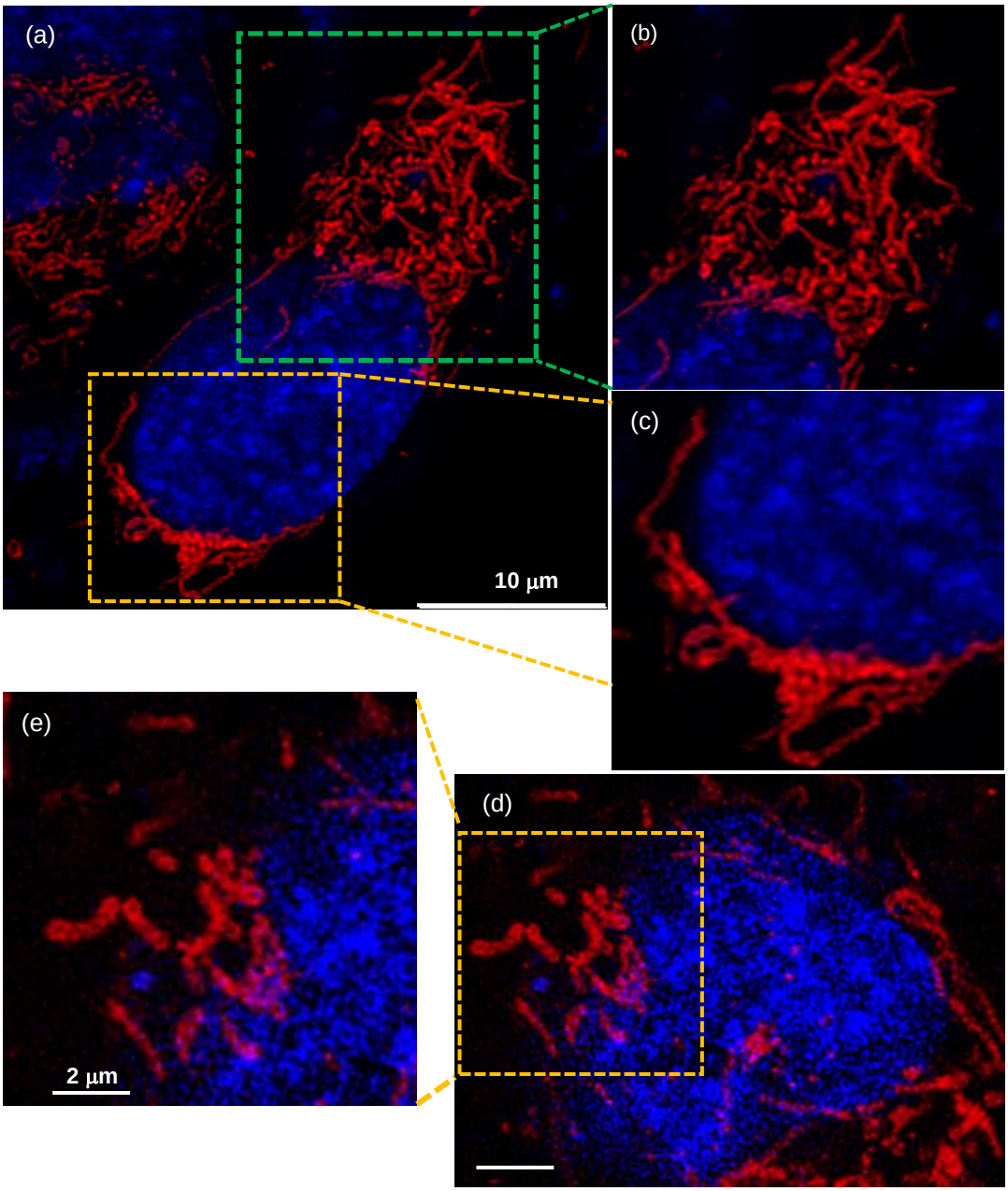

Figure 26. (a-e) High resolution lightning mode images of living HeLa cells stained with NIR Cy-5-Mal/TPP^{+}(red channel) and Hoechst (Blue channel), showing linear, elongated curved rod shape Mitochondria.

High resolution CLSM image with lightning mode (optical aperture 0.7 instead of 1.4) is obtained using 100× objective to get finer structural details of mitochondria. High resolution confocal images as well as 3D microscopic images show linear, elongated curved rods with a sharp outline under the microscope which specifies mitochondria (**Figure 27**). Mitochondrial target selectivity of Cy-5-Mal/TPP^+ is compared with the maleimide containing control molecule lacking TPP^+ functionality that exhibits poor mitochondrial colocalization with Mitotracker green in CLSM imaging with PCC: 0.62 and 0.59 for HeLa and A549 cells, respectively (**Figure 28**).

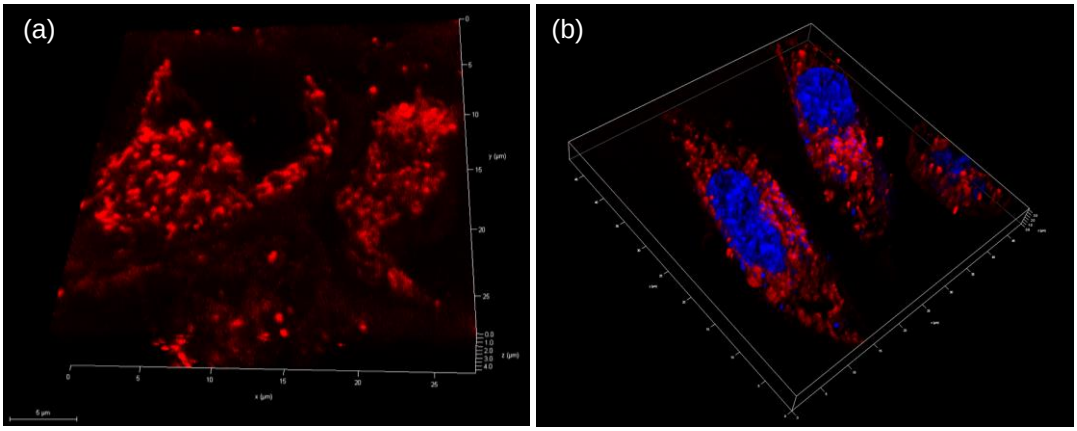

Figure 27. 3D Confocal images of living (a) cervical carcinoma HeLa cells and (b) lung cancerous A549 cells, stained with mitochondria targeting NIR fluorophore Cy-5-Mal/TPP^+.

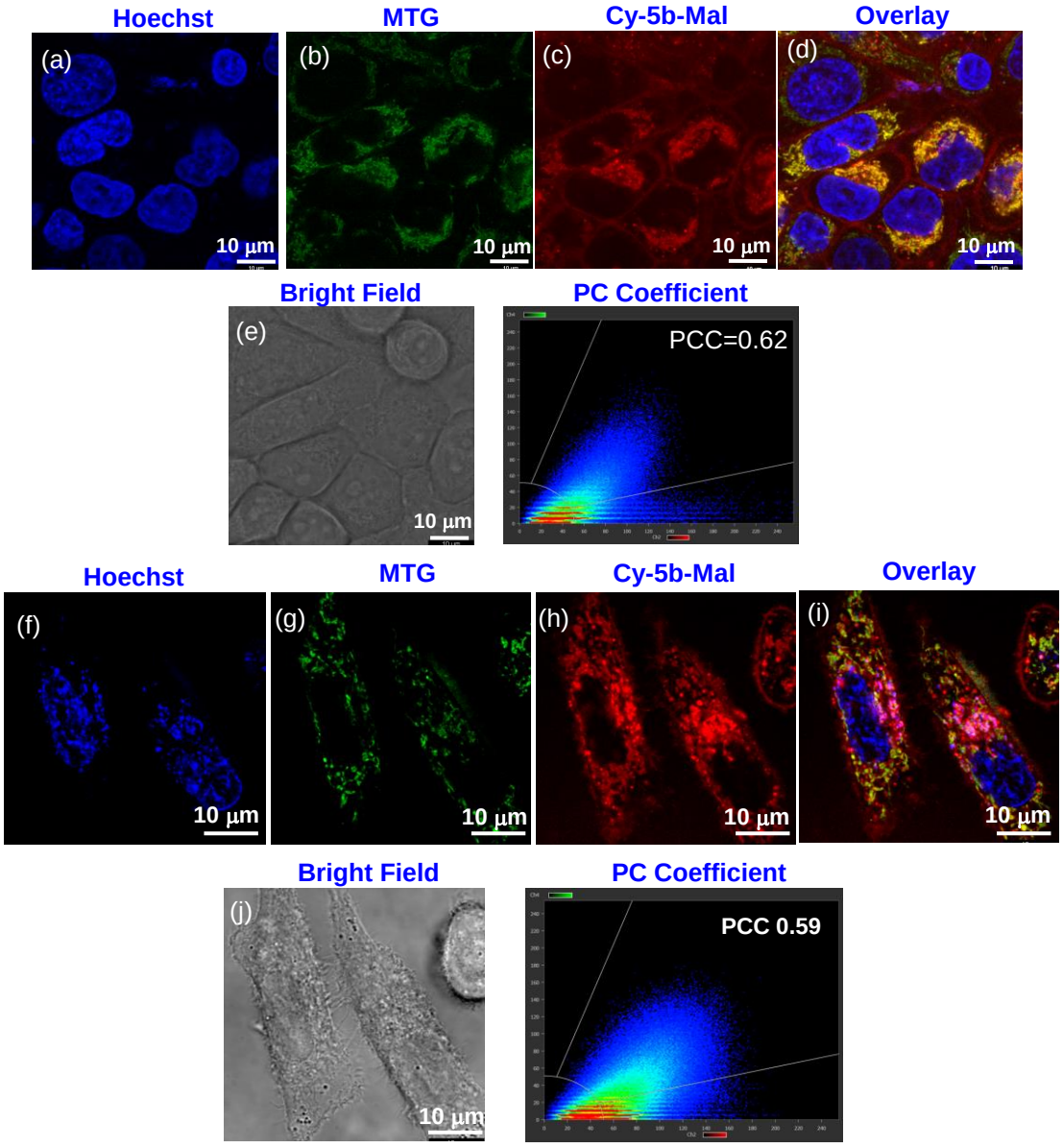

Figure 28. Confocal images of Cy–5b-Mal probe colocalized with MitoTracker Green FM (MTG) in living (a-e) HeLa and (f-j) A549 carcinoma cells, displaying poor colocalization in mitochondria with PCC of 0.62 and 0.59, respectively. Blue channel: Hoechst, laser λ_{ex} 405 nm; Green channel: MTG, laser λ_{ex} 488 nm; and Red channel: Cy-5b-Mal, laser λ_{ex} 638 nm.

We also examined the compatibility of Cy-5-Mal/TPP$^+$ for multicolor imaging purposes. It is noteworthy that due to the lack of suitable organelle target-specific chromophores with distinct absorption and emission bands, it remains a challenging task to track various cellular organelles of the same cell simultaneously to get a multicolor image.[49–51] Three-color fluorescence confocal images of HeLa cells featuring the plasma membrane (green color), nucleus (blue color), and mitochondria (red color) is accomplished by utilizing a negatively charged hydrophobic green emitting dye, CellMask Green for selectively anchor the plasma membrane, blue fluorescent Hoechst to highlight the nucleus, and Cy-5-Mal/TPP$^+$ to selectively target and label Cys exposed proteins of mitochondria (**Figure 29**).

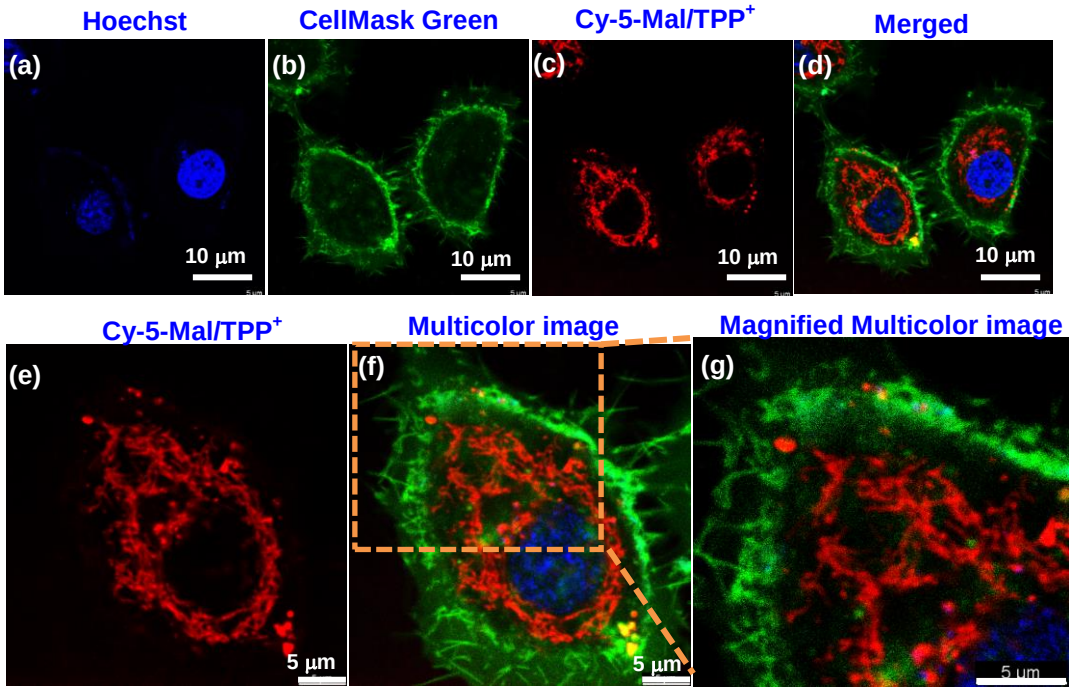

Figure 29. Multicolor CLSM images (a-g) of HeLa cells stained with hydrophobic green emitting plasma membrane anchoring dye CellMask Green, blue nucleus staining probe Hoechst, and mitochondria selective red emitting fluorophore Cy-5-Mal/TPP$^+$.

Mitochondrial Immobilization of Cy-5-Mal/TPP$^+$:

Immobilization of Cy-5-Mal/TPP$^+$ within the mitochondria was believed to be crucial to avoid leakage of the dye from the mitochondria under membrane depolarization related with different pathogenic events. Maleimide functionality of Cy-5-Mal/TPP$^+$ probe is likely to be immobilized within the mitochondria as the result of covalent attachment through Michael addition reaction with reactive thiol of Cys residues present in numerous mitochondrial proteins. On the basis of this dual localization effect it is anticipated that Cy-5-Mal/TPP$^+$ would retain in the mitochondria even after membrane depolarization. To examine immobilization of Cy-5-Mal/TPP$^+$ to the mitochondria in living cells, CLSM experiments are carried out both in the presence as well as absence of carbonyl cyanide *m*-chlorophenyl hydrazone (CCCP), a well-known oxidative phosphorylation uncoupler that induces opening of transition pores embedded on mitochondrial membrane, and eventually leads to dissipation of mitochondrial membrane potential ($\Delta\Psi_m$).[47] In this context CCCP is used to differentiate between cationic probes that are preferentially concentrate into the mitochondria due to highly negative $\Delta\Psi_m$ compare to plasma membrane and those that are covalently bound and incapable of leaking out after mitochondrial depolarization takes place. It is evident from CLSM data (**Figure 30**), fluorescence intensity of HeLa cells stained with Cy-5-Mal/TPP$^+$ remain intact even after ~20 min incubation with 5 μM CCCP at 37^{o}C, whereas identical cellular incubation carried out with Cy-5a/TPP$^+$, a control molecule lacking maleimide residue but have mitochondria targeting TPP$^+$ unit, shows significant drop of fluorescence signal from mitochondria (**Figure 30**). This result confirms that Cy-5-Mal/TPP$^+$ probe is firmly immobilized within the

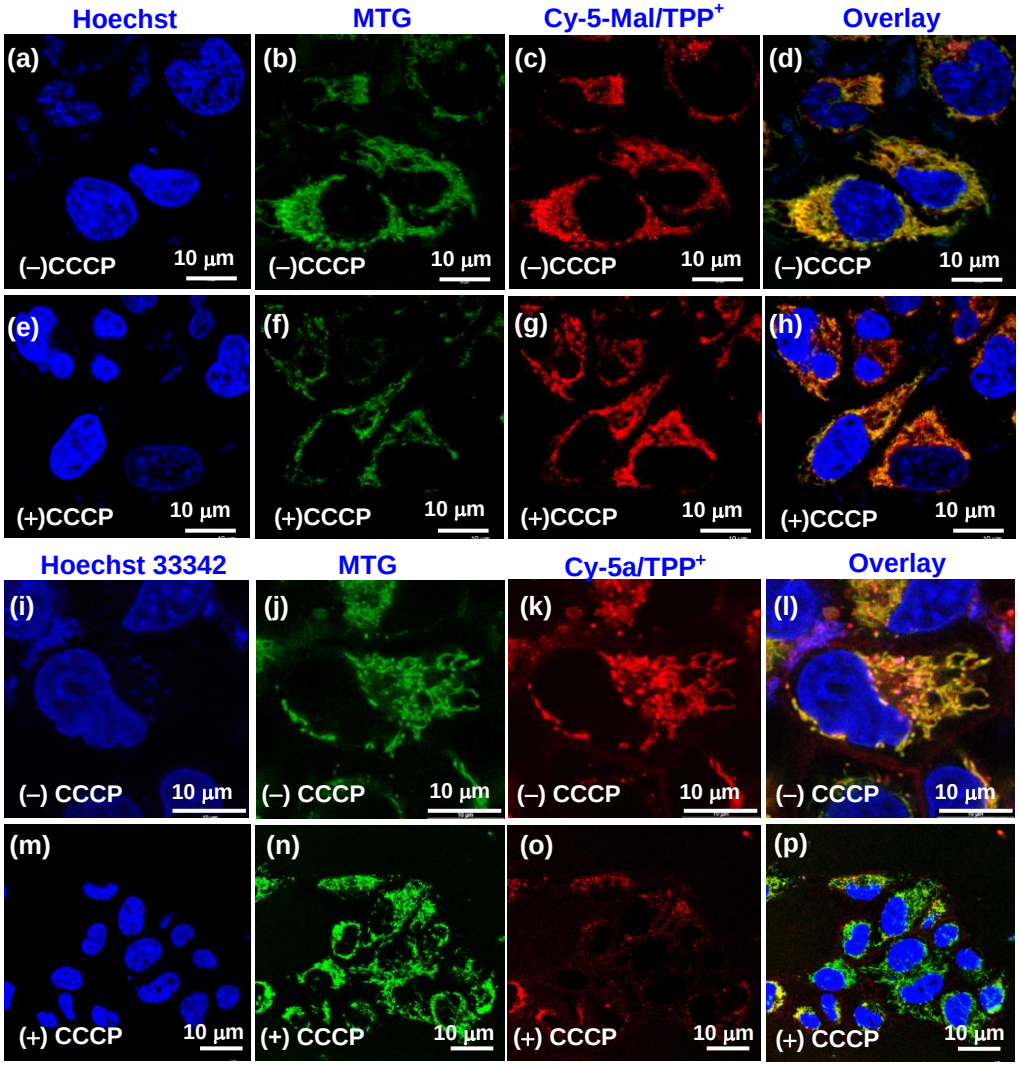

Figure 30. Confocal microscopic image analysis to confirm the immobilization of Cy-5-Mal/TPP$^+$ within the living HeLa cells mitochondria. Effect of CCCP, a well-known oxidative phosphorylation uncoupler, on the CLSM images of HeLa cells stained with Cy-5-Mal/TPP$^+$ (a–d, e-h), and control molecule Cy-5a/TPP$^+$(i-l, m-p). Confocal images of living HeLa cells prestained with Cy-5-Mal/TPP$^+$ showed no significant drop in fluorescence signal when incubated with 5 µM CCCP for 20min (e-h), while identical cellular staining conditions with Cy-5a/TPP$^+$ (m-p**)** gives weak fluorescence signal.

mitochondria in living cells; apparently, it indicates covalent attachments of maleimide with endogenous reactive thiol containing mitochondrial proteins.

Living cell mitochondrial protein labeling:

After confirming the selective cellular uptake and mitochondrial localisation by CLSM we next assessed the living cell mitochondrial protein labeling ability of Cy-5-Mal/TPP^+. First we treated the A549 cells separately with different concentrations of the probe (1 and 2 μM) in DMEM and incubated for 3 h at 37°C humidified with a 5% CO_2 incubator. After gentle washing treated cells were lysed; the resultant lysate was resolved by 10% sodium dodecyl sulphate-polyacrylamide gel electrophoresis (SDS-PAGE) and the fluorescently tagged mitochondrial proteins containing one or more equivalents of unsymmetrical Cy-5-Mal/TPP^+, formed as the consequence of this immobilization process were identified by in-gel fluorescence assay using Amersham Typhoon scanner quipped with NIR laser of 635 nm (**Figure 31**). Among the various protein spots obtained by Coomassie brilliant blue (CBB) staining (**Figure 31**), four distinct NIR fluorescence bands at ~71 kDa (most intense band), ~ 54 kDa, ~ 43 kDa and ~ 29 kDa were detected and after tryptic gel-digestion a few of these fluorescent spots were further analysed by MALDI-TOF-MS to get sharp peaks at 76709.321 kDa and 57217.493 kDa, corresponding to covalently bound Cy-5-Mal/TPP^+ and mitochondrial thiol containing protein complex (**Figures 32a and 32b**). Most importantly UniProt database study regarding human mitochondrial proteins which have high abundance of Cys residues and MALDI-MS peak indicates that ~ 76 kDa peak corresponds to stress protein-70, mitochondrial (mt-HSP70, encoded by HSPA9 gene) complexed with Cy-5-Mal/TPP^+.[52]

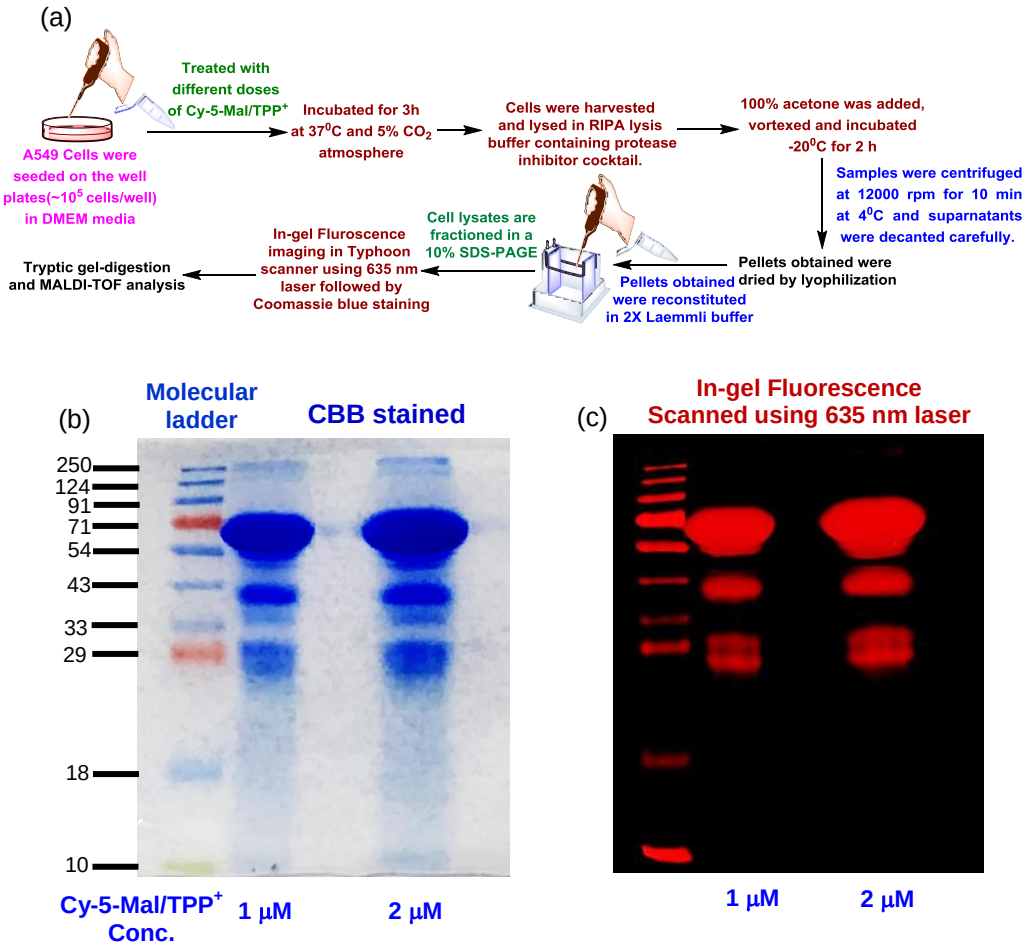

Figure 31. (a) Schematic presentation of live A549 cell mitochondrial Cys containing protein labeling with different concentrations of Cy-5-Mal/TPP$^+$ for 3 h SDS-PAGE analysis with A549 cell lysate. (b) All the protein bands are visualized by Coomassie Brilliant Blue staining. (c) In-gel fluorescence imaging of A549 cell lysate containing mitochondrial proteins labeled with NIR Cy-5-Mal/TPP$^+$ and scanned by Amersham Typhoon scanner quipped with NIR laser of 635 nm.

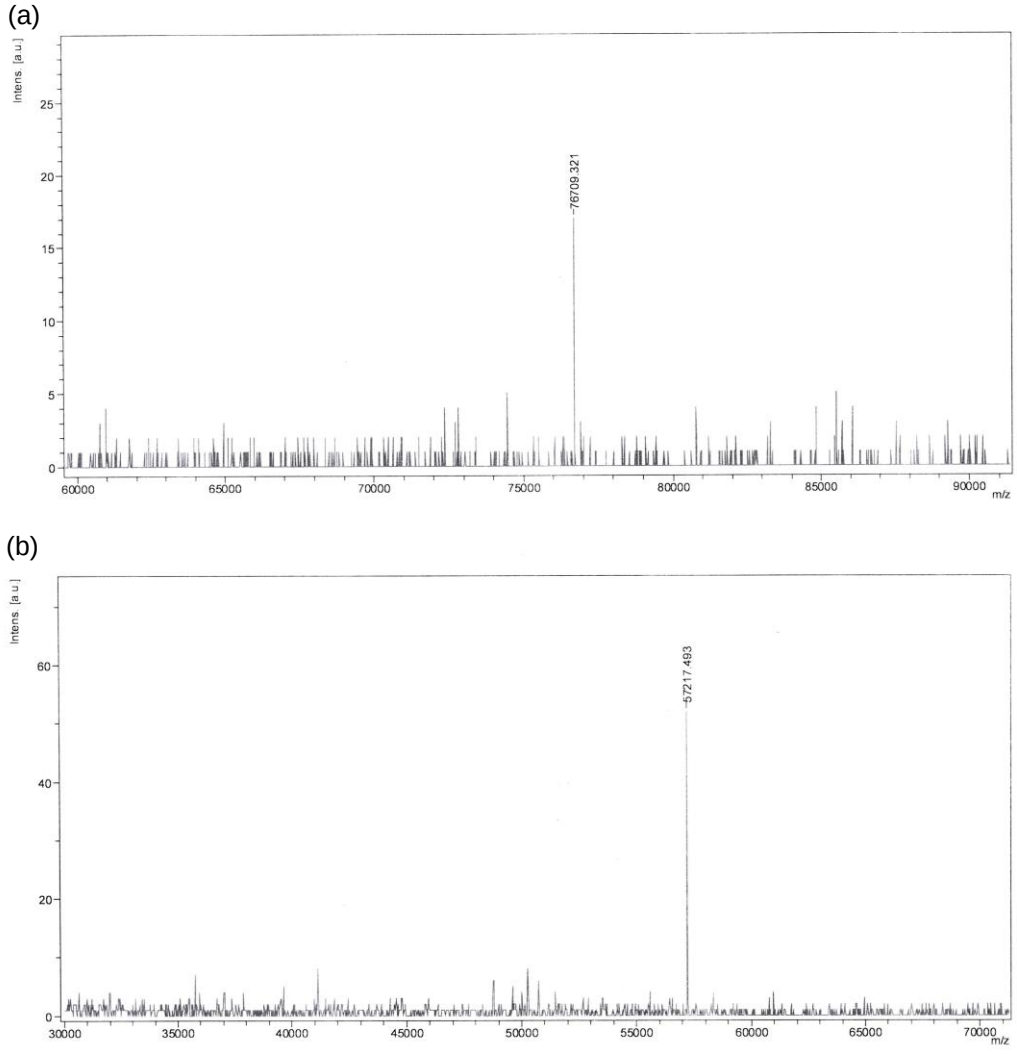

Figure 32. MALDI-TOF-MS of tryptic digested fluorescent gels spots corresponding to 71 kDa (most intense band) and ~54 kDa protein band indicating covalently bound form of Cy-5-Mal/TPP^+ and mitochondrial protein complex.

Computational study to locate binding site of HSPA9 with Cy-5-Mal/TPP$^+$:

Furthermore, we have carried out molecular docking, a computational tool to get the better understanding of binding interactions between HSPA9 (PDB ID: 6NHK) with Cy-5-Mal/TPP$^+$. Docking study revealed that Cy-5-Mal/TPP$^+$ have a mentionable binding affinity toward mortalin nucleotide-binding domain of HSPA9 with binding energy –9.8 kcal/mol (**Figure 33**) and this pocket contains two Cys residues (Cys 66 and Cys317) in close vicinity of

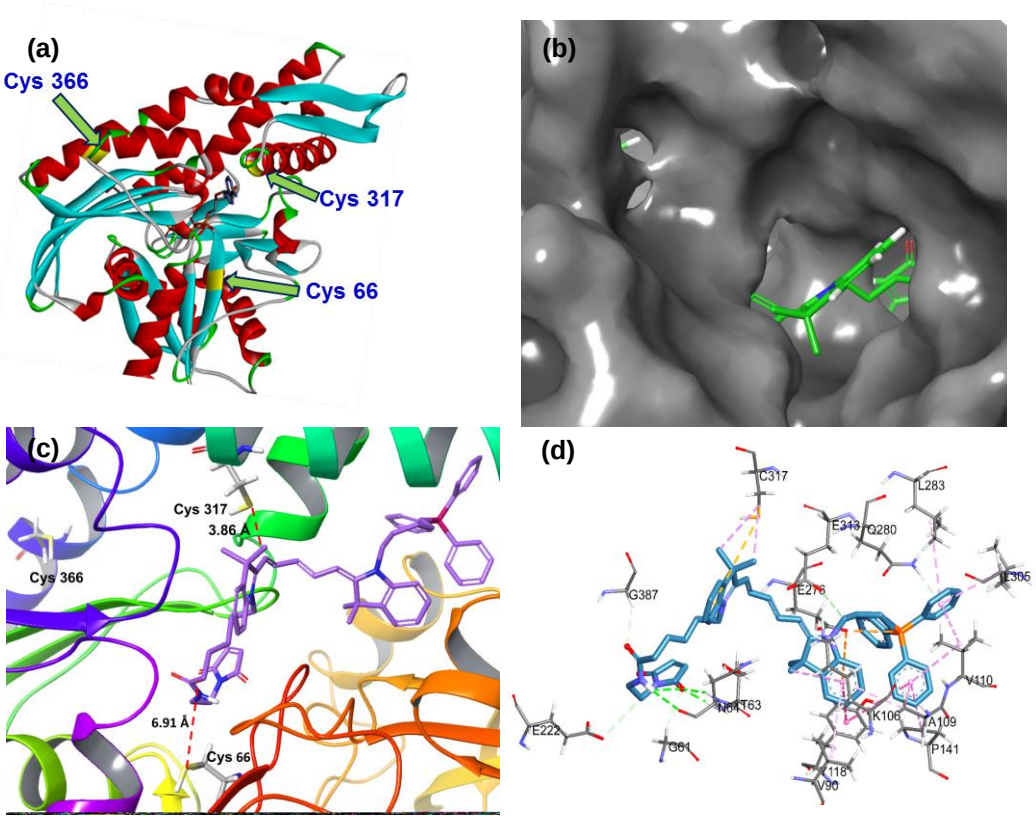

Figure 33. (a) Crystal structure of HSPA9 showing exposed Cys amino acid residues. Docking pose of Cy-5-Mal/TPP$^+$ in the (b) binding site of the HSPA9 and (c, d) its interaction with Cys 317 and Cys 66 and other amino acid residues as well as distance from those residues.

the target molecule (3.86 and 6.91 Å distance, respectively, **Figure 33c**). Most of the electronegative atoms of the molecules are buried under the alkyl group which makes it hydrophobic and less feasible for hydrogen bonding. The TPP^+ and adjacent 3,3-dimethylindoline part of the molecule interact with L283, Q280, L305, V110, A109, P141, K106, Y118, and V90, the involvement of π-electron cloud of the aromatic residues and one ionic interaction with E276 has also been observed. Hydrogen bonding is observed between maleimide and G387, E222, G61, N64, and T63 amino acid residues (**Figure 33d**).

To find the stability of HSPA9- Cy-5-Mal/TPP^+ complex, a 100 ns molecular dynamics simulation is performed, and found that the complex is stable in the binding site obtained in the molecular docking study. Overlay of the structures before and after the simulation shows minor conformation change of Cy-5-Mal/TPP^+ during the simulation (**Figure 34a**). The stability of the complex can be known with the help of a comparison of root-mean-square fluctuation (RMSF), root-mean-square deviation (RMSD), solvent-accessible surface area (SASA), and radius of gyration residual (R_g) in the trajectories of the complex with respect to the native protein. The RMSD of the free protein is 2.8-3.5 nm whereas the value of its complex with Cy-5-Mal/TPP^+ is 2.5-3.0 nm (**Figure 34b**). The RMSD fluctuation of two systems with time is ~0.5 nm and such fluctuation is higher in free protein. Therefore, the protein becomes stabilized after binding with Cy-5-Mal/TPP^+ in its active site. It is observed that the RMSD of Cy-5-Mal/TPP^+ molecule hiked massively at 18-25 ns time and then stabilized which may be due to the binding and stabilization of the molecule in the protein active site (**Figure 35a**).The compactness and the size of a protein in the presence and absence of Cy-5-Mal/TPP^+ can be understood with the help of the radius of gyration (R_g). For the free protein, the R_g is

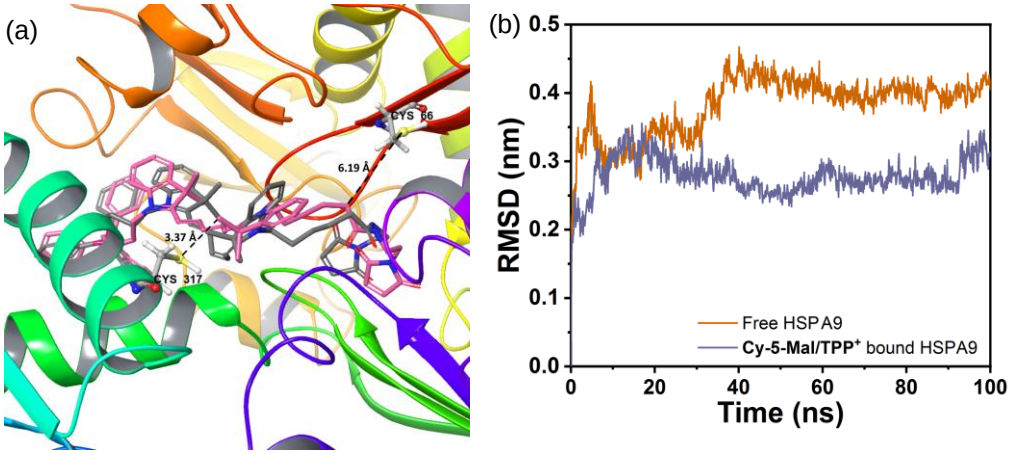

Figure 34. (a) Overlay of poses of Cy-5-Mal/TPP$^+$ in the HSPA9 before (grey) and after (magenta) the molecular dynamics; (b) RMSD of the protein in free state as well as bound with Cy-5-Mal/TPP$^+$.

almost constant around 2.1 nm. In this case, initially, the R_g value of the Cy-5-Mal/TPP$^+$ bound protein is higher than that of free protein. The scenario is reversed after 37700 ps (**Figure 35b**) which indicates the Cy-5-Mal/TPP$^+$ molecule can stabilize the protein after the binding which increases the compactness of the system and decreases its size. The solvent accessible surface area (SASA) of a protein can be calculated from the amino acid residues having hydrophobic side chains. In this case, the SASA value of the free protein and Cy-5-Mal/TPP$^+$ bound protein are 67 and 68 nm^2, respectively (**Figure 35c**). Hence, it may be concluded that the hydrophobic amino acid residues of the protein mainly buried inside the free protein and it is almost same after binding with Cy-5-Mal/TPP$^+$ during the MD time. The obtained RMSF of the amino acids in free protein and Cy-5-Mal/TPP$^+$ bound protein from the MD simulation indicate the residue numbers 317, 286, 283, 276, 222,

141, 66, 61, and 57 which are the residues in interaction with the Cy-5-Mal/TPP^+ molecule (**Figure 36a**).

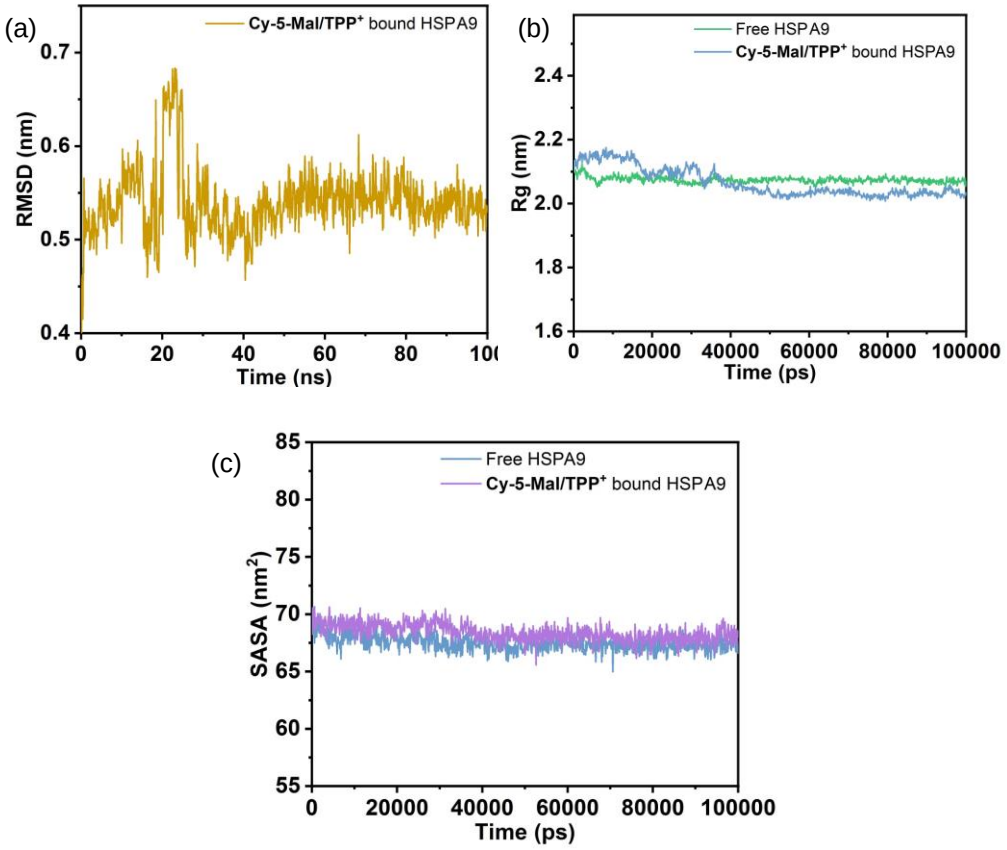

Figure 35. (a) RMSD of Cy-5-Mal/TPP^+, (b) Rg and (c) SASA of the protein in free state as well as bound state with Cy-5-Mal/TPP^+.

In the MD simulation, it is found that T63and N64 residues are involved in the hydrogen bonding with Cy-5-Mal/TPP^+ throughout the trajectory and minimum two hydrogen bonding are found to be common between them (**Figure 36b**). Their overall hydrogen bonding occupancy is only 32.45 % which indicates the interaction between Cy-5-Mal/TPP^+ and the

protein is π-staking (alkyl-π, amide-π, lone pair-π, and sulphur-π) driven. Such hydrophobic interaction driven binding of the molecule is also observed experimentally.

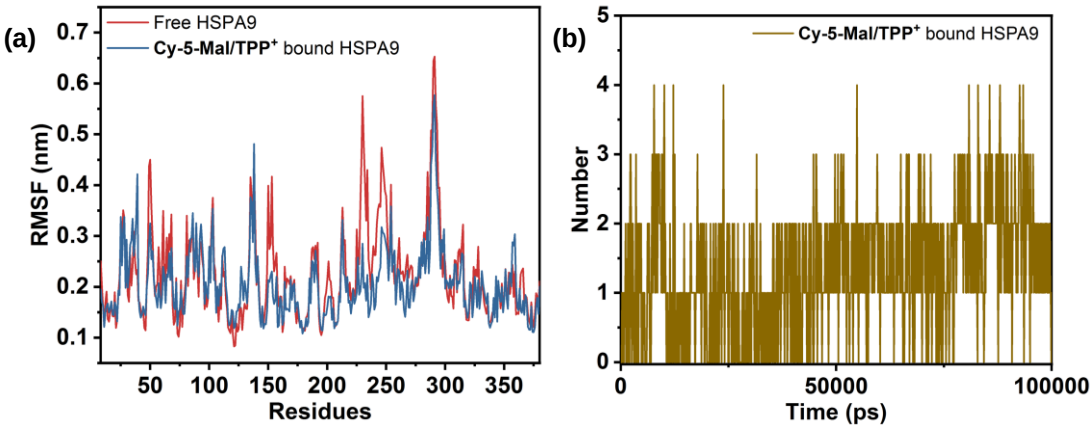

Figure 36. (a) RMSF of the protein in free state as well as bound with Cy-5-Mal/TPP$^+$. (b) The number of hydrogen bonding between the molecule and protein throughout the trajectory.

The free energy change (ΔG) of the interaction between Cy-5-Mal/TPP$^+$ and protein can be calculated by considering the gas-phase energy, electrostatic solvation energy as well as non-electrostatic contribution to solvation energy. The ΔG corresponding to this molecular interaction is evaluated through considering important conformations of Cy-5-Mal/TPP$^+$ bound protein complex. Here, the ΔG is calculated for the complex using the MM-GB/SA method. [54] The calculation shows that the ΔG of this interaction is found to be –32.71 kcalmol^{-1}. In this case, all the active site amino acid residues of the protein within the 5Å radius of Cy-5-Mal/TPP$^+$ are considered to move freely. From both experimental and theoretical studies, it proved that hydrophobic interaction like π-staking is the driving force for the efficient, stable and

spontaneous binding of Cy-5-Mal/TPP^+ in the Cys rich active site of the protein.

Conclusions

We have demonstrated dual targeting approach by introducing a maleimide and TPP^+ conjugated biocompatible ultra-bright NIR fluorescent probe Cy-5-Mal/TPP^+ that selectively localize and stain in live cell mitochondria as well as specifically label the exposed thiols of Cys containing mitochondrial proteins via thiol-maleimide bioconjugation chemistry. Moreover, due to excellent photophysical property, good water solubility, minimum cytotoxicity at lower concentration alongside specific thiol-maleimide bioconjugation chemistry make Cy-5-Mal/TPP^+ probe a perfect choice for detecting and tracing mitochondrial exposed thiol containing protein location, long-term live cell multicolour imaging, tracking and monitoring of mitochondrial morphology as well as dynamics during various biological and pathological conditions in live cells. This dual targeting covalent labeling approach is also compatible with SDS-PAGE, an in-gel fluorescence assay for labeling specific proteins in live A549 cells. Moreover, in-gel fluorescence with Cy-5-Mal/TPP^+ treated A549 cell lysate followed by MALDI MS/MS analysis with tryptic digested gel has been successfully performed to identify four mitochondrial thiol exposed proteins. Further the computational approach also supports HSPA9 protein- Cy-5-Mal/TPP^+ complex formation and their stability. This dual targeting probe can be efficiently used for live cell mitochondrial tracking, mitochondria targeted drug delivery, Cys exposed mitochondrial protein labelling, multicolor cellular imaging, and hold significant promise in multimodal targeted cancer theranostics applications.

References:

[1] Krall, N.; Da Cruz, F. P.; Boutureira, O.; and Bernardes, G. J. L. *Nat. Chem.***2016**, *8*, 103−113.

[2] Alamudi, S. H.; Satapathy, R.; Kim, J.; Su, D.; Ren, H.; Das, R.; Hu, L.; Alvarado-Martínez, E.; Lee, J. Y.; Hoppmann, C.; Peňa-Cabrera, E.; Ha, H.-H.; Park, H.-S.; Wang, L.; and Chang, Y.-T. *Nat. Commun.* **2016**, *7*, 11964.

[3] Matsuo, K.; Nishikawa, Y.; Masuda, M.; and Hamachi, I. *Angew. Chem., Int. Ed.* **2018**, *57*, 659−662.

[4] Amaike, K.; Tamura, T.; and Hamachi, I. *Chem.* Commun. **2017**, *53*, 11972-11983.

[5] Rhee, H. W.; Zou, P.; Udeshi, N. D.; Martell, J. D.; Mootha, V. K.; Carr, S. A.; and Ting, A. Y. *Science* **2013**, *339*, 1328−1331.

[6] Zhu, H.; Fan, J.; Du, J.; Peng, X. *Acc. Chem. Res.* **2016**, *49*, 2115–2126.

[7] Dzijak, R.; Galeta, J.; Vázquez, A.; Kozák, J.; Matoušová, M.; Fulka, H.; Dračínsky, M.; and Vrabel, Milan. *JACS Au* **2021**, *1*, 23−30.

[8] Hong, G.; Antaris, A. L., and Dai, H. *Nat. Biomed. Eng.* **2017**, *1*, 0010.

[9] Wu, D.; Cheung, S.; Devocelle, M.; Zhang, L.-J.; Chenb, Z.-L.; and O'Shea, D. F. *Chem. Commun.* **2015**, *51*, 16667−16670.

[10] Tamura, T.; and Hamachi, I. *J. Am. Chem. Soc.***2019**, *141*, 2782−2799.

[11] Boutureira, O.; and Bernardes, G. J. L. *Chem. Rev.* **2015**, *115*, 2174−2195.

[12] Sletten, E. M.; and Bertozzi, C. R. *Angew. Chem., Int. Ed.* **2009**, *48*, 6974−6998.

[13] Yasueda, Y.; Tamura, T.; Fujisawa, A.; Kuwata, K.; Tsukiji, S.; Kiyonaka, S.; and Hamachi, I. *J. Am. Chem. Soc.* **2016**, *138*, 7592−7602.

[14] Takaoka, Y.; Ojida, A.; and Hamachi, I. *Angew. Chem., Int. Ed.* **2013**, *52*, 4088−4106.

[15] Wiedemann, N.; and Pfanner, N. *Annu. Rev. Biochem.* **2017**, *86*, 685−714.

[16] Stankiewicz, M.; Nikolay, R..; Rybin, V.; and Mayer, M. P. *FEBS J.* **2010**, *277*, 3353–3367.

[17] McDonough, H.; and Patterson, C. *Cell Stress Chaperon.* **2003**, *8*, 303–308.

[18] Nunnari, J.; and Suomalainen, A. *Cell* **2012**, *148*, 1145−1159.

[19] Murphy, M.; and Hartley, R. *Nat. Rev. Drug Discovery* **2018**, *17*, 865−886.

[20] Vyssokikh, M. Y.; Holtze, S.; Averina, O. A., Lyamzaev, K. G., Panteleeva, A. A.; Marey, M. V.; Zinovkin, R. A.; Severin, F. F.; Skulachev, M. V.; Fasel, N.; Hildebrandt, T. B.; and Skulachev, V. P. *Proc. Natl. Acad. Sci. U. S. A.* **2020**, *117*, 6491−6501.

[21] Galluzzi, L.; K Blomgren.; and Kroemer, G. *Nat. Rev. Neurosci.* **2009**, *10*, 481−494.

[22] Bak, D. W.; Pizzagalli, M. D.; and Weerapana. E. *ACS Chem. Biol.* **2017**, *12*, 947–957.

[23]Chouchani, E.T.; Kazak, L.; Jedrychowski, M. P.; Lu, G. Z., Erickson, B.K., Szpyt, J., Pierce, K.A., Laznik-Bogoslavski, D., Vetrivelan, R., Clish, C.B. and Robinson, A.J. *Nature* **2016,** *532*, 112–116.

[24]Chouchani, E.T.; Methner, C.; Nadtochiy, S. M.; Logan, A.; Pell, V. R.; Ding, S.; James, A. M.; Cocheme, H. M.; Reinhold, J.; Lilley, K. S.; and Partridge, L. *Nat. Med.* **2013**, *19*, 753-759.

[25]Koniev, O.; and Wagner, A. *Chem. Soc. Rev.* **2015**, *44*, 5495-5551

[26] Abo, M.; and Weerapana, E. *J. Am. Chem. Soc.* **2015**, *137*, 7087−7090.

[27] Lee, M. H.; Park, N.; Yi, C.; Han, J. H.; Hong, J. H.; Kim, K. P.; Kang, D. H.; Sessler, J. L.; Kang, C.; and Kim, J. S. *J. Am. Chem. Soc.* **2014**, *136*, 14136–14142.

[28] Chen, G.; Fu, Q.; Yu, F.; Ren, R.; Liu, Y.; Cao, Z.; Li, G.; Zhao, X.; Chen, L.; Wang, H.; and You, *J. Anal. Chem*. **2017**, *89*, 8509–8516.

[29] Zhang, P.; Huang, H.; Banerjee, S.; Clarkson, G. J.; Ge, C.; Imberti, C.; Sadler, and Peter J. *Angew. Chem., Int. Ed.* **2019**, *58*, 2350–2354.

[30] Toda, N.; Asano, S.; and Barbas, C. F. *Angew. Chem., Int. Ed.* **2013**, *52*, 12592−12596.

[31] Shen, B.; Xu, K.; Liu, L.; Raab, H.; Bhakta, S.; Kenrick, M.; Parsons-Reponte, K. L.; Tien, J.; Yu, S.; Mai, E.; Li, D.; Tibbitts, J.; Baudys, J.; Saad, O. M.; Scales, S. J.; McDonald, P. J.; Hass, P. E.; Eigenbrot, C.; Nguyen, T.; Solis, W. A.; Fuji, R. N.; Flagella, K. M.; Patel, D.; Spencer, S. D.; Khawli, L. A.; Ebens, A.; Wong, W. L.; Vandlen, R.; Kaur, S.; Sliwkowski, M. X.; Scheller, R. H.; Polakis, P.; and Junutula, J. R. *Nat. Biotechnol.* **2012**, *30*, 184−189.

[32] Zhao, Z.; Tao, X.; Xie, Y.; Lai, Q.; Lin, W.; Lu, K.; Wang, J.; Xia, W.; and Mao, Z.-W. *Angew. Chem., Int. Ed.* **2022**, e202202855.

[33] Chen, Y.; Tsao,K.; Acton, S. L.; and Keillor, J. W. *Angew.Chem. Int. Ed.* **2018**, *57*, 12390–12394.

[34] Shi, M.; Fu, Z.; Pan, W.; Chen, Y.; Wang, K.; Zhou, P.; Li, N.; and Tang, B. *Angew. Chem., Int. Ed.* **2021**, *60*, 13564–13568.

[35] Li, M.-Y.; Li, K.; Liu, Y.-H.; Zhang, H.; Yu, K.-K.; Liu, X.; and Yu, X.-Q. *Anal.Chem.* **2020**, *92*, 3262-3269.

[36] Nodling, A. R.; E. Mills, M.; Li, X.; Cardella, D.; Sayers, E. J.; Wu, S. -H.; Jones, A. T.; Luk, L. Y. P.; and Tsai, Y. -H. *Chem. Commun.* **2020**, *56*, 4672−4675.

[37] Chen, L. B. *Annu. Rev. Cell Biol.* **1988**, *4*, 155−181.

[38] Modica-Napolitano, J. S.; and Aprille, J. R. *Adv. Drug Delivery Rev.* **2001**, *49*, 63−70.

[39] Saha, P. C.; Das, R. S.; Chatterjee, T.; Bhattacharyya, M.; and Guha, S. *Bioconjugate Chem.* **2020**, *31*, 1301− 1306.

[40] Saha, P. C.; Bera, T.; Chatterjee, T.; Samanta, J.; Sengupta, A.; Bhattacharyya, M.; and Guha, S. *Bioconjugate Chem.***2021**, *32*, 833−841.

[41] Bradford, M. M. *Anal. Biochem.* **1976**, *72*, 248−254.

[42] Webb, B.; and Sali, A. *Curr. Protoc. Bioinforma.* **2014**, *47*, 5.6.1-5.6.32.

[43] Laskowski, R. A.; MacArthur, M. W.; Moss, D. S.; and Thornton, J. M. *J. Appl. Crystallogr.* **1993**, *26*, 283–291.

[44] Phillips, J. C.; Hardy, D. J.; Maia, J. D. C.; Stone, J. E.; Ribeiro, J. V.; Bernardi, R. C.; Buch, R.; Fiorin, G.; Hénin, J.; Jiang, W.; McGreevy, R.; Melo, M. C. R.; Radak, B. K.; Skeel, R. D.; Singharoy, A.; Wang, Y.; Roux, B.; Aksimentiev, A.; Luthey-Schulten, Z.; Kalé, L. V.; Schulten, K.; Chipot, C.; and Tajkhorshid, E. *J. Chem. Phys.* **2020**, *153*, 044130.

[45] Vanommeslaeghe, K.; Hatcher, E.; Acharya, C.; Kundu, S.; Zhong, S.; Shim, J.; Darian, E.; Guvench, O.; Lopes, P.; Vorobyov, I.; and Mackerell, A. D. *J. Comput. Chem.* **2009**, *31*, 671–690.

[46] Sousa, S. F.; Fernandes, P. A.; and Ramos, M. J. *Proteins Struct. Funct. Bioinforma.* **2006**, *65*, 15–26.

[47] Matsuyama, S.; Llopis, J.; Deveraux, Q. L.; Tsien, R. Y.; and Reed, J. C. *Nat. Cell Biol.* **2000**, *2*, 318−325.

[48] Santo-Domingo, J.; and Demaurex, N. *J. Gen. Physiol.* **2012**, *139*, 415−423.

[49] Wang, L.; Tran, M.; D'Este, E.; Roberti, J.; Koch, B.; Xue, L.; and Johnsson, K. *Nat. Chem.* **2020**, *12*, 165–172.

[50] Lukinavicius, G.; Reymond, L.; Umezawa, K.; Sallin, O.; D'Este, E.; Gottfert, F.; Ta, H.; Hell, S. W.; Urano, Y.; and Johnsson, K. *J. Am. Chem. Soc.* **2016**, *138*, 9365−9368.

[51] Collot, M.; Fam, T. K.; Ashokkumar, P.; Faklaris, O.; Galli, T.; Danglot, L.; and Klymchenko, A. S. *J. Am. Chem. Soc.* **2018**, *140*, 5401−5411.

[52] Moseng, M. A.; Nix, J. C.; and Page, R. C. *J. Phys. Chem. B* **2019**, *123*, 3383–3396.

[53] Sun, X.; Riccardi, L.; De Biasi, F.; Rastrelli, F.; De Vivo, M.; and Mancin, F. *Angew. Chem., Int. Ed.* **2019**, *58*, 7702–7707.

[54] Wang, E.; Sun, H.; Wang, J.; Wang, Z.; Liu, H.; Zhang, J. Z. H.; and Hou, T. *Chem. Rev.* **2019**, *119*, 9478–9508.

Chapter 7

Summery and Outlook

Development of organelle targeting fluorophores that can selectively target and stain particular cellular compartments such as mitochondria, lysosome, Golgi apparatus, endoplasmic reticulum, etc., has become an emerging field of current research. In this thesis I have mainly focused on the design and synthesis of symmetrical as well as unsymmetrical cyanine fluorophores that can selectively target and image cellular mitochondria. For the development of such effective mitochondriotropics (mitochondria targeting agents), two important parameters, such as extraordinary biophysical membrane property of mitochondria ($\Delta\Psi_m$ −150 to −180 mV for normal cell and $(\Delta\Psi_m)_{cancer}$ ~ –220 mV) and the lipophilicity of the targeting molecules, have been considered. Moreover, the mitochondrial target specificity of the synthesized cyanine probes have been established by colocalization experiments carried out with commercially available mitochondria-targeting agents using confocal laser scanning microscopy (CLSM).

Several cyanine-peptide conjugates anchoring with mitochondria selective lipophilic cationic triphenylphosphonium (TPP^+) targeting moiety have also been developed, which selectively accumulate inside the malignant mitochondria driven by a large negative inner mitochondrial membrane potential [$(\Delta\Psi_m)_{cancer}$ ~ –220 mV]. After reaching the CAC these peptide conjugated fluorophores self-assemble to form supramolecular secondary nanostructure inside the malignant mitochondria and trigger mitochondrial dysfunction initiated cellular apoptosis. Annexin V-FITC/PI apoptosis detection assay was used to determine the signal pathway of mitochondria targeted cellular dysfunction.

In this thesis, I have also reported a water soluble lipophilic cationic dual targeting NIR unsymmetrical cyanine-5 probe conjugated with maleimide and triphenylphosphonium (TPP^+) functionalities for selective targeting and

labeling of cysteine (Cys) exposed proteins inside the live cell mitochondria. These fluorescently modified proteins obtained by such spatially limited chemoselective reactions are then identified by in-gel fluorescent assay and further characterised by MALDI-TOF-MS carried out with Cy-5-Mal/TPP^+ treated A549 cell lysate to confirm their localization in live cells.

The novel observations of this thesis are:

- Water-soluble mitochondria selective molecules that consist of a target-specific moiety anchor with a near-infrared (NIR) imaging agent through variable spacer length has been synthesized and characterized. The uptake of cyanine-5 (Cy-5) dye into mitochondria exhibit clear chain-length dependence, the Cy-5b with longer alkyl chain and higher partition coefficient (log *P*) is the most effective for mitochondrial targeting. Submicromolar concentration of the targeting dye is enough to localize and stain mitochondria within minutes. Moreover, these symmetrical NIR cyanine dyes are also useful for determination of mitochondrial membrane potential via monitoring the mitochondrial membrane depolarization process.
- I have used a MW-assisted SPPS protocol for the rapid and effective synthesis of unsymmetrical NIR Peptide/Cyanine conjugate. These self-assembling peptide-based molecules forming visible and NIR emitting nanotubes are used for selective mitochondria targeting and imaging. These bio-functional nanotubes at the specific intracellular site hold promising approaches to control cellular function and fate. This unique bio-inspired NIR fluorescent peptide-based nanotube may lead to potential methods for image-guided organelle specific delivery, nanobiotechnology in cancer, and targeted nanotheranostic applications. Meanwhile, mitochondria targeted supramolecular chemistry is utilized to trigger programmed cell death.

- I have demonstrated dual targeting approach by introducing a maleimide and TPP^+ conjugated biocompatible ultra-bright NIR fluorescent probe Cy-5-Mal/TPP^+ that selectively localize and stain in live cell mitochondria as well as specifically label the exposed thiols of Cys containing mitochondrial proteins via thiol-maleimide bioconjugation chemistry. Moreover, due to excellent photophysical property, good water solubility, minimum cytotoxicity at lower concentration alongside specific thiol-maleimide bioconjugation chemistry make Cy-5-Mal/TPP^+ probe a perfect choice for detecting and tracing mitochondrial exposed thiol containing protein location, long-term live cell multicolour imaging, tracking and monitoring of mitochondrial morphology as well as dynamics during various biological and pathological conditions in live cells.

List of Publications and Research Works Included In the Thesis:

As a First Author:

1. Targeting and Imaging of Mitochondria Using Near-Infrared Cyanine Dye and Its Application to Multicolor Imaging**.** **Pranab Chandra Saha**, Tanima Chatterjee, Rudradip Pattanayak, Rabi Sankar Das, Ayan Mukherjee, Maitree Bhattacharyya, and Samit Guha*****. *ACS Omega*, **2019**, *4*, 14579−14588.

2. Supramolecular β-Sheet Forming Peptide Conjugated with Near-Infrared Chromophore for Selective Targeting, Imaging, and Dysfunction of Mitochondria. **Pranab Chandra Saha**, Rabi Sankar Das, Tanima Chatterjee, Maitree Bhattacharyya, and Samit Guha*. *Bioconjugate Chem.* **2020**, *31*, 1301−1306.

3. Supramolecular Dipeptide-Based Near-Infrared Fluorescent Nanotubes for Cellular Mitochondria Targeted Imaging and Early Apoptosis. **Pranab Chandra Saha**, Tapas Bera, Tanima Chatterjee, Jayeeta Samanta, Arunima Sengupta, Maitree Bhattacharyya, and Samit Guha***.** *Bioconjugate Chem.* **2021**, *32*, 833–841.

4. Near-Infrared Unsymmetrical Cyanine Maleimide Conjugate for Live Cell Mitochondria Targeted Imaging and Labeling of Mitochondrial Thiol Exposed Proteins. **Pranab Chandra Saha**, and Samit Guha***** (manuscript under preparation)**.**

List of Publications and Research Works That Not Included In the Thesis:

As a Second Author:

1. Design and Synthesis of Near-Infrared Mechanically Interlocked Molecules for Specific Targeting of Mitochondria. Rabi Sankar Das, **Pranab Chandra Saha**, Nayim Sepay, Ayan Mukherjee, Sudipta Chatterjee, and Samit Guha*****. *Org. Lett.* **2020**, *22*, 15, 5839–5843.

2. Acidic pH-Activatable Visible to Near-Infrared Switchable Ratiometric Fluorescent Probe for Live-Cell Lysosome Targeted Imaging. Ayan Mukherjee, **Pranab Chandra Saha**, Rabi Sankar Das, Tapas Bera, and Samit Guha***.** *ACS Sens.* **2021**, *6*, 2141–2146.

3. Construction of Self-Assembling Lipopeptide-Based Benign Nanovesicles to Prevent Amyloid Fibril Formation and Reduce Cytotoxicity of GxxxGxxxGxxxG Motif. Tapas Bera, **Pranab Chandra Saha**, Tanima Chatterjee, Samiran Kar and Samit Guha***.** *Bioconjugate Chem.* **2022,** *33*, 1201−1209.

PRESENTATION/PARTICIPATION IN INTERNATIONAL/NATIONAL/SYMPOSIUM/ CONFERENCES:

1. Poster presentation "***Near-Infrared Self-Assembling Peptide For SelectiveTargeting of Mitochondria***". Pranab Chandra Saha, and Samit Guha*. International Conference on Chemistry on Chemistry for Human Development (ICCHD-2020) held at Heritage Institute of technology, Kolkata, India, 9–11th January, 2020.

2. Poster presentation "***Amyloid-β Peptide Fragment Conjugated With Near-Infrared Chromophore For Selective Targeting And Imaging Of Mitochondria***". Pranab Chandra Saha, Rabi Sankar Das, Ayan Mukherjee, Tapas Bera, and Samit Guha*. National Seminar on Emerging Trends in Chemical Sciences under Centre for Advanced Studies II Program, Organized by Department of Chemistry, Jadavpur University, Kolkata-700032 on January 07, 2020.